
STRA Conference Proceedings 2023
Email: convener@eurasiaresearch.info
Website: https://straevents.org/

Presidential Note

On behalf of the members and office bearers of Scientific and Technical Research Association (STRA), it is a pleasure to welcome the Conference participants whose research papers are the great contribution into the work of the Association. Being an international community of researchers, practitioners, students and educationists, STRA is promoted by Eurasia Research, and concentrates on the development of innovative approaches in the field of science and technology. The purpose of STRA gatherings is bringing together worldwide researchers and professionals, encouraging intellectual progress and creation of the opportunities for networking and collaboration. As such, I strongly appeal all participants, whether this is your first time at our Conference or you have attended in the past, to make the most of this opportunity and to take the time to connect, collaborate, and communicate with fellow attendees. The STRA conferences serve as an outstanding forum to share ideas, which in turn have the potential to become extraordinary scientific and technological innovations for the benefit of humanity. In closing, I wish you an enjoyable, memorable, and productive time at the Conference and look forward to the partnerships that result from your networking and discussions.

Prof. Liudmyla Gryzun

STRA President, PhD & Post-Doctoral Degree in Pedagogical science

Full Professor of Simon Kuznets Kharkiv National University of Economics

Information Systems Department (Kharkiv, Ukraine)

Table of Contents:

I.

Scientific and Technical Research Association (STRA) is an international community of researchers, practitioners, students, and educationists for the development and spread of ideas in the field of science and technology.
STRA is promoted by Eurasia Research. STRA aims to bring together worldwide researchers and professionals, encourage intellectual development, and treat opportunities for networking and collaboration. These objectives are achieved through academic networking, meetings, conferences, workshops, projects, research publications, academic awards, and scholarships.
The driving force behind this association is its diverse members and advisory board, who provide inspiration, ideas, efforts and drive collaborations. Scholars, Researchers, Professionals are invited to become a member of STRA and join this ever-growing network, working for benefit of society and research with the spirit of sharing and mutual growth.

Salient Features:

- 15000 + and growing network of professionals
- Professional and Experienced team
- Conferences in Asia, Europe & Africa
- Events at reputed institutes and grand venues
- Lifetime membership
- Strong Social Media Platform for networking
- Young Researcher Scholarships
- Research publication in international journals

II. PRESIDENT

Dr. Liudmyla Gryzun, Full Professor, Information Systems Department, Simon Kuznets Kharkiv National University of Economics, Kharkiv, Ukraine

VICE-PRESIDENT

Dr. Elza M M Fonseca, Faculty of Engineering, Laeta, Inegi, Polytechnic Institute of Bragança, Portugal

Prof. Bahaa Talaat Shawky, Microbial Chemistry Department, Genetic Engineering and Biotechnology Research Division, National Research Centre, Dokki, Giza, Egypt

III. STRA COMMITTEE MEMBERS

1.	Asst. Prof.-Ing. Ralph Hammann LEED A.P.	Thomas D. Hubbard Professor in Architecture, University of Illinois at Urbana-Champaign
2.	Dr. Elza M M Fonseca	Faculty of Engineering, Laeta, Inegi, Polytechnic Institute of Bragança, Portugal
3.	Prof. Bahaa Talaat Shawky	Microbial Chemistry Department, Genetic Engineering and Biotechnology Research Division, National Research Centre, 33 El Bohouth Street (former El Tahrir Street), Dokki, Giza, 12622, Egypt
4.	Dr. Hidayatul Aini Binti Zakaria	School of Ocean Engineering, Universiti Malaysia Terengganu, Malaysia
5.	Asst. Prof. Mohammed Alsumiri	Department of Electrical and Electronics Engineering Technology, Yanbu Industrial College, Yanbu, Saudi Arabia
6.	Dr. Ersin Aytac	Department of Environmental Engineering, Faculty of Engineering, Bulent Ecevit University, Zonguldak, Turkey
7.	Dr. Syafaruddin	Department of Electrical Engineering, Universitas Hasanuddin, Indonesia
8.	Dr. Melfei Bungihan	College of Teacher Education, Quirino State University, Diffun, Quirino, Philippines
9.	Dr. Sivakumar Naganathan	Civil Engineering, Universiti Tenaga Nasional, Kajang, Selangor, Malaysia
10	Asst. Prof. Jacqueline E. Hilario	Department of Environmental Science, School of Arts, Sciences and Teacher Education, Emilio Aguinaldo College, Manila, Philippines
11	Asst. Prof. Saratha Sathasivam	School of Mathematical Sciences, Universiti Sains Malaysia, Penang, Malaysia
12	Diena Noviarini	Faculty of Economics, State University of Jakarta, Indonesia
13	Dr. Muharrem Karaaslan	Ph.D. Physics Department from the University of Cukurova, Adana, Turkey
14	Dr. Anna Gyulkhandanyan	Department of Pathological Biochemistry, Group of Bioengineering, Institute of Biochemistry of the National Academy of Sciences of Armenia, Yerevan, Armenia

15	Dr. Paulo A. G.Piloto	Professor, Dep. of Applied Mechanics, Polytechnic Institute of Bragança Campus Santa Apolónia, 5300-253 Bragança, Portugal
16	Soumyajit Goswami	Sr. Advisory Consultant, IBM, India
17	Dr. Iman Farshchi	Head of School, School of Civil, Engineering, Linton University College, Malaysia
18	Aminur Rahman	Institute of Bioscience, Universiti Putra Malaysia, 43400 UPM Serdang, Selangor, Malaysia
19	Prof. Azilawati Jamaludin	Research Scientist, National Institute of Education, 1 Nanyang Walk, Singapore
20	Shorouq Ahmed	Chemist & Research Associate, Nanotechnology and Advanced Material Research Program (Nam), Energy and Building Research Center (Ebrc) Kuwait Institute for Scientific Research, Kuwait
21	Prof. (Dr.) Hamid Ali Abed Al-asadi	Computer and Communication Network Engineering Ph.D. Computer Science Dept., Education College for Pure Science, Basra University, Basra, Iraq
22	Ir. Dr. Adjunct Prof. Nor Halim Bin Hasan	Deputy Director, Department of Occupational Safety and Health Seremban, Negeri Sembilan, Malaysia
23	Hamed Taherdoost	Ph.D. of Computer Science Phd of Management Information System Master of Information Security, CEO at Hamta Business Solution Sdn Bhd / Ahoora Ltd
24	Dr. Selcuk Gumus	Chemistry, Yuzuncu Yil University, Van, Turkey
25	Dr. Aysegul Gumus	Chemistry, Yuzuncu Yil University, Van, Turkey
26	Associate Professor Dr Sallehuddin Ibrahim	Department of Control and Mechatronic Engineering, Faculty of Electrical Engineering, University Technology Malaysia, Skudai, Johor, Malaysia
27	Dr. S. Balamurugan	Director-Research &Development, Mindnotix Technologies, India
28	Dr. Mohammad Arif Kamal	Associate Professor, Architecture Section, Aligarh Muslim University, India
29	Dr. Anirban Das	Professor, Department of Computer Science, University of Engineering & Management, Kolkata, India
30	Dr. Yousef Daradkeh	Associate Professor and Assistant Dean for Administrative Affairs,

		Department of Computer Engineering and Networks, Prince Sattam bin Abdulaziz University (PSAU) - KSA
31	Cecília R.C. Calado	Professor, ISEL-Instituto Superior de Engenharia de Lisboa, Instituto Politécnico de Lisboa, Lisboa, Portugal
32	Professor Dr. Hjh. Norma Binti Alias	Ibnu Sina Institute for Fundamental Science Studies, 81310 Technology University of Malaysia, Skudai, Johor, Malaysia
33	Dr. Liudmyla Gryzun	Full Professor of Computer Science Department, G.S. Skovoroda Kharkiv National Pedagogical University, Kharkiv, Ukraine
34	Malini Nair	Lecturer, Faculty of Business, Higher Colleges of Technology, Sharjah Women's College, UAE
35	Yin Ling Lai	Dean, Faculty of Engineering and Quantity Surveying, INTI International University, Nilai, Malaysia
36	Ramin Masoudi	Assistant Professor, Department of Mechanical Engineering, American University in Dubai, Media City, Dubai, UAE
37	Ing. Ts. Dr. Mohd Faisal Hushim	Lecturer, Automotive & Combustion Synergies Group (ACSG), Faculty of Engineering Technology, Universiti Tun Hussein Onn, Parit Raja, Malaysia
38	Dr. (Mrs) W. G. Samanthi Konarasinghe	Institute of Mathematics and Management, Sri Lanka

IV. PREFACE:

Scientific & Technical Research Association (STRA) is a conglomeration of academia and professionals for promotion of research and innovation, creating a global footprint. STRA aims to bring together worldwide researchers and professionals, encourage intellectual development and providing opportunities for networking and collaboration. These objectives are achieved through academic networking, meetings, conferences, workshops, projects, research publications, academic awards and scholarships. STRA strives to enrich from its diverse group of advisory members. Scholars, Researchers, Professionals are invited to freely join STRA and become a part of a diverse academic community, working for benefit of academia and society through research and innovation.

For this conference around 40 Participants from around 11 different countries have submitted their entries for review and presentation.
STRA has now grown to 16,450 followers and 9500 members from 85 countries.

Membership in our scholarly association STRA is chargeable.
List of members: https://straweb.org/membership/list-of-members/
Membership Application form link: https://straevents.org/membership?association=stra

Proceedings is a book of abstracts, all the abstracts are published in our conference proceedings a day prior to the conference.
You can get our conference proceedings at: https://straweb.org/conference/proceedings/

We hope to have an everlasting and long-term friendly relation with you in the future.
In this context we would like to share our social media web links: https://www.facebook.com/eurasiaresearch/

You will be able to freely communicate your queries with us, collaborate and interact with our previous participants, share and browse the conference pictures on the above link.
Our mission is to make continuous efforts in transforming the lives of people around the world through education, application of research & innovative ideas.

Editor: Dr. Anupam Krishna

ISSN: 2457-0648

STRA Full name: - Scientific & Technical Research Association

Address: - B-305 South Block Eurasia Research World Trade Park, Malviya Nagar Jaipur, India

E-mail: convener@eurasiaresearch.info

Conference website- https://straevents.org/stra

The recommended citations:

Author Surname, First Initial. Second Initial. (Year). Conference paper title. In Editor First Initial. Editor Surname (Ed.), Proceedings Book Title (pp. page range of paper). Place of Publication: Publisher.

V. PUBLICATION PROCESS:

All accepted original research papers in the English Language will be published in selected journals as per the publication policy, as available on the conference website. Once you receive the Invitation/ Acceptance letter that means your full paper is also accepted for publication in an International Journal, if you follow the communicated editorial instructions/ guidelines.

The journal publication will be peer-reviewed, checked for plagiarism, indexed, archived, open access, referenced by CrossRef and will carry ISSN number and DOI.

Even if your full paper is not yet ready, you may participate in the desired conference with your abstract. The abstract must contain the following:

- Article Title
- Full Names/ Emails/ Affiliations of the authors
- Abstract in 100-300 words
- 3-7 Keywords
- You may update your submitted abstract/ title/ co-authors/ submit your full-paper on a later stage (before the conference).

You may submit your full original paper for publication in the conference journal, when it is complete, till the conference date. The last date of submission is the conference day itself. While submitting the full paper, please provide the following in the email:

- Full paper in MS Word format. (Ideally, a research paper should be 2500-3000 words).
- Details of 2 reviewers with their names, affiliations, contact numbers and email IDs (If possible send two emails for each reviewer).
- Duly filled and scanned the 'Consent to Publish' form with a handwritten signature.

We follow the following steps for publication in our associated International Journals. The publication process takes around 70 days, starting from the end of the conference.

A list of registered papers is sent to all the participants of the conference within a week's time after the conference. Please see, if your paper is included in the list. If not, please write back to us for inclusion. This list would also mention for any deficiency/incompleteness found in the submitted paper. You would be given 10 days to return your complete papers/ required information.

After this, the editorial team would send all complete papers for review (usually 5-7 reviewers). The review process takes around 30 days.

Following this, our editor would send the editorial comments/ suggestions to the corresponding author. Please improve the paper as indicated in the review and send it back to us within 10 days.

If the paper received is complete in all regards as per the comments/ suggestions, it would be

sent for final publication, else we would send it again to you and finally, 5 days would be given to you for its improvement.
Finally, the paper is published and the authors are informed about the published paper by email, which contains the paper URL, DOI, Citation, and other related information.

If you fail to meet the deadlines/ correct the paper as per review comments, the paper may be rejected or it will be postponed for publication in the next issue. Normally, the entire process takes around 70 days.

Authors may request the conference secretariat for withdrawing their paper, for publishing it elsewhere (in the journal of their choice). In such cases, the requested papers are removed from the publication process. The withdrawal requests may be given to the conference secretariat before the commencement of the publication process (7 days after the conference).

Publishing Cover

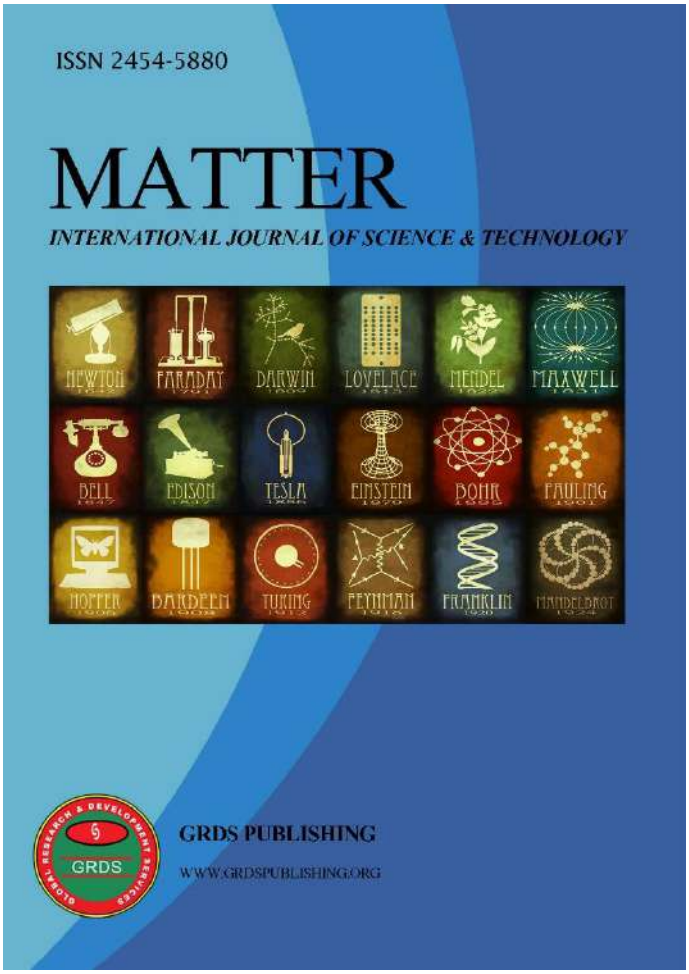

VI. ACKNOWLEDGEMENT

Our sincere thanks go to our outstanding supporters who made this great and interesting conference possible.

VII. STRA INSTITUTIONAL MEMBERS

VIII. KEYNOTE SPEAKERS 2023

Some special thanks go to our outstanding Key-Note speakers, not only for their inspiring andhighly interesting presentations but also for their input and contributions in the discussions and Q&A sessions during the conference:

Topic: Flexible Approach to Strategic Planning for Modern Business Organization

Dr. Rawani is Director of National Institute of Technology Raipur (India). He has received his M.Tech. in Industrial Engineering and Management from I.I.T. Kharagpur and Ph.D. in Strategic Management from I.I.T. Delhi. He has about 40 years of teaching/research and administrative experience of educational institutes. Dr. Rawani has published more than one hundred and fifty research papers in International/National Journals and International Conferences. He has produced nine Ph.D. under his supervision. He has delivered invited lectures in many countries including Switzerland, Singapore, Malaysia, China, Mauritius, Dubai, USA, Hong Kong, Thailand and Indonesia. He has served as reviewer for many International Journals and conferences. Dr. Rawani is conferred with fellowship award by Indian Institute of Industrial Engineering, Mumbai for outstanding contribution in promotion of Industrial Engineering Profession. In 2022, Dr. Rawani has been conferred with the 'Education Leadership Award' by World Education Congress, 'Exemplary Leadership Award' by APAC News Network, 'Director of the year' Award by Universal Mentors Association and 'Shiksha Ratna Award' by Reverie Language Technologies. He was also conferred with 'International Corporate Leadership Award in the field of Education' in 2015 at Bangkok and with 'Pride of Asia International Award' in 2014 by Economic Growth Society of India. He has also received 'Rashtriya Gaurav Award' in 2010 by India International Friendship Society, India.

Prof A M Rawani
Director of National Institute of Technology Raipur, India

Topic: Would Be Quality Management and Organizational Excellence

Malini Nair is a Business Faculty at the Higher Colleges of Technology. She teaches classes in Quality, Auditing, Innovation & Entrepreneurship, Management and Leadership as well as Economics. She is interested in the use of interventions, technologies, and tools that facilitate group/team processes and lead to better task outcomes through Quality standards. She has developed and taught several courses related to Quality, HR, Innovation, Marketing and Economics to both MBA and undergraduate students. She is currently a member of the Program Advisory Committee for Quality at the University level. She is a Doctoral candidate pursuing her PhD in Business and Management. She has written several research papers and continues do so. She has received a SEED grant for one of her research papers. She is actively involved in Community projects and her forte is mentoring and encouraging her students to actively participate in these initiatives. Prior to her appointment as a faculty, she has an immense amount of industry experience especially in the retail sector in the UAE. She studied Economics Honors and attended the prestigious Birla Institute of Technology (BIT) in India where she obtained her Master's degree in Business Administration. She went on to work as a Group HR Manager and continued to teach as she believes in sharing the knowledge gained through the industry. Her initiatives at the college level have been highly commended.

Malini Nair
Co-Curriculum Chair for the Quality Program in the Business Division at Sharjah Women's Campus, United Arab Emirates

Topic: Are we Introducing Buildings and Technology to serve Humankind?

Saqer Sqour is a Professor in Architecture at the Department of Architecture, Al al-Bayt University, Jordan. A visiting Teacher at different universities such as UET, Lahore, Pakistan; Cairo University, Egypt; University of Jordan, Yarmouk University, and Tafilah Technical University, (in Jordan); and Al Yamamah University, Riyadh, Saudi Arabia. Worked as an Ex-Director of Architecture and Interior Architecture, Al-Yamamah University, Saudi Arabia.
Ex-Director of Municipal Affairs, Ex-Deputy Undersecretary and Advisor to the Minister, Ministry of Local Administration; Ex-Mayor of Tafilah Greater Municipality.

Dr. Saqer Sqour
Professor, Architecture Department, College of Engineering, Al al-Bayt University, Jordan

Topic: Facile Fabrication and Identification of Phyto-Based Materials for Environmental Remediation and Therapeutic Applications

Dr. (Mrs.) Fahmida Khan has been with Department of Chemistry, National Institute of Technology Raipur, India for the last 37 years and has been working in the position of Professor of Department of Chemistry. She has a Ph.D. in Chemistry and awarded merit certificate for her research paper by department of Atomic energy and Indian Chemical Society, and SERC visiting fellowship by Ministry of Science and Technology. She has competence and expertise in areas such as Teaching, Research, and has been serving many senior level administrative positions. Prof. Khan's Research focuses on nuclear chemistry, analytical chemistry, environmental chemistry, corrosion science, nanomaterials, DNA binding, drug designing, molecular docking, and molecular dynamics simulation of protein-ligand complexes. She has delivered several oral presentations at National and International conferences. She is the author and co-author of numerous peer-reviewed journal articles and book chapters. She serves an active member on Board of Governors, advisory boards and different committees of NIT Raipur, India and as well as for numerous reputed organizations in India.

Dr. (Mrs.) Fahmida Khan
Professor in Chemistry, Department of Chemistry, National Institute of Technology Raipur, India

Topic: Digitalization of Smaller Businesses

Shahryar Sorooshian has his BSc, MSc, and Ph.D. in industrial engineering, along with an MBA certificate in business analytics. In 2016, he became an accredited management consultant and, in 2018, passed the required assessments to become a certified professional in engineering management. later, he also became a Lean six sigma belt holder and a certified graduate technologist. He has been awarded an honorary professorship in management and industrial engineering in 2022. Consequently, most of his research and consultation works are now related to industrial management and business analytics. He has worked in industries, business schools, and universities in a variety of roles ranging from consultant to lecturer and professor. Currently, he is an associate professor in the Department of business administration (University of Gothenburg).

Associate Professor Shahryar Sorooshian
School of Business, Economics and Law, University of Gothenburg, Sweden

Topic: Serum Metabolomics to Discover Biomarkers of Diagnosis and Prognosis in Critically Ill Patients

Cecília Calado has a Ph.D. and an MSc in Biotechnology and a degree in Biochemistry. She is a professor at the Lisbon High Engineering Institute (ISEL- Instituto Superior de Engenharia de Lisboa, https://www.isel.pt/en/), where coordinates the BSc and MSc in Biomedical Engineering and the R&D Lab. in Medical Bioengineering. She presents a broad experience in R&D in the Development of Platforms to Discover Drugs and Diseases Biomarkers and Bioprocess Monitoring.

Cecília R.C. Calado
ISEL-Instituto Superior de Engenharia de Lisboa, Portugal

Topic: Improving the Handling of Humanitarian Disasters in the Banten

Diena Noviarini, is a renowned scholar from State University of Jakarta. She is also an advisory member of STRA. Diena Noviarini is working with the Ministry of Research and Technology as part of Ministry of Education and Cultural, Indonesia. She is a Lecturer in Public Sector Reform Program assignments which is ISO 9001:2008 and Researcher in State University of Jakarta, Indonesia since 2011. She is also a holder of series Research Intellectual Copyrights from the Ministry of Intellectual and Copyrights at a total of 9 Certificate of Copyrights. Her accomplishments are include – Graduate and Member of Young Leader Programme JICA 2010, the Indonesian Ministry of Research and Technology's Grant Year 2017, the Chair Associate of SICSSAM Korean Conference 2017 & the Keynote Speaker in ICSTR 2018 and ICSTR 2019, the Indonesian Ministry of Research and Technology's Grant Year 2018 and Indonesian Ministry of Education and Cultural in Public Society devotion Grant Year 2020.

Diena Noviarini
State University of Jakarta
Advisory Honorary member of STRA

Topic: Technological and Algorithmic Solutions for In-Door Navigation Problem in Modern University Campus

Dr. Liudmyla Gryzun is a Full Professor of Information Systems Department at National University of Economics preparing IT specialists for various branches of economy. Liudmyla earned a M.A. in Applied Mathematics from the State University of Kharkiv (Ukraine); PhD and Post-Doctoral Degree in Pedagogical science from National Pedagogical University of Kharkiv (Ukraine). Her sphere of research is focused on the synchronized curriculum and holistic educational content design in higher education; Artificial Intelligence application to pedagogical problems solution; Petri networks apparatus as a tool for modelling in education; IT tools for inquiry-based and holistic learning etc. Dr. L. Gryzun's recent successful contributions include: (1) work as an international expert of the Open European-Asian Research Analytics Championship under the Program of the International Academy of Sciences and Higher Education (London, UK) (2012-2017); (2) participation in the European educational fair for STEM teachers "Science on the stage" (2019); (3) work as an invited speaker of the International internship "Digital future: blended learning" organized by DAAD German Academic Exchange Service (2022-2023); (4) work as a member (since September 2021 as a President) of the International organization Scientific and Technical Research Association (STRA), presenting the results of her research as a Keynote speaker at the at the number of Eurasia Research International conferences (2018 – 2023).

Dr. Liudmyla Gryzun
PhD & Post-Doctoral Degree in Pedagogical Science
Full Professor of Simon Kuznets Kharkiv National University of Economics, (Kharkiv, Ukraine), Information Systems Department

Technological and Algorithmic Solutions for In-Door Navigation Problem In Modern University Campus

Dr. Liudmyla Gryzun

Department of information systems, Simon Kuznets Kharkiv National University of Economics, Kharkiv, Ukraine

Abstract: The work treats the problem of in-door navigation in the context of the development of mobile application

for efficient orientation in modern university campus. In the progress of elaboration of algorithmic and technological solutions, the peculiarities of the in-door navigation were analyzed. The capabilities of existing software implementing similar functions of this subject domain were evaluated. There were revealed some limitations of the said software. The specification of functional and non-functional requirements for the application for in-door navigation at university was provided. Its architecture was determined as a set of interconnected modules, for whose development proper interface, technological and algorithmic solutions were elaborated and highlighted. The main stages of design and development of the said application in the context of the elaborated solutions are presented. The functionality of the application is characterized and analyzed. It was concluded that during the design it became possible to overcome the main limitations inherent in similar software of indoor navigation. The results of the application implementation in the educational practice of a national university are presented. Feedback from the application users (university visitors of different categories) was collected during the approbation and analyzed. Users were asked to fill in a survey form evaluating the quality of implementation of both functional and non-functional requirements for the application on a five-point scale. As a result, there were revealed and realized the ways of the application improvement. The prospects for further research are formulated.

Keywords: in-door navigation, technological and algorithmic solutions, mobile application for navigation in university campus.

Topic: Research Prospects in the Field of Machine Learning and NLP

Dr. Ani Thomas is Professor in the Information Technology Department & also HOD (IT & MCA) at Bhilai Institute of Technology, Durg (C.G.). Her post-graduation is in the Computer Applications discipline from Govt Engg. College, Raipur. She was awarded a Doctoral degree in the Discipline of Computer Applications on "Automated Tool Design of Subjective Question Answering using Text Mining" in July 2013. She is the Dean of Computer and Information Technology now and was Chairperson, of the Board of Studies (Information Technology) in Chhattisgarh Swami Vivekananda Technical University for the past four years. She is the research guide of 8 PhD scholars and 3 have been awarded PhD degrees. She has conducted and delivered several Keynote sessions in ACM, ISTE and CCOST-sponsored workshops. She has been a Research paper Reviewer for IEEE-sponsored conferences and Faculty Coordinator for events conducted by many IITs. She is a Life fellow member of Professional bodies: 'The Indian Society for Technical Education' and 'The Computer Society of India' and also an Editorial board member of many journals. She got the best paper award at the national conference TECHNOVISION 2007. She and her team has bagged 2nd position in Slot filling task, a research software project competition organized by NIST, Govt. of USA. Dr. Thomas has teaching experience of 24 years and research experience of 15 years with areas of academic interest in Artificial Intelligence & Expert Systems, Natural Language Processing, and Machine Learning Using Text Mining. She has 6 Copyrights registered in the Computer Software category from Govt. of India and completed one Sponsored Project. She has published a number of research papers; authored one book; 2 book chapters in Scopus publications; 36 in International / National Journals and 30 in International Conferences / National Conference forums. She has organized several professional activities to date including Faculty Development Programs, Conferences and e-workshops.

Dr. Ani Thomas, Professor in Information Technology Department, HOD (IT & MCA), Bhilai Institute of Technology, Durg (C.G.), India

Topic: Generation Marketing, Z Generation, CSR Activities

Dr. Habil Garai-Fodor Mónika is having an academic career as an educator of the Tessedik Sámuel College as an assistant lecturer in 2003. During 2009-2016. She was vice-head of department of the Budapest Economics University (formerly Budapest Economics College), Institution of Marketing, as a college associate professor. Currently she is an associate professor at Obuda University Keleti Károly Faculty of Business and Management and she is the vice-dean of the faculty as well. Her main research and teaching areas are consumer behaviour, marketing communication, and marketing research. Apart from her duties in higher education she works for the business as well. She was lead researcher of the Radar Research International Marketing Advisor Co. Ltd., and she was the country director of communication by the Continental Hungaria Co. Ltd. for four years. Currently, she is an expert at the Profession Conference Organiser Co. Ltd., president of the Employer Branding Committee, furthermore, member of the Hungarian PR Committee's Employer Branding Section.

Dr Habil. Garai-Fodor Mónika
Dean, Associate Professor Keleti Károly
Faculty of Business and Management, Óbuda University
Budapest, Hungary

Topic: Digital Immortality and Future Research

Dr. Baloglu, completed her undergraduate at Technical University of Istanbul, her MBA in production management at University of Istanbul, and her PhD in Information Technology at University of Istanbul. She has experience of 15 years in production and technology management. She worked for various plants including manufacturing, service and consulting companies as middle or top manager. For instance, Ernst and Young Consulting Turkey is one of the companies, where she added important values within 5 years. Also she worked in SAP Business for a long time and managed various SAP/ERP projects in Turkey and also abroad. Now she is serving in ERP, CRM and e-business categories as senior consultant and lecturing at various universities. She gave the lectures and courses in the Universities of Bilgi, Işık and Yeditepe. Additional to these she is sometimes giving conference seminars and company trainings in her expertise areas. Dr. Baloglu has about 15 professional and academic papers, published in various technology magazines and books (10). And she currently works for Marmara University - Dept. of Business Informatics under title of Assoc. Prof and also lectures the some courses in Yeditepe University as part time lecturer such as e-business, innovation management, IOT, Agro IT, ERP, eSCM.

Assoc. Prof. Dr. Arzu Baloglu
IT Senior Mentor, Auditor and Author
Dept. of Industrial and Computer Engineering
Engineering Faculty, Marmara University, Istanbul, Turkey

Topic: Omics Application to Discover Biomarkers of Outcome of Critically Ill Patients

Cecília Calado, has a PhD and an MSc in Biotechnology, and a degree in Biochemistry. She is professor at the Lisbon High Engineering Institute (ISEL- Instituto Superior de Engenharia de Lisboa, https://www.isel.pt/en/), were coordinates the BSc and MSc in Biomedical Engineering and the R&D Lab. in Medical Bioengineering. She presents a broad experience in R&D in Development of Platforms to Discover Drugs and Diseases Biomarkers and Bioprocess Monitoring.

Cecília R.C. Calado
ISEL-Instituto Superior de Engenharia de Lisboa, Portugal

Topic: Education, Training and the Future of Work: Issues and Challenges in Southeast Asia

Assoc. Prof. Dr. Airil Haimi Mohd Adnan is currently on special attachment to the Ministry of Higher Education Malaysia as Senior Principal Assistant Director. A senior academic at Universiti Teknologi MARA (UiTM), Shah Alam, Malaysia, he is also Professor (III) at the Polytechnic University of the Philippines and recently inducted as Research Fellow at the Human Resources Development Corporation of Malaysia. As a multiple award winning researcher, writer and multidisciplinary social scientist with 23 years' of experience in the field of education, he supports the Education 4.0 movement and is holding / has held Visiting Scholar / Research Fellow / Adviser positions in Brunei, Indonesia, Singapore, and New Zealand. He has also produced 150+ international proceeding papers, journal articles, book chapters and books; written 500+ academic articles for ASEAN newspapers and magazines, and appeared 200+ times on ASEAN television and radio.

Dr Airil Haimi Mohd Adnan
Associate Professor, Universiti Teknologi MARA (UiTM)
Senior Principal Assistant Director, Ministry of Higher Education Malaysia
Professor (III), Polytechnic University of the Philippines

Topic: The Internationalization of Higher Education: Prospects, Challenges, and the Way Forward

Assoc. Prof Dr. Radzuwan holds a PhD in Education from the University of Nottingham, United Kingdom, and he pursued postdoctoral studies at the University of Leeds, exploring Applied Linguistics in an educational context. He is interested in researching teacher education, professional development, and contemporary discourse in online settings. He was nominated by Clarivate Analytics (Web of Science) for the Malaysia Research Star Award in the category of Research and Innovation Excellence (Researcher in Arts and Applied Arts) in 2019, 2021 & 2022. He is the Minister Counsellor of Education at the Embassy of Malaysia in Amman, Jordan and responsible for the internationalization of Malaysia's tertiary education in Jordan, Turkiye, Kuwait, Lebanon, Syria, and Palestine.

Dr. Radzuwan Ab Rashid
Associate Professor, Faculty of Languages and Communication
Universiti Sultan Zainal Abidin, Malaysi

Topic: Digital Dilemma: Navigating Youth Mental Health in the Age of Social Media

Dr. Abdelhak Senadjki is an esteemed Associate Professor of Economics at the Faculty of Business and Finance at Universiti Tunku Abdul Rahman (UTAR) in Malaysia. With his academic expertise and research experience, he has established himself as a well-respected scholar in the field of Economics. Dr. Senadjki holds a PhD from Universiti Sains Malaysia (USM) for his thesis titled 'Vulnerability to Poverty: A Study of Rural Population in Kelantan and Terengganu, Malaysia,' which he completed in 2013. He also received his Master of Economic Management from USM in 2008, and a bachelor's degree in Economics from University of Algiers in 2003. As an accomplished academician, Dr. Senadjki has received the USM fellowship from 2010 to 2013, during which he served as an academic researcher. His research interests include Energy Economics, Developmental Economics, Housing Economics, Health Economics, Employee Creativity and Innovation, and Organisational Culture. Dr. Senadjki has served in various leadership roles, including Head of Programme (Postgraduate Studies) from 01/01/2017 to 31/12/2018, Acting Head of Department of Economics from 01/02/2020 to 31/05/2020, and the Head of Postgraduate Programme PhD (Economics) from 23/03/2022 to date. Dr. Senadjki has contributed significantly to the academic community through his research and publications. He has published widely in various local and international refereed journals, WOS, Scopus, chapters in books, and research papers. His academic expertise is highly sought after, and he serves as a reviewer for several refereed journals, including the Journal of Islamic Accounting and Business Research, Journal of Development Career, International Journal of Social Economics, The Social Science Journal, Cogent Economics and Finance, Cogent Food and Agriculture, Journal of Poverty, Health Education and Behaviour Management, Sage Open, Academy of Accounting and Finance Studies Journal, Journal of Advances Management Research, International Review of Economics and Finance, Sustainability, Urban Science, Scientia Iranica, Sage Open, Social Responsibility Journal, Organizations and Markets in Emerging Economies, International Journal of Housing Markets and Analysis, Housing Studies, and others. Dr. Senadjki's contributions to the academic community have not gone unnoticed, and he has received several international and national awards. These awards include the 2019 Emerald Literati Awards, FIIB Business Review High Impact Research Award, Top Reviewer Awards (Cogent Economics & Finance), Best Papers Awards, Best Presenter Awards, and others. In addition to his academic achievements, Dr. Senadjki is also a Train-The-Trainer (TTT) Certified Trainer, showcasing his commitment to teaching and mentoring the next generation of scholars.

Dr. Abdelhak Senadjki
Associate Professor of Economics, Faculty of Business and Finance
Universiti Tunku Abdul Rahman (UTAR) in Malaysia

Topic: "Path of Happiness" Charitable Non-Governmental Organization for People with Developmental Disabilities Aged 18-65

Svetlana is a Ph.D. in Education Sciences, Associate Professor, lecturer of chair of Special Pedagogy and Psychology of Armenian State Pedagogical University SPU after Khachatur Abovyan. She is Vice Dean for Science and International Cooperation / Faculty of Special and Inclusive Education She attended 35 Professional pieces of training in Dubai, Barcelona /Spain/, USA /Boston, San Diego/, London, United Kingdom, Germany, Moscow, Ukraine /Kramatorsk/ etc. She has published 34 scientific articles, methodical manuals. Her more than 50 scientific articles have been published in national and foreign cited journals, as well as textbooks (for people with special educational needs, their families and professionals). She was awarded more than 50 diplomas, certificates and letters of thanks.

Svetlana S. Muradyan
Associate Professor, Ph.D. in Education Sciences,
Lecturer of Chair of Special Pedagogy and Psychology of ASPU, Armenia

Topic: Potential MLC901 as Adjuvant Treatment for Spinal Cord Injury

Dr. Dewa Putu Wisnu Wardhana completed her medical degree from Udayana University, Bali, Indonesia in 2009. In 2015 she was working as a Neurosurgery specialist in the Neurosurgery Department and as a Medical Faculty of Airlangga University, Surabaya, Indonesia in 2015. She has completed her Clinical Neurosurgery (and Spine Surgery) fellowship at Brain & Spine Clinic, Gleneagles Hospital, and Mt. Alvernia Hospital, Singapore in 2016 and Clinical Spine fellowship at Center of Minimally Invasive Spinal Surgery Shin-Yurigaoka General Hospital, Kanagawa, Japan. In 2017, she completed Clinical fellowship for Skull Base Surgery from the Department of Neurosurgery, Osaka City University, Graduate School of Medicine, Osaka, Japan. She has been a Neurospine consultant since 2021. She is appointed as an Editorial board on Ganesha Medicina journal in 2021. She has also been a reviewer board member in the following journals: Jurnal Kedokteran dan Kesehatan Indonesia/JKKI 2019, Neurologico Spinale Medico Chirurgico/NSMC journal 2019, Bali Medical Journal/BaliMedJ 2019.

Dr. Dewa Putu Wisnu Wardhana
Neurosurgeon, Lecturer, Universitas Udayana, Denpasar, Bali, Indonesia

Topic: Nurses' Knowledge and Skills in Safe and Quality Care for Patients with Spinal Cord Injury

Dr. Jennifer P. Reyes completed her Bachelor of Science in Nursing at St. Jude College, her Master of Arts in Nursing major in Nursing Administration at the Philippine College of Health and Sciences, Inc., and her Doctor of Education major in Educational Administration at the Pamantasan ng Lungsod ng Maynila and currently she is taking her 2nd Doctorate Degree – Doctor of Philosophy in Nursing at Philippine Women's University. She worked as a staff nurse to Head Nurse in the clinical area for 6 years (1998-2004) before joining the academe in June 2004. She rose from the rank and file, from Instructor III to Assistant Prof. III to Associate Professor II handling different nursing subjects in the classroom and clinical areas. She assumed various administrative positions as follows: designated as Nursing Laboratory Coordinator to College Secretary to Associate Dean. In 2014-2016 she was appointed as the Dean of the College Nursing for the undergraduate (BSN) and graduate programs (MAN). She was selected as one of the Young Leaders by the National Academy of Science and Technology, Philippines Department of Science and Technology to attend and participate in the Future Health Leader Workshop last November 2015. She was also invited as one of the HEIs representatives and served as Department of Health Partners on the following DOH Academy activity programs:

1. DOH 1st Partner's Forum at Manila Pavilion Hotel, UN Ave. Manila on June 30, 2016;
2. DOH 2nd Partner's Forum at Lewis Hotel, Clark Pampanga on October 26-28, 2016;
3. DOH Academy Orientation and Consultative Meetings at Selah Garden Hotel, Pasay City on February 28, 2017.

She is also one of the core team members of the HELP Program in Partnership with the Rock of Ages Ministry and Pamantasan ng Lungsod ng Maynila College of Nursing from January 2018 up to present-time. She does volunteer work by giving health education, life and spirit seminars, and gift-giving activities to persons deprived of liberty (prisoners) in the different prisons in Metro Manila, Philippines. Moreover, she Served/Invited as an Adviser/Panelist during Oral Defense for Undergraduate and Graduate Programs (Theses and Dissertation Proposals and Final Defense) under PLM CN and PLM CED and an International Paper Reviewer Member: GRDS Publishing, and an Invited Member of External Advisory Board USLS Journal – University of St. La Salle. She is also a Research Oral Presenter/ invited Keynote Speaker and Conference Chair at different International Research Conferences and has published research papers in local and international journals. She also co-authored published books: Title of Publication: Professional Education for Educators Across All Professions 2nd Edition (Co-Author) ISBN: 978-621-8084-45-2 and Title of Publication: Aliswag LifeLong Learning Series: Research Procedure Manual (For Graduate School) 2nd Edition (Co-Author) ISBN: 978-621-8084-45-2. Currently, she is a member of the PLM CN College Research Committee and Ang Nars Healthcare Workers CPD and Research Committee. She is also a member of different professional organizations: Life-time Member - Healthcare and Biological Sciences Research Association (HBSRA), Life-time Member - Philippine Nurses Association Inc. (PNA), Member – Eurasia Research Inc., Member – Professional Organization of Researchers and Educators of the Philippines (POREP), Member (Core Team) – Ang Nars Healthworkers Coalition, Member – Philippine Association of Nursing Authors for Clinical, Community Education and Administration(PANACCEA), Member – UNIFFIED Manila + Chapter, Member – Association of Higher Education Multidisciplinary Researchers, Inc., Member – Association of nursing Service Administrators of the Philippines, Inc. (ANSAP Inc.)

Dr. Jennifer Paule Reyes
Associate Professor II, College of Nursing
Pamantasan Ng Lungsod Ng Maynila, Manila, Philippines

IX. LIST OF ONLINE CONFERENCES

Online Live International Conference

21st February 2023

Video link for the Live Conference: [Click Here]

Participants from the following countries:

Online Live International Conference
17th March 2023

Video Link for the Live Conference: Click Here

Participants from the Following Countries:

Online Live International Conference

26th April 2023

Video Link for the Live Conference: Click Here

Participants from the Following Countries:

Online Live International Conference

03rd May 2023

Video Link for the Live Conference: Click Here

Participants from the Following Countries:

Online Live International Conference

12th May 2023

Video link for the Live Conference: [Click Here]

Participants from the following countries

Online Live International Conference

24th June 2023

Video link for the Live Conference: Click Here

Participants from the following countries

Online Live International Conference
04th July 2023

Video link for the Live Conference: Click Here

Participants from the following countries

Online Live International Conference

21st July 2023

Video link for the Live Conference: Click Here

Participants from the following countries

Online Live International Conference
10th August 2023

Video link for the Live Conference: Click Here

Participants from the following countries

Online Live International Conference

13 September 2023

Video link for the Live Conference: Click Here

Participants from the following countries

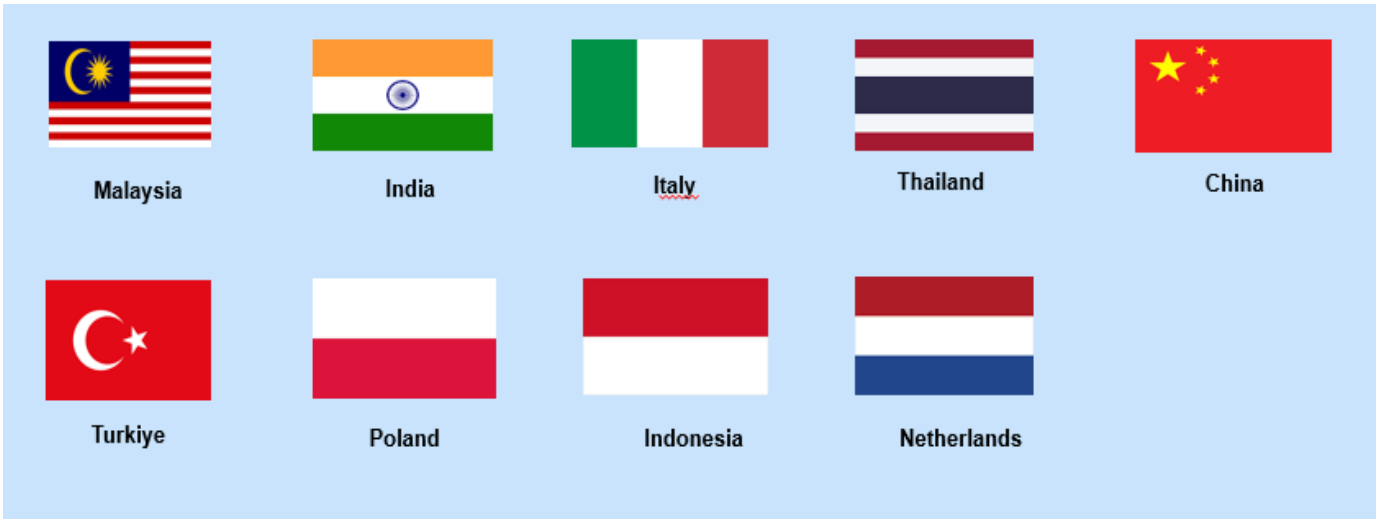

Online Live International Conference
27 September 2023

Video link for the Live Conference: Click Here

Participants from the following countries

Online Live International Conference
06th October 2023

Video link for the Live Conference: Click Here

Participants from the following countries

Online Live International Conference
21st November 2023

Video link for the Live Conference: Click Here

Participants from the following countries

Online Live International Conference
21st November 2023

Video link for the Live Conference: Click Here

Participants from the following countries

Online Live International Conference
04th December 2023

Video link for the Live Conference: Click Here

Participants from the following countries

Online Live International Conference
18th December 2023

Video link for the Live Conference: [Click Here]

Participants from the following countries

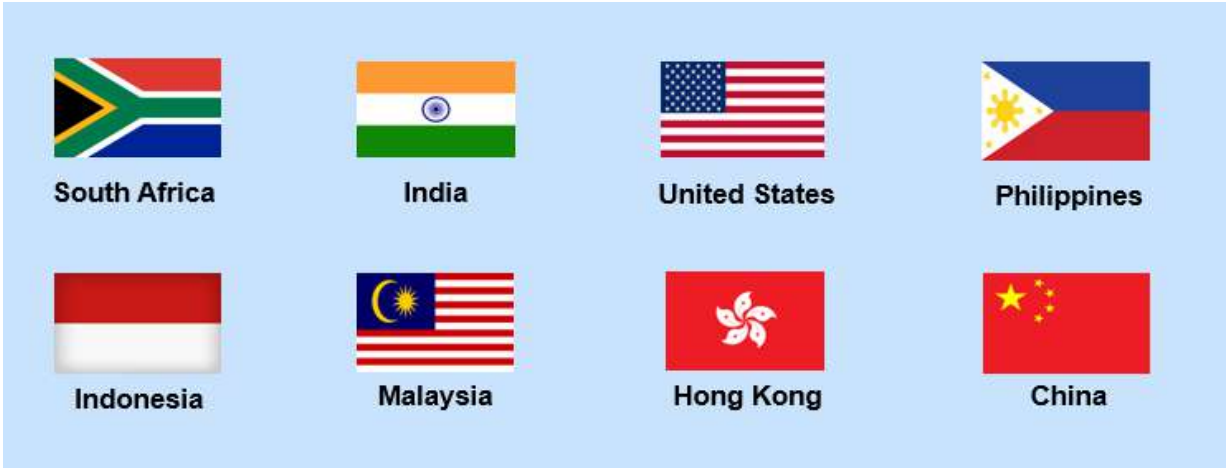

Online Live International Conference
19th December 2023

Video link for the Live Conference: Click Here

Participants from the following countries

X. LIST OF FULL PAPERS

Analysis of Fish Waste and Co-Substrate Mixture on Biogas Production and Solid Waste Reduction in an Anaerobic Digester

Iffah Nurfaiz
Department of Civil and Environmental Engineering, Faculty of Engineering, Universitas Indonesia, Depok, West Java, Indonesia

Cindy Rianti Priadi
Department of Civil and Environmental Engineering, Faculty of Engineering, Universitas Indonesia, Depok, West Java, Indonesia

Ayik Abdillah
Department of Civil and Environmental Engineering, Faculty of Engineering, Universitas Indonesia, Depok, West Java, Indonesia

Abstract: Indonesia is the second-largest global producer of marine resources, with over 62,388 Fish Processing Units (UPI) located around the country. In the management of marine products, fish waste constitutes approximately 30-40% of total fish weight and consists of heads, bones, fins, skin, and offal, whereas liquid waste can come from fish blood and fish wash water, both of which can be harmful to the aquatic environment and are a source of eutrophication in coastal areas. Anaerobic digester (AD) processing is an approach to generate biogas and digestate which is appropriate for fertilization. The study used two pilot scale reactors with 110 cm in diameter, 160 cm in height, and 1200 L in volume. The composition of fish waste, food waste, cow dung, and sawdust were used in the following ratios: 40: 40: 15: 5 (reactor A) and 30: 30: 20: 20 (reactor B). The objective of this study was to evaluate the effectiveness of the anaerobic co-digestion process in terms of reducing solids, increasing biogas production, and analyzing its composition. According to the results, there was a reduction in solid waste of 97.42% (reactor A) and 97.95% (reactor B). The daily production of biogas from reactors A and B is 155,8 and 133,56 liters, respectively. Methane yield in this result were 122.37 L.CH4/kg.VS (reactor A) and 131.76 L.CH4/kg.VS (reactor B). The results of the research indicate that there is not a significant difference between the composition ratios in reactor A and reactor B regarding solid reduction, biogas volume, or methane yield. As a result, the two composition ratios can be used to determine the composition of waste treatment using an anaerobic digester.
Keywords: Anaerobic Digester, Biogas, Fish Waste, Reactor

1. Introduction: Indonesia is a maritime country dominated by 77% of its territorial waters and 23% of its land area with 17,504 islands (Arianto, 2020). According to the Statistics and Information Data Center of the Ministry of Maritime Affairs and Fisheries (2022) states that Indonesia has a water area of 6,400,000 km2 consisting of 3,400,000 km2 of sovereign territory and 6,070,000 km2 of sovereign territory with a coastline length of 108,000 km (BPS, 2020). Indonesia is the second-largest fish producer in the world; 6.43 million tons of fish were caught there overall in 2020 (FAO, 2022). Based on data from the Statistics and Information Data Center of the Ministry of Maritime Affairs and Fisheries (2022), stated that there were approximately 62,388 Fish Processing Units (UPI) spread across Indonesia in the form of Micro, Small and Large Medium Enterprises (BPS, 2020). Fish waste management in Indonesia has not received much attention up to this point due to the country's generally still fairly conventional approach to fish management, which means that the industry's location near a fishing ground serves as a source of material. Furthermore, unawareness of fish waste processing is a significant contributing factor (Oktavia et al., 2012). In the management of marine products, fish waste is the biggest problem, because fish processing waste has a proportion of 30-40% of the total weight of fish consisting of heads, bones, fins, skin, and offal, while liquid waste can come from fish blood and fish wash water (Afreen & Ucak, 2020). This can be a threat to the aquatic environment if the waste produced is not managed properly, as a result it **s**can be one of the sources ofeutrophication in coastal areas because waste discharged directly into the sea causes excess nutrients. Basically, many efforts have been made to manage and utilize seafood waste, especially fish waste as a form of prevention of environmental pollution. For example, fish processing industry in the Rembang, Central Java that processes soft meat as an additive to making tempeh and rotten meat as animal feed, then in the coastal area of Kedungrejo Village, Muncar District, Banyuwangi Regency has built a fish waste processing plant that processes fish waste into fish oil, fish petis and organic bio-fish liquid fertilizer (Agustin, 2015) (Wulandari & Pramono, 2020). Using the technology of an Anaerobic Digester (AD) to produce biogas and digestate, a byproduct that can be used as fertilizer, is another alternative management method for fish waste treatment. Anaerobic digestion (AD) is a complex biological process in which anaerobic bacteria decompose organic matter in the environment with little or no oxygen. The products of anaerobic digestion are biogas and digested substrate, commonly called digestate, and are used as fertilizer in agriculture. Biogas is produced by anaerobic digestion of biodegradablematerials such as manure, sewage, plant materials,and crop residues. Waste feedstocks for biogasproduction can be solids, slurries, concentrated liquids and diluted. In fact, biogas is also made from residual organic matter from ethanol and biodiesel production. The yield of biogas from any substrateis highly dependent on the C/N ratio of the material, concentration, pH, temperature (Dioha et al., 2013). Biogas generally consists of 55-65% methane, 35-45% carbon dioxide, 0-3% nitrogen, 0-1% hydrogen, and 0-1% hydrogen sulfide (Salam, 2015). The technology known as anaerobic digester (AD) has been widely and successfully implemented throughout the world. Based on the findings of research by Cadavid- Rodríguez et al., (2019), the analysis's results estimate the annual energy production generated from using 509 tons of fish waste, producing 489 MWh of energy that can satisfy 230 fishing families' needs for cooking or electricity (Cadavid-Rodríguez et al., 2019). Based on the results of research conducted by Shodiq (2020) using two variations of the substrate mass composition of organic waste and fish waste in reactor A (100:0) and reactor B (80:20) with a 21 days of feeding period in a pilot scale reactor, reactor A and B havea Total Solid (TS) reduction value of 55.92% and 33.40%; and Volatile Solid Destruction (VSD) of 40.28% and 30.28%, respectively. The average results of biogas production and methane gas (methane yield) in reactors A and B are biogas volume of 69 L/kg.VS and 67 L/kg.VS and methane yield of 11 L.CH4/kg.VS and 8 L.CH4/kg.VS, respectively. Statistically, reactor A (100:0) produced more output regarding biogas production and methane yieldB (Shodiq et al., 2020). High concentration of ammonia and long-chain fatty acids (LCFA) found in fish waste could lower the production of methane gas during the anaerobic digestion stage of the biogas production process in anaerobic digesters(Kafle et al., 2013), consequently, resulting in low C/N circumstances. Therefore, in this study, additional substrates were used in the form of organic waste/food waste which has a C/N ratio of 11-27, sawdust which has a C/N value of 500 (Natalina et al., 2017) and cow dung, which, according to research findings by Dioha et al. (2023) has a C/N value of 24.

Apart from being caused by the C/N ratio factor, these substrates were chosen because they are easily available in Indonesia(Dioha et al., 2013). This research was carried out on a pilot scale in 2 (two) reactors (Reactors A and B) for 4 (four) months at Al Hikam Islamic Boarding School. The composition of fish waste, food waste, sawdust, and cow dung varied, were used to investigate to understand the effect of adding nutrients as a method of increasing biogas and reducing bacterial growth inhibitors, such as Volatile Fatty Acids (VFA). This study aimed to evaluate the anaerobic digester process in terms of solids reduction, biogas productivity, and performance.

2. Methodology:

2.1. Substrate: In this study, food waste used from Cimanggis Market, South Tangerang, Banten, which has been sorted and chopped to make it smaller. Fish waste used from King Fish Market, Depok, West Java, which has been sorted. The cow dung substrate used comes from a cattle farm in South Tangerang area. The sawdust used comes from the remaining wood sanding by wood craftsmen in Depok, West Java.

2.2. Reactor Design: The reactor was constructed out of cylindrical fiber and had dimensions of 110 cm in diameter, 160 cm in height, and 1200 L in volume. The reactor is divided into 2 (two) parts, namely the upper part with a height of 40 cm and the lower part with a height of 80 cm. Both parts are separated by a diaphragm to separate the substrate that has not been processed at the bottom and the substrate that has been processed at the top with a pipe located in the middle for the substrate channel that comes out due to pressure from the gas formed so that if overflows to the top. There is a gas outlet on top of the reactor, which can be controlled by an opening and closing gas valve. The pressure of the gas exiting the reactor is measured by a manometer (Priadi, C. R. , & Abdillah, 2019).

Figure 1: *Reactor Biogas Design Patent P00201910803*

2.3. Research Methods:

2.3.1 Preliminary Study: The initial characteristics of the substrate were tested in the preliminary study to ascertain its characteristics and content. It also served as a reference for calculating the mass of substrate to be used through mass calculation. The Total Solids (TS) and Volatile Solids (VS) characteristics of each substrate were tested initially, as shown in Table 1.

Table 1: *TS and vs. Measurement*

Item	TS (%)	VS (%)
Fish Waste	21	82
Food waste	23	97
Cow Dung	24	73
Sawdust	90	100

(Source: Author Testing, 2023)

In this study, the amount of substrate used as feeding or input material is determined by calculating the mass of the substrate, which necessitates testing the substrate's initial properties based on its TS and VS values. The percentage ratio of the composition used in this study in order is reactor A, namely 40: 40 : 15 : 5 and reactor.
B is 30: 30 : 20 : 20. Additionally, according to research by Bonanza & Sarto (2016),
2.5 kg VS/m3.day is the most ideal Organic Loading Rate (OLR) for feeding an Anaerobic Digester (AD) reactor during operation (Bonanza & Sarto, 2016). The following equation is used to calculate mass:

$$M = \frac{OLR \times V}{\%TS \times \%VS} \quad (1)$$

Description:

M = Input substrate mass (kg)

OLR = Organic loading rate (kg VS/m3.day) V = Reactor active volume (m3)

TS = Input TS concentration (%) VS = Input VS concentration (%)

The substrate mass calculation results are shown in Table 2, and before continuing on to the operational stage, C/N testing is carried out to determine whether the test results have met the necessary C/N ratio for biogas formation. According to research by Zulkarnaen et al. (2018), a good C/N ratio on the substrate is in the range of 27 to 35 (Zulkarnaen et al., 2018).

Table 2: *Substrate Mass Calculation*

Substrate	**Reactor A (kg) (40 : 40 : 15 : 5)**	**Reactor B (kg) (30 : 30 : 20 : 20)**
Fish Waste	3.56	1.89
Food Waste	3.56	1.89
Cow Dung	1.33	1.26
Sawdust	0.43	1.26
Feeding Amount (kg)	**8.89**	**6.29**
C/N Ratio Testing Result	**27.40**	**35.38**

(Source: Author Testing, 2023)

2.3.2 Acclimatization Process: The acclimatization process aims to provide adaptation for microorganisms to the new environment and food source. Fish waste, food waste, cow dung, and sawdust were gradually added during the 5 (five) weeks of the study's acclimatization process, as shown in Table 3.

Table 3: *Acclimatization Process*

Week-1	Week-2	Week-3	Week-4	Week-5
20%	40%	60%	80%	100%

(Source: Author Testing, 2023)

Temperature, pH, TS and VS testing, volume, C/N ratio, and methane yield are all measured during the acclimatization process. The reactor may continue on to the operating stage once it has produced biogas that contains methane.

2.3.3 Operational and Experiment Process: A freezer is used to ensures nutrient stability in the substrate during research. The operational process took 3 (three) weeks with the feeding process is carried out 5 (five) times a week, from Monday to Friday. (Figure 2)

Figure 2: *Feeding Process*

During the operational process, temperature and pH parameter measurements are carried out 5 (five) times a week (Monday-Friday) in the input and output section using a pH meter. TS and VS measurements are performed 3 (three) times a week (Monday, Wednesday, Friday) in the output section, while TS and VS input tests were only carried out 1 (one) time (because a freezer is used to store the same substrate) and tested in the laboratory. The C/N ratio is performed 1 (one) time a week (Friday) at the output and tested in the laboratory. Biogas composition is tested using the Gas Chromatography- Mass Spectrometry (GC-MS) method by placing biogas into a 1 liter tedlar bag, and biogas volume is measured using a flowmeter.

2.4 Research Data Analysis:

Research using quantitative data, therefore, it is necessary to conduct statistical tests to analyze and find out the condition of the value of the data obtained, so that a conclusion is obtained regarding the relationship between each parameter in reactors A and B. Data processing in this study used IBM SPSS Statistic 25 software application. The independent T-test is a method used to analyze parameter statistics. The following formula can be used to determine TS Reduction and VSD:

$$\%\mathrm{TS} = \frac{\mathrm{C} - \mathrm{A}}{\mathrm{B} - \mathrm{A}} \mathrm{x}100 \qquad (2)$$

$$\%\mathrm{VS} = \frac{\mathrm{C} - \mathrm{D}}{\mathrm{C} - \mathrm{A}} \mathrm{x}100 \qquad (3)$$

Description:

A = Weight of cup (gram)

B = Weight of cup and wet sample before heating (gram)

C =Weight saucer and sample after heating at 105oC (gram) D =Weight saucer and sample after heating at 550oC (gram)

Total Solid Reduction (TSR) and Volatile Solid Destruction (VSD) can be calculated with the following equation:

$$\%\ \mathrm{TS\ Reduction} = \left(\frac{\mathrm{TS\ input} - \mathrm{TS\ output}}{\mathrm{TS\ input}}\right) \mathrm{x}100 \qquad (4)$$

$$\% \text{ VSD} = 1 - \left(\frac{\text{VS output x } (1 - \text{VS input})}{\text{VS input x } (1 - \text{VS output})}\right) \text{x} 100 \quad (5)$$

3. Result and Discussion:

3.1. Temperature Parameters Measurement Result:

One of the conditions for anaerobic processes to proceed rapidly and produce large amounts of high-quality biogas with a high methane yield is optimal temperature. This is because microorganism growth is influenced by temperature (Yenni et al., 2012). The comparison of temperature measurements in reactors A and B shows a difference that is not much different, both substrate measurements at the input and output points. This can be seen in Figure 3. In the input section, the temperature in reactor A ranges from 22.7 – 29.3oC, while in reactor B, the temperature ranges from 26.1 – 29.3oC. In the output section, the temperature ranges from 27.8 – 30.2oC and reactor B ranges from 27.8 – 30.2oC. Bacteria work optimally at mesophilic temperatures (25-40°C, with an optimum temperature of 35°C) (Kothari et al., 2014)(Forster-Carneiro et al., 2013). The temperature conditions of reactor A and reactor B measured in the output section show that the temperature inside the reactor is at mesophilic temperature, which means that these conditions are suitable for the growth of decomposing microorganisms.

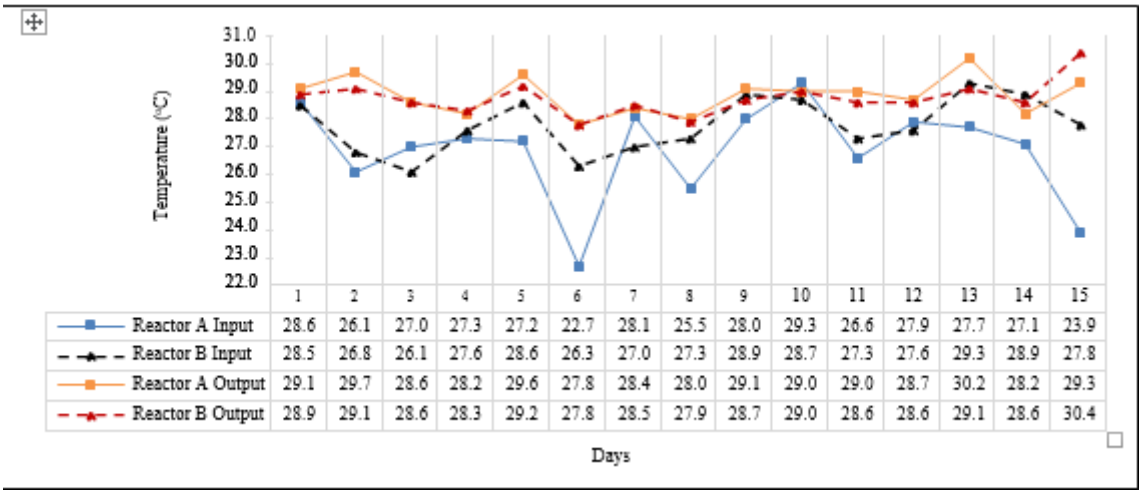

	1	2	3	4	5	6	7	8	9	10	11	12	13	14	15
Reactor A Input	28.6	26.1	27.0	27.3	27.2	22.7	28.1	25.5	28.0	29.3	26.6	27.9	27.7	27.1	23.9
Reactor B Input	28.5	26.8	26.1	27.6	28.6	26.3	27.0	27.3	28.9	28.7	27.3	27.6	29.3	28.9	27.8
Reactor A Output	29.1	29.7	28.6	28.2	29.6	27.8	28.4	28.0	29.1	29.0	29.0	28.7	30.2	28.2	29.3
Reactor B Output	28.9	29.1	28.6	28.3	29.2	27.8	28.5	27.9	28.7	29.0	28.6	28.6	29.1	28.6	30.4

Figure 3: *Temperature Measurement*

3.2. pH Parameters:

In general, pH is a measure of the acidity or alkalinity of a solution. Solutions with a pH of less than 7 are called acids, while solutions with a pH of more than 7 are called alkaline or alkaline (Liansyah Pratama et al., 2015). Degree of acidity isone of the important factors in the anaerobic fermentation process. The degree of acidity in the digester should be maintained in the range of 6.8 -7.2 (Náthia-Neves et al., 2018).

The comparison of pH measurements in reactors A and B shows a difference that is not significant from both substrate measurements at the input and output points which can be seen in Figure 4. In the input section, the pH in reactor A ranges from 5.1 – 7.9 while in reactor B, the temperature ranges from 5 – 9.6. In the output section, pH ranges from 7.8 – 8.4 and reactor B ranges from 7.8 – 8.5. This pH condition is very influential on the hydrolysis process and the next process, namely acidification and methanation. The optimum acidity required by acidogenic bacteria is 5 to 6.5, while the optimum pH for methanogenesis bacteria is above 6.5 (Kurniawan, 2016).

The pH in both reactors is categorized as alkaline based on the measurement results; this may be because the reactor is filled with substrate made primarily of fish waste, which has a high protein content (Nges et al., 2012), so that the pH levels show the presence of microorganisms that break down organic materials. The pH can become alkaline when proteins and organic nitrogen break down into ammonium (NH4)

(Polprasert, 1989). It is hypothesized that a denitrification process-in which nitrate nitrogen and nitrite are reduced to nitrogen gas under anaerobic conditions—occurs because the bioreactor used is closed (anaerobic), causing a drop in an oxygen levels (O2). Nitrogen will dissolve in relatively high pH environments and then release as ammoniac (NH3) (Doraja et al., 2012). The pH level at alkaline conditions in both reactors has an impact on biogas productivity. If, the pH is higher than 8.5 pH will have an adverse effect on the population of methanogenic bacteria, which will slow down the rate of biogas formation of the reactor (Yonathan et al., 2012).

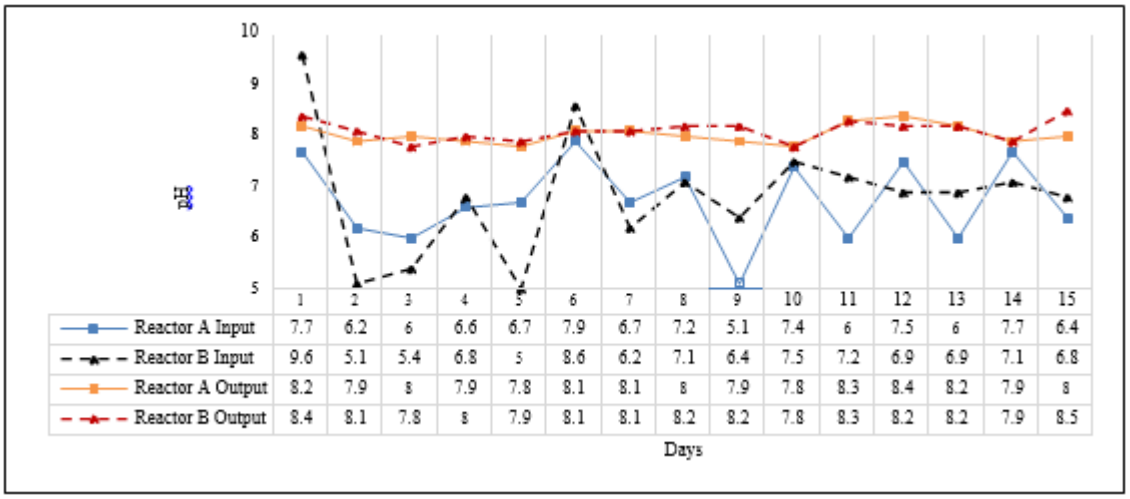

	1	2	3	4	5	6	7	8	9	10	11	12	13	14	15
Reactor A Input	7.7	6.2	6	6.6	6.7	7.9	6.7	7.2	5.1	7.4	6	7.5	6	7.7	6.4
Reactor B Input	9.6	5.1	5.4	6.8	5	8.6	6.2	7.1	6.4	7.5	7.2	6.9	6.9	7.1	6.8
Reactor A Output	8.2	7.9	8	7.9	7.8	8.1	8.1	8	7.9	7.8	8.3	8.4	8.2	7.9	8
Reactor B Output	8.4	8.1	7.8	8	7.9	8.1	8.1	8.2	8.2	7.8	8.3	8.2	8.2	7.9	8.5

Figure 4: *pH Measurement*

3.3. Comparison of Total Solid Reduction (TSR) and Volatile Solid Destruction (VSD) Parameters:

TS and VS are important parameters that can determine the characteristics of the slurry. TS is used to determine the feeding rate of the anaerobic digester and provides clues as to when overhauls are needed. Meanwhile, VS provides an estimate of the amount of substrate that can potentially be converted to methane. TS test results on inputs are 21.07% (Reactor A) and 28.29% (Reactor B). While VS testing on input is 87.21% (Reactor A) and 72.97% (Reactor B). TS and VS testing can be seen in Figure 5-6.

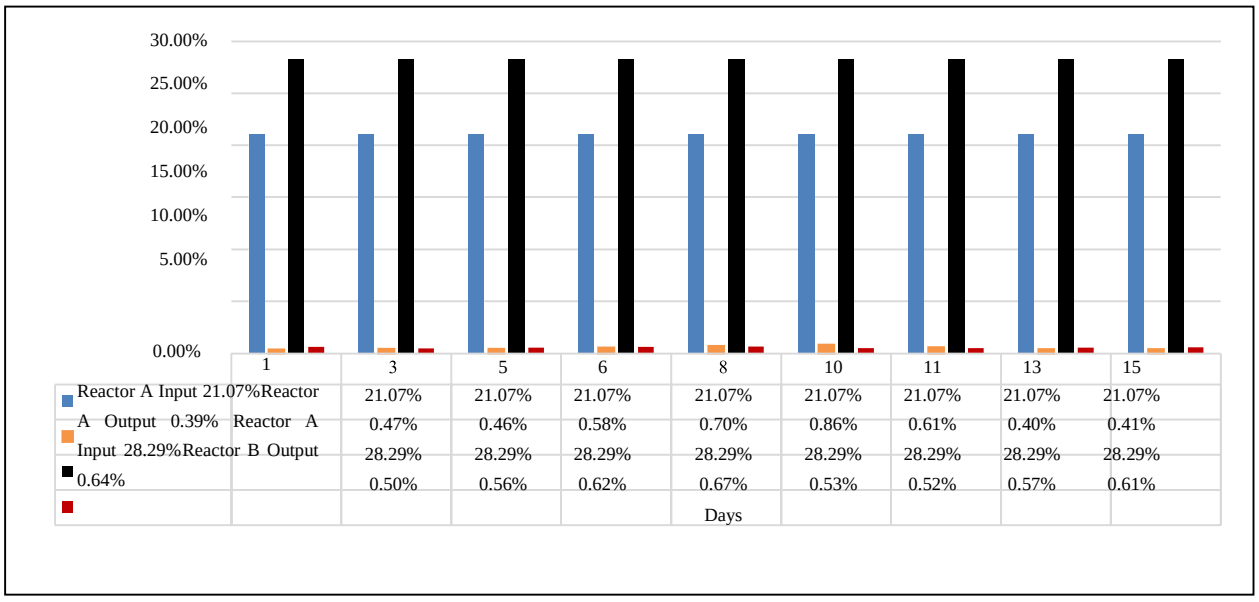

	1	3	5	6	8	10	11	13	15
	21.07%	21.07%	21.07%	21.07%	21.07%	21.07%	21.07%	21.07%	21.07%
	0.47%	0.46%	0.58%	0.70%	0.86%	0.61%	0.40%	0.41%	
	28.29%	28.29%	28.29%	28.29%	28.29%	28.29%	28.29%	28.29%	
	0.50%	0.56%	0.62%	0.67%	0.53%	0.52%	0.57%	0.61%	

Figure 5: *Total Solid Measurement*

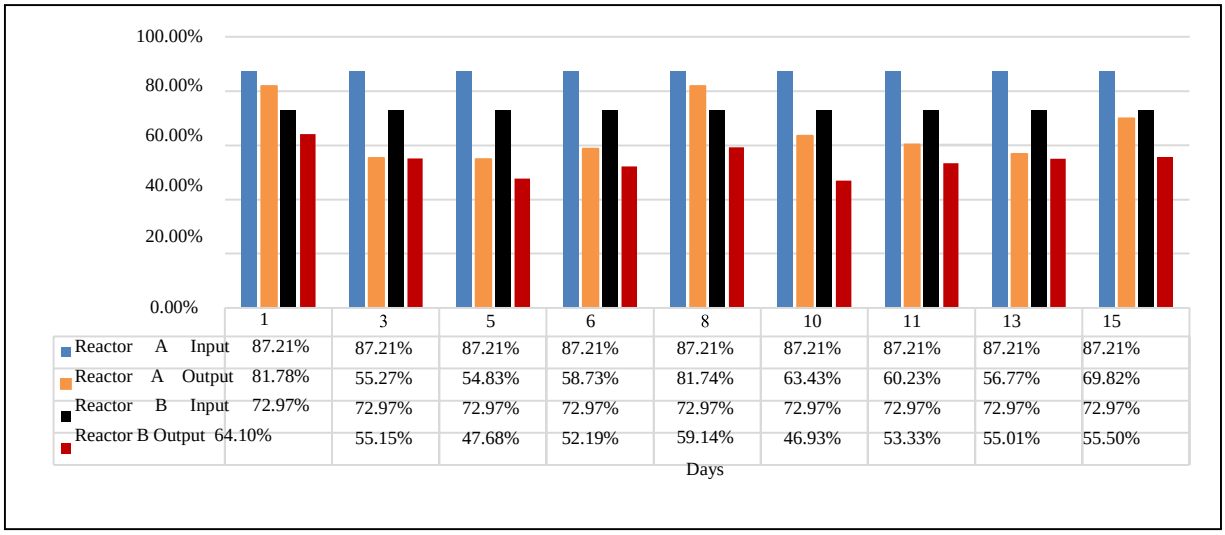

Figure 6: *Volatile Solid Measurement*

Based on the TS and VS measurement data above, the results of Total Solid Reduction (TSR) and Volatile Solid Destruction (VSD) calculations can be seen in **Figure 7-8.**

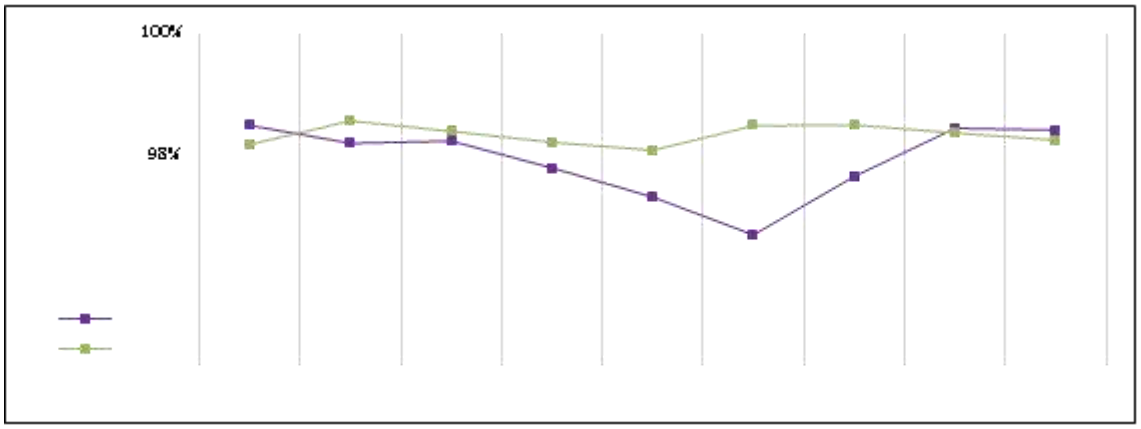

Figure 7: *Total Solid Reduction Measurement*

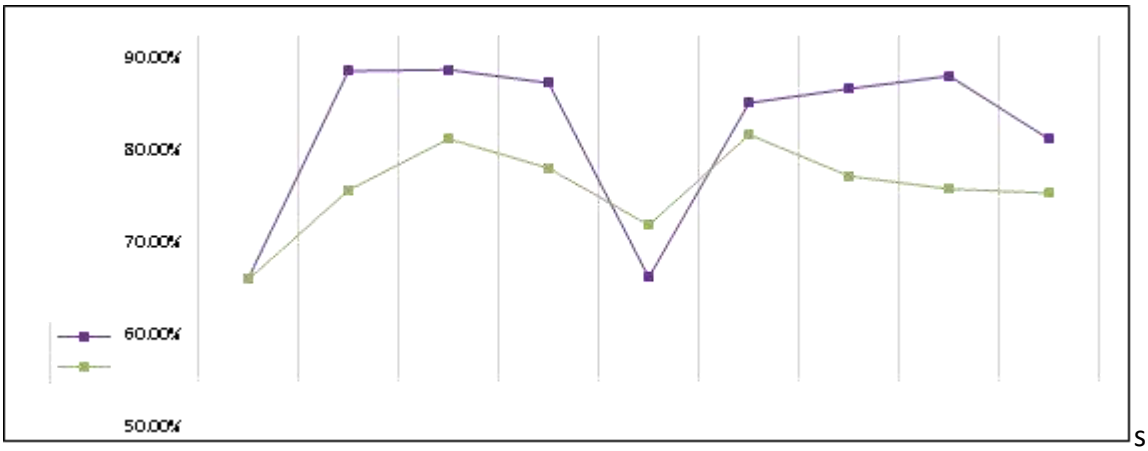

Figure 8: *Volatile Solid Destruction Measurement*

The TS Reduction value is the percentage of the difference between TS input and TS output in the reactor. The amount of degraded solids can affect the amount of biogas and methane production. This is because the organic material in the substrate is successfully broken down into simpler compounds by bacteria. The compound is an ingredient in the biogas formation process. So, it can be concluded that the higher the

percentage of TS Reduction, the greater the potential for biogas production. TS Reduction in reactor A has an average 97.42% and reactor B has an average of 97.95%. Therefore, it can be concluded that the solids reduction in reactor B is higher than reactor
A. The solid reduction results in Shodiq's research (2020), which only uses food waste and fish waste substrates (100: 80), may have a lower reduction value (33.40%) than the results of the two reactors (Shodiq et al., 2020).
The Volatile Solid Destruction (VSD) value is the percentage of the difference between VS input and VS output in the reactor. The VSD value is used as a parameter to measure the stability of the process in anaerobic digestion (Gray, 2008). VSD in reactor A has an average of 67.87%, while reactor B has an average of 54.88%. Therefore, it can be concluded that the average VSD in reactor A is higher than that of reactor B. The results of the two reactors arguably have a high VSD value when compared to the VSD results conducted in Shodiq's research (2020) which only used food waste and fish waste substrates (100: 80), which was 30.28% (Shodiq et al., 2020).

3.4. Comparison of Biogas Composition:

Biogas consists of methane (CH4), carbon dioxide (CO2) and may have small amounts of hydrogen sulfide (H2S), moisture and some other gases (Ryckebosch et al., 2011). Biogas is generally composed of 55- 65% methane, 35-45% carbon dioxide, 0-3% nitrogen, 0-1% hydrogen, and 0-1% hydrogen sulfide (Salam, 2015). Based on the test results in this study, the composition contained in biogas includes methane, carbon dioxide and hydrogen sulfide. Reactor A had an average methane content of 64.19%, an average carbon dioxide of 35.57%, and an average hydrogen sulfide of 0.24%. While reactor B has an average methane content of 64.12%, carbon dioxide an average of 35.79%, and hydrogen sulfide 0.08%.
Salam (2015) reported that the methane content in both reactors complied with regulations based on the biogas content. Reactors A and B have higher methane content values when compared to the percentage of methane content produced in Zamazal's research (2016). With only fish waste and cow dung inoculum, Zamazal's (2016) study found that the values of CH4 and CO2 were 51% and 47%, respectively (Zamazal et al., 2016). The results of biogas composition testing can be seen in Figure 9.

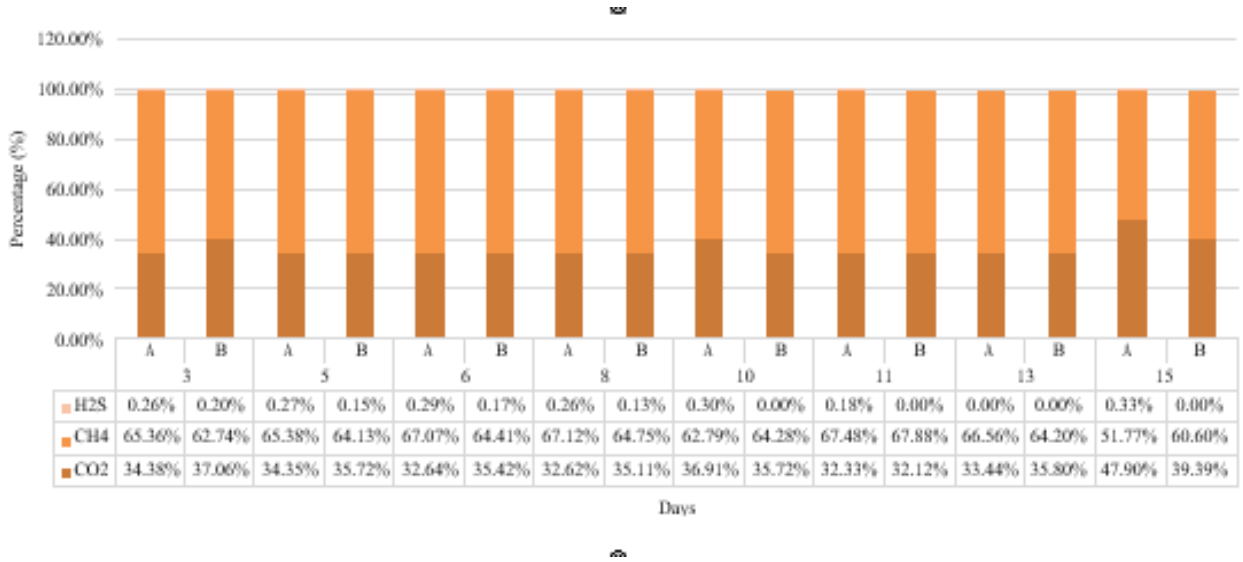

Figure 9: *Biogas Composition Measurement*

3.5. Comparison of Biogas Volume:

Biogas is one of the main products of anaerobic digestion treatment in addition to sludge. Based on the results of biogas volume measurement, it was found that reactor a produced biogas on average 155.8 liters/day and reactor B produced biogas on average 133.56 liters/day. The volume of biogas in each rector can be seen in Figure 10. It can be concluded that reactor A and reactor B do not have a significant difference.

Methane yield in this result were 122.37 L.CH4/kg.VS (reactor A) and 131.76 L.CH4/kg.VS (reactor B) which can be seen in Figure 11. It can be concluded that reactor A and reactor B do not have a significant difference. According to research carried out in Braganca, Brazil by Dayse et al. (2023), methane yields between 76 and 138 mL•gvs-1 were produced using fish waste and cow dung, and the methane content was higher than 50%. The results presented a Green House Gases (GHG) reduction of 1,619 tons of CO2e and an electricity production of 372 MWh•year-1 to 956 MWh•year1 (da Silva et al., 2023). This demonstrates how adding co-substrates like sawdust, dung from cows, and organic waste along with fish waste can significantly boost the amount of biogas produced during the waste treatment process in anaerobic digesters.

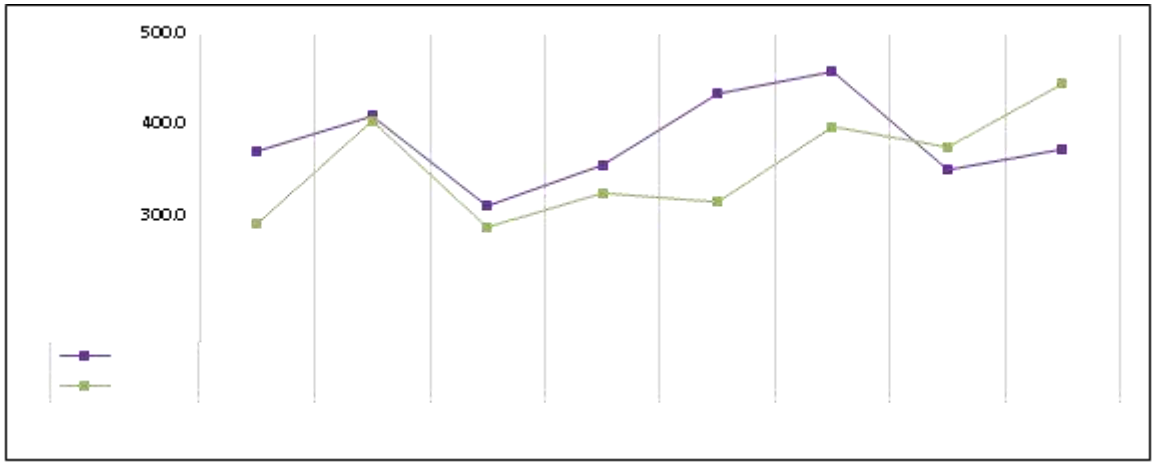

Figure 10: *Biogas Volume Measurement*

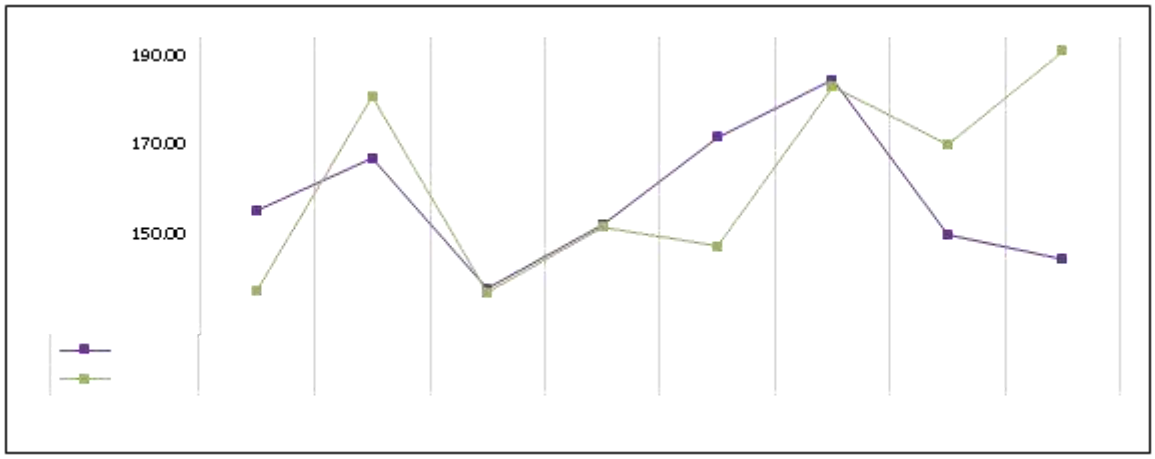

Figure 11: *Methane Yield Calculation*

4. Conclusion:

Fish waste can be one of the substrate that can be processed into biogas, but because there are several contents in fish waste that have high concentrations of ammonia and Long Chain Fatty Acid (LCFA), so that, it can affect the condition of the C/N ratio down, it is necessary to add several other substrates that can help increase the C/N ratio and help accelerate degradation in the anaerobic process. Therefore, this study was conducted preliminary study using a mixture of fish waste substrate, food waste, cow dung, and sawdust, so that, the test results of C/N 27.40 (reactor A) and 35.38 (reactor B) were obtained. This is in accordance with the research of Zulkarnaen et al (2018), which states that a good C/N ratio on the substrate is in the range of 27 – 35, so, it can be continued to the operational stage. Based on this research, it can be concluded that processing into biogas with anaerobic digester method using substrates of fish waste, food waste, cow dung, and sawdust at a composition ratio of 40: 40 : 15 : 5 and 30: 30 : 20 : 20 can be done effectively, it can be seen from the solids that have been reduced to 97.42% (reactor A) and 97.95% (reactor B), and generated

155.8 liters/day of biogas in reactor A and 133.56 liters/day of biogas in reactor B. Reactor A yielded an average of 122.37 L.CH4/kg.VS, while reactor B yielded an average of 131.76 L.CH4/kg.VS. Statistical testing with the T-Test test method also showed that reactor A and reactor B did not have a significant difference in the reduction or amount of biogas volume and methane yield. The results of the research indicate that there is not a significant difference between the composition ratios in reactor A and reactor B with regard to reduction, biogas volume, or methane yield. As a result, the two composition ratios can be used to determine the composition of waste treatment using an anaerobic digester.

5. Acknowledgments:

The author acknowledges financial support from the UK-Indonesia Consortium for Interdisciplinary Sciences (UKICIS) project and teamwork from PT Alkana Kreasi Energi (AKE).

6. References:

Afreen, M., & Ucak, I. (2020). Fish processing wastes used as feed ingredient for animal feed and aquaculture feed. Journal of Survey in Fisheries Sciences, 6(2), 55–64. https://doi.org/10.18331/SFS2020.6.2.7

Agustin, A. (2015). Adaptation of Coastal Communities in the Management of Fish Factory Waste in Muncar, Banyuwangi Regency. Social Student Journal, Brawijaya University, vol. 2, no. 4, pp. 1–16.

Arianto, M. F. (2020). The Potential of Coastal Areas in Indonesia," J. Geogr., vol. 20, no. 20, pp. 1–7.

Bonanza, B. S. W., & Sarto, S. (2016). Effect of Variation in Organic Loading Rate of Citrus Fruit Waste Biohydrogen Production in a Continuous Reactor. Process Engineering Journal, vol. 10, no. 2, p. 43. https://doi.org/10.22146/jrekpros.33336

BPS. (2020). STATISTICS OF MARINE AND COASTAL RESOURCES: CLIMATE CHANGE IN COASTAL AREA.

Cadavid-Rodríguez, L. S., Vargas-Muñoz, M. A., & Plácido, J. (2019). Biomethane from Fish Waste As A Source of Renewable Energy for Artisanal Fishing Communities. Sustainable Energy Technologies and Assessments, 34,110–115. https://doi.org/10.1016/j.seta.2019.05.006

da Silva, D., Cavalcanti, J. V. F. L., do Nascimento, A. F. J., Peres, S., Alves, M., & Benachour, M. (2023). Biogas Production and Greenhouse Gas Mitigation Using Fish Waste from Bragança/Brazil. Chemical Industry and Chemical Engineering Quarterly, 29(00), 4–4. https://doi.org/10.2298/ciceq220614004s

Dioha, I. J., Ikeme, C., Nafi, T., Soba, N. I., & Mbs, Y. (2013). Effect of Carbon To Nitrogen Ratio on Biogas Production. International Research Journal of Natural Sciences, 1(3), 1–10.

Doraja, P. H., Shovitri, M., & Kuswytasari, N. D. (2012). Biodegradation of Domestic Waste by Using Natural Inoculum from Septic Tanks," Science Journal, ITS, vol. 1, no. 1, pp. 44–47.

FAO. (2022). State of the World Fisheries and Aquaculture - 2022 (SOFIA). https://www.fao.org/3/cc0461en/cc0461en.pdf

Forster-Carneiro, T., Berni, M. D., Dorileo, I. L., & Rostagno, M. A.(2013). Biorefinery Study of Availability of Agriculture Residues and Wastes for Integrated Biorefineries In Brazil. Resources,Conservation and Recycling, 77, 78–88. https://doi.org/10.1016/j.resconrec.2013.05.007

Gray, D. M. D. (2008). " Anaerobic Digestion of Food Waste " http://www.ejurnal.its.ac.id/index.php/sains_seni/article/view/788/244

Kafle, G. K., Kim, S. H., & Sung, K. I. (2013). Ensiling of Fish Industry Waste for Biogas Production: A Lab Scale Evaluation of Biochemical Methane Potential (BMP) and Kinetics. Bioresource Technology, 127, 326–336. https://doi.org/10.1016/j.biortech.2012.09.032

Kothari, R., Pandey, A. K., Kumar, S., Tyagi, V. V., & Tyagi, S. K. (2014). Different Aspects of Dry Anaerobic Digestion for Bio-Energy: An overview. Renewable and Sustainable Energy Reviews, 39, 174–195. https://doi.org/10.1016/j.rser.2014.07.011

Kurniawan, W. (2016). Test of Biogas Potential from Patin Fish Offal Waste (Pangasius sp.) and Kiambang

Mixture (Salvinia molesta) in Anaerobic Batch. Wahyuni 2013. Liansyah Pratama, D., Hanggita, S., & Supriadi. (2015). Department of Fishery Products Technology, Faculty of Agriculture. Fishtech-Journal of Fishery Products Technology Biogas Production Potential Test on Kiambang (Salvinia molesta) and Cork Fish Offal Waste Mixture (Channa striata) Using Batch Anaerobic Digester, Vol. 4, no. 2, pp. 111–119. https://doi.org/10.36706/fishtech.v4i2.3505

Natalina, Sulastri, & Aisah, N. N. (2017). The Effect of Variations in the Composition of Sawdust, Cow Manure and Goat Manure on Composting," Journal of Engineering Engineering and Science. vol. 1, no. 2, pp. 94–101.

Náthia-Neves, G., Berni, M., Dragone, G., Mussatto, S. I., & Forster-Carneiro, T. (2018). Anaerobic Digestion Process: Technological Aspects and Recent Developments. International Journal of Environmental Science and Technology, 15(9), 2033–2046. https://doi.org/10.1007/s13762-018-1682-2

Nges, I. A., Mbatia, B., & Björnsson, L. (2012). Improved Utilization of Fish Waste By Anaerobic Digestion Following Omega-3 Fatty Acids Extraction. Journal of Environmental Management, 110, 159–165. https://doi.org/10.1016/j.jenvman.2012.06.011

Oktavia, D., Mangunwidjaja, D., Wibowo, S., Candra Sunarti, T., Mulyorini Rahayuningsih, D., & Tech. Industry FATETA-IPB. (2012). Fishing Waste Processing Using Proteolitic and Lipolitic Indigenous Microba.

Polprasert, C. (1989). Organic Waste Recycling.

Priadi, C. R. , & Abdillah, A. (2019). Biogas Reactor and Method for Converting Organic Waste Into Methane- Rich Gas and Probiotic Sludge. (Patent No. P00201910803).

Ryckebosch, E., Drouillon, M., & Vervaeren, H. (2011). Techniques for Transformation of Biogas To Biomethane. Biomass and Bioenergy, 35(5), 1633–1645. https://doi.org/10.1016/j.biombioe.2011.02.033

Salam, B. (2015). Biogas from Anaerobic Digestion Of Fish Waste. Proceedings of the International Conference on Mechanical Engineering 2009 (ICME2009) 26- 28. December 2009, Dhaka, Bangladesh, December 2009, 7–10.

Shodiq, J., Teknik, F. (2020). Potential of Fish Waste and Waste Management. Faculty of Engineering. Environmental Engineering Study Program

Wulandari, S., & Pramono, H. (2020). Processing of Waste of Canning and Swimming Crab (Portunus Pelagicus) In PT. Sumber Mina Bahari Rembang, Central Java. Journal of Marine and Coastal Science, 7(2), 78. https://doi.org/10.20473/jmcs.v7i2.20716

Yenni, Dewilda, Y., & Mutia Sari, S. (2012). Test of Biogas Formation from Vegetable and Fruit Waste Substrate with Waste Content Co-Substrate Cow Rumen," Environmental Tech. Journal, UNAND, vol. 9, no. 1, pp. 26–36.

Yonathan, A., Prasetya, A. R., & Pramudono, B. (2012). Biogas Production from Water Hyacinth (Eichhornia Crassipes): Consistency and pH Study of The Produced Biogas. Chem and Industry Tech. Journal., vol. 1, no. 1, pp. 412–416. http://ejournal- s1.undip.ac.id/index.php/jtkiTelp/Fax:

Zamazal, P., Winaya, I. N. S., & Astawa, K. (2016). Biogas Utilization Using Fish Waste with Constant Volume of Inoculum Cow-Dung. 1(1), 74–77.

Zulkarnaen, I. R., Tira, H. S., & Padang, Y. A. (2018). Effect of Carbon and Nitrogen Ratio (C/N ratio) in Cow manure on the Production of Biogas from the Process of Anaerobic," Dynamics of Mechanical Engineering Journal, pp. 1–16.

Consistent Planning of Energy System Transition - Methodology to Achieve Global Climate Goals

Christoph Engels
Computer Science, University of Applied Sciences and Arts, Dortmund, Germany

Abstract: The urgent need for decarbonization and the mitigation of climate change have spurred significant investments in the transformation of our energy systems. To effectively combat climate change and achieve global climate goals, the transition to sustainable and low-carbon energy sources is imperative. However, this complex endeavor presents various challenges, including huge investment needs which define the energy systems structure for the next decades.
Energy grids play a crucial role in balancing the energy system, but they are also influenced by political and economic decisions, further complicating the planning process. This article explores the methods employed for consistent planning of energy system transformation, emphasizing the alignment of goals and strategies at different planning levels, from global to municipal, while considering the unique characteristics and uncertainties associated with each level. It proposes a combination of countercurrent processes derived from business planning and scenario techniques to cope with complexity and uncertainty.
Keywords: Energy System Transformation, Global Climate Goals, Decarbonization, Consistent Countercurrent Planning, Energy Grid, Uncertainty, Scenario Technique, Simulation

1. Introduction: Typically, the planning of energy system transformation begins with a top-down approach, anchored in the global 1.5-degree target and its implementation into national reduction plans. These national guidelines are further allocated to specific energy sectors, considering various technological substitutions like district heating from geothermal or biomass sources versus air-electric heat pumps. Given the localized constraints such as limited potential for renewable energy generation or local blockades, the top-down guidelines need validation through a bottom-up process. This is similar to counter-current planning in business operations and ensures consistency across all planning levels. Engels et al., 2021 and Mameghani et al., 2022 describe such an approach in the context of the ramp-up of electric mobility in Germany, exploring multiple potential scenarios.

2. Hierarchical Counter-Current Planning: The planning process for energy system transformation is a multi-level endeavor, as illustrated in Figure 1: Planning Hierarchy. Beginning with top-down directives that set the maximum allowable global temperature increase at Level I, these directives are cascaded down to Level II, where they are translated into national goals for the future energy mix correlated with CO2 emissions. The composition of this energy mix is quantified using Key Performance Indicators (KPIs), such as installed generation capacity (installed P). These national goals are further regionalized through Level III and IV, ultimately culminating in investment decisions at specific geographical locations.

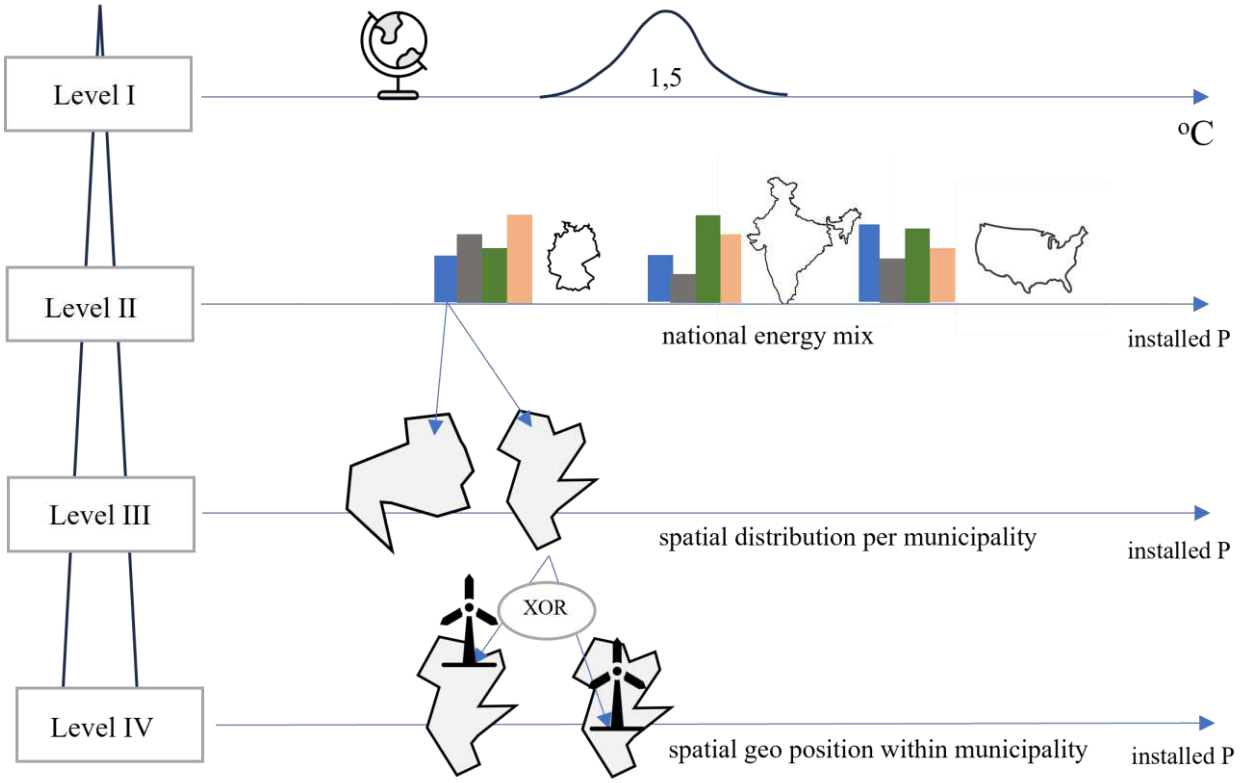

Figure 1: *Planning Hierarchy*

To achieve this, distribution factors are necessary to account for the anisotropic nature of local conditions. During this process of breaking down the directives, it becomes evident that regional goals cannot always be met due to local resistance or supply constraints, or conversely, they might be exceeded. Therefore, in countercurrent planning, the aggregation of planned or already-installed capacities takes place from Level IV back up to Level II. At the national level, the deviation between the initial target and realistically achievable capacities can be analyzed, and appropriate measures can be initiated. At the lowest Level IV, the expansion relies on discrete decisions. Therefore, in estimating the supply task, simulation methods such as Agent-Based Modeling come into play (see Kittl et. al 2019). Through multiple counter-current iterations, a consistent hierarchy concerning installed capacity is established.

3. Scenario based planning: The uncertainty in planning arises not only from the complex task of hierarchical distribution of installed generation capacities across planning levels but also from factors like consumer behavior and technological focus in the energy system transformation. For example, uncertainties may arise from choices between individual electric mobility and public transport. These uncertainties are addressed by defining various scenarios that describe different internally consistent transitions. Scenario technique remains the weakest forecasting method among all statistical prediction tools but is able to reflect different future developments. In using scenario technique there is a danger of overestimating the probability of the chosen scenarios. But beside these characteristics it should be advanced ahead of the usage of single expectation value predictions. The scenarios are constructed based on different assumptions, such as variations in consumer preferences, technological advancements, and policy changes. These assumptions help in modeling the possible trajectories of the energy system under different conditions. Once the scenarios are established, they are used to estimate the future supply task, taking into account the unique characteristics and dynamics of each scenario.

Putting these parts together, a formal KPI schema is proposed for planning installed capacities, see formula (1).

$$P_{installed}\left(T, t, S, L, \underline{x}\right) \qquad (1)$$

where

$$T \in (PV, Wind, Biomass, Water, Lignite, Natural\ Gas, Hard\ Coal, Nuclear \dots)$$

$$t \in [2023, 2053]$$

$$S = scenario\ ID$$

$$L \in (Level\ II, Level\ III, Level\ IV)$$

$$\underline{x} \in ((lat, lon), geographical\ area)$$

This definition accounts for the hierarchical nature of the planning process, the incorporation of uncertainty through scenario analysis, and the need to achieve consistency in energy system transformation at multiple vertical hierarchical planning levels and between different energy sectors horizontally. This schema can be used to form a multidimensional model taking T as elements of a KPI vector describing the energy mix, t as the time dimension, S as a scenario dimension, an L and x forming the hierarchical geographical dimension shown in Figure 2: Multidimensional Planning Schema in ADAPT notation, see Symmetry Corp., 2023. The ADAPT notation can be used to build an analytics data schema directly for the KPI under investigation.

Consistency among Hierarchies: Engels, Konen, 2007 have proposed a forecasting methodology to provide vertical consistent predictions among multiple aggregation levels within a hierarchy of the KPI predicted by explicit or implicit coupling of independent data driven machine learning models.

Consistency within the Scenarios: To ensure consistency and feasibility, the supply task is validated through different simulations. These simulations, such as Monte-Carlo based Market Models, Powerflow Models and Agent-Based Modeling, help in understanding how different factors interact within each scenario. They can also reveal potential challenges and bottlenecks that need to be addressed for the energy system to meet its goals, see Entso-E 2023. To cope with the high complexity of the underlying system, Level II and Level III and IV are separated among each other. Level II focusses on transmission and energy market aspects while Level III and IV reflect the local distribution of energy, see Engels et. al. 2021. If the entire is not divided along its hierarchy it would be computationally infeasible to simulate it as a whole.

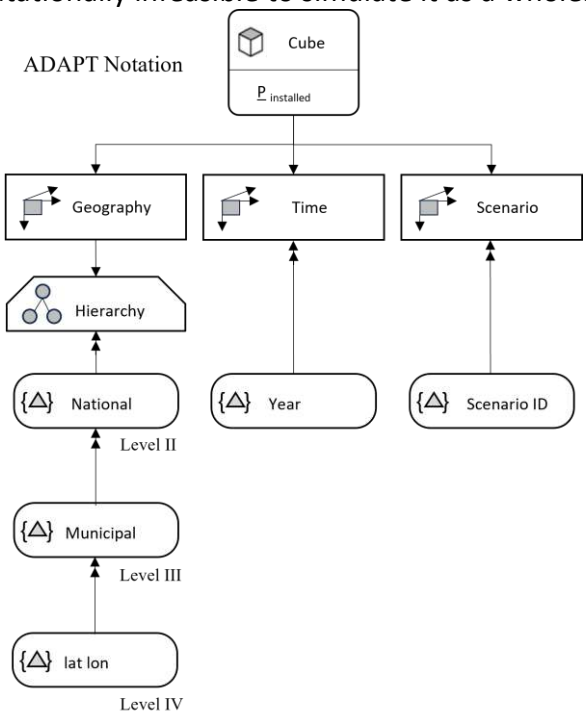

Figure 2: *Multidimensional Planning Schema*

Case Example: How does the described framework manifest in reality? To illustrate this, let's consider the example of Europe, where, between the global and national levels, we also find the supranational level of European states. After an assessment of expected generation performance at the level of individual facilities (Level IV), coordination of grid development and resilience assessment takes place within the scenario-based Ten-Year Network Development Plan (TYNDP). In this plan, European network operators within the ENTSO-E organization non-bindingly synchronize their expansion plans every two years. The TYNDP compilation includes bottom-up collected network projects and validates the consistency of the planning figures through cross-sector market and network simulations. The market simulation reflects the dispatch of generators, while the network model assesses the network's capacity for supply situations. The scenarios and planning figures determined by TYNDP are incorporated into national plans. In Germany, the Federal Network Agency initially adopts its own scenario framework for expected generation performance, which then serves as the basis for network development plans.

4. Summary and Outlook: This paper has transferred planning and forecasting concepts from business planning to build an integrated framework for vertical and horizontal planning within energy systems. It is based on the countercurrent planning process and scenario technique. The framework may serve as a blueprint for the alignment of current planning approaches of future energy systems and may help to provide a common terminology for all planning participants within the distributed planning processes.

References: BNetzA, (2023 September 26), Netzausbau, Retrieved from https://www.netzausbau.de/Wissen/Ausbaubedarf/Szenariorahmen/de.html

Engels, C., Feismann, D., Giavarra, D., Mameghani, E., Maier, A., Schiwek, R., (2021, September). Integrated Network Development & Planning - from forecasting to grid screening and concepts, CIRED 2021 Conference, Geneva, Paper No 0257. DOI: 10.1049/icp.2021.1992

Engels, C., Konen, W. (2007, October). Adaptive Hierarchical Forecasting. 4th IEEE Workshop on Intelligent Data Acquisition and Advanced Computing Systems: Technology and Applications, 2007. IDAACS 2007. DOI: 10.1109/IDAACS.2007.4488400

Entso-E, (2023 September 26), TYNDP, Retrieved from https://www.entsog.eu/tyndp#

Kittl, C., Hiry, J., Wagner, C., Pfeiffer, C., Rehtanz, C., Engels, C. (2019, June). Large scale agent based simulation of distribution grid loading and its practical application. CIRED 2019 Conference, Madrid, Paper No 1099. https://www.researchgate.net/publication/337445298_Large_scale_agent_based_simulation_of_distribution_grid_loading_and_its_practical_application#fullTextFileContent

Mameghani, E., Hauptmeier, E., Schiwek, R., Engels, C., Maier, A., Tübben, S. (2022, June). Refinement in E-Mobilty Ramp-Up global Grid Expansion Planning, CIRED workshop 2022, Porto, Paper No 1291. DOI: 10.1049/icp.2022.0777

Symmetry Corp., (2023, September 26), Getting Started with ADAPT, Retrieved from http://www.symcorp.com/downloads/ADAPT_white_paper.pdf

Impact of the LS Factor Estimation Methods on Mean Annual Soil Loss

Christopher Uche Ezeh
Geography, Kwame Nkrumah University of Science and Technology, Kumasi Ghana

Kwasi Preko
Department of Physics, Kwame Nkrumah University of Science and Technology (KNUST) UPO, P. O. Box PMB Kumasi, Ghana

Kwaku Adjei
Department of Civil Engineering, Regional Water and Environmental Sanitation Centre (RWESCK), Kwame Nkrumah University of Science and Technology (KNUST), PMB, University Post Office, Kumasi AK448

Ogbonnaya Igwe
Department of Geology, Faculty of the Physical Sciences, University of Nigeria, Nsukka

Sarah Schönbrodt-Stitt
Department of Remote Sensing, Institute of Geography and Geology, University of Wuerzburg, Am Hubland, D-97074 Wuerzburg, Germany

Mensah Yaw Asare
Department of Geomatic Engineering, Faculty of Engineering, Kwame Nkrumah University of Science and Technology, Kumasi Ghana

Abstract: Soil erosion was assessed in Anambra State using three different LS factor estimation methods. This was done to appreciate the effect of each approach on mean annual soil loss in the area. It showed that soil loss from the LS factor based on the slope in percent gives a fairly good result with little underestimation. The soil loss based on slopes in radians performed best with a slight overestimation. The one based on degrees' slope performed the least with a high underestimation. The PBIAS of soil loss based on percent slope was -9.04 % with a mean annual soil loss of 25.25 t ha-1yr-1, the one based on radians had a PBIAS of 2.81 % with a mean annual soil loss of 28.54 t ha-1yr-1 and the one based on degrees slope had a PBIAS of -46.43 %. With a mean annual soil loss of 14.87 t ha-1yr-1. The result from field measurement yielded 27.76 t ha-1yr-1. The coefficient of variations was 241.47 %, 192.01 %, and 157.97 %, respectively, for slope in percent, radians and degree. Soil erosion is a highly variable phenomenon which was reflected by the high coefficient of variations. It shows that modelling soil erosion in the state with the LS factor estimation based on slopes in radians and percent yields better results. We believe this finding will be useful to authorities and scientists interested in soil erosion studies in the State. It is recommended that a similar study be extended to other terrains with moderate slopes.
Keywords: Soil Erosion, Soil Loss, LS Factor, RUSLE, Nigeria, Slope.

Introduction: Soil erosion by water is a principal cause of soil degradation in the humid tropics. It distorts soil fertility by washing away the rich topsoils and also contributing to water pollution. The USLE model which was revised (RUSLE) is widely used for assessing erosion (Renard et al., 1997; Wischmeier and Smith, 1978). It has become the most widely used model for soil erosion studies (Benavidez et al., 2018; Alewell et al., 2019). Other revised versions are RUSLE1 and RUSLE2. Its use has been extended to larger scales such as watersheds, a region, or a globe (Naipal et al., 2015; Panagos et al., 2015). Its extension to a larger scale is

associated with greater uncertainties. Also, its output is affected by the method employed to estimate the factors used in the model. One such factor that is very critical to the output of the model is the topographic (LS) factor. Some scholars argued that methods employing slope in percent are better for estimating the LS factor in moderate to very steep areas (Nakil and Khire, 2016). Others argue that the method using slope in radians is more suited for regions with complex topography (Moore and Burch, 1986a; Andreoli, 2018). They contend that it accounts for the convergence and divergence of flows (Andreoli, 2018). On this account, the study tested the effect of 3 LS estimation methods each based on slopes in degrees, percent, and radians to understand their effect on mean annual soil loss in the area. The output of each was compared with the output from field measurement. This allowed us to understand the best performing method for estimating the LS factor for the region. The study is necessary to guide scientists and stakeholders in the planning and management of soil erosion in Anambra State. Also, to the authors' best knowledge, this gap is yet to be filled in the area despite being a state highly ravaged by soil erosion.

Materials and Methods: The study covers Anambra State Nigeria. The location is shown in Figure 1. It has the Aw climate with much rain in the summer (June- Oct). Its rainy season spans 7 to 8 months. The study used open source data comprising CHIRPS daily rainfall data at 0.05 o resolution (2021-2022) (CHIRPS, 2022), soil data was obtained from Innovative Solutions for Decision Agriculture at 30 m resolution (iSDASoil, 2022), the Digital Elevation Model (DEM) data were obtained from obtained from the USGS Earthexplorer website (NASA, 2022; USGS, 2023). The landcover data were obtained from the ESRI website at https://livingatlas.arcgis.com/landcoverexplorer/#mapCenter=7%2C6.177%2C10&mode=step&timeExtent=2017%2C2022&year=2022&downloadMode=true. It has 10 m spatial resolution. The data were used to estimate the 5 key factors of the RUSLE model (eq. 1).

$$SL = R \times K \times LS \times C \times P \qquad (1)$$

where SL is soil loss (t ha-1 yr-1), R is erosivity factor (MJ mm ha−1 h−1 yr−1), K is erodibility factor (t ha h MJ−1 mm−1), LS is topographic factors of slope length and steepness, C is crop or cover factor, and P is management practices factor.

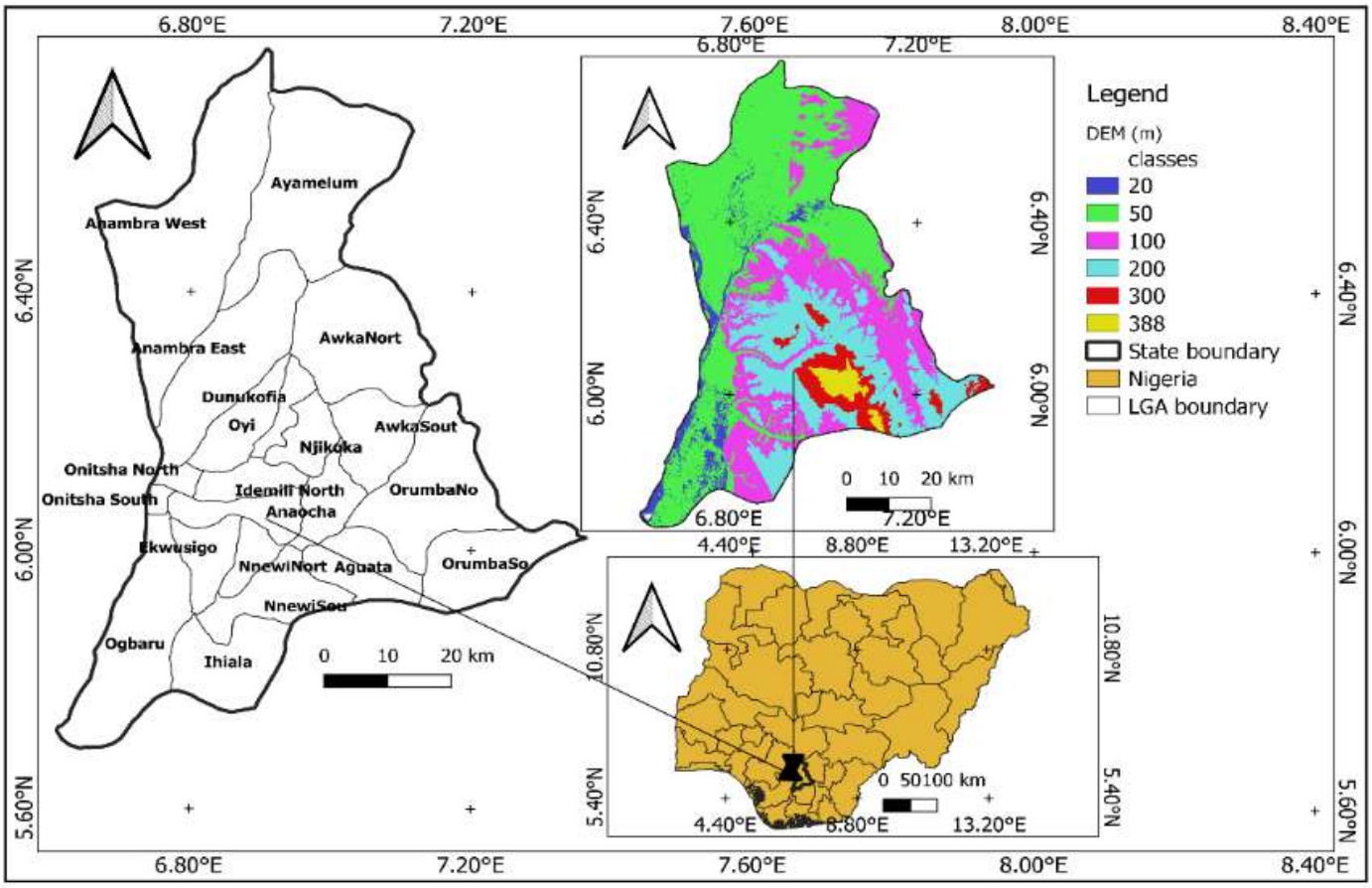

Figure 1. *Map of Nigeria Showing Anambra State*

The R factor describes the rain energy impact on soil loss. The higher the rain intensity and amount, the higher the erosion (Roose, 1977; Ziadat and Taimeh, 2013). The Roose (1977) method was used (eq. 2).

$$R = 0.05 \times AR \times a \tag{2}$$

where R is erosivity, AR is mean annual rainfall, a =1.73. The K factor was estimated with a widely used method in the tropics (eq. 3) (Tsige et al., 2022).

$$K = f_{csand} \times f_{cl-si} \times f_{orgC} \times f_{hisand} \tag{3}$$

where

$$f_{csand} = 0.2 + 0.3 \exp\left[-0.256 m_s \left(1 - \frac{m_{silt}}{100}\right)\right] \tag{4}$$

$$f_{cl-si} = \left(\frac{m_{silt}}{m_c - m_{silt}}\right)^{0.3} \tag{5}$$

$$f_{orgC} = 1 - \frac{0.25 \times orgC}{orgC + \exp\left[3.72 - 2.95 orgC\right]} \tag{6}$$

$$f_{hisand} = 1 - \frac{0.7\left(1 - \frac{m_s}{100}\right)}{1 - \frac{m_s}{100} + \exp\left[-5.51 + 22.9\left(1 - \frac{m_s}{100}\right)\right]} \tag{7}$$

where K is erodibility in t ha h MJ−1 ha−1 mm−1 fcsand is the fraction of coarse sand, fcl-si is the fraction of clay minus silt, forgC is the fraction of organic carbon, and fhisand is the fraction of fine sand.

The LS factor is estimated by a method using slope in percent (eq.8) (Wischmeier and Smith, 1978) herein denoted with WS, radians (eq. 9) (Moore and Burch, 1986b)) herein denoted with MB, and degree (eq. 10) (Desmet and Govers, 1996; Panagos et al., 2015) denoted with DG.

$$LS = \left(\frac{\lambda}{22.13} \right)^{m} \times \left(0.065 + 0.045s + 0.0065s^{2} \right) \quad (8)$$

where LS is the topographic factor which is dimensionless, m is the parameter of slope varying from o.2 to 0.5 depending on steepness, and s is the slope in percent.

$$LS = \left(\frac{\lambda}{22.13} \right)^{m} \times \left(\frac{\sin \beta}{0.0896} \right)^{n} \quad (9)$$

where m = 0.4 (ranges from 0.4-0.6), n = 1.3 (ranges from 1.22-1.3 depending on steepness). is flow accumulation multiplied by the cell size of the DEM, is the slope in radians.

$$Li,j = \frac{\left(Ai,j-in + D^{2} \right)^{m+1} - Ai,j-in^{m+1}}{D^{m+2} \times xi,j^{m} \times 22.13^{m}} \quad (10)$$

where is the contributing area at the grid cell's inlet (i,j) in metres square. D is the grid cell size (m), , and the is the aspect direction of the grid cell (i,j). m is associated with the ratio of rill to interill erosion on a landscape, thus:

$$m = \frac{\beta}{\beta + 1} \quad (11)$$

where

$$\beta = \frac{\frac{\sin \theta}{0.0896}}{\left[0.56 + 3 \times \left(\sin \theta \right)^{0.8} \right]} \quad (12)$$

θ is the slope angle in degrees. m ranges between 0 and 1. It is close to when the ratio of rill to interrill is nearer to 0. According to Desmet & Govers (1997), this technique is suitable for complex topography, though it has been criticized by Mitasova et al (1996). The C factor was estimated by value assignment from tables from existing research in a similar environment. Thus, shrub was assigned 0.015, agriculture 0.38, water 0.00, barren land 1.00, forest 0.08, and settlement 0.8 (Wischmeier and Smith, 1978; Koirala et al., 2019; Moisa et al., 2021; Egbueri et al., 2022; Merchán et al., 2023). The P factor was assigned 1 due to the unavailability of data on conservation practices in the area.

Result and Discussion: The estimated soil losses (Figure 2) with the LS methods were 25.25 t ha-1yr-1 (WS), 28.54 t ha-1yr-1 (MB), 14.87 t ha-1yr-1 (DG), and 27.76 t ha-1yr-1 (field). It shows that the PBIAS was -9.04 %, 2.81 %, and -46.43 %. Following, Moriasi et al. (2007) recommendation, all the models can be used for soil loss prediction, however, the WS and MB performed best and are recommended for soil loss prediction in the State.

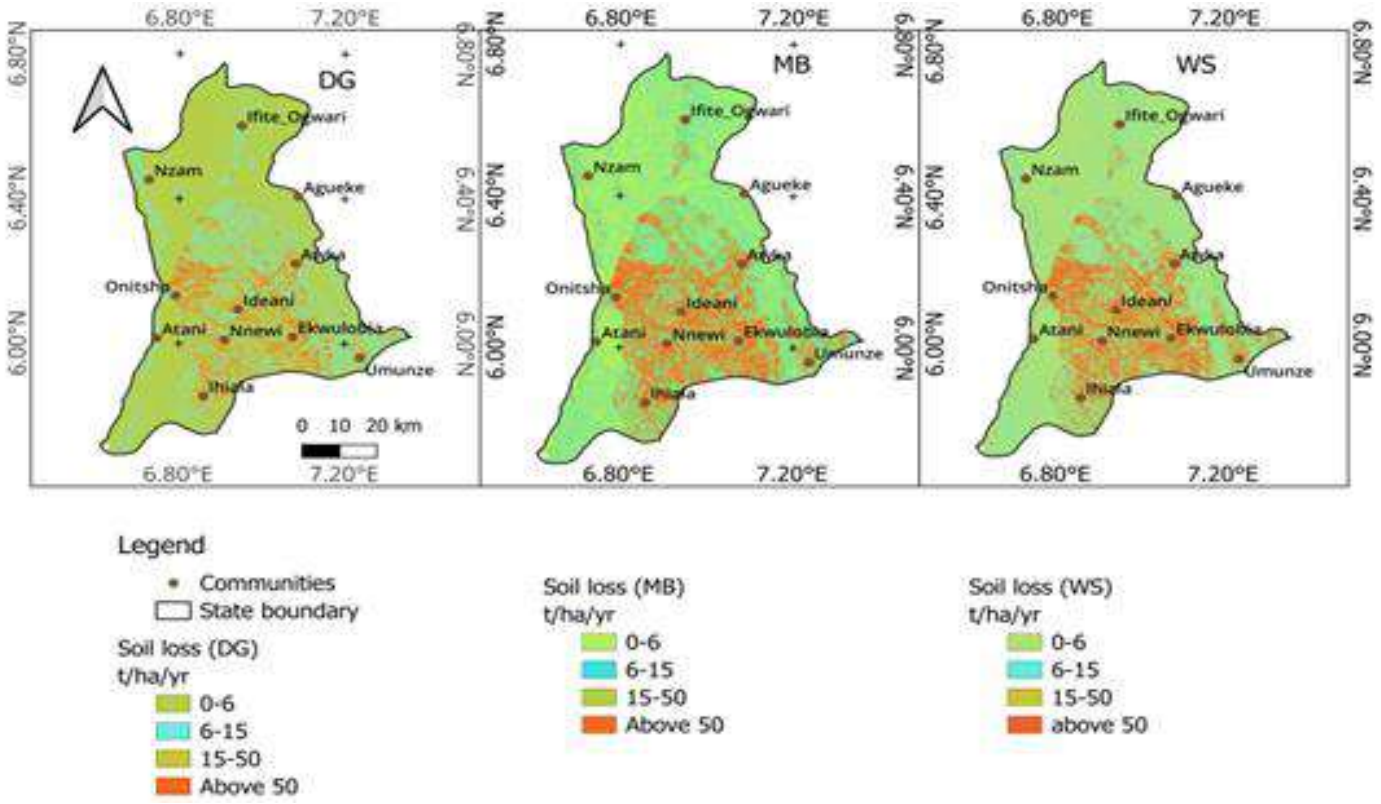

Figure 2. *Estimated Soil Loss in Anambra*

The LGAs where soil loss was above 40 t ha-1yr-1 are Aguata, Anaocha, Awka South, Idemili North, Idemili South, Njikoka, Nnewi North and South, Onitsha North, and Oyi LGAs. These are all areas with notable gullies in the State. This was confirmed via fieldwork. This showed that though, the model does not account for gullies, areas of extreme soil loss above 40 t ha-1yr-1 are also areas of intense gully erosion. This is in line with Andreoli (2018) that sheet and rill erosion are theoretically within the range of 0 to 5 t ha-1yr-1 while areas with gullies can be high reaching 1000 t ha-1yr-1. Based on this, the MB model highlighted all the LGA where large gullies exist while the WS omitted Onitsha North as it had only 37.56 t ha-1yr-1. The DG method underestimated all the areas as none of the LGA had soil loss up to 40 t ha-1yr-1. Therefore, the 3 different methods of estimating the LS method highlighted areas of high erosion risks but the DG method underestimated the severity of soil erosion in the State. Also, t-test result shows that there is significant difference between the estimated mean annual soil loss using the WS or MB method and the DG method (p-value = 0.0003/0.002). There is insufficient evidence the reject the null hypothesis for the test between the WS and the MB method at 0.05 confidence level (p-value = 0.23). Thus, the MB and WS methods performed best in predicting soil erosion in the Anambra State. Hence, in erosion studies over Anambra State, the WS or the MB method is recommended.

Conclusion: Soil erosion prediction using the RUSLE model was carried out in Anambra State Nigeria using 3 different methods of LS factor estimation. The result indicates that soil erosion is a severe problem of land degradation in the area. Also, it shows that the mean annual soil loss in the State was 25– 30 t ha-1yr-1 with variations as erosion is severer in the central and southern parts than the northern and western parts. The DG method of LS estimation underperformed in predicting soil loss in the State, unlike the MB and WS methods. Therefore, soil erosion in the Anambra State is best estimated in the RUSLE model using the MB and WS methods of LS estimation.

Acknowledgement: The Corresponding author expresses his gratitude to the German Federal Ministry of Education and Research (BMBF) for funding his PhD studies through the West African Science Centre for

Climate Change and Adapted Land Use (WASCAL). The corresponding author also expresses his gratitude to the Intergovernmental Panel on Climate Change (IPCC) and The Prince Albert II of Monaco Foundation. The Corresponding author is very grateful to them for the support that produced this research output. However, the thoughts and all expressions in the manuscript are exclusively by the author and should under no circumstances be considered as reflection of the position of the funding bodies.

References: Alewell, C., Borrelli, P., Meusburger, K., Panagos, P., 2019. Using the USLE: Chances, challenges and limitations of soil erosion modelling. International soil and water conservation research 7, 203–225. https://doi.org/10.1016/j.iswcr.2019.05.004

Andreoli, R., 2018. Modeling erosion risk using the RUSLE equation. QGIS and Applications in Water and Risks 4, 245–282. https://doi.org/10.1002/9781119476726.ch8

Benavidez, R., Jackson, B., Maxwell, D., Norton, K., 2018. A review of the (Revised) Universal Soil Loss Equation ((R) USLE): with a view to increasing its global applicability and improving soil loss estimates. Hydrology and Earth System Sciences 22, 6059–6086. https://doi.org/10.5194/hess-22-6059-2018

CHIRPS, 2022. Climate Hazards Group InfraRed Precipitation with Station data (CHIRPS) daily rainfall data.

Desmet, P.J.J., Govers, G., 1996. A GIS procedure for automatically calculating the USLE LS factor on topographically complex landscape units. Journal of soil and water conservation 51, 427–433.

Desmet, P.J.J., Govers, G., 1997. Comment on'Modelling topographic potential for erosion and deposition using GIS'. International Journal of Geographical Information Science 11, 603–610. https://doi.org/10.1080/136588197242211

Egbueri, J.C., Igwe, O., Ifediegwu, S.I., 2022. Erosion risk mapping of Anambra State in southeastern Nigeria: soil loss estimation by RUSLE model and geoinformatics. Bulletin of Engineering Geology and the Environment 81, 91. https://doi.org/10.1007/s10064-022-02589-z

iSDASoil, 2022. Innovative Solutions for Decision Agriculture (iSDA), 30 m resolution soil map of Africa.

Koirala, P., Thakuri, S., Joshi, S., Chauhan, R., 2019. Estimation of soil erosion in Nepal using a RUSLE modeling and geospatial tool. Geosciences 9, 147. https://doi.org/10.3390/geosciences9040147

Merchán, L., Martínez-Graña, A.M., Alonso Rojo, P., Criado, M., 2023. Water Erosion Risk Analysis in the Arribes del Duero Natural Park (Spain) Using RUSLE and GIS Techniques. Sustainability 15, 1627. https://doi.org/10.3390/su15021627

Mitasova, H., Hofierka, J., Zlocha, M., Iverson, L.R., 1996. Modelling topographic potential for erosion and deposition using GIS. International journal of geographical information systems 10, 629–641. https://doi.org/10.1080/02693799608902101

Moisa, M.B., Negash, D.A., Merga, B.B., Gemeda, D.O., 2021. Impact of land-use and land-cover change on soil erosion using the RUSLE model and the geographic information system: a case of Temeji watershed, Western Ethiopia. Journal of Water and Climate Change 12, 3404–3420. https://doi.org/10.2166/wcc.2021.131

Moore, I.D., Burch, G.J., 1986a. Physical basis of the length-slope factor in the universal soil loss equation. Soil Science Society of America Journal 50, 1294–1298. https://doi.org/10.2136/sssaj1986.03615995005000050042x

Moore, I.D., Burch, G.J., 1986b. Modelling erosion and deposition: topographic effects. Transactions of the ASAE 29, 1624–1630. https://doi.org/10.13031/2013.30363

Moriasi, D.N., Arnold, J.G., Van Liew, M.W., Bingner, R.L., Harmel, R.D., Veith, T.L., 2007. Model evaluation guidelines for systematic quantification of accuracy in watershed simulations. Transactions of the ASABE 50, 885–900. https://doi.org/10.13031/2013.23153

Naipal, V., Reick, C., Pongratz, J., Van Oost, K., 2015. Improving the global applicability of the RUSLE model–adjustment of the topographical and rainfall erosivity factors. Geoscientific Model Development 8, 2893–2913. https://doi.org/10.5194/gmd-8-2893-2015

Nakil, M., Khire, M., 2016. Effect of slope steepness parameter computations on soil loss estimation:

review of methods using GIS. Geocarto international 31, 1078–1093. https://doi.org/10.1080/10106049.2015.1120349
NASA, 2022. Shuttle Radar Topographic Mission (SRTM) 30 m Digital Elevation Model (DEM).
Panagos, P., Borrelli, P., Meusburger, K., 2015. A new European slope length and steepness factor (LS-Factor) for modeling soil erosion by water. Geosciences 5, 117–126. https://doi.org/10.3390/geosciences5020117
Renard, K.G., Foster, G.R., Weesies, G.A., McCool, D.K., Yoder, D.C., 1997. Predicting soil erosion by water: A guide to conservation planning with the Revised Universal Soil Loss Equation (RUSLE). Agriculture handbook 703, 407.
Roose, E.J., 1977. Use of the universal soil loss equation to predict erosion in West Africa, in: Soil Erosion: Prediction and Control. Soil Conservation Society of America Ankeny, IA, pp. 60–74.
Tsige, M.G., Malcherek, A., Seleshi, Y., 2022. Improving the Modified Universal Soil Loss Equation by Physical Interpretation of Its Factors. Water 14, 1450. https://doi.org/10.3390/w14091450
USGS, 2023. The United States Geological Survey (USGS) 30 m resolution Landsat 7 and 8 images.
Wischmeier, W.H., Smith, D.D., 1978. Predicting rainfall erosion losses: a guide to conservation planning. Department of Agriculture, Science and Education Administration.
Ziadat, F.M., Taimeh, A.Y., 2013. Effect of rainfall intensity, slope, land use and antecedent soil moisture on soil erosion in an arid environment. Land Degradation & Development 24, 582–590. https://doi.org/10.1002/ldr.2239 s

Comparative Studies on The Techniques of Production of Linde Type A Zeolite from Nigeria Raw Kaolin Deposit and them Ion Exchange Behaviour

Abdulsalami Kovo
Department of Chemical Engineering, Federal University of Technology, Minna, Nigeria

Prof. M. S. Haruna
National Agency for Science and Engineering Infrastructure, Abuja, Nigeria

Dr. A. R. Agava
National Agency for Science and Engineering Infrastructure, Abuja, Nigeria

N. J. Sani
National Agency for Science and Engineering Infrastructure, Abuja, Nigeria

Abstract: Conventional hydrothermal and alkaline fusion methods have been successfully used to produce Linde Type A Zeolite from Nigeria raw kaolin deposit. The synthesized zeolites were characterized by X-ray diffraction (XRD). The percent crystallinity was estimated from the peak area. The percent crystallinity of as-synthesized Zeolite A ranged from 22.52 to 30.70 % for samples synthesized by conventional hydrothermal method (AC) and from 28.74 to 43.35 % for those produced by alkaline fusion route (AF). The AF's gave better results than AC's samples. It was concluded that the fusion process aid in transformation of quartz and kaolinite into large amount of amorphous aluminosilicate (metakaolinite). In each case a replicated 23 two-level factorial design was used to study the influence of three different variables/ parameters (crystallization temperature, crystallization time and ageing time) on the quality of the synthesized zeolites (expressed in terms of CEC). The magnitude of the effect of these parameters and their interaction were also investigated

using factorial analysis. The crystallization temperature is the most significant factor and the interaction between the ageing time and crystallization temperature is less significant on the CEC. In both cases the other variables were found to be statistically significant. The average CEC for samples AC and AF respectively ranged between 264.32 – 585.75 and 303.31 – 627.74 meq/100 g. Some of the calculated CEC values are quite high compared to the theoretical value of 548 meg/100 g for zeolite A which may be due to presence of some unidentified/undetected phases or impurities that has adsorption capacity. The synthesized zeolites showed high CEC as compared to other commercial zeolites and therefore can be used in the removal of heavy metals from aqueous phase.
Keywords: Zeolite, Alkaline fusion, Factorial design, Cation exchange capacity and Crystallinity.

1.0 Introduction: Design of experiments (DOE) has become one of the most popular statistical techniques since 1990s. When planning a test series, several experimental strategies can be used and one suitable method that is increasingly been adopted as an experimental strategy is the factorial design as it takes into consideration the interactions between factors and examine if a factor has an influence on a specific variable or not (Montgomery, 2005). Cation exchange capacity which is a significant property of zeolites results from the presence of loosely bound cations of alkali and alkaline earths elements, often called exchangeable cations in the structure of the zeolites which are easily exchanged when zeolites come in contact with solutions of "saturating" or "indexing" ions (Konstantinos, 1999). The commonly exchangeable ions are Ca2+, Mg2+, K+, Na+ and NH4+ and it is usually expressed as milliequivalents per gram (or per 100g) of material. The reaction between a zeolite and an ionic solution is illustrated as: N1(Z) + N2(S) N2(Z) +N1(S) (1.1) N1 is the exchangeable cation in the zeolite Z and N2 is the saturating or index ion in solution S. According to the work of Mumpton (1999), CEC increase with the aluminum content of the zeolite because more extra framework cation is needed to balance the charge. The most widely used cation exchange process is by treating zeolites with aqueous solutions that contains the cation to be introduced. This is achieved by suspending the zeolites in the solution under the appropriate conditions (amount and concentration of the salt, temperature and pH) for ion exchange, followed by filtration and washing of the filter cake. Most common synthetic zeolites are types A, X, Y and ZSM-5. Due to their exceptional properties, both natural and synthetic zeolites are commercially used in adsorption, ion-exchange, as molecular sieve and as catalyst. Most natural zeolites are of lower Si/Al ratios, since structure-directing agents necessary for formation of siliceous zeolites are absent. Also, the catalytic activity of natural zeolites is limited by their inadequate supply, non-uniform pore size, impurities and low surface areas (Kovo, 2011). As a result of these shortcomings synthetic zeolites were developed mimicking the conditions of their natural counterparts but at lower temperature and shorter time (Auerbach, 2003; Kovo, 2011). Synthetic zeolites are generally synthesized by hydrothermal processes using commercial chemicals (sodium aluminate, aluminium hydroxide, silica gel, sodium metasilicate) as a source of silica and alumina which are quite expensive generally. The use of clay (kaolin) as a combined source of silica and alumina is economical because it reduces the cost of producing zeolite from expensive chemicals (Kovo, 2011). Previous work of Kovo, 2011 on the synthesis of zeolitic material from Ahoko kaolin was carried out by conventional hydrothermal method (which is based on dissolution of metakaolin with alkaline solutions, mainly NaOH followed by hydrothermal crystallization of the aluminosilicate gel) using one- factor-at-a-time approach which fails to detect interaction among variables. In this work, design of experiments (two-level factorial design) was used in the transformation of Ahoko kaolin into zeolite A by two different methods: (i) Conventional hydrothermal alkaline activation (ii) Alkaline fusion prior to hydrothermal treatment. The second method tends to dissolve more of the aluminosilicate and also aid in transformation of quartz and kaolinite into sodium silicate and metakaolinite (Rios, Williams, and Fullen 2008; Espejel-Ayala, Schouwenaars, Dura´n-Moreno, Ramı´rez - Zamora, 2013). Since zeolites vary with location and the optimal way to learn about zeolite synthesis is by examining a single zeolite synthesis from different perspectives (Auerbach, 2003).

2.0 Materials and Experimental Procedure: The raw material is kaolin which is sourced from Ahoko in Kogi

state, Nigeria . Prior to zeolite production , the kaolin was refined/beneficiated to reduce the quartz content. This is followed by drying and pulverizing using porcelain mortar and pestle. The chemicals used are: sodium hydroxide pellets (97.5%), sodium hydroxide powder (99%), sodium metasilicate (95%), ammonium acetate (98%), ethanol (99%) and deionised water.

2.1 Experimental Design for Factorial Analysis: In order to reduce the total number of experiments, two level experimental designs with three factors was used. The experimental factors which were chosen from literature are ageing time (hr), crystallization time (hr) and crystallization temperature in (oC). The number of experiments is expressed as

$$N = (2k) \times R \qquad (2.1)$$

Where; N= Number of experiments, k = Number of factors and R = Number of replica

Table 2.1: Levels of Independent Variable for Zeolite A

Levels	Low	High
Coding	-1	+1
Ageing Time (hr)	3	12
Crystallization time (hr)	3	6
Crystallization temperature (^oC)	70	100

Table 2.2: Factorial Design Matrix for Zeolite A Synthesis Using Conventional Hydrothermal Treatment (AC) and Alkaline Fusion (AF) Methods.

Samples		Ageing Time (hr)	Crystallization Time (hr)	Crystallization Temperature (^oC)
AC	AF			
AC1	AF1	3	3	70
AC2	AF2	12	3	70
AC3	AF3	3	6	70
AC4	AF4	12	6	70
AC5	AF5	3	3	100
AC6	AF6	12	3	100
AC7	AF7	3	6	100
AC8	AF8	12	6	100

2.2 Synthesis of Zeolitic Materials: **2.2.1 Conventional hydrothermal Alkaline Activation**: The metakaolin (which served as a combined source of silica and alumina) was obtained by calcinations of refined kaolin in a muffle furnace at 600oC for 1 hour using a crucible. The production of Linde type A zeolite (LTA) was carried out from reaction mixture with molar composition.

$$4.25Na_2O:Al_2O_3:2SiO_2:275.4H_2O$$

In order to produce zeolite A with the above molar composition, 2.434 g of NaOH pellets was dissolved in 35 g of distilled water in reaction beakers and subsequently 1.574 g of metakaolin was added under stirring condition. The aluminosilicate gel was aged at room temperature for different ageing time. Hydrothermal treatment of the aged mixture was carried out in an autoclave at varying crystallization time and temperature. At the end of which the mixture was filtered and washed with distilled water until pH of filtrate were about 8. The samples were subsequently dried in an oven at 80oC for 3 hours and characterized with aid of XRD.

2.2.2 Alkaline Fusion method: In this method, 6.2 g of kaolin (combined source of silica and alumina) was dry mixed with 7.44 g of NaOH powder (kaolin/NaOH = 1/1.2) for 30 minutes. The mixture was heated in a muffle furnace at 600oC for 1 hour. The fused product of kaolin and NaOH was ground and then 4.4 g of this was dissolved in 21.5 ml of distilled water under stirring (in ratio of 4.9 ml of water/g of fused product) under stirring condition to form the amorphous precursors followed by ageing at room temperature and hydrothermal treatment at different crystallization temperatures and times. At the end of the hydrothermal treatment, the sample was filtered, washed (to a pH of 9) and dried in an oven for 6 hours at 80oC. The products obtained were characterized by XRD. Rios et al. (2008) used this technique to synthesize zeolite

with molar composition of

$$3.9Na_2O:Al_2O_3:2SiO_2:153.9H_2O$$

2.3 Determination of Cation Exchange Capacity: The cation exchange capacity (CEC) was determined using the ammonium acetate saturation method at room temperature under standard atmospheric pressure (1atm) using zeolite powders. About 150 mg of the <125 µm size fraction was accurately weighed from each sample and transferred to a mechanical shaker where 10 ml of 1N solution of sodium acetate (CH_3COONa) was mixed for 5 minutes. The mixture was then centrifuged in order to obtain a clear supernatant solution which was decanted. This procedure was repeated another two times to ensure that all cations in the zeolite have been replaced with Na ion. The Na-laden zeolite was washed with 30 ml of 99% ethanol and shaken in a mechanical shaker for 5 min. The supernatant was removed, and the procedure was repeated one more time to ensure that the zeolite was clean and laden only with Na. The Na laden zeolite was then mixed with 1N ammonium acetate solution (CH_3COONH_4) buffered at pH 7 to replace the exchanged sodium ion with ammonium ion. The suspension was well shaken, left overnight and centrifuged. The clear liquid was decanted. The same procedure was repeated with CH_3COONH_4 five times adding fresh 10ml of CH_3COONH_4 to ensure that all Na ions were replaced by NH_4 ion. After each step, the supernatant of CH_3COO^- solution was decanted to a 100 ml volumetric flask which was diluted to 100 ml with ammonium acetate solution and the sodium ion concentration in this supernatant was determined by atomic absorption emission spectroscopy. The sodium binding capacity was then calculated from:

$$q_e=((c_o-c_b)\times V)/(MW\times m) \quad (2.2)$$

Where qe is the exchanged Na ions per weight of zeolite (mg/100 g) or CEC value, co is the Na concentration (mg/L), and cb is the Na concentration in the blank (mg/L). Both co and cb were measured by AAS. V is the volume of the aqueous phase (ml), equal to 100 ml in this experiment; m is the amount of zeolite (g), equal to 150mg and MW is the molecular weight of Na (g).

3.0 Characterization of Zeolitic Materials: The nature of phase and percent purity (crystallinity) of as-synthesized zeolites were identified using an AXS Bruker advance-8 Diffractometer using CuKα (λ=0.1541nm) radiation at 40 kV and 40 mA. Using a scan speed of 0.04o in the 2θ range of 5-50o, the diffraction patterns of as-synthesized zeolites were obtained.

4.0 Results:

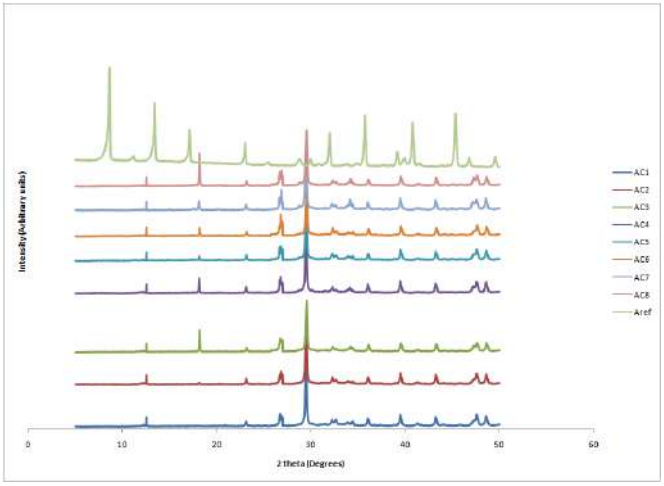

Figure 4.1: XRD Pattern of Laboratory Synthesized Zeolite A (AC Samples)

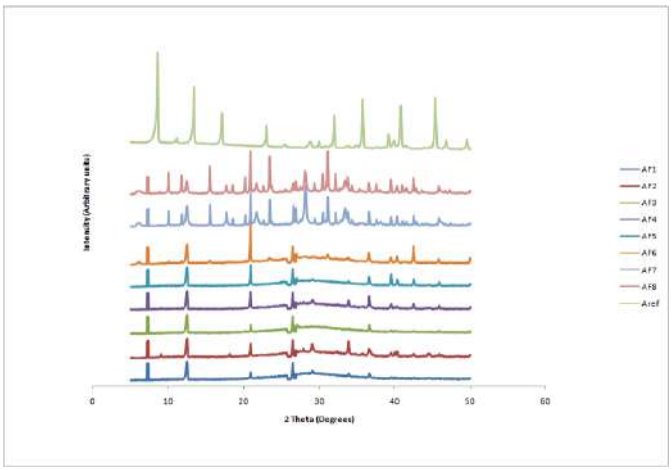

Figure 4.2: XRD Pattern of Laboratory Synthesized Zeolite A (AF Samples)

Figures 4.1 and 4.2 show the XRD pattern of the as-synthesized zeolite A using both conventional hydrothermal and alkaline fusion prior to hydrothermal treatment methods respectively. From the conventional hydrothermal method, the formation of zeolite A was observed through the peak diffraction at 2θ = 12.49, 17.69, 24.04, 35.83, 39.53, 43.61, 47.41 and 48.02 as reported by Traecy and Higgins (2001). The zig-zag peaks in the background indicates the presence of amorphous phase of metakaolinite. The peak at 2θ is 28.53 confirm the presence of sodalite. This is in accordance with Ostwald's rule of successive reaction. From the analysis of the peak area, percent crystallinity was estimated. The percent crystallinity ranged from 22.52 - 30.70 with sample AC7 having the highest percent crystallinity. While the characteristic peak of zeolite A synthesized by alkaline fusion method was observed at 2θ between the range of 7.21, 10.19, 12.49, 20.47, 24.04 and 36.59. The peak due to quartz was observed to be present at 2θ = 26.6 (Treacy and Higgins, 2001) in both instances. The percent crystallinity ranged from 28.74 - 43.35 % with sample AF6 having the highest percent crystallinity. Although the zeolite peaks are weak, but they are quite consistent with the reference especially the AF samples. From the analysis of the results for the two methods of synthesis, except samples AF2 and AC2, samples synthesized through alkaline fusion route (AF) possess higher percent crystallinity than the samples synthesized by conventional method (AC), also the first diffraction peak appeared at 2θ = 7.21 and 12.49 for AF's and AC's samples respectively. This can be attributed to the fact that the fusion aid in transformation of quartz and kaolinite into large amount of sodium silicate amorphous aluminosilicate (metakaolinite), which indicates that the fusion process was very effective in extracting the si species in these mixture (Rios et. al., 2008 and Espejel-Ayala et al., 2013). The absence of peak diffraction at 2θ for some of the samples could be due to incomplete transformation of MTK or due to low crystallinity at that point. The full factorial design presented in Tables 2.2 and their uncoded values are shown in Figure 4.3.

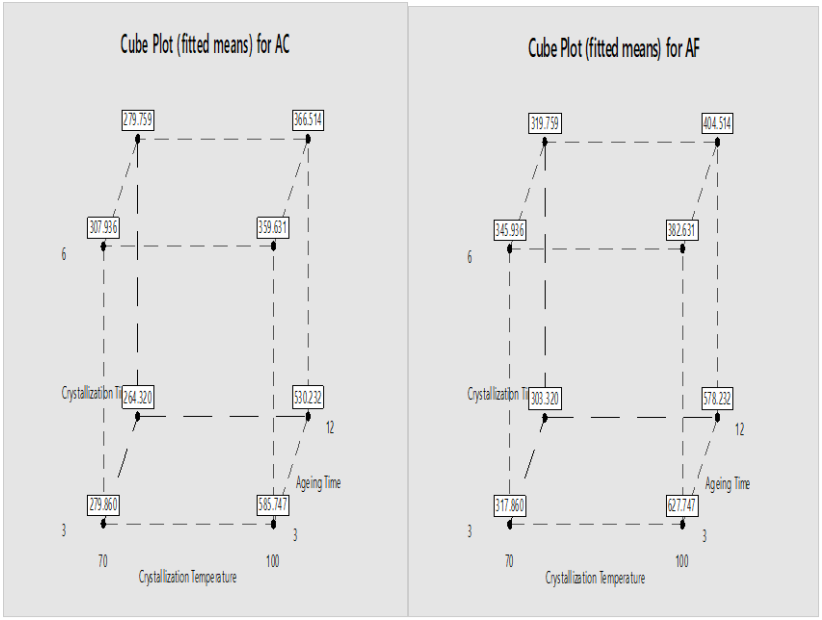

Figure 4.3. Cube Plots for Zeolite A CEC Response

The cube plot was used to examine how the process variables affect the zeolite A CEC. The plots show the response surface plot of zeolite A CEC. The cube plot corner points represent a different factorial design and illustrate the average zeolite A CEC result for the synthesis based on the process variables level. Some of the calculated CEC values are quite high compared to the theoretical value of 548 meg/100 g for zeolites A which may be due to presence of some unidentified/undetected phases or impurities that has adsorption capacity. These values are higher than the reported values of San Cristobal (2010) who reported a CEC of 292.8 meq/100 g for zeolite A.

4.1 Factorial Analysis Results for the Synthesized Zeolites: The factorial analysis was carried out using Excel 2013 and Minitab release 17. For all the analysis, the t-distribution, coefficients, P-values and estimated effects for the experimental results were obtained. The sum of squares and the F-distribution were also determined. The 95% confidence level was used for the statistical calculations. The effect defined as the increase or decrease of the zeolite CEC when process factor was changed was also determined. A negative effect indicates a decrease in zeolite CEC as the process factor setting is increased. A positive effect designates an increase in zeolite CEC as the process factor setting is increased. The effect of the magnitude is used in ranking the influence of the factors on the experimental results. The regression equation coefficients were also acquired from the fit of the zeolite CEC results, if the P-value is <0.05, then the factor is significant statistically at the chosen 95% confidence level.

4.1.1 Factorial Analysis Results Showing Effects of Crystallization Temperature, Crystallization Time and Ageing Time on Zeolite a CEC: Tables 4.1 and 4.2 show the estimated effects and coefficients for zeolite – A CEC. The result of the estimated effects suggests that the model contains three main effects, which can be evaluated in the absence of significant interactions and three two-way interaction effects. The p-values for all three main effects are less than 0.05 (Crystallization temperature = 0.000, Crystallization time = 0.000 and ageing time = 0.000). Therefore, there is evidence of a significant effect. The p-value result from the Tables also indicates that there is significant interaction between crystallization temperature and crystallization time (0.000) and between crystallization time and ageing time as their terms have p-values less than 0.05 (α=0.05). The Tables also show that crystallization temperature has the greatest effect (177.56 and 176.56) on zeolite A CEC. In addition, the tables show that setting the crystallization temperature high produced higher zeolite A CEC than setting the crystallization temperature low. The interaction between crystallization temperature and crystallization time has the second greatest effect (-108.34 and -115.84) on zeolite A CEC. The negative sign shows the settings of the two process variables have antagonistic effect (need to be at opposite setting). The result of the main effect plots show that the crystallization temperature is set high and crystallization time is set low to produce zeolite A of high CEC. Crystallization time has the third greatest

effect (-86.58 and -93.58) on zeolite A CEC. In addition, setting the crystallization time high produced lower zeolite A CEC than setting the crystallization time low. Ageing time has the fourth greatest effect (-23.09 and -17.09) on zeolite A CEC. In addition, higher ageing time produced lower zeolite A CEC than lower ageing time. The interaction between crystallization temperature and ageing time has the smallest effect (-1.23 and 3.27) on zeolite A CEC. In addition, setting the interaction high produced lower zeolite A CEC than setting the interaction low. The values in brackets are for AC and AF respectively.

Table 4.1: Estimated Effects and Coefficients for Zeolite A (Samples AC) CEC

Term	Effect	Coef	SE Coef	T-Value	P-Value
Constant		-1143.	2.56	145.35	0.000
Crystallization Temperature	177.56	19.95	2.56	34.71	0.000
Crystallization Time	-86.58	227.9	2.56	-16.93	0.000
Ageing Time	-23.09	29.5	2.56	-4.51	0.002
Crystallization Temperature*Crystallization Time	-108.34	-3.102	2.56	-21.18	0.000
Crystallization Temperature*Ageing Time	-1.23	-0.426	2.56	-0.24	0.816
Crystallization Time*Ageing Time	12.44	-6.95	2.56	2.43	0.041
Crystallization Temperature*Crystallization Time*Ageing Time	18.76	0.0926	2.56	3.67	0.006

Table 4.2: Estimated Effects and Coefficients for Zeolite A (Samples AF) CEC

Term	Effect	Coef	SE Coef	T-Value	P-Value
Constant		-1161.	1.56	262.56	0.000
Crystallization Temperature	176.56	20.747	1.56	56.53	0.000
Crystallization Time	-93.58	244.7	1.56	-29.96	0.000
Ageing Time	-17.09	30.27	1.56	-5.47	0.001
Crystallization Temperature*Crystallization Time	-115.84	-3.343	1.56	-37.09	0.000
Crystallization Temperature*Ageing Time	3.27	-0.437	1.56	1.05	0.326
Crystallization Time*Ageing Time	14.94	-7.61	1.56	4.78	0.001
Crystallization Temperature*Crystallization Time*Ageing Time	20.76	0.1025	1.56	6.65	0.000

Pareto charts of the standardized effect for zeolite A CEC response in Figure 4.5 show that there are three significant effects ($\alpha = 0.05$). These significant effects include crystallization temperature (A), crystallization time (B) and ageing time (C). In addition, it is observed that the Pareto plots show that the largest effect is crystallization temperature (A) because it extends the farthest. In 2011, Kovo concluded that temperature is an important parameter that influences zeolite crystallization because a small change in heating temperature can cause instant transformation in the zeolite phase. The effect for the interaction between the crystallization temperature and ageing time (AC) is the smallest because it extends the least. The ageing time and crystallization temperature interaction is not significant at $\alpha = 0.05$ level in the estimated effects and coefficients in Tables 4.1 and 4.2.

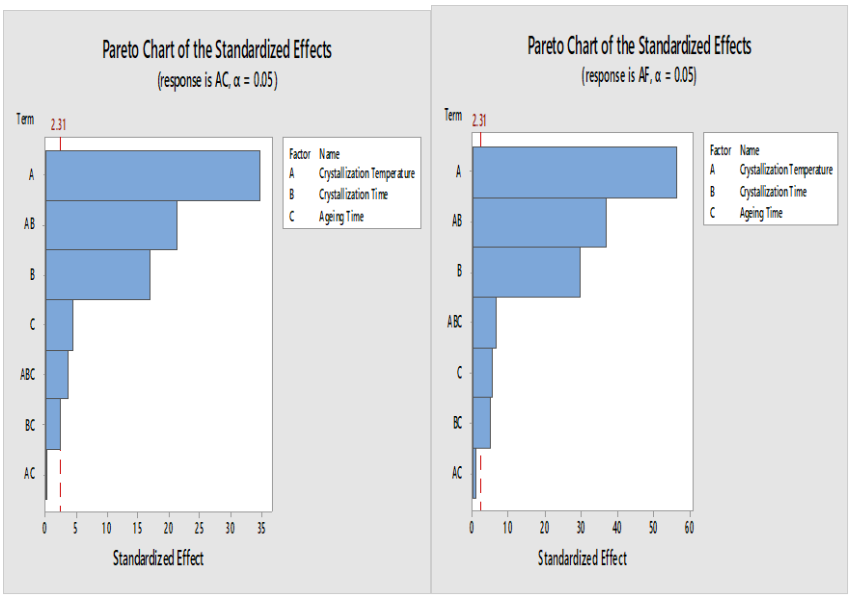

Figure 4.5. Pareto Charts of the Standardized Effect for Zeolite A CEC Response

Main effect plots of the fitted means of Figure 4.6 indicate the following: Crystallization temperature: Crystallization temperature produced higher CEC at high temperature (100oC) than at low temperature (70oC) as the fitted mean increased from 280 to 460 and 320 to 490 for both AC and AF respectively. Crystallization time: Crystallization time produced higher zeolite A CEC at low crystallization time (3 hrs) than at high crystallization time (6 hrs) as the fitted mean decreased from 420 to 330 and 460 to 370 respectively for both AC and AF. Ageing time: lower ageing time (3 hrs) produced zeolite A of higher CEC than higher ageing time (12 hrs) as the fitted mean decreased from 370 to 360 and 420 to 300 respectively in both cases. The earlier analysis obtained from p-values of Tables 4.1 and 4.2 show that the three main effects were significant at the 0.05 α-level. By comparing the slopes of the lines on the Main Effect plots of Figure 4.6, the relative magnitude of the synthesis process factor effects were compared. These plots show that there seem to be a large difference in the magnitude of the effects with crystallization temperature being the largest (steepest slope) followed by crystallization time (steeper slope) and ageing time being the smallest.

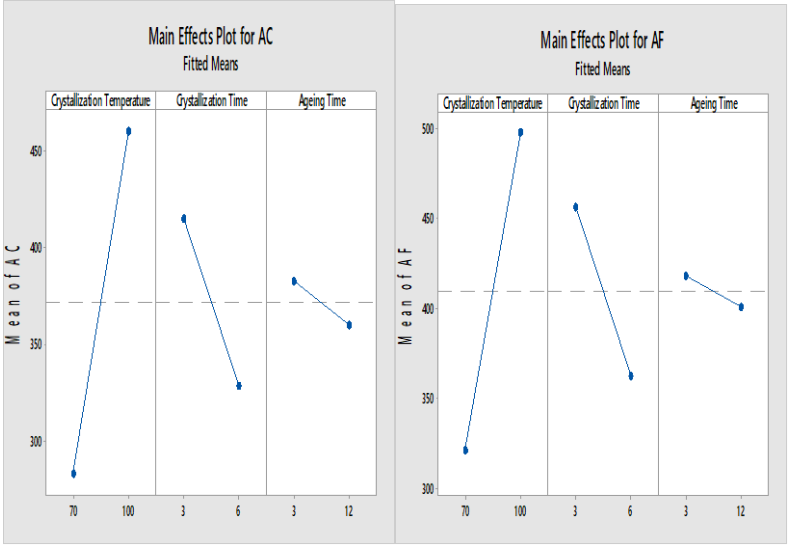

Figure 4.6. Main Effect Plots for Zeolite A CEC Response

Surface plot of zeolite A CEC against crystallization time and crystallization temperature of Figure 4.7 shows how crystallization temperature and crystallization time are related to zeolite A CEC. To maximize zeolite A CEC, high setting of crystallization temperature of 100oC and low setting of crystallization time of 3 hrs, while holding ageing time at 7.5 hrs should be chosen.

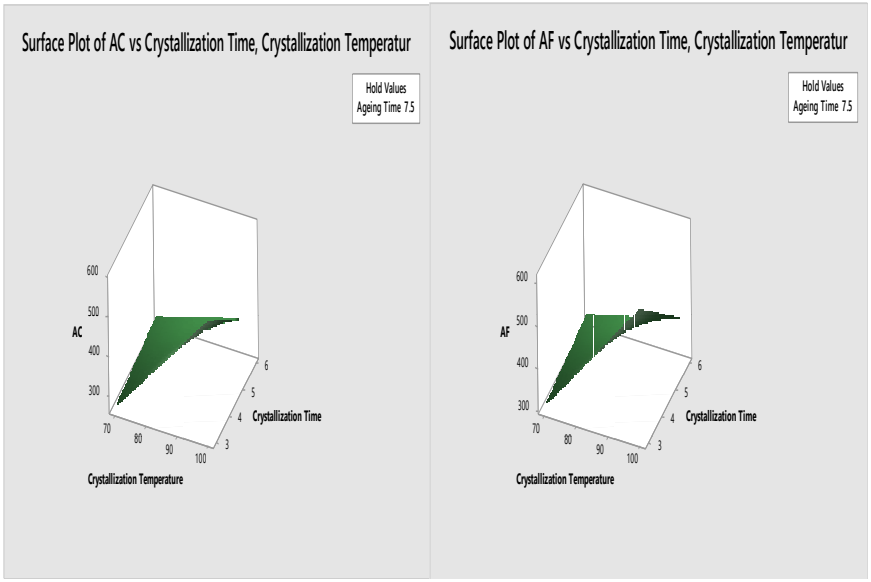

Figure 4.7. Surface Plots of Zeolite A CEC against Crystallization Time and Temperature

The model Equations can be built up from estimated coefficients for zeolite A CEC of Tables 4.1 and 4.2. For conventional hydrothermal method, Y_p=-1143.6+19.95x_1+227.9x_2+29.5x_3-3.102x_1 x_2-0.4261x_1 x_3-6.95x_2 x_3+0.0926x_1 x_2 x_3 (4.1) For alkaline fusion method, Y_p=-1161.6+20.747x_1+244.7x_2+30.27x_3-3.343x_1 x_2-0.4371x_1 x_3-7.61x_2 x_3+0.1025x_1 x_2 x_3 (4.2) Where x_1 = Crystallization temperature x_2 = Crystallization time and x_3 = Ageing time (The model equations are valid if x1, x2 and x3 ≠ 0)

Table 4.5: Statistical Parameters of the Model Correlating Zeolite A CEC to Crystallization temperature, Crystallization time, and Ageing time

	Values	
Statistical Parameters	AC	AF
S	10.2303	6.2462
R^2	99.60%	99.86%
R^2adjusted	99.25%	99.73%
R^2predicted	98.39%	99.43%

Table 4.5 shows the model proportion of the response variability that is (R2), the predicted R2, which is the level of prediction of the future data by the model and the adjusted R2 useful for comparing models from the same data with different numbers of terms. The R2 value lies between 0 and 100%. The model predicts better when R2 value is closer to 100% (Doddapaneni, Tatineni, Potumarthi and Mangamoori, 2007). The sum of squares of the prediction errors (PRESS) for assessing model's predictive ability from Table 4.5 is 10.2303 and 6.2462 for AC and AF samples respectively. Low PRESS value is an indication that the model fits the data as Montgomery (2005) reported that the model fits the data better when the PRESS is smaller.

5 Conclusion: Using both conventional hydrothermal and alkaline fusion methods, zeolite-A (NaA) have been successfully synthesized from Ahoko kaolin. It has also been demonstrated by this study the application of factorial analysis in determining the zeolite synthesis parameters that are having significant effect on zeolite CEC. For all the analysis the samples synthesized. From the percent crystallinity estimated from the peak area, the AF's gave better results than AC's samples. Some of the calculated CEC values are quite high compared to the theoretical value of 548 meg/100 g which may be due to presence of some unidentified/ undetected phases or impurities that has adsorption capacity. The synthesized zeolites showed high CEC as compared to other commercial zeolites and therefore can be used in the removal of heavy metals from aqueous phase. From the factorial analyses, the effects of crystallization temperature, crystallization time

and ageing time and their interactions were investigated and for zeolite A (both AC and AF), the crystallization temperature is the most significant factor and the interaction between the ageing time and crystallization temperature is less significant on the CEC.

References: Auerbach, S., K. A. Carrado, and P. K. Dutta (2003). Handbook of zeolite science and technology, New York, Marcel Decker Inc 1170. A.G. San Cristóbal, R. Castelló, M.A. Martín Luengo, and C. Vizcayno (2010). Zeolite prepared from calcined and mechanically modified kaolins: A comparative study. Applied Clay Science 49, 239–246. Bashir Yousif, S. A, (2011). "The Effect Of Modification Techniques On The Performance Of Zeolite-Y catalysts In Hydrocarbon Cracking Reactions", PhD Thesis, Faculty of Engineering and Physical Sciences, School of Chemical Engineering and Analytical Science, the University of Manchester. Breck, D. W. (1974). Zeolite Molecular Sieves. John Wiley and Sons Ltd, New York. Doddapaneni, K. K, Tatineni, R., Potumarthi, R., Mangamoori, L. N. (2007). Optimization of media constituents through response surface methodology for improved production of alkaline proteases by Serratia rubidaea. J Chem Technol Biotechnology. 82, 721–729. Doungmanee, R., Ronbanjob, A., Varong, P and Prasert, P. (2006): Zeolite Synthesis from Fly Ash from Coal-fired Power Plant by Fusion Method, The 2nd Joint International Conference on "Sustainable Energy and Environment (SEE 2006)", Bangkok, Thailand. D. Karami and S. Rohani (2009): Synthesis of pure zeolite Y using soluble silicate, a two-level factorial experimental design, Chemical Engineering and Processing, 48, 1288–1292. F. Espejel-Ayala, R. Schouwenaars, A. Dura´n-Moreno, R. M. Ramı´rez –Zamora (2013). Use of drinking water sludge in the production process of zeolites, Res Chem Intermed DOI 10.1007/s11164-013-1138-8. George E. C. and Hara P. (2008): "Synthesis of FAU Type Zeolite Y from Natural Raw Materials: Hydrothermal SiO2-Sinter and Perlite Glass". The Open Mineralogy Journal, 2, 1-5. G. Gobanu, D. Ignat, G. Carja, S. Ratoi, C. Luca. (2008). Zinc-modified forms of zeolites by wet impregnation method, Chem. Bull, "POLITEHNICA" Univ. (Timisoara), 53 (67), 1-2. Jalil, R. U., Karim H. Hassan and Inam, H. A. (2010). Preparation of type 4A zeolite from Iraqi kaolin: characterization and properties measurements: Journal of the Association of Arab Universities for Basic and Applied sciences, 9, 2-5. Janjira W. (2002), Synthesis and Kinetic Study of Zeolite Na-A from Thai Kaolin. Master of Science in Chemistry Thesis Suranaree University of Technology. Konstantinos P. K. (1999). Cation exchange capacity of zeolitic volcaniclastic materials: Applicability of the ammonium acetate saturation (AMAS) method. Clay and clay minerals, 47(6), 688-696. Kovo A. S. (2011). Development of zeolites and zeolite membranes from Ahoko Nigeria kaolin. PhD Thesis, Faculty of Engineering and Physical Sciences, School of Chemical Engineering and Analytical Science, the University of Manchester. Mainganye, D., Ojumu, T.V., and Petrik, L.F. (2012). Development of scale-up conditions for the synthesis of zeolites from South African coal fly ash: effect of fly ash composition and synthesis time. 62nd Canadian Chemical Engineering Conference, Vancouver, British Columbia, Canada, 14-17. Montgomery, D. C. (1999). Experimental Design for Products and Process Design and Development. The Statistician, 48(2), Tempe: USA, 159-177. Montgomery, D. C. (2005). Design and Analysis of Experiments. New York: John Wiley & Sons. Mu Mu, H. and Mya Mya, O. (2008). Preparation of Zeolite Y Catalyst for Petroleum Cracking, World Academy of Science, Engineering and Technology (48). Mumpton, F. A. (1999). Proceedings of the National Academy Science USA. Colloquium Paper 96, 3463-3470. M. A. Ismail, M. A. Z. Eltayeb and S. A. Abdel Maged (2013): synthesis of Zeolite A from Sudanese montmorillonite clay to remove nickel and copper ions from aqueous solution. International journal of chemical and biochemical sciences 4, 46-56. M. M. J. Treacy and J. B. Higgins (2001). Collection of Simulated XRD Powder Patterns for Zeolites 4th revised Edition Elsevier, New York. Noureddine, H., Viviane, R., Ammar, H. and Marie, N. P. (2010): Factorial design of experiment (DOE) for parametric exergetic investigation of a steam methane reforming process for hydrogen production. Chemical Engineering and Processing 49, 500–507. N. O. Omisanya, C. O. Folayan, S. Y. Aku and S. S. Adefila, (2012): Synthesis and characterisation of zeolite A for adsorption refrigeration application, Advances in Applied Science Research, 3 (6):3746-3754. Available online at www.pelagiaresearchlibrary.com. O.A.AbdelMoamen, I.M.Ismail, N.Abdelmonem and R.O.AbdelRahman (2015): Factorial design analysis for optimizing the removal of cesium and strontium ions on synthetic nano-sized zeolite, Journal of the Taiwan Institute of Chemical Engineers, 55, 133–144. Rios, C.

A., Williams, C. D., and Fullen M. A., (2008). Nucleation and growth history of zeolite LTA synthesized from kaolinite by two different methods. Journal of applied clay science, unedited manuscript. Ruren, X., Wenqin, P., Jihong, Y., Qisheng, H. and Jiesheng, C. (2007). Chemistry of zeolites and related porous materials: Synthesis and structure, John Wiley and sons (Asia) pte. Sudaporn, T., (2004). Synthesis of zeolites from perlite and study of their ion exchange properties. PhD Thesis, Department of Chemistry, Suranaree University of Technology. Syed Sameen, A. Z. and Sohrab, R. (2005). Progress Towards a Dry Process for the Synthesis of Zeolite - A Review, Reviews in Chemical Engineering, 21(5), 265-306. Taylor, A. E. (2007). Microwave synthesis and occlusion reactions of zeolites, PhD thesis, School of Chemistry, The University of Birmingham. Xinmei, L., Zifeng, Y., Huaiping, W., Yantuo, L. (2003). In-situ Synthesis of NaY Zeolite with Coal-Based Kaolin, Journal of Natural Gas Chemistry (12), 63-70. Yuanhao, D. (2015). Statistical Analysis and Optimization of Ammonia Removal from Aqueous Solution by Zeolite and Ion-exchange Resin. Master of Applied Science In Environmental Engineering, Department of Civil Engineering, University of Ottawa Ottawa-Carleton, Institute for Environmental Engineering Ottawa, Ontario, Canada. Zeolite and catalysis: Synthesis, reactions and Applications, Edited by Ji˘r´ı ˘ Cejka, Avelino Corma, and Stacey Zones, 2010, WILEY-VCH Verlag GmbH & Co. KGaA, Weinheim.

Effect of Different UV Exposure Energy on Polyimide-Based Nonvolatile Resistive Photomemory Device

Xin-Rong Wu
Department of Electronic Engineering, Feng Chia University, Taichung, Taiwan

Pei-Ying Jiang
Department of Electronic Engineering, Feng Chia University, Taichung, Taiwan

Syuan-Yi Li
Department of Electronic Engineering, Feng Chia University, Taichung, Taiwan

Wen-Luh Yang
Department of Electronic Engineering, Feng Chia University, Taichung, Taiwan

Abstract: Recently, many researchers pay attractive attention to organic memory technology. Polyimide film was used as the resistive switching layer of nonvolatile photomemory in this study. In order to improve the performance of the device, different wavelengths of Ultraviolet (UV) light were used to operate the device, and its impact on the polyimide film was discussed. In this paper, three different UV light bands, UVA, UVB, and UVC, are used to switch devices between low resistance state (LRS) and high resistance state (HRS). It can be seen from the results that all three kinds of energies of UV light can transform the polyimide film from HRS to LRS successfully. According to the data, after 1s of UVB irradiation, the LRS current of polyimide-based photomemory device is the largest, and the data retention ability is also the best, the second is to irradiate UVA, and the last is to irradiate UVC. The results of the optical properties and electrical properties are coincidental. Therefore, different UV energies can affect this photomemory device.
Keywords: Nonvolatile, Organic, Photomemory, Polyimide, Resistance, Ultraviolet

1. Introduction: With the in-depth study of organic materials, the conductivity of organic materials has opened up new research fields for people, and a large number of organic semiconductor materials have emerged. It has even been found that many performances of organic semiconductor materials are better

than inorganic semiconductor materials. For example, the material is easy to obtain, low in manufacturing cost, capable of low-temperature processing, and has good absorption characteristics in the visible light region, and the emission spectrum can cover the entire visible light region, and even extend to the UV and near- infrared (NIR) light regions. Therefore, in today's various devices, organic materials are undoubtedly the focus of much attention (C.-C. Chen, Chiu, Sheu, & Wei, 2008; F.-C. Chen, 2018; Ouyang et al., 2017; Palma & Duart, 2017). Optical manipulations are non-destructive. In addition to being able to operate the device in a wide range and improve the operating efficiency, it can also improve the performance of the device (Gemayel et al., 2015; Wakayama, Hayakawa, & Seo, 2014; H. Wu et al., 2021; Zhou et al., 2017). In recent years, the rapid development and transmission of optical signals have led to the development of many optoelectronic devices, such as photodetectors, phototransistors, and photodiodes (Cheng, Yang, & Hsu, 2009; Dini, Calvete, & Hanack, 2016; Wang et al., 2019; Yang & Ma, 2019). With the rapid development of artificial intelligence (AI) technology, photodetectors can be combined with other components to perform calculations on data, so it is also widely used in image processing(Lei et al., 2015; Nalwa, 2020). However, if photodetectors remove the light, the data cannot be stored, and non-volatile memory is needed as an auxiliary. In order to solve the above problems, the research and development of photomemory with storage characteristics has become a trend that has attracted much attention (H. Chen, Liu, Hu, Al-Ghamdi, & Fang, 2015; Fang & Hu, 2017). The storage mechanism of most photomemories is based on the Charge Trap Type (C. Huang et al., 2017). With down scaling of the device, the photomemory reduces the memory window ratio due to the reduction of charge carrier traps, and the excessive erase voltage causes RC delay (Jia et al., 2019; Yin, Akey, & Jaramillo, 2018). Recently, Wu et al. developed a polyimide (PI)-based non-volatile resistive photomemory (C.-C. Wu, Chen Jr, & Yang, 2022). They use PI as the resistive layer of resistive memory (Hsiao et al., 2015). The PI film is photosensitive to UV light, and its molecular structure can be changed by UV light irradiation. The high-energy-gap aromatics are transformed into low-energy-gap quinoids so that the PI film can switch between HRS and LRS (Costa, Taveira, Lima, Mendes, & Santos, 2016). The conduction mechanism of this photomemory is Charge Transfer. Its device size depends on the size of the electrodes. Therefore, there will be no device scaling limitations (Ismail et al., 2016; Tseng et al., 2007; Zhou et al., 2018). Here, different wavelengths of UV light were used to perform device-switching operations and discuss the relative characteristics of the device after different UV irradiation.

2. Materials and Methods: First, 4,4’-Oxydiphthalic Anhydride (ODPA) was stirred with the N-methyl-2-pyrrolidone (NMP) solution for 30 minutes, then 4,4'-oxydiphenylamine (ODA) was added to the solvent and stirred for 12 hours. To complete the preparation of PAA solvent. Next, the PAA solution was dropped onto the TaN for spin coating, and the spin coater pre-rotation speed was set to 1500 rpm for 5 seconds for the first time, and then 3000 rpm for 30 seconds. The device entered high temperature for dehydration and the cyclization reaction was heated to 260°C at high temperature and baked for 30 minutes in nitrogen. During this period, the PAA underwent a dehydration reaction and cyclization reaction to form a polyimide solid film. This step is also known as imidization, which is shown in Figure 1. Finally, the polyimide film was pasted with a metal mask and put into a metal thermal evaporation system to complete the top electrode. The thickness of the top electrode was about 100 nm. The polyimide photomemory can be completed. Figure 2 illustrates a schematic diagram of the PI photomemory device. Optical analysis was performed with a UV-vis spectrometer (Evolution 201, Thermo Fisher Scientific, Waltham, MA, USA). The current-voltage (I–V) characteristics were measured using the Keithley 4200A- SCS parameter analyzer (Tektronix, Beaverton, OR, USA).

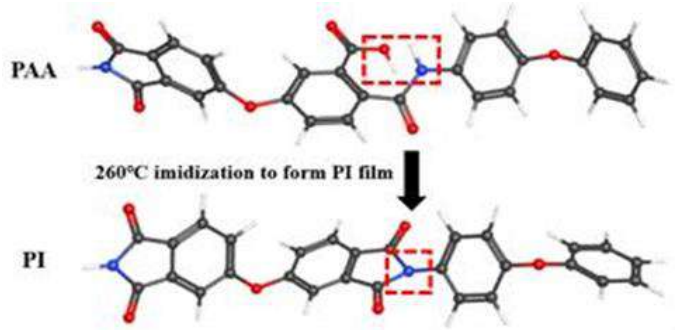

Figure 1: Schematic 260℃ Imidization To Form The PI Film (J. S. Huang, Liu, Chen, Tseng, & Yang, 2022)

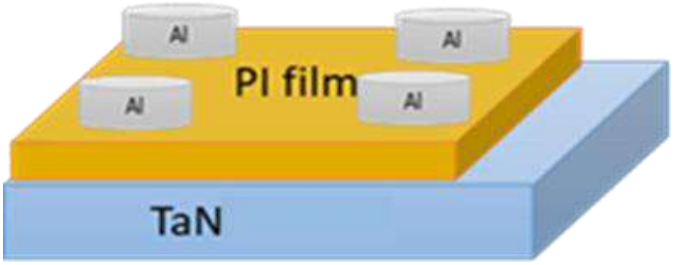

Figure 2: Schematic Diagram of The Device Structure

3. Results and Discussion: 3.1 Optical Characteristics: In order to know the influence of different UV light on PI thin films, the optical properties of PI thin films were measured by UV–vis spectroscopy. Figure 3 shows the maximum absorption of the PI film in the initial state, after 1 s of UVA irradiation, after 1 s of UVB irradiation, and after 1 s of UVC irradiation. The absorption of the aromatic PI is about 0.9 ~1.0. After irradiating UVB, its absorption drops to 0.7~0.9, which is an obvious change. Although the absorption of the PI film decreases after UVA and UVC irradiation, the magnitude is very small. Figure 4 illustrates the wavelengths corresponding to the absorption peaks of PI films in the initial state, after 1 s of UVA irradiation, after 1 s of UVB irradiation, and after 1 s of UVC irradiation. The absorption peak wavelength of aromatic PI falls at about 345nm. However, after irradiating with UVB light for one second, its absorption peak wavelength gradually shifts to the right(redshift), and the maximum can even reach about 365nm. In addition, after the PI film is irradiated with UVA and UVC light, its absorption wavelength also has a red shift phenomenon. The redshift phenomenon is attributed to the conjugate effect of the unsaturated bonds in the quinoid PI (Cheng et al., 2009). This means that the number of aromatic PI converted into quinoid PI gradually increases, resulting in a decrease in the energy band gap of the film. Figure 5 shows the chemical structures of quinoid PI and Aromatic PI (C.-C. Wu et al., 2022). In terms of the energy of UV light, UVC has the highest energy. However, the data results showed that the PI film changed the most after UVB irradiation. This is attributed to the best absorbance of PI film at 290-320 nm, as shown in Figure 6, but UVC wavelength ranges from 100 nm to 280 nm. Therefore, the film has poor absorption capacity for UVC.

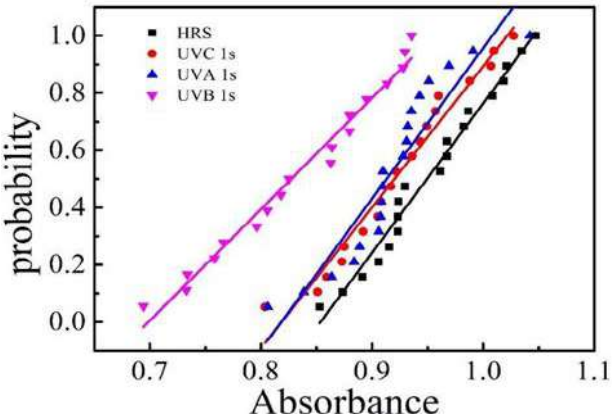

Figure 3: The Wavelength of The Maximum Absorption Peak of PI Film in the UV-Vis Region

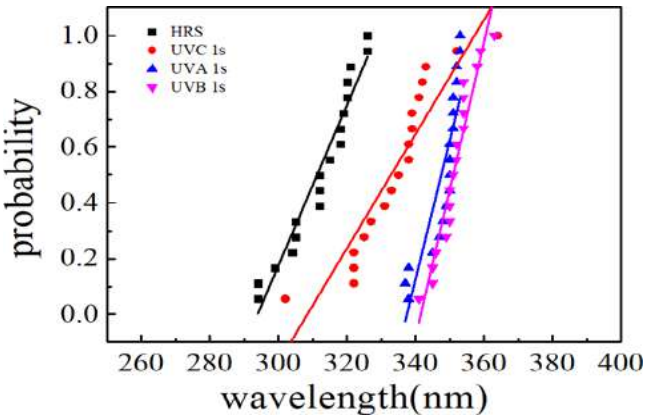

Figure 4: The Wavelength of The Maximum Absorption Peak of The PI Film

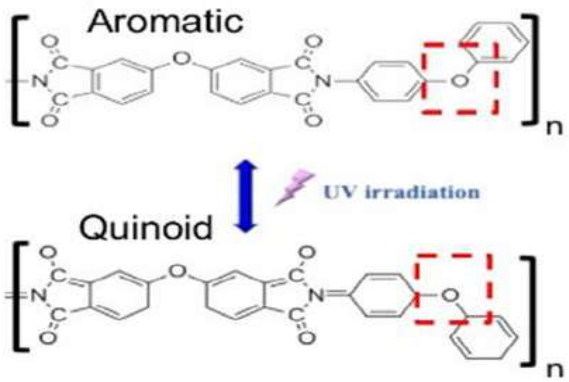

Figure 5: Chemical Structure Diagram Of The PI Molecules In Their Aromatic And Quinoid Forms (C.-C. Wu Et Al., 2022)

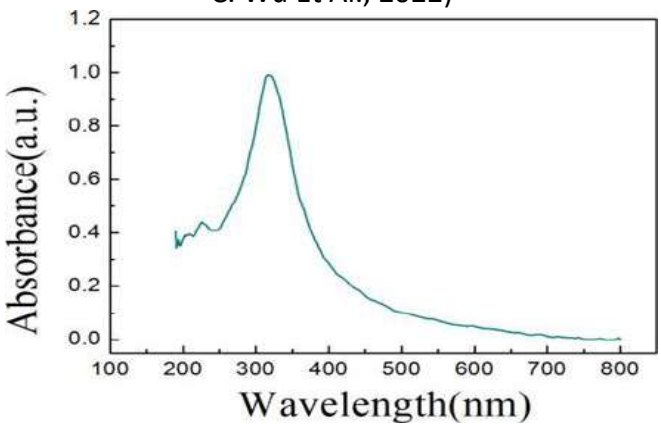

Figure 6: *UV-Vis Spectrum of The PI Films*

3.2 Electrical Characteristics: This paragraph mainly focuses on the electrical measurement results and analysis of the components, including the current in the LRS and the data storage capacity of the photomemory. The main current conduction mechanism of the device in HRS is hopping conduction, while the current conduction mechanism in the LRS is ohmic conduction(C.-C. Wu et al., 2022). Figure 7 shows the I-V characteristics of the device after irradiating UVA, UVB, and UVC for 1 second. It can be calculated that the resistance values of the LRS are 0.00342, 0.00428, and 0.00167 respectively. Table 1 shows the difference in current and resistance in LRS after different UV light irradiation, and the photoresponse of the optical storage device can be clearly seen. The data retention ability represents the time that the photomemory can retain the light information after receiving the light source without applying a bias voltage. The effect is known as persistent photoconductivity (PPC). After irradiating UVA, UVB, and UVC light for 1 second, the data retention ability of the device at room temperature is shown in Figure 8a-c. The data retention time

after UVA irradiation is about 7500 seconds, while the data retention time is about 10200 seconds after UVB irradiation, and 6100 seconds after UVC irradiation. The device is switched by three different ultraviolet light irradiations, all of which have very excellent data storage capabilities. In addition, the measurement results of the electrical and optical properties are consistent with each other. The magnitude of the current value in the LRS is related to the conduction path of the device. Therefore, the data retention capability of the device is also affected by the number of conduction paths.

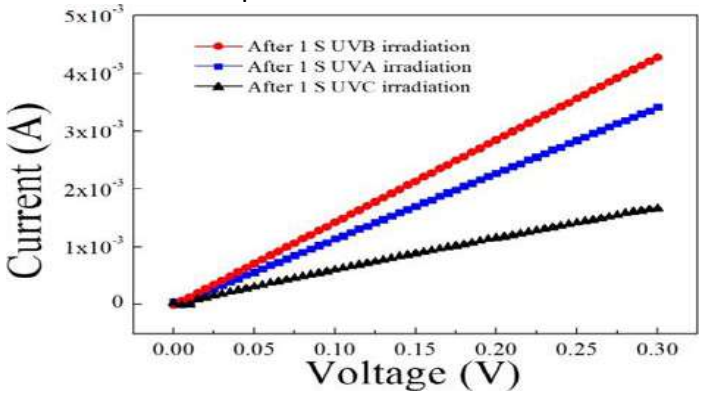

Figure 7: *I-V Curve of The Device in LRS (UVA, UVB, UVC Irradiated For 1 S)*

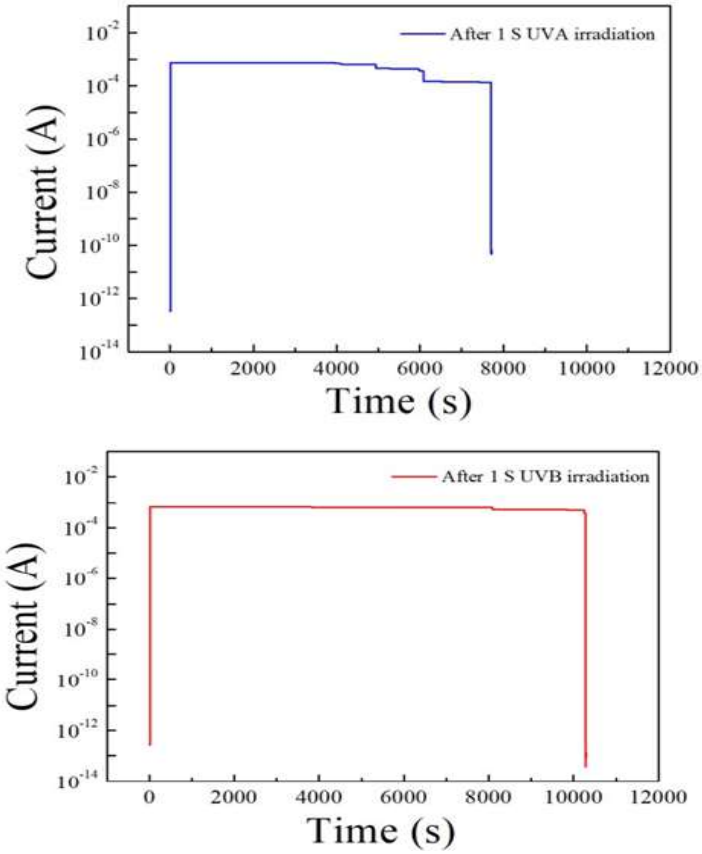

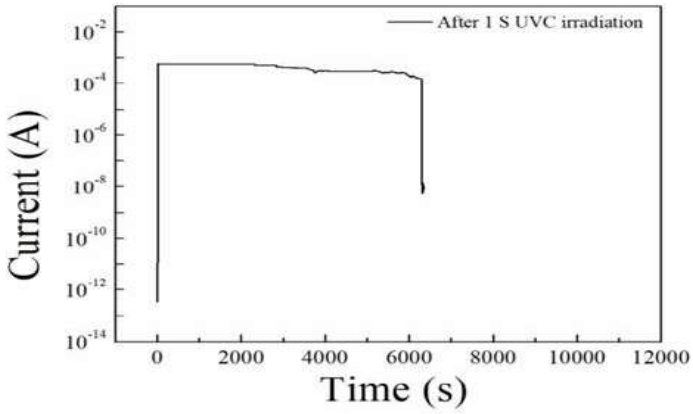

Figure 8: The Data Retention Time of The Photomemory After 1 S Of (A) UVA, (B)UVB, (C) UVC Irradiation

Table 1: The Polyimide Photomemory With Current and Resistance Values in Lrs After Different Illumination

	Irradiate 1 s		
	Voltage (V)	***Current (A)***	***resistance (Ω)***
UVA	0.3	0.00342	87.7
UVB	0.3	0.00428	70.1
UVC	0.3	0.00167	179.6

4. Conclusions: In summary, this study demonstrated the effect of the different UV on the physical properties, electrical properties of the PI film. The PI-based resistive photomemory can be switched by UV light of three different wavelengths. Compared with other photomemories, it has excellent data retention ability. Furthermore, in terms of switching efficiency, the device irradiated with UVB is the best, followed by UVA, and finally UVC. In this paper, it is proved that the absorption rate of PI film to UV light affects the switching efficiency of the device.

5. Acknowledgments: This work was supported by the National Science and Technology Council, Taiwan, through Grant No. MOST 109-2221-E-035-018-MY3.

6. References:
Chen, C.-C., Chiu, M.-Y., Sheu, J.-T., & Wei, K.-H. (2008). Photoresponses and memory effects in organic thin film transistors incorporating poly (3-hexylthiophene)/CdSe quantum dots. Applied Physics Letters, 92(14), 143105.

Chen, F.-C. (2018). Organic Semiconductors. In B. D. Guenther & D. G. Steel (Eds.), Encyclopedia of Modern Optics (Second Edition) (pp. 220-231). Oxford: Elsevier.

Chen, H., Liu, K., Hu, L., Al-Ghamdi, A. A., & Fang, X. (2015). New concept ultraviolet photodetectors. Materials Today, 18(9), 493-502.

Cheng, Y.-J., Yang, S.-H., & Hsu, C.-S. (2009). Synthesis of conjugated polymers for organic solar cell applications. Chemical Reviews, 109(11), 5868-5923.

Costa, J. C., Taveira, R. J., Lima, C. F., Mendes, A., & Santos, L. M. (2016). Optical band gaps of organic semiconductor materials. Optical Materials, 58, 51-60.

Dini, D., Calvete, M. J., & Hanack, M. (2016). Nonlinear optical materials for the smart filtering of optical

radiation. Chemical Reviews, 116(22), 13043-13233.
Fang, H., & Hu, W. (2017). Photogating in low dimensional photodetectors. Advanced science, 4(12), 1700323.
Gemayel, M. E., Börjesson, K., Herder, M., Duong, D. T., Hutchison, J. A., Ruzié, C., . . . Hecht, S. (2015). Optically switchable transistors by simple incorporation of photochromic systems into small-molecule semiconducting matrices. Nature Communications, 6(1), 6330.
Hsiao, Y.-P., Yang, W.-L., Lin, L.-M., Chin, F.-T., Lin, Y.-H., Yang, K.-L., & Wu, C.-C. (2015). Improving retention properties by thermal imidization for polyimide-based nonvolatile resistive random-access memories. Microelectronics Reliability, 55(11), 2188-2197.
Huang, C., Zhang, C., Yang, J., Sun, B., Zhao, B., & Luo, X. (2017). Reconfigurable metasurface for multifunctional control of electromagnetic waves. Advanced Optical Materials, 5(22), 1700485.
Huang, J. S., Liu, T. Y., Chen, H. J., Tseng, T. R., & Yang, W. L. (2022). Impact of Different PAA Solid Content Applied to Polyimide-Based Resistive Random-Access Memory. Paper presented at the Materials Science Forum.
Ismail, M., Ahmed, E., Rana, A., Hussain, F., Talib, I., Nadeem, M., . . . Shah, N. (2016). Improved endurance and resistive switching stability in ceria thin films due to charge transfer ability of Al dopant. ACS Applied Materials & Interfaces, 8(9), 6127-6136.
Jia, R., Wu, X., Deng, W., Zhang, X., Huang, L., Niu, K., . . . Jie, J. (2019). Unraveling the mechanism of the persistent photoconductivity in organic phototransistors. Advanced Functional Materials, 29(45), 1905657.
Lei, S., Wen, F., Li, B., Wang, Q., Huang, Y., Gong, Y., . . . George, A. (2015). Optoelectronic memory using two-dimensional materials. Nano Letters, 15(1), 259-265.
Nalwa, H. S. (2020). A review of molybdenum disulfide (MoS 2) based photodetectors: from ultra-broadband, self-powered to flexible devices. RSC advances, 10(51), 30529-30602.
Ouyang, C., Liu, J., Liu, Q., Li, Y., Yan, D., Wang, Q., . . . Cao, A. (2017). Preparation of main-chain polymers based on novel monomers with d− π–a structure for application in organic second-order nonlinear optical materials with good long-term stability. ACS Applied Materials & Interfaces, 9(12), 10366-10370.
Palma, R. J. M., & Duart, J. M. M. (2017). Novel advanced nanomaterials and devices for nanoelectronics and photonics. Paper presented at the Nanotechnology for Microelectronics and Photonics.
Tseng, R. J., Baker, C. O., Shedd, B., Huang, J., Kaner, R. B., Ouyang, J., & Yang, Y. (2007). Charge transfer effect in the polyaniline-gold nanoparticle memory system. Applied Physics Letters, 90(5), 053101.
Wakayama, Y., Hayakawa, R., & Seo, H.-S. (2014). Recent progress in photoactive organic field-effect transistors. Science and Technology of Advanced Materials.
Wang, Z., Zhang, S. R., Zhou, L., Mao, J. Y., Han, S. T., Ren, Y., . . . Zhou, Y. (2019). Functional Non-Volatile Memory Devices: From Fundamentals to Photo-Tunable Properties. physica status solidi (RRL)–Rapid Research Letters, 13(5), 1800644.
Wu, C.-C., Chen Jr, T., & Yang, W.-L. (2022). Polyimide-based ultraviolet-operated nonvolatile photomemory device. Applied Physics Letters, 121(21).
Wu, H., Wang, M., Huai, L., Wang, W., Zhang, J., & Wang, Y. (2021). Optical storage and operation based on photostimulated luminescence. Nano Energy, 90, 106546.
Yang, D., & Ma, D. (2019). Development of organic semiconductor photodetectors: from mechanism to applications. Advanced Optical Materials, 7(1), 1800522.
Yin, H., Akey, A., & Jaramillo, R. (2018). Large and persistent photoconductivity due to hole-hole correlation in CdS. Physical Review Materials, 2(8), 084602.
Zhou, L., Han, S.-T., Shu, S., Zhuang, J., Yan, Y., Sun, Q.-J., . . . Roy, V. (2017). Localized Surface Plasmon Resonance-Mediated Charge Trapping/Detrapping for Core–Shell Nanorod-Based Optical Memory Cells. ACS Applied Materials & Interfaces, 9(39), 34101-34110.

Zhou, L., Mao, J., Ren, Y., Han, S. T., Roy, V. A., & Zhou, Y. (2018). Recent advances of flexible data storage devices based on organic nanoscaled materials. Small, 14(10), 1703126.

Loss Analysis in Bread Production Process Using Material Flow Cost Accounting-Technique

Bunyaporn Yoddee
Master's Degree Program in Industrial Engineering, Faculty of Engineering, Chiang Mai University, Chiang Mai, Thailand

Rungchat Chompu-Inwai
Department of Industrial Engineering, Faculty of Engineering, Chiang Mai University, Chiang Mai, Thailand

Abstract: The case study factory manufactures a range of bread and bakery products for distribution in the North of Thailand. Losses from the production process were recently discovered, which besides being lost costs, also impacted the environment. This research is conducted under the concept of Material Flow Cost Accounting (MFCA) to analyze the losses from each process of the case study bread factory. This is to pinpoint where most of the losses occur and suggest methods for future improvement. This research is conducted with the principle of Plan Do Check Action (PDCA). The "Plan" was to determine a target product, which in this case was raisin bread, as it accounted for the largest proportion of production. Subsequently, a study was conducted of the production process, and a scope under the "Do" stage of the procedure was determined. Input and output factors were identified for each Quantity Center (QC) in both physical units and financial units. Subsequently at the "Check" stage, an analysis of costs was conducted for each QC with the MFCA technique. This was divided into positive product, meaning costs generating revenue, and which were manifest in the product, and negative product, which were costs not generating revenue and were losses from each production stage. Finally, at the "Action" stage, negative products were ranked by priority at every QC. A Pareto diagram was used to identify and evaluate opportunities for improvement. The research found that the total costs to produce one production lot of raisin bread were 2,935.55 THB, which were divided into materials costs of 2,270.79 THB (77.35%), system costs of 500.30 THB (17.04%) and energy costs of 164.46 MB (5.60%). Overall, negative product was 25.19%, and this was negative product was 19.41% in materials, which was wastage and losses from dough and fillings being deposited in the machinery, and the failure of packaging films when they were being installed in the packing machine. It was also found that negative materials costs arose maximum in the QC of packing. The conclusions from this research are that it has informed about losses arising in the production process and evaluated them in the form of costs, which should help in proposing methods to reduce this wastage in the future.
Keywords: Material Flow Cost Accounting, Bread, Loss

1. Introduction: Although consumption levels of bread among the Thai public are considered low compared to other countries, the Thai bread and bakery industry shows clear ongoing growth trends. Consumer demand is increasing from urban consumer behavior preferring convenience foods and snacks. Production in Thailand's bread and bakery industry is expanding. As an industry, technology is being applied to production with the introduction of modern machinery enabling more efficient production. There is also a constant state of product development adding value to the products, to make their attributes more outstanding and diverse. Coupled with a more modern transportation system, the shelf life of products has been extended, all of which are factors supporting growth in the bread and bakery industry (Raiwa, 2016). However, the bread industry also has an environmental impact. Bread is a food made from wheat flour mixed

with water and yeast. Other ingredients are added to provide color, taste and aroma for each category of bread. The ingredients are integrated into dough which is then formed into shapes and proven at the appropriate temperature and humidity to get the yeast working, before baking. The industrial production of bread requires efficient flour milling machines and kneading machines, and large ovens with temperatures of over 230°C, which require a lot of energy. The transportation of raw materials and the finished bread to stores also require gas and oil. Moreover, to produce flour, 66% or 2/3 of greenhouse gas emissions come from growing the wheat crop, which is the key raw material for flour and bread. Another impact on the environment is waste from the production process and consumption, such as expired product which must be discarded in large volumes, compared to total production volumes (Bunditterdsakul, 2017). Research of the literature discovered that many studies had the target to reduce waste from the production process and evaluate environmental impacts from the production of industrial bakeries, such as Arunpanich, (2010) evaluated the product life cycle of bread in the baked goods industry. This research indicated that sourcing raw materials, which were dried yeast, wheat flour and sugar, had the most environmental impact. It was therefore proposed to use alternative raw materials in some parts of the manufacturing process. The case study factory conducted the production and distribution of a diverse range of bakery products in the north of Thailand. The factory is currently facing issues similar to other factories in the same industry, such as waste and losses from the production process. For instance, at the forming stage there is dough which was formed, but did not pass the size, shape or weight standards which had been specified, making it a waste product. However, in some cases it was possible to rework the product or sell it as animal feed. Still, it is a lost cost and also impacts the environment. This research is therefore applying the technique of Material Flow Cost Accounting, (MFCA) to analyze the costs lost from each stage of the factory's bread production process, to pinpoint where the most losses occur, and seek methods for improvement in the future. MFCA is one of a number of tools used to evaluate environmental impacts which originated in Germany. It was seriously adapted in Japan and from there MFCA has been applied in many countries and specified as ISO-14051 (Nakajima, 2006). MFCA is a technique to characterize and indicate losses from work processes, systems or inefficient production technology, or to improve a system. Volumes of production are analyzed to compare them with volumes of raw materials brought in. When the production obtained has a weight or amount lower than the amount of raw materials brought in, this illustrates loss arising in the production process. Losses of material are evaluated in the form of costs. Costs are divided by costs generating revenue or manifest in the product which are called positive product, and costs not earning revenue as well as losses in the production process, which are called negative product (Chattinwat et al., 2014). In the literature, it is found that although the bakery industry has not had MFCA applied to it very much, MFCA has been applied to a wide range of other industries including ceramics, timber and furniture, textiles, metallurgy and plastics, as well as the food industry. For instance, Bux, (2022) applied MFCA to the beef, pork and poultry industries of Italy. The research indicated that MFCA was of benefit in making business decisions focused on quantity, quality and cost, which is different from general considerations of the financial statement, while enabling analysis and management of waste in the factory.

2. Research Methodology and Results: This research made analysis of costs of losses arising in the production process of bread by applying the MFCA technique according to the PDCA cycle (ISO, 2011) with the methods of research shown in Figure 1.

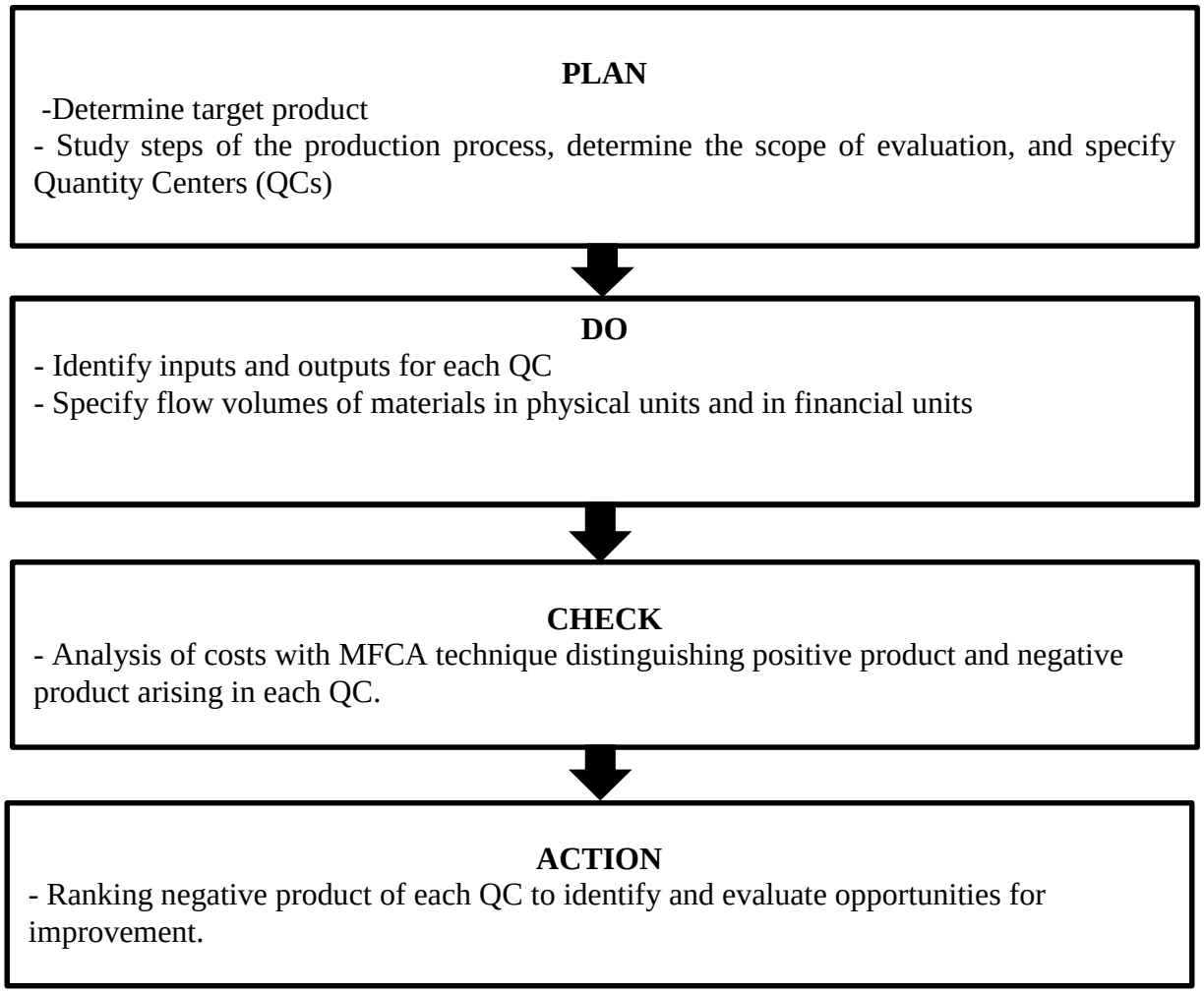

Figure 1: *Research methodology*

Details and results of the research are as follows:

2.1 Determining the target product, study of production procedure, determining a scope and Quantity Centers

After consultation with the case study factory, the factory wanted to study its raisin bread product first, as it had the highest proportion of production, as high as 50% of the same category of bread products. Total production is 700 to 800 items daily (1 production lot). This was therefore determined to be the target product for this research. The bread bun with a raisin filling (depicted in Figure 2) had a central circumference of 6.4-6.8 cm with a weight per item of 35-39 gram, containing averagely 17.15 gram of filling. This research studied the data of 1 production lot.

Figure 2: *Target product (raisin bread)*

Researchers performed a study of the raisin bread production process with steps shown in Figure 3. This starts from mixing the dough and extruding the dough, then forming the pieces of dough, with weight tested there of 23-26 gram. If the weight is up to standard, the dough is sent for decoration and then to the next step of the process. If the weight is not to standard, the dough is returned to the extrusion machine once more. The buns are then placed on racks holding 24 buns each. The decoration involves an egg glaze and sprinkling white sesame seeds for decoration. When decoration is complete, employees put the racks on a truck and push them to the Proving Room. The proving processes the dough to rise. In this room, the temperature and moisture are controlled for the yeast to work fully and enable the dough to rise fully. From there the dough is left for a specified period of time. The next check is that if the dough is not yet standard size, the proving process will continue. Once the desired size is obtained, the racks are removed from the trucks to enter the baking process, where the baking is in a large tunnel oven, for 25-30 minutes. After baking is complete, the employees bring the racks back to the trucks, at which stage, they are inspected by weighing, and waste product is selected out and discarded. Waste at this stage of the process finds customers who are willing to buy it at a reduced price and use it to make fish food. The good product is sent for packing. The packing process is automated packing machines, with film cut at 132 mm intervals at a speed of 87 packs per minute. This is the end of the production process.

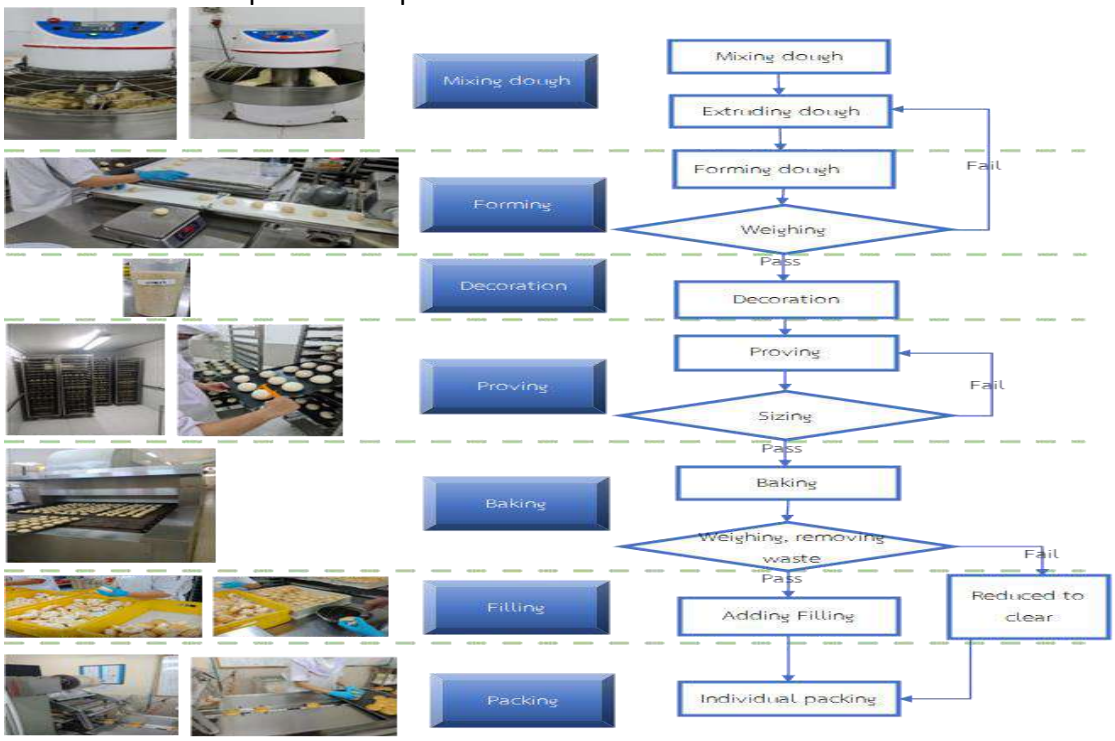

Figure 3: *Steps of producing raisin bread*

The next step of specifying the scope of evaluation means specifying a start point and end point of the production process and specifying Quantity Centers (QC) which have volumes of material passing through in the manufacturing process. QCs are specified according to steps in the production process, so QC1 is the Mixing Dough stage, QC2 is the Forming stage, QC3 is the Decoration stage, QC4 is the Proving stage, QC5 is the baking stage, QC6 is the Filling stage, and QC7 is the Packing stage respectively.

2.2 Identifying Inputs and Outputs for each Quantity Center: This stage has the objective to show volumes of production factors entering and exiting the production process with outputs identified for each QC. The inputs are materials and energy while the outputs are product, waste and energy waste. Data is collected at the work stage of the raisin bread process at the case study factory. The inputs and outputs for each QC are connected by the scope of consideration. This stage starts from specifying volumes of material flows in physical units, in which all volumes of inputs and outputs are studied in units of weight (kilogram, kg). This

enables a study of the balance of materials at each QC, in which inputs should equal outputs. Table 1 is the Material Balance Table of QC1, Dough Mixing. It can be seen that at this stage, the material is dough, with a weight of 18.220 kg, which gives product weighing 18.043 kg. Waste dough attached to the machine weighs 0.177 kg, which is a 0.98% proportion of negative product by weight. As for the material balances of other QCs, they are not shown here, but are prepared in the same way.

Table 1: *Material Balance Table at QC1, Mixing Flour*

Material Balance Table, QC1					
Input: Material		***Output: Waste***		***Output: Product***	
Material	***Amount (kg.)***	***Waste***	***Amount (kg.)***	***Product***	***Amount (kg.)***
Dough	18.220	Waste dough in machine	0.177	Good dough	18.043
Total (kg.)	18.220	Total (kg.)	0.177	Total (kg.)	18.043
% weight	100%	% weight	0.98%	% weight	99.02%
Cost input		***Cost of loss (negative product)***		***Cost of product (positive product)***	
Total (THB)	477.22	Total (THB)	4.68	Total (THB)	472.54
% of cost	100%	% of cost	0.98%	% of cost	99.02%

As already mentioned, the data of inputs and outputs at each QC are connected throughout by the scope of consideration. Therefore, it is possible to create a Material Flow Model which is shown in Figure 4, which is a diagram showing the details and amounts of material. Total wastage is identified at that QC, for all the categories and all inputs, both currently occurring, and product flowing from the previous QC. For instance, in Figure 4, considering QC2 at the forming stage, the material flowing from the previous step in the process (QC1 Mixing Dough), this is dough which has some parts stuck to the machines, as waste in the mixer and the extrusion machine at QC1, with the remaining 18.043 kg. going to QC2, the forming stage. There is no new additional material being passed through QC2, causing additional losses of dough stuck in the machine at QC2 of 0.157g, with a remaining positive product (dough) of 17.886 kg, and other QCs can be explained in the same way. Subsequently are determination of amounts of material flow in units of money. In each QC, data is collected on costs in 4 areas which are, material cost (MC), energy costs (EC), system costs (SC) and waste management costs (WC), detailed as follows. Material cost: Inputs and outputs (product and waste) at each QC can be identified from finding the product of the physical units of material (in this study, weight), and the unit price of that material. For instance, in the Material Balance Table at QC1 one in table one, the dough mixing stage, the material being input was dough with a weight of 18.220 kg, which has a price of 26.192 THB/kg. THB means Thai baht; which 1 US dollar is approximately 35 baht on the day of the research. Therefore, the costs for the inputs at QC1 are calculated to be 477.22 THB, of which 472,54 THB is positive product and 4.68 THB is negative product. Energy costs are the costs or expenses for energy used at each QC, with the data collected directly from the machine or electrical equipment being used, which is then timed, to calculate the energy cost. System costs are expenses arising in the process that are extraneous to material costs. energy costs and waste management costs, such as labour, maintenance, depreciation and transportation. Labour costs were calculated from employees' real work times at each QC. The company has completely deducted depreciation on machinery according to accounting procedure, and so this parameter was not considered. Waste management costs are costs concerned with the disposal of waste arising at every QC, including waste disposal charges and disposal including transportation. Waste management costs are all determined to be negative product. However, this research did not have a waste management cost, as waste at every stage of the process was sold as a discount to make into animal feed, so there was no need for disposal.

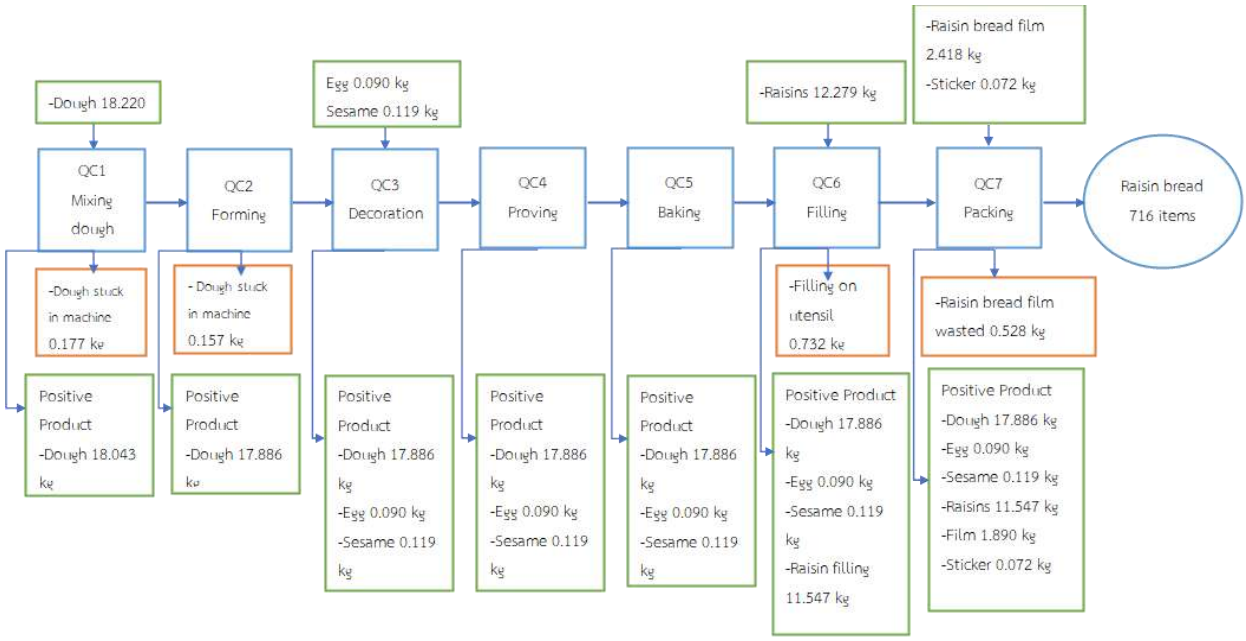

Figure 4: *Material Flow Model*

2.3 Analysis of costs with the MFCA technique, which distinguishes positive product and negative product arising in each QC

Making costs at each QC into positive product from previous process (including MC, SC and EC) were combined into a new input cost at the QC to consider. It is combined costs before allocation. Analysis of proportions of positive product and negative product uses the "Law of Mass Balance" in which input mass must equal output mass plus waste in the process, considering material flowing from the previous QC. The combined materials cost is allocated by category of material flowing into the QC. Volumes of the proportions of real positive product and negative product arising is used as the criteria, using data from the Material Flow Model in Figure 4. As for the allocation of system costs and energy costs to positive product and negative product, this can be calculated from the proportion of negative product from the weight arising

Table 2: *Material Flow Cost Matrix at QC1*

Cost	**Material Flow Cost Matrix QC1**				
	MC	***SC***	***EC***	***WC***	***Total Cost***
Previous input	-	-	-	-	-
(new) input	477.22	56.67	27.15	-	561.04
Total	477.22	56.67	27.15	-	561.04
Positive product	472.54	56.11	26.88	-	555.54
Negative product	4.68	0.56	0.27	-	5.50

Table 2 shows the Material Flow Cost Matrix at QC1, in which QC1 is the starting QC, so there is no input of positive product from the previous QC (or previous input). MC, SC and EC are combined before allocation to be 477.22 THB, 56.67 THB and 27.15 THB respectively. Allocation of positive product and negative product of the material is as previously explained. The allocation of SC and EC can use negative product in the allocation. A QC one this was equal to 0.98% by weight. Therefore, SC can calculate positive product and negative product to equal 56.11 THB and 0.56 THB respectively. EC can calculate positive product and negative product which are equal to 26.88 THB and 0.27 THB respectively. Calculating costs on the principles of MFCA at other QCS is done in the same way, requiring taking the positive product from the previous process (all of MC, SC and EC), to combine into a new input cost at the QC under consideration. This is a

combined cost before allocation. For instance, in the calculations at QC 2, it is necessary to use the positive product of MC, SC and EC costs, which are 472.54 THB, 56.11 THB and 26.88 THB from QC1 to combine with new input costs at QC2, which are combined costs before allocation.When calculating costs from QC1 to QC7 in series, reports of costs arise according to category of positive product and negative product, separated into MC, SC, EC and WC, as shown in Table 3, Combined Material Flow Cost Matrix of every QC. From Table 3, it can be seen that combined costs to produce one production lot of raisin bread are 2,935.55 THB, which is divided into materials costs of 2,270.79 THB (77.35%), system costs of 500.30 THB (17.04%), energy costs of 164.46 THB (5.60%), while there is no waste management cost. Negative product is calculated at 25.19%, of which negative product in material costs is 19.41%. The highest is waste product getting deposited in the machinery, and failed packing film, which were not generating revenue.

Table 3: *Combined Material Flow Cost Matrix of all QC*

Cost	MC	SC	EC	WC	Total cost
Combined result	2,270.79	500.30	164.46	0.00	2,935.55
	77.35%	17.04%	5.60%	0.00%	100%
Positive product	1,701.09	373.19	121.93	0.00	2,196.21
	57.95%	12.71%	4.15%	0.00%	74.81%
Negative product	569.70	127.11	42.53	0.00	739.34
	19.41%	4.33%	1.45%	0.00%	25.19%

2.4 Ranking the importance of negative products from each QC using a Pareto Diagram: This stage of the procedure is to rank the importance of negative products from each QC to identify and evaluate opportunities for improvement. The Pareto diagram was used shown in figure 5, from which it can be seen that materials costs for negative products at QC7 had the highest value, which was film to pack the raisin bread which had been wasted, an amount of 0.528 kg, or a value of 457.65 THB. Therefore, the case study factory should focus on remedying the cause of this issue before moving on to remedy other matters later.

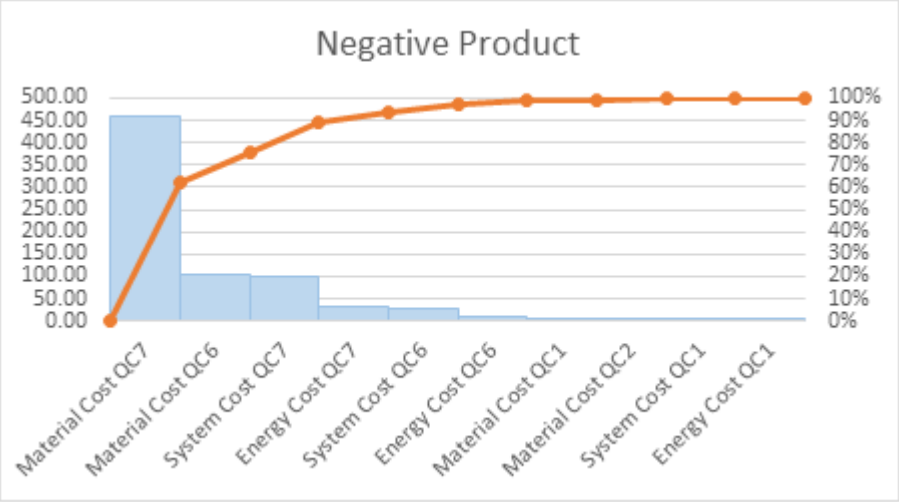

Figure 5: *Pareto Diagram showing negative product from each QC*

3. Conclusions and suggestions: This research implemented the technique of Material Flow Cost Accounting (MFCA) to analyze losses from each stage of the production of raisin bread at the case study factory. This went through the stages process stages of mixing dough, forming, decoration, proving, baking, filling and packing. The methodology followed the principles of Plan Do Check Action (PDCA), and the procedures of MFCA. The research showed how total costs to produce one production lot of raisin bread could be divided

into which proportions of materials cost, system cost and energy costs. It was also possible to distinguish positive product costs, meaning costs generating revenue and manifest in the product, and negative product costs, meaning costs not generating revenues and which were waste at each stage of production. This informed of the waste arising at each stage of production, evaluated in the form of costs. This pinpointed the stages of greatest waste, assisting parties concerned to propose methods to reduce this wastage in the future. The research discovered that the greatest waste was at the packing stage, by wasting film used for packing the raisin bread, a result of employees setting the packing speed to be too fast. As a result, employees stationed at the end of the packing machine could not insert the bread in time, with a result of empty packs coming out. There was also wastage of film in the initial phase of setting the machine. When the roll of film was exhausted, it had to be replaced with a new roll. Therefore, to reduce waste and negative product, the research is proposed to pack products with film of the same kind in large volumes, in a single instance, for continuous production until the roll of film was exhausted, so film would not be wasted while making the initial settings for the machine on several occasions. Also, there should be studies to specify an optimal packing speed, in line with the work-rate of the employees. The benefits from this research of finding ways to reduce waste and loss in the production process of raisin bread at the case study factory, are that this research methodology can also be applied to other products of the case study factory. Also, the research methodology is useful to other entrepreneurs and particularly those at a similar level to the case study factory, which would be Small and Medium-sized Enterprises (SMEs), which have the greatest proportion in Thailand, and have a key role in developing the national economy. This gives the SMEs capabilities to compete and be more resilient by reducing their costs and increasing their profits. Eventually, this will improve the country's macro economy.

4. Acknowledgements: The researchers would like to thank all executives and employees of the case study factory for providing information and excellent cooperation with the research.

5. References:
Arunpanich, K. (2010). Life Cycle Assessment of Pound Bread Products in Bakery Industry. [Master of Engineering Thesis, Thammasat University].

Bunditterdsakul, L. (2017, August 23). Shocking study results as bread is slowly killing our planet. Green News. https://greennews.agency/?p=14960&fbclid=IwAR2OK-izbMCvLqmz4Kkc8YiJKNvyMDFbn1Bp7NzESE5o43kQ84OrzYqQJAs

Bux, C. (2022). Material flow cost accounting (MFCA) to enhance environmental entrepreneurship in the meat sector. Journal of Environmental Management, https://www.sciencedirect.com/science/article/abs/pii/S0301479722005746

Chattinwat, W., Laosirithaworn, W., Cheewsuthisilp, S., Chompuinwai, R., Kasemset, C., Chaijaruwanich, A., & Nakkhiao, W. (2014). A case study of material flow cost accounting applications in Thailand.

ISO. (2011). Environmental Management – Material Flow Cost Accounting- General Framework, Switzerland.

Nakajima, M., 2006. "The New Management Accounting Field Established by Material Flow Cost Accounting (MFCA)," Kansai University Review of Business and Commerce, 8, 1-22.

Raiwa, P. (2016). Thai bakery industry. Food Institute. https://fic.nfi.or.th/area-based-Industry-detail.php?smid=1126

E & Group Super App

Hanan Al Masawi
Innovation and Change Management, Hamdan Bin Mohammed Smart University, Dubai, United Arab Emirates

Abstract: This study looks at E&, one of the biggest telecommunications firms in the Middle East and Africa (MEA), and its new product development (NPD) innovation strategy. Despite already having a substantial online presence through 23 different applications, E&'s segmented service offering presents difficulties for quality control and administration. To solve this problem, E& suggests creating a "Super App" that combines the functionality of various apps into a single, all-encompassing tool, increasing customer value and engagement. E& hopes to develop an application that encourages everyday user engagement through a combination of free and paid offerings by drawing on Forrester Research findings. The creation of the Super App is consistent with E&'s ongoing innovation strategy and dedication to digitization, which aims to offer value for its clients through comprehensive digital solutions. It also aligns with the company's strategic orientation, achieving its TARGET plan, and its three primary pillars: E& life, E& enterprise, and E& capital. But in order to implement the Super App, considerable organizational adjustments will be needed, as well as the formation of a first team with a wide range of duties, from user experience design to legal compliance. With a proactive change management approach, lean and agile practices, and a dedication to ongoing improvement, E& is well-positioned to meet these challenges. The creation of The Super App is a critical step in E&'s journey to becoming a digital leader because it offers an integrated digital solution that satisfies consumer needs and promotes business expansion.

1. The New Product Development Innovation: E& is one of the largest Telecommunications companies in the UAE and Middle East and Africa (MEA) region that have big aspirations for the future and realized the increased competition that led them to conduct transformational changes to better position themselves for the future (E&, 2023a). Thus, currently, they serve more than 155 million users in 16 countries and have a market capitalization of more than 200 billion AED (E&, 2023a). E& currently has 23 smart mobile apps listed in Apple and Google stores with three applications in Google store that have +1M downloads, one application with +5M downloads, and two applications with +500K downloads (E&, 2023b). Thus, having 20+ applications will require multiple teams to manage and update frequently, where it is challenging to keep the quality of all applications which are already reflected in the customer reviews that vary from 1.9 to 4.6 out of 5 for E& applications (E&, 2023b). The proposed NPD Innovation for E& is to develop an E& Super App that will combine the features of 5-10 applications into one super application to provide more value to the customer and engage them effectively. According to research by Forrester Research, findings revealed that the average person uses 5 applications in a day, and 26-27 applications only every month (Perez, 2015). Hence, the goal will be to develop a super application that includes features that will drive the users to use the application every single day to use both the free and paid services which will reflect significantly on E& financials and targets. E& will utilize its infrastructure to build an integrated super app that will have the following features: Instant messaging, one-to-one Voice and Video Calls, Group Video calls, money transfer feature, digital wallet, online grocery purchases, special offers, interactive multiplayer games, online bills payment, on-demand services, booking hotels, buying goods and services, parking tickets, creation of payment links for Small businesses, Smiles Points and awards. In addition to a personalized virtual assistance integrated tool that helps customers with their tasks and setting schedules for their priorities based on their habits via sending reminders and notifications. This means that around 10 of the current E& mobile applications will be deactivated and the users will be transferred to the new super application. Hence, looking into the transformation of mobile applications in China, specifically WeChat, it is now more than a chat application as they offer various features for its users. In the case of E&, currently, their group of applications has the

features of instant messaging, points, offers, and grocery but understanding that the average user only uses 5 applications a day it will be critical to be the application that is used the most and on a daily basis through the development of a super application. E& has to invest in a smooth and user-friendly user interface, since a study conducted by Miniukovich & De Angeli (2014), showed that the mobile phone user takes only 5 minutes to build an impression on the application. Thus, having a slow response application, not user-friendly, non-responsive user interface, and not aligned with different models of phones could negatively affect the aspired targets (Yu et al., 2020). The backend of the application needs to be developed in a way that having various services and integrations doesn't cause errors and bugs (Yu et al., 2020).

2. The Technological Innovation: The introduction of smartphones, downloading applications from an online store, saving information in the cloud and the ability to develop integrated applications with a customer-friendly user interface have shaped how modern human beings live, perform their transactions, and plan for their day. As the technological innovation is a super application it will be developed for IOS and Android users. To make it more effective it will understand the interest and demographics of their users through Artificial Intelligence, and automated data analysis to better highlight the services that they need and most likely use to perform transactions. For example, for teenagers, it will show offers for the cinema, products, and services that most teenagers will be attached to and willing to purchase. In addition, the application will be flexible so that E& can add new features and services in future iterations. For example, whenever doing a transaction, the customer could dedicate a small portion of the amount to be invested in stocks. However, it will require a lot of effort to meet the legal requirements. As the super application grows the opportunities are limitless, as E& can allow their users to list classified advertisements similar to Dubizzle to sell or buy their cars, used items, properties, and more.

3. The Innovation Strategy: E& is determined on differentiating itself from the competitors through innovation, digitalization, growth opportunities, and utilizing the available tools and systems such as AI, machine learning, and big data. It's currently strongly positioned in the MEA market and looks toward adding more value to its current and future clients through its innovations. E& has already created a culture that empowers and fosters innovation and launches new products and services to its customers. E& has launched a clear and proactive process to support innovation that starts from analyzing issues or opportunities which produces ideas that go through the evaluation phase, development phase, and finally production phase. E& is flexible as it has the willingness to experiment, iterate and improve, and collaborate with various entities to produce new products and services. An example is Hasantuk System which provides a smart fire detection system linked between households and police & firefighting departments across the UAE through the Internet. E& environment supports innovation and collaboration across the different teams and departments, and it has launched the E& capital pillar which acquires and invests in startups and projects that serve the values and goals of the enterprise. The organization has a portfolio of innovations and investments as it aims to lead and increase its growth in the future. In the smartphone application market, the first movers have the most benefit, but it is never too late. When comparing the instant messaging applications, E& launched GoChat in 2021 and it only has +1 million users on the Android store, but if we look at Whatsapp, Telegram, Line, Skype, and Viber, Imo they all have +1 Billion downloads which are 1000 times bigger than what E& has at the moment. Thus, it will be essential to have a very compelling and competitive offer to gain more active and loyal users through offering free features, high quality, and highly reliable applications that have at least 10X benefits for the users. It will not be easy to shift WhatsApp users, or Imo users to use another Chat application, it should be much more than that which strengthens the value of having a super application. Another smart approach could be if E& can secure enough funding to potentially acquire an instant messaging application with a large user base, and develop it to be a super application, or acquire a large base service demand application and add the instant messaging applications and the other features to be a super application.

4. Alignment with the Strategic Direction: E& has introduced their TARGET strategy to maximize their current and future growth opportunities in which each letter is the first letter of a sentence (E&, 2023a). Their strategy focuses on empowering societies by being the market leader of future digital solutions, increasing the value generated to the consumers by both innovation and digitization, and developing their talents and raising their capabilities (E&, 2023a). Looking at the Super Application NPD it directly aligns with their values as it will be a daily tool to empower the societies with their day-to-day basic needs and wants, moreover, it is an innovative and digital solution that will lead to a bigger value generated to both E& and the consumers. The innovative solution will reshape the lives of E& consumers in a better way, as it will save time and combine the needed and wanted services in one place by being one click away, which will also reflect positively on the economic growth of businesses and will strongly improve the competitiveness and effectiveness of E& in the 16 countries that they currently operate. Having a super application means that the company will be agile and open to various collaborations to achieve the fullest potential, thus it will enable E& to collaborate with the most promising startups, as well as large global corporations to create and generate additional value which will introduce to E& potential acquisition and investment opportunities to diversify their revenues more and provide unique and competitive solutions to the customers. E& will be utilizing their talents more effectively, instead of having 20 different teams working on 20 applications, or a team that is responsible for 5 applications, they will have integrated divisions that work in a cross-connected from using lean and agile methodologies to reiterate and improve the customer experience continuously, they will have one application that must not have a rate less than 4.5/5 in the Android and Apple Stores. E& have introduced three pillars in February 2022 as part of its new identity which are E& life, E& enterprise, and E& capital (Person, 2022). The super application will be connected directly to E& Life which focuses on launching next-generation technologies and smart solutions focused on the single consumer digital lifestyle in the field of entertainment, retail, and financial technologies (Person, 2022). Currently E& has dispersed solutions in separate applications that aren't connected (Person, 2022). Hence, the super application will act as an accelerator toward achieving the vision of the E& Life pillar (Person, 2022).

5. The New Product Development Team: There are 8 essential functions that are required in the initial phase of the project which are: The Product Manager will lead the members and manage the product to ensure that it stays within budget and time with the right features. The User Experience & User Interface Designers will be responsible for developing a user-friendly application, interface, and smooth interaction and navigation. The Mobile App & Backend Developers will be responsible for using the appropriate programming languages, and APIs, and designing the databases, and system architecture for the application to be stable, secure, and scalable. The Data Analysts will analyze the user attitude, preferences, and behavior by collecting and analyzing the data to create the optimum experience for the application. The Growth & Marketing Officers will create and perform a marketing plan to reach new users and keep the existing users engaged through campaigns and initiatives. The Customer Support Officers will reply to and fix user issues by answering their emails, reviews, and concerns. The Business & Partnership Development Managers will develop strategic partnerships with local and global stakeholders such as merchants, and service providers so that their services are integrated into the application. The Legal and Compliance Officers will ensure that the application is aligned with the laws and regulations and that all agreements don't cause any potential legal risks.

6. Managing Organizational Change: E& has already gone through a transformational change last year to set new values, vision, pillars, and mission (Person, 2022). Thus on a bigger scale organizational change has occurred in E& which could cause resistance to change by employees thus the organization requires to have a change and communication plan to engage with their employees, starting to increase the sense of urgency, engaging the middle managers to reach out to their teams, providing the necessary tools, training and coaching to bring their teams to speed with the new ways of doing things, and enabling the employees to contribute with their innovative ideas and feedback during the change process. In terms of the changes that

will result from the development of a super application, the initial 10 smartphone applications will have a decommissioning plan once the new super application is launched. To reach that level, E& will need to evaluate and ensure that they already have a very talented development team that can execute such a project efficiently, as well as cancel the duplicated roles due to having only one super application. The affected department employees will be scared to lose their jobs, thus it is important to allow a fair amount of time for affected employees to find other departments or job opportunities and have clear communication between the managers and employees. E& need to analyze the new jobs that will appear since instead of having a project manager responsible for a single application, there will be managers responsible for single or multiple modules or features in the super application. Hence, in the long run, the change will create more jobs as the application user base and features increase.

7. Conclusion: In conclusion, through the previous years the world, individuals, and large corporations realized that change is the only constant, and if you don't change you might end up losing your market share within a few months or years. The telecommunication sector isn't safe from disruptions, thus developing new innovative products is a means to protect and potentially increase the market share of a company. E& has already positioned itself for the future through transformational change and clear pillars, and a path toward digitalization and innovation (Person, 2022). The proposed innovation will combine the efforts that E& has already done into a single super application which will allow initially more than 155 million E& users to use for their day-to-day activities as well as non E& users to benefit from both the free and paid features across the world. It requires massive investment, resources, expertise, and iterations to develop the optimum super application in which E& has already positioned itself well as they have the investments, resources, and expertise to execute such projects. E& has developed single applications, and the journey will be to focus on integration, rebuilding the main core to be able to accommodate continuous change, and adding and removing features as per the needs of the customers in various geographical locations.

8. Appendix: E& (2023a) Our strategy. Available at: https://www.eand.com/en/whoweare/our-strategy.jsp (Accessed: April 26, 2023).

E& (2023b) Etisalat UAE: Download our apps: My etisalat uae, Switch TV, smiles, ETISALAT UAE | DOWNLOAD OUR APPS: MY ETISALAT UAE, SWITCH TV, SMILES. Available at: https://www.etisalat.ae/en/c/apps.html (Accessed: April 26, 2023).

Miniukovich, A. and De Angeli, A. (2014) "Visual Impressions of Mobile App Interfaces," Proceedings of the 8th Nordic Conference on Human-Computer Interaction: Fun, Fast, Foundational [Preprint]. Available at: https://doi.org/10.1145/2639189.2641219

Perez, S. (2015) Consumers spend 85% of time on smartphones in apps, but only 5 apps see heavy use, TechCrunch. Available at: https://techcrunch.com/2015/06/22/consumers-spend-85-of-time-on-smartphones-in-apps-but-only-5-apps-see-heavy-use/ (Accessed: April 26, 2023).

Person (2022) "Etisalat by E&" launched as the new brand identity for Etisalat UAE, reflecting recent E& Group positioning, ZAWYA. Zawya. Available at: https://www.zawya.com/en/press-release/companies-news/etisalat-by-e-and-launched-as-the-new-brand-identity-for-etisalat-uae-reflecting-recent-e-and-group-positioning-peal19rc (Accessed: April 26, 2023).

Yu, M. et al. (2020) "Unravelling the relationship between response time and user experience in Mobile applications," Internet Research, 30(5), pp. 1353–1382. Available at: https://doi.org/10.1108/intr-05-2019-0223

Grinding and Mechanical Activation of Lizardite Using Dry Stirred Media Mill for Mineral Carbonation

Hakan Ciftci
Mining Engineering Department, Afyon Kocatepe University, Afyonkarahisar, Turkey

Abstract: Mechanical activation of Ca/Mg silicates by grinding is a pre-treatment of some mineral carbonization processes. In this study, the mechanical activation of lizardite ore from a chromite beneficiation plant waste by grinding in a stirred media mill was studied. For grinding studies, grinding times of 10, 20, and 30 minutes and stirring speeds of 600, 800, 1000, and 1200 rpm were the parameters investigated, while the ball charge rate was 60% and the ore charge rate was kept constant as 40%. This way, the effects of grinding time and stirring speed on particle size distribution and energy consumption were investigated. At the end of the grinding studies, the stirring speed was determined as 1200 rpm, and the grinding time was 10 minutes for the finest particle size distribution. The particle size distribution data were determined as d10: 2, 7 µm, d50: 13, 6 µm, d90: 57.6. The energy consumption for the grinding process performed in these parameters was calculated as 130 kWh/ton.
Keywords: Lizardite, Serpentine, Grinding, Mechanical Activation, Stirred Media Mill, Attritor Mill.

1. Introduction: The mineral carbonation technique prevents the emission of CO_2 gas, formed due to various industrial processes, into the atmosphere by chemically binding to calcium and magnesium silicates (Li & Hitch, 2018). Three different techniques are used in mineral carbonation, and these are thermal activation, chemical activation, and mechanical activation. In these three methods, silicate minerals' crystal structures deteriorate, increasing the carbonation rate (Aminu et al., 2017; Azdarpour et al., 2015; Haug et al., 2010). Mechanical activation is a grinding process that is performed to decrease particle size and enlarge the surface area of minerals. Grinding causes the removal of hydroxyls (dehydroxylation) of hydrated minerals and so yields a highly disordered crystal structure. This is the recently favored process for magnesium silicates to produce disordered crystalline structures for mineral carbonation uses (Alex et al., 2016). Olivine and serpentine group minerals are the most appropriate Ca/Mg silicate mineral raw materials for CO_2 mineral carbonation, as they are abundant in nature and bind relatively more CO_2 per unit mass (Goff et al., 2000). Lizardite, the most common mineral of the serpentine group, is a trioctahedral phyllosilicate type mineral and has the general chemical formula of $Mg_3Si_2O_5(OH)_4$. Layered (1:1) and hydrated lizardite minerals generally contains 12.1-13.5% H_2O, 41.0-42.1% SiO_2, and 38.3-40.9% MgO in their crystal structure (Çiftçi et al., 2021; Dlugogorski & Balucan, 2014). The carbonation process of magnesium silicates can be determined by reactions (1) and (2), respectively.

$$Mg_2SiO_4 + 2CO_2 \rightarrow 2MgCO_3 + SiO_2 \quad (1)$$

$$Mg_3Si_2O_5OH_4 + 3CO_2 \rightarrow 3MgCO_3 + 2SiO_2 + 2H_2O \quad (2)$$

Studies on the mechanical activation of serpentine minerals such as lizardite by grinding to be used in the mineral carbonation process are limited (Li & Hitch, 2018; Nelson, 2004). This study investigated the

mechanical activation of lizardite mineral, produced as a chromite ore beneficiation plant waste, by a stirred media mill. The effects of stirring speed and grinding time on particle size distribution and energy consumption were investigated in detail.

2. Materials and Methods

2.1. Materials: The lizardite ore used in this study was taken from the waste site of OGELMAN Mining Company's chromite ore beneficiation facility in Harmancık/BURSA.

2.2. Methods

2.2.1. Characterization studies: Before the mineralogical and chemical analysis, the sample was dried at 105oC for 24 h and ground in a ring mill for 2 min. Mineralogical analysis was performed using a Shimadzu XRD-6000 instrument to determine mineral compositions of the sample. Elemental composition of the sample was determined by chemical analysis using a Rigaku ZSX Primus II XRF spectrometer. Particle size analysis were performed using a Malvern Mastersizer 2000 instrument (Çiftçi et al., 2020).

2.2.2. Grinding studies: The procedure of our previous study was followed for grinding experiments (Çiftçi & Özçatal, 2021). A vertical stirred media mill with an effective volume of 1 L was used for the grinding experiments. A pin-type shaft was used as the stirrer, and yttrium-stabilized zirconium oxide balls (3 mm: 598 g, 5 mm: 1967 g, total volume: 530 mL) were used as the grinder media. Before grinding, the sample was dried at 100oC for 24 h. After the balls and sample were added to the mill chamber, the mill cooling water was turned on, and the stirring process was started. The energy consumed in the grinding experiments was recorded with an electricity meter attached to the circuit. The operating parameters of each grinding experiment are summarized in Table 2.1.

Table 2.1 *Operational Parameters of the Grinding Experiments*

Exp. no	1	2	3	4	5	6	7	8	9	10	11	12
Stirring speed (rpm)	600	600	600	800	800	800	1000	1000	1000	1200	1200	1200
Grinding time (min)	10	20	30	10	20	30	10	20	30	10	20	30

3. Results and Discussion: The chemical analysis results of the sample used in the grinding studies are given in Table 3.1. Accordingly, it was determined that the sample consisted mainly of Si and Mg elements and showed a high rate of loss on ignition (15%). These obtained data showed that the sample was a serpentine group mineral. The exact mineralogical composition was determined by XRD analysis.

Table 3.1 *Chemical Composition of the Lizardite Sample*

Component	SiO_2	Al_2O_3	Fe_2O_3	MgO	CrO	CaO	SO_3	LOI
Content, wt.%	32.22	0.73	7.10	39.3	0.97	0.84	0.18	14.94

LOI: loss on ignition.

Figure 1: *XRD Pattern of the Lizardite Sample*

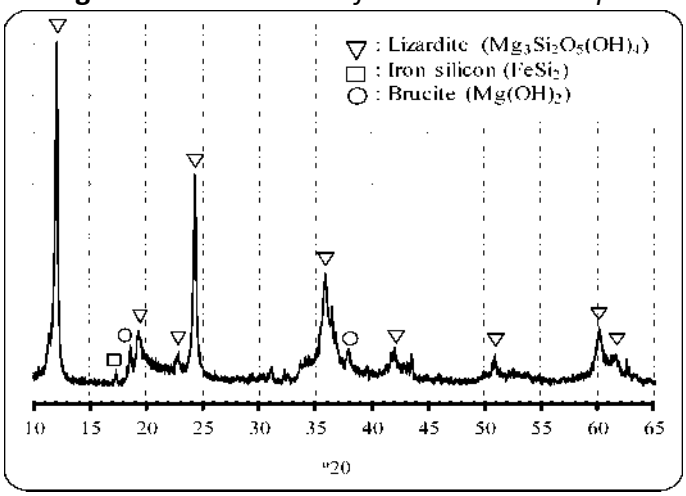

The XRD pattern of the sample (Figure 1) showed that all of the materials representing the sample content had a certain crystal structure. Additionally, it was determined that the sample mainly consisted of lizardite minerals and the presence of small amounts of brucite and iron silicon. Stirring speed and grinding time are the most effective working parameters in grinding processes with stirred media mills. The results of the grinding experiments were evaluated with the particle size distribution curves of the ground samples obtained. All comparative graphs were drawn in order to evaluate the obtained data accurately (Figures 2 and 3). The grinding chamber experiences a heightened level of energy and strength due to the stirring speed, resulting in an increased probability of the grinding media impacting and wearing down the particles. As the stirring speed continues to rise, the stress intensity inside the mill chamber progressively amplifies, substantially affecting the interaction between the grinding media and the material to be ground (Çiftçi & Özçatal, 2021; Altun et al., 2012; Hasan et al., 2017).

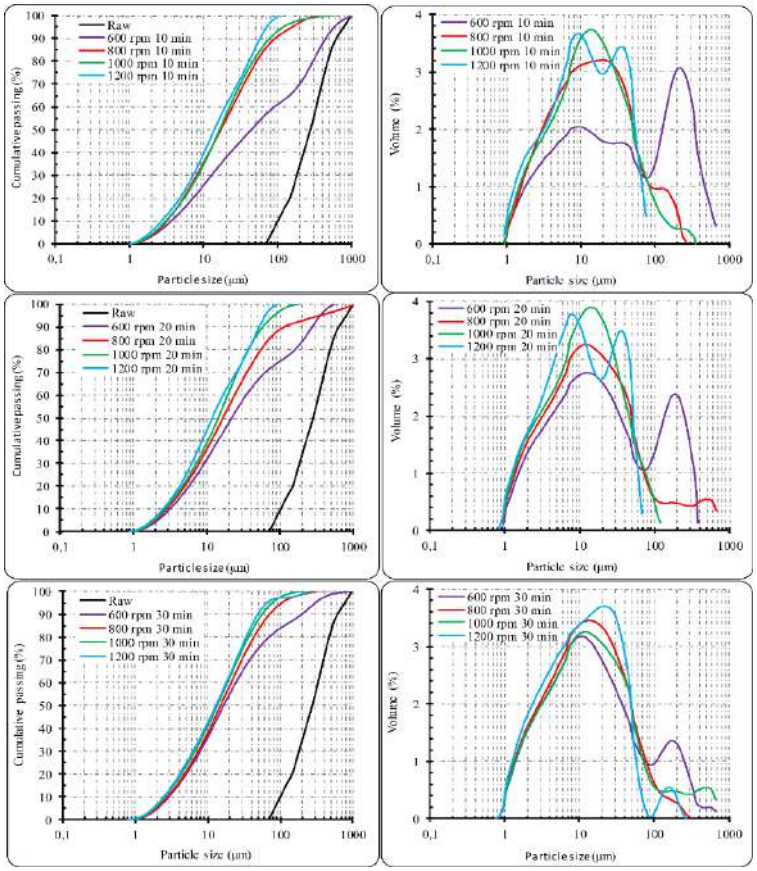

Figure 2: *Particle Size Distributions of the Ground Products as a Function of Stirring Speed*

Figure 3: *Particle Size Distributions of the Ground Products as a Function of Grinding Time*

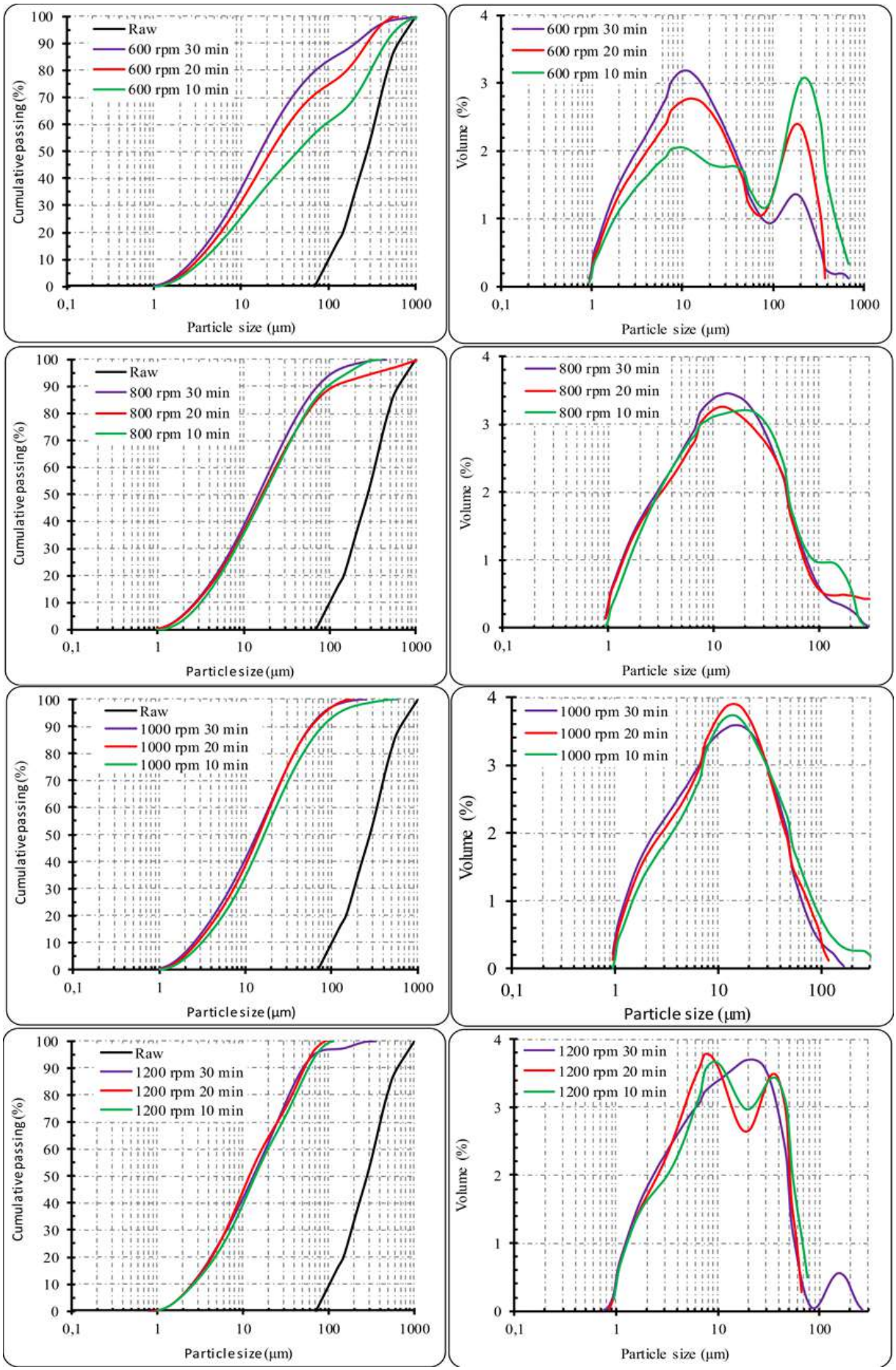

Figure 2 shows the effects of stirring speed on particle size distribution at constant grinding times. Accordingly, increasing the stirring speed at the fixed grinding times resulted in smaller particle sizes. While the difference between the particle size distributions obtained at different stirring speeds was sharper at low grinding times, such as 10 min, it was determined that the difference was much less with increasing the grinding time to 30 min. The most striking result in Figure 2 was that the particle size distribution at 600 rpm remained much larger in all grinding times compared to other stirring speeds. The result seen from the curves in Figure 2(right) was that most of the samples were grouped in 2 or 3 different particle sizes, showing a heterogeneous particle size distribution.

Figure 3 shows the effects of grinding time on the particle size distribution at constant stirring speeds. According to the results obtained from these comparative curves, it was determined that the grinding time had a significant effect on the particle size distribution at low grinding speeds (600 and 800 rpm). At the same time, it was not so effective at high mixing speeds, especially at 1200 rpm. In Figure 3, after grinding at 1200 rpm for 30 min, the particle size distribution mostly remained below 100 µm, while a small portion of the sample showed a secondary size distribution above 100 µm. This result was not observed in 10 min and 20 min of grinding under the same conditions. In fact, as the grinding time increases under normal conditions, the particle size is expected to decrease more. However, the emergence of such a situation can be attributed to the agglomeration of the particles that have passed to very fine sizes due to increasing the grinding time more than necessary. In addition to the Van der Waals forces, the agglomeration is also caused by the binding effect of the water produced by dehydroxylation due to grinding for such materials.

The d10, d50, and d90 values of the grain size distributions obtained at the end of milling are also summarized in Table 3.2. As an example, the d50 value of a sample (such as 600 rpm 10 min) indicates that 50% of the sample size is below that value (44.16 µm). As seen in this table, it was determined that the grinding time was very effective at low mixing speeds, and the mixing speed was very effective at low grinding times. For example, grinding time did not seriously affect d90 values in grinding at 1200 rpm. However, while the d90 value was 449.2 µm at 600 rpm milling for 10 min, the d90 value decreased significantly to 202.2 µm when grinding was extended to 30 min. In this respect, it has been proven that grinding at high mixing speeds in mixed media mills yields finer-sized products and saves time.

Table 3.2 *Particle Size Distributions of the All Ground Products*

Stirring speed (rpm)	Grinding time (min)	d_{10} (µm)	d_{50} (µm)	d_{90} (µm)
Raw	Raw	100.00	270.00	600.00
600	10	3.66	44.16	449.23
	20	3.19	21.93	277.81
	30	2.90	16.60	202.17
800	10	3.18	17.14	111.18
	20	2.86	16.46	93.44
	30	2.77	14.94	71.30
1000	10	3.08	16.36	77.59
	20	2.71	14.24	57.74
	30	2.54	13.54	56.76
1200	10	2.68	13.85	57.58
	20	2.60	11.94	52.37
	30	2.52	13.16	49.92

The stress intensities are heightened by progressively increasing the stirring speed, consequently boosting the grinding speed. This effect is primarily attributed to the increased probability of particle collisions with the grinding media. Additionally, as the stirring speed rises further, the kinetic energy of the grinding media also rises, leading to its transfer to the particles and facilitating the process of particle breakage.

Figure 4: *Energy Consumptions of the All Grinding Experiments*

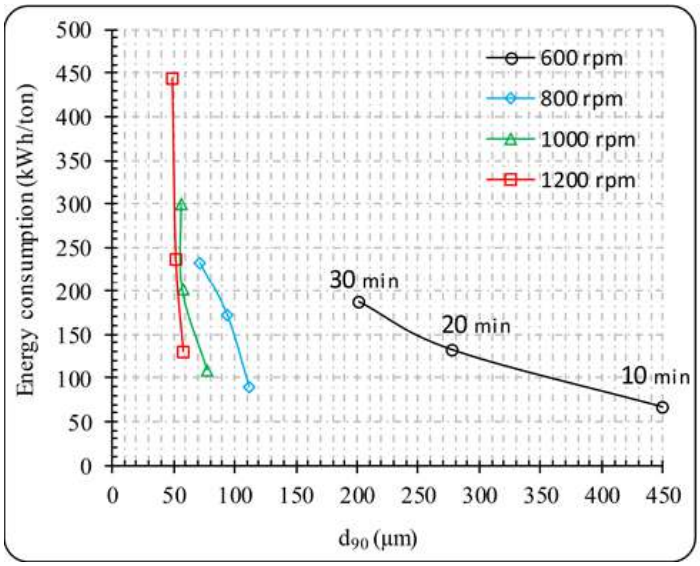

Stirring speed (rpm)	Grinding time (min)	d_{90} (µm)	Energy consumption (kW/ton)
600 rpm	10	449.2	67.8
	20	277.8	132.1
	30	202.2	187.8
800 rpm	10	111.2	90.4
	20	93.4	172.1
	30	71.3	232.9
1000 rpm	10	77.6	109.5
	20	57.7	201.7
	30	56.8	300.8
1200 rpm	10	57.6	130.4
	20	52.4	238.2
	30	49.9	443.3

Energy consumption is another point to be considered while evaluating the product obtained in grinding processes with particle size distributions. Because while determining the optimum operating parameters, energy consumption should be assessed in terms of cost. The electrical energy values consumed in all grinding trials are given in Figure 4. Accordingly, the connection between grinding time and energy consumption in the mill has been reaffirmed, showcasing a linear association. The same situation was observed for the energy consumption depending on the mixing speed. It was determined that as the mixing speed increased, the energy consumption increased proportionally. Notably, when the mill attains meta-steady state dynamics, the mill's power consumption stabilizes and remains consistent, as evidenced in other studies (Çiftçi & Özçatal, 2021; Santosh et al., 2020). This pattern has been observed in other investigations as well (Çiftçi & Özçatal, 2021; Hacıfazlıoğlu & Korkmaz, 2020; Toraman, 2013; Toraman & Katırcıoğlu, 2011). As a result, considering the data in Table 2, it was determined that grinding operations in mixed media mills were more appropriate at high mixing speeds and low grinding times. In this way, it has been proven that the product milled to much finer sizes is obtained with less energy consumption. Considering these results in this study, it was determined that the most suitable grinding conditions were 1200 rpm stirring speed and 10 min grinding time.

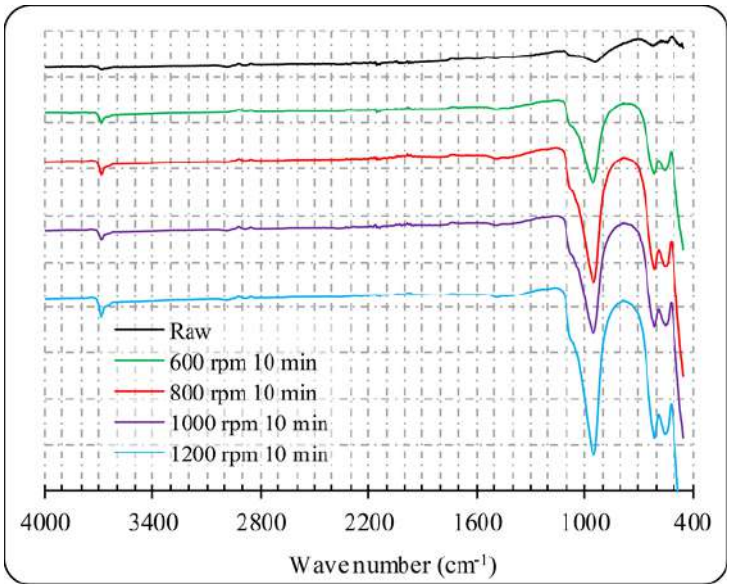

Figure 5: FT-IR Spectrums of Some Ground Products

FT-IR spectra are given in Figure 5 to examine the changes in the functional groups in the structure of the ground samples. After mechanical activation, the positions of the bands remain almost the same, but they become stronger and clearer. This outcome can be understood by referring to Rayleigh's equation, which establishes a connection between the scattering of light and the size of the particles. Essentially, the phenomenon can be explained by the fact that larger particles scatter light more effectively (Li & Hitch, 2017). In addition, OH stretching, which is more pronounced at a wavenumber of 3680 cm-1 due to dehydroxylation by grinding, is attributed to the structural hydroxide groups of the milled samples.

4. Conclusion: The Chromite plant waste sample was subjected to dry grinding experiments using a pin-type vertical stirred media mill. Characterization studies revealed that the sample predominantly consists of lizardite. Two operational parameters, grinding time and stirring speed, were investigated while keeping the material and ball charge constant. It was concluded that stirred media mills could effectively dry grind lizardites into ultrafine particle sizes. Additionally, it was determined that the optimum grinding conditions in stirred media mills were low grinding time (≤10 min) at high stirring speed (≥120 rpm). In this way, it was seen that a finer-sized product was obtained with lower energy consumption. By utilizing specific operational parameters (60% ball charge, 40% material charge, 1200 rpm stirring speed, and 10 min grinding time), a ground lizardite product with a d90 value of approximately 57.6 µm was achieved. The selected operational parameters resulted in an energy consumption of 130.4 kWh/ton during the grinding process.

5. References:

Alex, T. C., Kumar, R., Roy, S. K., & Mehrotra, S. P. (2016). Mechanical activation of Al-oxyhydroxide minerals–a review. Mineral Processing and Extractive Metallurgy Review, 37(1), 1-26. https://doi.org/10.1080/08827508.2015.1055626

Altun, O., Benzer, H., & Enderle, U. (2013). Effects of operating parameters on the efficiency of dry stirred milling. Minerals Engineering, 43, 58-66. https://doi.org/10.1016/j.mineng.2012.08.003

Azdarpour, A., Asadullah, M., Mohammadian, E., Hamidi, H., Junin, R., & Karaei, M. A. (2015). A review on carbon dioxide mineral carbonation through pH-swing process. Chemical Engineering Journal, 279, 615-630. https://doi.org/10.1016/j.cej.2015.05.064

Aminu, M. D., Nabavi, S. A., Rochelle, C. A., & Manovic, V. (2017). A review of developments in carbon dioxide storage. Applied Energy, 208, 1389-1419. https://doi.org/10.1016/j.apenergy.2017.09.015

Çiftçi, H., Arslan, B., Bilen, A., Arsoy, Z., & Ersoy, B. (2021). Optimization of leaching conditions for extraction of magnesium from a chromite beneficiation plant tailing predominantly containing lizardite. Bulletin of the Mineral Research and Exploration, 164(164), 251-259. https://doi.org/10.19111/bulletinofmre.827630

Çiftçi, H., & Özçatal, M. (2021). Dry Grinding of Bentonite by Stirred Media Mill. Journal of Characterization, (1), 62-69. https://doi.org/10.29228/JCHAR.55663

Çiftçi, H., Ersoy, B., & Evcin, A. (2020). Purification of Turkish bentonites and investigation of the contact angle, surface free energy and zeta potential profiles of organo-bentonites as a function of CTAB concentration. Clays and Clay Minerals, 68, 250-261. https://doi.org/10.1007/s42860-020-00070-0

Dlugogorski, B. Z., & Balucan, R. D. (2014). Dehydroxylation of serpentine minerals: Implications for mineral carbonation. Renewable and Sustainable Energy Reviews, 31, 353-367. https://doi.org/10.1016/j.rser.2013.11.002

Eswaraiah, C., Venkat, N., Mishra, B. K., & Holmes, R. (2015). A comparative study on a vertical stirred mill agitator design for fine grinding. Separation Science and Technology, 50(17), 2639-2648. https://doi.org/10.1016/j.rser.2013.11.002

Goff, F., Guthrie, G., Lipin, B., Fite, M., Chipera, S., Counce, D., ... & Ziock, H. (2000). Evaluation of ultramafic deposits in the Eastern United States and Puerto Rico as sources of magnesium for carbon

dioxide sequestration (No. LA-13694-MS). Los Alamos National Lab.(LANL), Los Alamos, NM (United States).
Hacıfazlıoğlu, H., & Korkmaz, A. V. (2020). Performance comparison of stirred media mill and ball (BOND) mill in bauxite grinding. Particulate Science and Technology, 38(4), 404-408. https://doi.org/10.1080/02726351.2018.1547342
Hasan, M., Palaniandy, S., Hilden, M., & Powell, M. (2017). Calculating breakage parameters of a batch vertical stirred mill. Minerals Engineering, 111, 229-237. https://doi.org/10.1016/j.mineng.2017.06.024
Haug, T. A., Kleiv, R. A., & Munz, I. A. (2010). Investigating dissolution of mechanically activated olivine for carbonation purposes. Applied Geochemistry, 25(10), 1547-1563. https://doi.org/10.1016/j.apgeochem.2010.08.005
Li, J., & Hitch, M. (2018). Mechanical activation of magnesium silicates for mineral carbonation, a review. Minerals Engineering, 128, 69-83. https://doi.org/10.1016/j.mineng.2018.08.034
Nelson, M. G. (2004). Carbon dioxide sequestration by mechanochemical carbonation of mineral silicates. Report No. DE-FG26-99NT41547. University of Utah. Salt Lake City, Utah.
Santosh, T., Soni, R. K., Eswaraiah, C., Rao, D. S., & Venugopal, R. (2020). Optimization of stirred mill parameters for fine grinding of PGE bearing chromite ore. Part. Sci. Technol, 39(6), 663-675. https://doi.org/10.1080/02726351.2020.1795016
Toraman, O. Y., & Katırcıoglu, D. (2011). A study on the effect of process parameters in stirred ball mill. Advanced Powder Technology, 22(1), 26-30. https://doi.org/10.1016/j.apt.2010.02.018
Toraman, O. Y. (2013). Dry fine grinding of calcite powder by stirred mill. Particulate Science and Technology, 31(3), 205-209. https://doi.org/10.1080/02726351.2012.694135

Strain Gauge Testing of 3D-Printed CFRP Sandwich Structure

Paweł Zur
Department of Engineering Processes Automation and Integrated Manufacturing Systems, Silesian University of Technology,
Gliwice, Poland

Alicja Żur
Department of Engineering Processes Automation and Integrated Manufacturing Systems, Faculty of Mechanical Engineering, Silesian University of Technology, Gliwice, Poland

Piotr Michalski
Department of Engineering Processes Automation and Integrated Manufacturing Systems, Faculty of Mechanical Engineering, Silesian University of Technology, Gliwice, Poland

Andrzej Baier
Department of Engineering Processes Automation and Integrated Manufacturing Systems, Faculty of Mechanical Engineering, Silesian University of Technology, Gliwice, Poland

Abstract: In this article, the authors present composite sandwich-type CFRP structures and a study of their properties by strain gauge testing. The paper presents the modeling of a parameterized elementary unit

serving as the core of a 3D printed structure using Fused Deposition Modelling (FDM) technology. The properties of these structures with different outer layers made of pure epoxy resin and resin with 10% and 20% carbon fiber powder were then investigated. Based on the results of the strain gauge tests, material models were reconstructed for each resin layer, which can be used in computer FEM studies of more complex components. As an application example, a strength analysis of the driver's seat of a Greenpower car made with printed sandwich structures coated with carbon fiber powder resin was conducted.
Keywords: 3D Printing, Carbon Fiber, CFRP Composite, Sandwich Structure, Strain Gauge Testing

1. Introduction: The purpose of the study was to investigate strain gauging of innovative compo-site sandwich structures. The premise of the study is to model a scalable elementary unit that can then be multiplied to form the core of a sandwich structure. In this article, the authors examine the mechanical properties of such elements using resistance strain gauge testing. In recent years, the importance of Continuous Fiber Reinforced Thermoplastic Composites (CFRTPCs) has increased considerably. Numerous industrial requirements for new materials led to the development of innovative manufacturing and design forms. New composite manufacturing technologies and new composite technologies allow traditional materials to be replaced by light structures, and are not inferior in mechanical properties to traditional materials. As described in this paper, a new type of CFRP materials and a new composite manufacturing approach have been developed. - 3D print in Fused Deposition Model-ling (FDM) technology considering the print to be a lightweight structure reinforced with epoxy resin layer with the addition of carbon fiber powder. Innovation in the manufacturing process is essential and urgent to further develop and apply CFRTPC material. [1-3]. At present, FDM is used not only for visual aids, conceptual models, and proto-types but also for manufacturing of functional parts. 3D printing technology based on material extrusion can be used for printing multiple materials and multiple color printing of plastics, food, and even living cells. The technology is widely used because it is low in cost and can be built in fully functional parts. 3D printing technology, also known as additive manufacturing, involves producing a given object or component by adding material layer by layer and creating a three-dimensional (3D) structure. It re-duces the cost of assembly by producing complex geometry and flexible functional components from STL files by depositing two-dimensional (2D) layers of melted polymeric material on a build platform. Using CAD (Computer Aided Design) software, it is needed to create and design appropriate print models in advance. [4,5,6,7]. Low-precision is a relative term, but some applications do not require high-precision (prototypes or displays), in order for FDM to be more acceptable in the industry for mass production of printed parts, accuracy is the fundamental requirement. Many researchers have analyzed various control parameters to achieve the desirable characteristics of the component and have also been working on optimizing the process parameters [4,8]. Several factors affect the quality of the final elements. – printing temperature, printing speed, layer height, print architecture (infill pattern), cooling rate. [1,9]. Currently, there are a number of articles in which the authors study the properties of particular predefined filling structures of 3D prints. In the notable majority of these articles, they treat the effect of filling and other parameters on mechanical properties. Modeling custom structures and using them in 3D printing is no longer such a popular topic. The topic has been addressed by, for example: Audibert et al. [10] in which the authors study shapes built from bone geometry, as well as author Bodaghi et al. [11] where the aim of that paper was to introduce auxetic meta-sandwiches printing technology for reversible energy absorption applications. Saufi et al. [12] proposed using a shape inspired by nature - the starfish. The bio-inspired structure has been studied for its ability to absorb energy and high strength. The topic addressed in this article - parametric spatial structure reinforced with carbon fiber dust and epoxy resin, is an innovative and previously unaddressed issue. Currently, new composite manufacturing technologies combined with new materials can replace traditional materials with light structures with similar resistance. These structures allow the weight and materials needed for the production of the elements to be reduced [13,14]. Designing structures to improve load bearing capability with reduction of weight and impact resistance is one of the multidisciplinary research fields, with potential ap-plications in a wide variety of areas, such as automotive, space, civil, and biomedical, among others. Advanced scalable technologies, such as 3D printing, can be used to explore the

mechanical behavior of various predictive complex geometric shapes, to create innovative engineering materials. [15,16,17]. Composite materials are materials composed of at least two materials (phases) with different properties and have properties superior to each component separately, but also superior to those derived from a simple summarization of these properties [5,14]. Examples of such materials are polymers reinforced with carbon fibers. They are widely used in the aerospace industry due to their high resistance, corrosion resistance, and fatigue resistance. [18] It is a well-known practice to add various types of fillers to epoxy resin to enhance its strength or modify selected properties [14,19-25]. Among the fillers used are silica, quartz flour, glass or carbon fiber dust, short fibers, and graphene. However, the authors propose a new approach by mixing carbon fiber powder into the epoxy resin. Sandwich composite structures are widely used in weight-restricted applications, such as in the automotive or aerospace industry. Researchers have developed better mechanically resistant alternative materials, such as hexagonal and reintroduced honeycomb cores, and the structure of lattice trusses and cell auxetic structures. However, these structures have several serious limitations, mainly manufacturing methods – eg. extrusion, forming and corrugation [26-30]. Other studies have shown that it is highly challenging to manufacture lattice structures, e.g. cubic diamond or gyroid structure, by traditional subtractive methods. Using 3D printing could help overcome these difficulties and suggests new ways of manufacturing the support structures and cores [31-37]. In this article, the authors also propose an innovative method to manufacture such composites using 3D printing with FDM technology. The printed cores of the structure are then coated with a layer of epoxy resin along with the admixture of 10% and 20% carbon fiber powder. The resulting CFRP composite allows for diversified applications: 3D printing makes it possible to produce a core of any shape, while the res-in with the addition of carbon fiber powder, unlike classical laminates, also allows uniform coverage of surfaces with almost any degree of complexity and refraction. In the next part of the study, strain gauge tests were performed. The principle of the resistance strain gauge is based on the strain gauge effect of the resistance material. This effect was first observed in 1856 by William Thomson. It consists of a change in the electrical resistance of the material with a change in its length. The sensor's resistance material deforms during operation. In the linear range of the stress characteristics, as a function of the elongation of the elastic element, the deformation is reversible, and the resistance function is linear. [38]. Strain gauges can be made of many metals and alloys. The most common are constantan (an alloy of copper and nickel in a ratio of 3:2) and nichrome (an alloy of 80% nickel and 20% chromium). The most important advantages of strain gauge testing include its small size, and therefore the ability to take measurements in hard-to-reach places, high measurement accuracy, and relatively low cost. However, this method is not without its disadvantages, which certainly include the long preparation time for the test that involves proper surface preparation and sticking of the strain gauges, as well as the disposability of the strain gauges used, as once a strain gauge is stuck on, it cannot be peeled off without damaging it. [38,39]. The purpose of this study of sandwich CFRP structures is to implement them as an infill for the driver's seat in a Greenpower electric car. Silesian Greenpower is the students' interfaculty project that focuses on design and construction of the electric racing vehicle. However, the Greenpower car is not a regular EV. It is an one-person lightweight construction. The Greenpower car is designed for specific type of races and is not admitted to road traffic. The main restriction in the design of the car is imposed by the organizers, the power source and type of the motor driving the car, which increases competition level and equalizes the chances of teams. Greenpower electric vehicles are characterized by low weight (about 90 kg without the driver) and rather low speeds (about 50 km/h), so they do not require such exorbitant strength properties and thermal resistance, and more critical here is the low weight and the possibility of unit production of custom parts at low cost. [40,41]. The driver's seat is a car component that has several tasks, primarily to ensure the driver's safe position in the car but also to provide comfort while driving. Therefore, it is ideal to design a seat for a particular driver to best suit his or her ergonomics. This approach has one disadvantage - the cost of making such a unitary seat increases significantly due to the uniqueness of the component. The use of structures and methods studied in this article will reduce the cost of manufacturing such a seat. In addition, such structures can be used in the design of damping suspension components, such as bushings, using more resilient materials. [13,42,43].

2. Materials and Methods: In this section, the model and sample preparation process and the tests test methodology of the conducted are described. First, the modelling of the core structure was prepared for the Finite Element Method (FEM) analysis. The obtained CAD model was further used to prepare a sandwich structure composite. The core of the structure was 3D printed and laminated. The prepared samples were subjected to strain gauge testing. Then the material model was retrieved on the experimentally acquired data. Lastly, an FEM analysis of the driver's seat has been conducted.

2.1 CAD Model: The first step of this study was preparing a CAD model of the support structure geometry. For this purpose, the Siemens NX 12 program was used. The main idea was to prepare a model of an elementary unit, designed with the help of parameterized variables. The use of parameterization in the model allows to adjust the size and change the geometry within a given range. Two geometries with truss characteristics were pro-posed - type one with vertical supports only, and type two with additional diagonal supports. The geometry of the models is shown in the figure. The models consisted of a hexagonal cube with the following variables: height (h), thickness of bases (b), and thickness of supports (s), both vertical and diagonal supports. The elements used in the subsequent tests were 8x8x8 mm, the thickness of the bases was 0.5 mm, while the thickness of the supports was 1.5 mm. Additional diagonal support was created using a circular array with the element spaced every 90 degrees. This ensures that the diagonal supports on opposite walls are arranged perpendicular to each other.

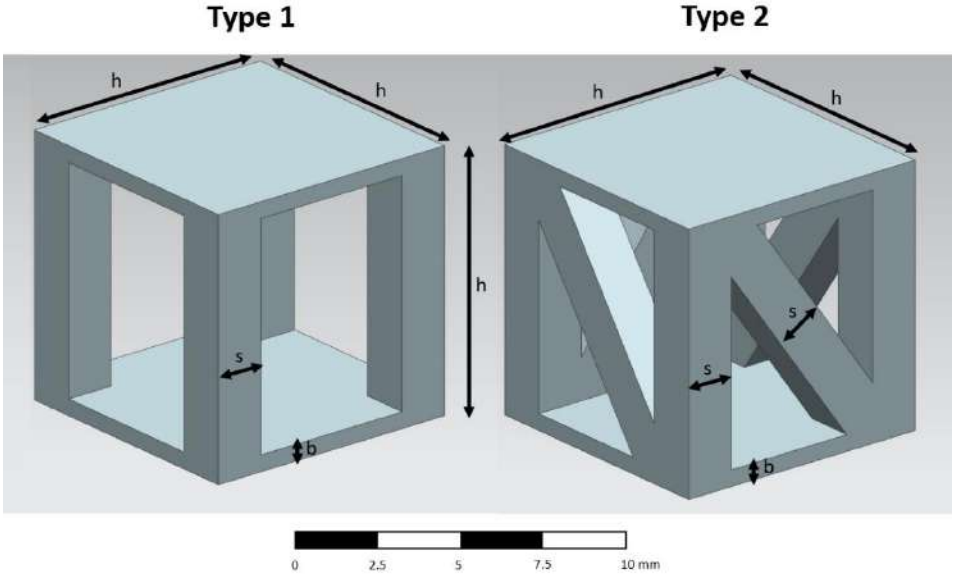

Figure 1: *Comparison Of Two Types Of Elementary Units Along With Scalable Parameters: H – Height, S – Support Thickness, B – Base Thickness*

The elementary units were used to create the core structure of a sandwich-type element. Also, two variants of the core were proposed - consisting of one or two layers of elementary units. To create the infill, an elementary unit was multiplied using the Pattern Feature option. A grid of 160 elements was created, 16 by 10 elements with 2 mm spacing between cubes. For a model with two layers, the number of elements was doubled. Additionally, two thin layers of 0.5 mm thickness were added as bonding sur-faces. The size of the modeled core structure is 158x98x9 mm for the model with one layer and 158x98x17 mm for the model with two layers of elements. A comparison of the prepared core models is shown in Figure 1 above and in Table 1 below.

Table 1: *Comparison of Sandwich Core Structure Types*

	Structure A	**Structure B**	**Structure C**
Elementary unit	Type 1	Type 2	Type 1
Number of units	160	160	320

As can be seen from the table above and the data on the weight of each sample, structures with additional diagonal support are heavier than samples without this support - for samples with one layer the difference is 30%, while for samples with two layers the difference is 40% in weight.

2.2 Finite Element Method Analysis: In the next step, the designed structures were subjected to FEM strength testing. For this purpose, Ansys Workbench 19.2 software with the Nastran calculation module was used. Static Structural was selected as the test type. The material adopted for the FEM analysis was Ultra PLA by Noctua. The following manufacturer data were entered for the material constants: Young's modulus – 2,65 GPa, density – 1.3 g/cm3 and Poisson's ratio 0.33. Next, a mesh was created with an element size of 4 mm applied for outer layers. The next step was the task of setting the boundary conditions of the test, simulation of 3-point bending of the plates. The element was supported from below on the two edges along the width of the element which were offset by 10 mm from the edge of the sample. One fixed support and one sliding support were used (1 degree of freedom was left free – rotating along Y axis). A circle with a diameter of 50 mm was drawn on the upper surface, to which a force of 200 N was applied. The single layer element prepared for the FEM testing is shown in Figure 2. Analogous boundary conditions were used for all types of tested structures.

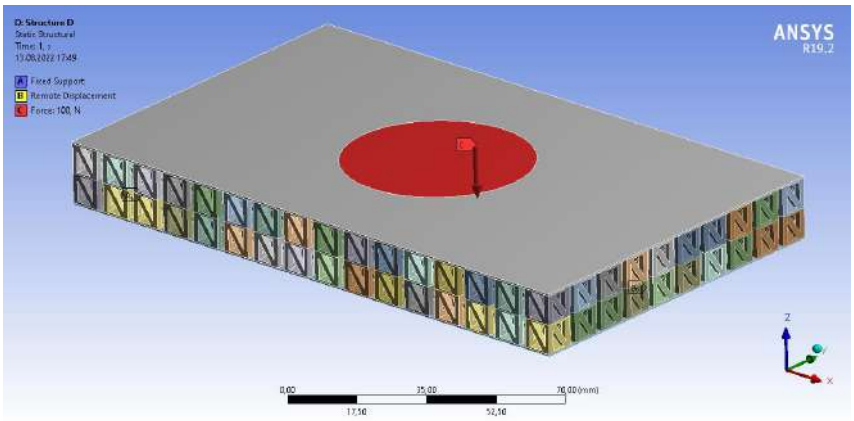

Figure 2: Double Layer Element (Structure D) Prepared for the FEM Analysis

2.3 3D Printing and composite fabrication: The components designed and discussed in the previous two subsections were then printed using FDM (Fused Deposition Modelling) technology on a Prusa MK3S printer. The material chosen for printing was PLA (Polylactic Acid), and the filament used was Noctua's Ultra PLA. The parameters used are shown in Table 2.

Table 2: 3D Printing Parameters

Parameter	**Value**
Printing temperature	210°C
Heatbed temperature	60°C
Layer height	0.2 mm
Nozzle diameter	0.4 mm
Cooling rate	100%
Number of outlines	2

PLA is one of the widely used thermoplastics in FDM. PLA is increasingly used as a biodegradable thermoplastic. In addition, the process of rapid prototyping with PLA requires less energy and a lower temperature. [1]. The elements are intended to be applied in the Silesian Greenpower electric race car. However, the only heat in the car is generated by the electric motor, which doesn't generate any fumes ad is located far away from the seat and has no influence on the degradation of the seat material. Therefore, high-temperature performance is not required in this specific application. The printed samples were then laminated. For this

purpose, LG700 epoxy resin with HG700 hardener from GRM Systems was used. This epoxy system is suitable for both RTM and manual lamination. It is characterized by very low viscosity, good heat resistance, very flexible and strong veneers. Epoxy resin LG700 with hardener HG700 has a 25 minutes processability time [44]. The resin was mixed with the hardener in a weight ratio of 100:35, and then the addition of carbon fiber powder was mixed in different ratios – 10% and 20% by weight. Selected carbon fiber powder was from Easy Composites. It is compatible with different resins – epoxy, polyester, vinylester and polyurethane. It has fiber diameter of 7.5 µm and fiber length of 100 µm. It has density of 1800 kg/m3. This carbon fiber powder is characterized by tensile strength of 3150 MPa and Young's modulus of 200 GPa [45]. The microscope image of the applied car-bon fiber powder is presented in Figure 3 below. The image was taken using an optical microscope with a magnification of 40 times. It is visible, that the powder consists of very short fibers.

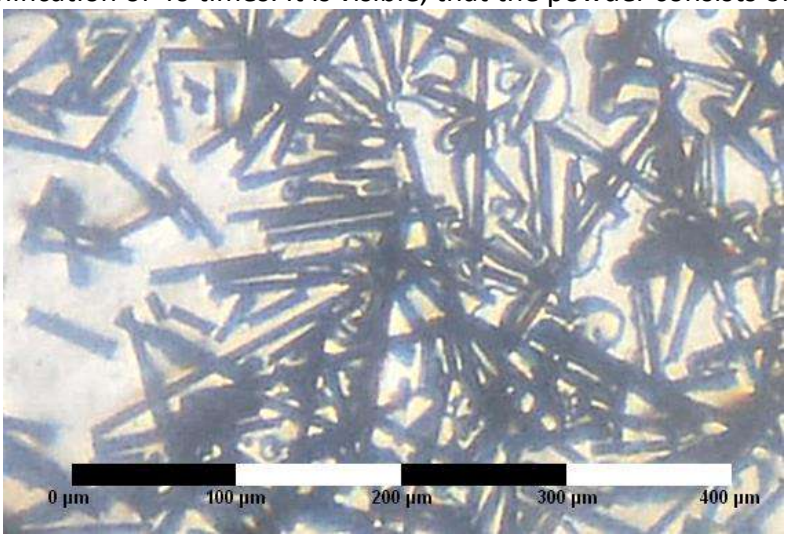

Figure 3: Microscope Image of Carbon Fiber Powder

Addition of carbon fiber powder can significantly improve the mechanical proper-ties of the resin. It increases tensile strength and modulus and electrical conductivity. It upgrades thermos-dimensional stability of the produced parts. Also, very high ten-sile strength and isotropic orientation it reduces shrinkage of the com-posite. Carbon fiber powder addition was 10% and 20% by weight. The carbon fiber powder was used as a reinforcing additive. Two samples without the addition of carbon fiber powder were also left as reference samples. A summary of all the samples made is shown in the Table 3 below.

Table 3: Samples Prepared for Strain Gauge Testing

Sample	Core structure	Coating
1	Structure A	No coating
2	Structure B	No coating
3	Structure A	Pure epoxy resin LG700
4	Structure B	Pure epoxy resin LG700
5	Structure A	LG700 + 10% carbon fiber powder
6	Structure B	LG700 + 10% carbon fiber powder
7	Structure A	LG700 + 20% carbon fiber powder
8	Structure B	LG700 + 20% carbon fiber powder

For each laminate layer, 10 g of resin mixture was provided, thus obtaining an ap-proximately 1 mm laminate layer on each side of the printed structure. The sample prepared for further testing is shown in Figure 4. The liquid mixture of epoxy and car-bon fiber powder was poured onto the surface of the 3D-printed core. The

epoxy resin has self-leveling properties, therefore then the samples were placed on a flat surface to ensure even distribution of the laminate and a smooth surface. Samples were laminated manually. The authors were considering vacuum laminating, but as there was no requirement to press the resin into standard carbon fiber fabric, they chose the simpler method.

Figure 4: Sample 6 Prepared for the Strain Gauge Testing

Then TF-5 resistance strain gauges with a gain parameter k of 2.15 and a resistance R of 120 Ohms were attached to the samples. The strain gauges were attached 1 strain gauge per sample - in the center of the lower surface, which is shown in Figure 5 below.

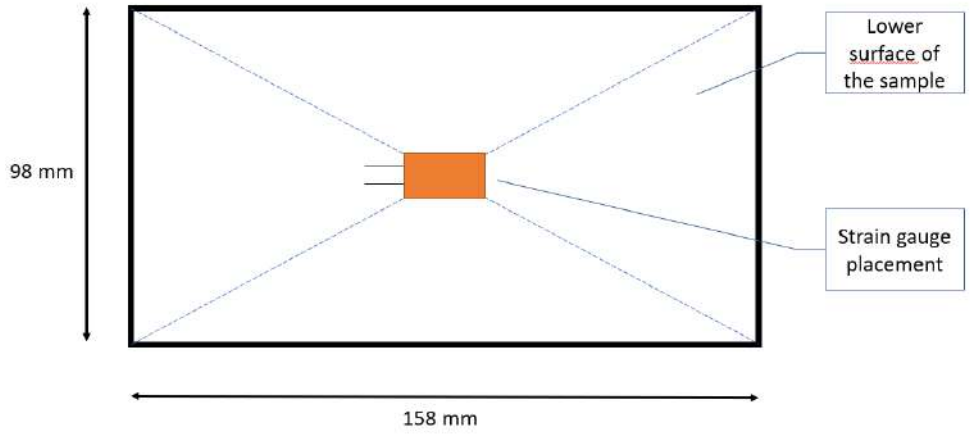

Figure 5: Placement of the Strain Gauge on the Sample

2.4 Strain Gauge Testing: In the next stage, the manufactured samples were subjected to strain gauge tests. For this purpose, a test stand equipped with a pneumatic actuator, support elements, sensors, and control software was prepared. The strain gauge test stand is shown in Figure 6.

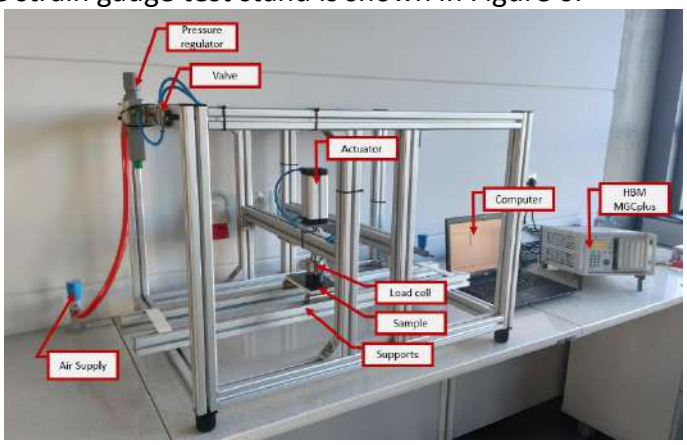

Figure 6: Strain Gauge Test Stand

The workstation used an actuator with a stroke of 100 mm, a piston diameter of 40 mm, a piston rod diameter of 12 mm, and a maximum pressure of 10 bar as the load-setting element. To repeat the test carried out previously by the FEM method and properly reproduce the load of the element on the surface of a circle with a diameter of 50 mm, a stamp of the appropriate size and mounting was 3D printed. In addition, the stand included a Pneumax pressure regulator, a Festo valve, and an HBM load cell used to accurately read the force applied to the specimen during the test. The specimen was supported on two metal cylinders at a distance of 10 mm from the edge of the specimen. An MGCplus controller and HBM software were used as control and result reading software. The data collecting system was MGCplus AB22A of the German company HBM. The device is able to connect up to 6 expansion cards. In our case, the ML455i and ML801b cards were used to collect data. The HBM U2B force sensor with a measuring range of 0-500N was connected to the ML455i card. A strain gauge with the previously specified parameters has been connected to the ML801b card. Each sample was loaded with a force of 200 N. The results were collected on the computer with CatmanEasy software.

2.5 Material's Model Definition: Based on the results obtained during the test strain gauge testing, the boundary conditions were recreated in ANSYS Workbench 19.2 software to determine material parameters (Young's modulus) for each sample. The samples are described in chapters 2.2 and 2.3. Additional layers on the top and bottom surfaces with a thickness of 1 mm were added to the sample models previously described in Section 2.2. These layers represent the additional resin layers that were tested during the previous test. The boundary conditions (restraint and specimen loading) remained the same from the initial FEA analysis. The PLA material model was modified so that the strain results obtained correspond to those obtained in the strain gauge test. The value of Young's modulus was modified to value of 1.55 GPa. Three additional material models were introduced for resins with different reinforcing additives (LG 700 epoxy resin, resin with 10% and 20% addition of carbon fiber powder). For each resin, a density of 0.65 g/cm3 and a Poisson ratio of 0.33 were assumed. Young's modulus was left as the only variable. The Young's modulus value for each material was then modified to replicate the results read at the strain gauge restraint in the previous test.

2.6 FEM Analysis of the Driver Seat: Although the elementary unit is very similar to an ordinary lattice structure, its parameterization and the ability to arrange it freely gives it a number of advantages - for example, the ability to lay out the elements along a curve, which allows the elementary units to fit a given geometry. This property makes it possible to arrange them in such a way that the applied load on the top surface is always perpendicular to the di-rection in which the units present the greatest strength - such an arrangement is not possible using a standard lattice fill pattern. This solution has been presented in Figure 7. In standard lattice structures, there are greater chances of shear stresses occurring. This feature allows the use of sandwich-type structures also for the manufacture of components that are not perfectly flat, unlike the structures currently in use.

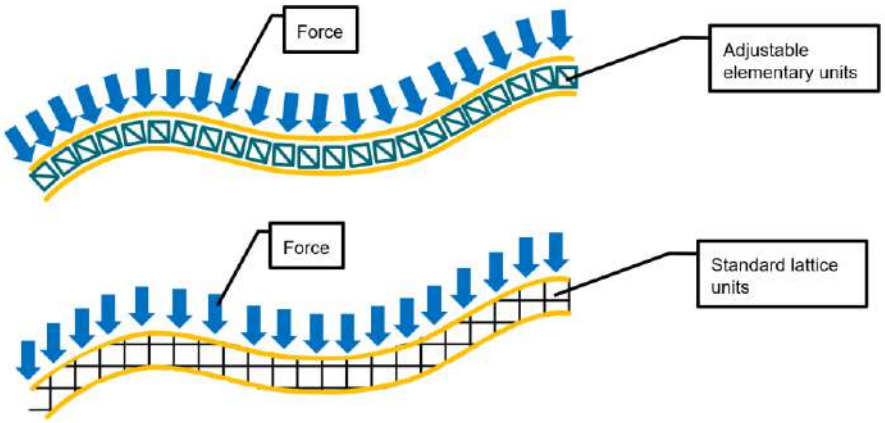

Figure 7: Advantages of Adjustable Elementary Units

In the final stage of the research, in order to verify the application of the previously presented elements and structures, a section of the driver's seat for the Greenpower electric car was designed. The model was created with Siemens NX 12 software using all the assumptions and elements presented in the previous chapters. The seat consist-ed of a core of 3,000 elements with Structure B and two outer layers of 0.5 mm thickness representing epoxy resin with the addition of 20% carbon fiber powder. The ap-plication of the driver's seat model (marked in blue) in the car is presented in the Figure 8 below.

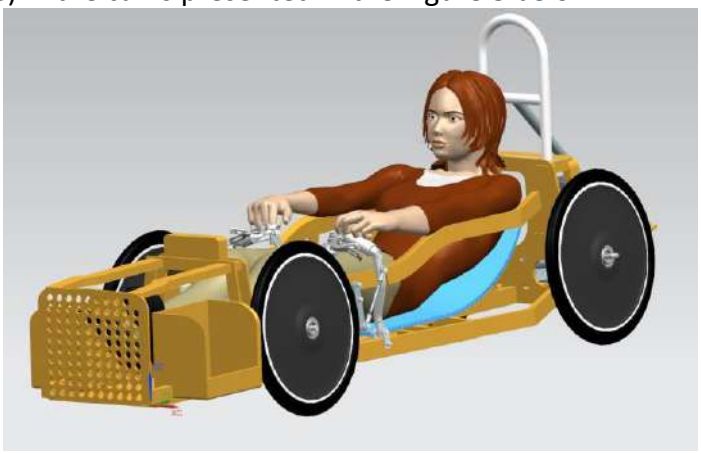

Figure 8: Application of the Driver's Seat in Green power Car

Next, an FEA analysis of the designed seat was carried out in ANSYS Workbench 19.2. Because the component is symmetric, only half of the model was used for the analysis to reduce the calculation time. PLA material was assigned for the core elements, while epoxy resin with 20% carbon fiber powder was assigned for the outer layers. A model mesh was created with an element size of 4 mm for the outer layers. The model was fixed in two areas: on the bottom surface representing the attachment of the seat to the floor of the car, and on an additional edge simulating the support of the seat under the back. The boundary conditions of the model are shown in Figure 9.

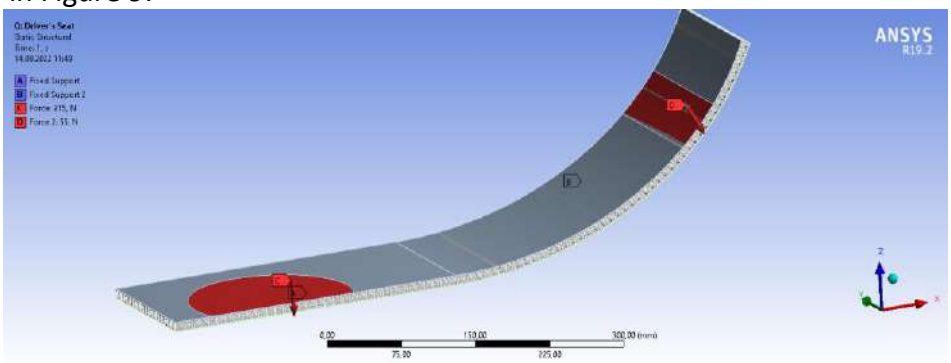

Figure 9: Boundary Conditions for FEM Analysis of the Green power Driver's Seat

The seat was loaded with two forces representing the pressure caused by the driver's own weight. The driver's weight was taken as 63 kg, as an average weight of the drivers who drove the car in the last season. The lower surface of the seat is affect-ed by 68% of the weight, that is, 43 kg, and the part below the back is affected by 17%, that is, 11 kg. Since only half of the seat was analyzed in the model, half of the forces corresponding to each weight - 215 N and 55 N - were taken as loads.

3. Results: This section successively describes the results from the Finite Element Method analysis carried out in Ansys Workbench 19.2 software and results from the strain gauge testing.

3.1 Finite Element Analysis: As a result of the numerical Finite Element Method analysis carried out in the Siemens NX software, the values of deformation and von Mises stress for each core structure sample have been obtained. The results acquired for each sample type are presented in Table 4.

Table 4: Results of FEM Analysis for Each Sample Type

	Structure A	Structure B	Structure C	Structure D
von Mises stress [MPa]	23.89	17.43	16.63	11.86
Strain [mm/mm]	$9.05 \cdot 10^{-3}$	$6.71 \cdot 10^{-3}$	$6.30 \cdot 10^{-3}$	4.55·10-3
Deformation [mm]	1.76	1.06	0.91	0.36

It can be noted that both factors – the diagonal support and layering of elementary units had significant influence on the results. The stresses in Structure A with one lay-er of elementary units without diagonal support were 23.89 MPa, while the strain value was 9.05•10-3 mm/mm and deformation was 1.76 mm. For Structure B with one layer and diagonal support, the values were 17.43 MPa, 6.71•10-3 mm/mm and 1.06 mm, respectively. The stresses in Structure B compared to Structure A are 27% lower, while the strain is 26% lower and deformation is 40% lower. The results for Structure B are shown in Figure 10. For Structure C with two layers of elementary units without diagonal support, the stress was 16.63 MPa, strain 6.30•10-3 mm/mm and the deformation was 0.91 mm. Stress in Structure C is 30% less than in Structure A, but only 5% greater than in Structure B. Strain value is 30% lower than for Structure A and only 6% lower than for Structure B. Deformation, on the other hand, is 48% less than in Structure A and 14% less than in Structure B. For Structure D with two layers of reinforced units, the stress was 11.86 MPa, so 27% less than in Structure C and 32% less than in Structure B. Strain value was 4.55•10-3 mm/mm, so 32% lower than for Structure B and 28% lower than for Structure C. The deformation in Structure D was 0.36 mm, so 60% less than in Structure C and 66% less than in Structure B.

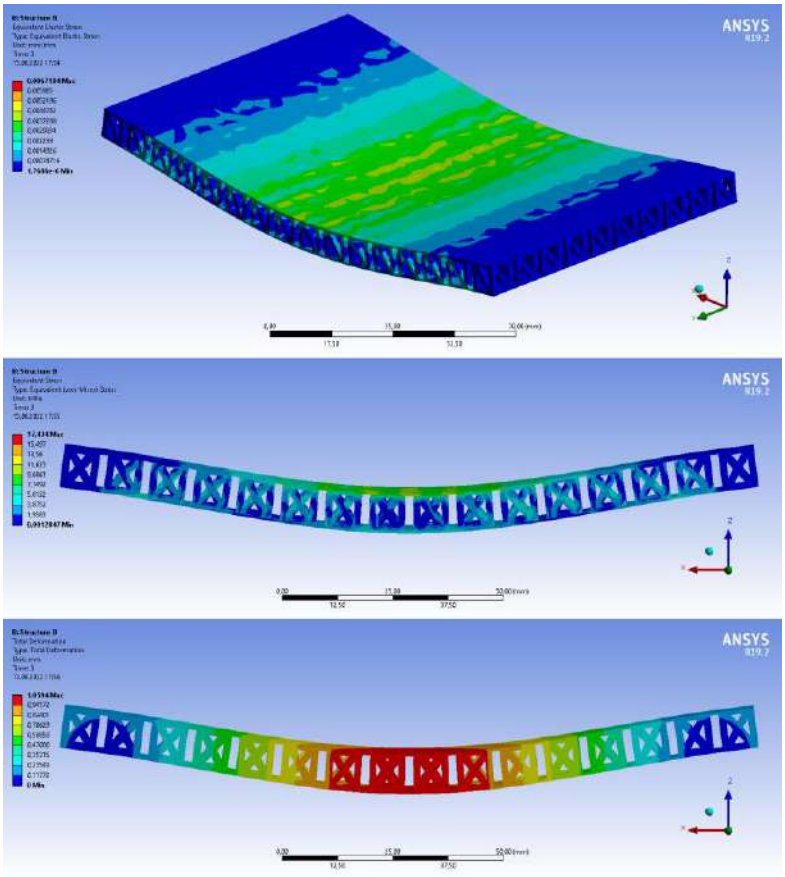

Figure 10: FEM Results For Structure C – Above: Strain Results, Middle: Von Mises Stress Results, Be-Low: Deformation Results

From the information above, it can be concluded that it is more advantageous to use a core with one layer, but with an additional diagonal support than two layers without this support; then we obtain only 5% greater

stresses and 6% greater strain values, while maintaining 19% less element weight. An additional layer of reinforced elements reduced stress and strain values by 32%, while deformation was reduced by more than 60%.

3.2 Strain Gauge Testing: When the samples were loaded with a force of 200 N, readings were obtained from strain gauges attached to the bottom of the samples. The readings for each sample are shown in Table 5 below.

Table 5: Strain Readings [mm/mm] of Strain Gauge Test for Each Sample

	Sample 1	**Sample 2**	**Sample 3**	**Sample 4**
100 N	$1.9 \cdot 10^{-3}$	$1.63 \cdot 10^{-3}$	$1.45 \cdot 10^{-3}$	$9.2 \cdot 10^{-4}$
150 N	-	$2.46 \cdot 10^{-3}$	$2.17 \cdot 10^{-3}$	$1.31 \cdot 10^{-3}$
200 N	-	$3.55 \cdot 10^{-3}$	-	$1.79 \cdot 10^{-3}$
	Sample 5	**Sample 6**	**Sample 7**	**Sample 8**
100 N	$9.3 \cdot 10^{-4}$	$6.47 \cdot 10^{-4}$	$7.25 \cdot 10^{-4}$	$4.96 \cdot 10^{-4}$
150 N	$1.24 \cdot 10^{-3}$	$9.29 \cdot 10^{-4}$	$1.08 \cdot 10^{-3}$	$8.11 \cdot 10^{-4}$
200 N	-	$1.22 \cdot 10^{-3}$	-	$1.16 \cdot 10^{-3}$

From the table above, it can be seen that none of the samples with Structure A core (Samples 1, 3, 5 and 7) reached a force of 200 N - the failure of the samples occurred earlier. Sample 1 without reinforcement of any resin layer did not even reach 150 N. The diagonal support gives a noticeable strengthening of the entire structure - all samples reached a force of 200 N, even Sample 2 without resin layers. From the reading for a force of 200 N, it can be seen that a layer of pure epoxy res-in gives a stiffening of the structure, and thus less deformation by 50% compared to PLA alone. It can also be noted that the 10% addition of carbon fiber powder reduces deformation relative to pure epoxy resin by 32% and relative to PLA alone by up to 66%. The addition of 20% powder reduced strain relative to the 10% addition by only 5%. Based on the results, the stiffness of each sample was calculated using Equation (1), $k=F/\delta$ (1) where: F [N] – force acting on the body, δ [mm] – the displacement produced by the force in the same direction. A graph was then drawn to show the change in stiffness of the specimen depending on the type of structure as well as the addition of the laminate layer. The results are shown in Figure 11.

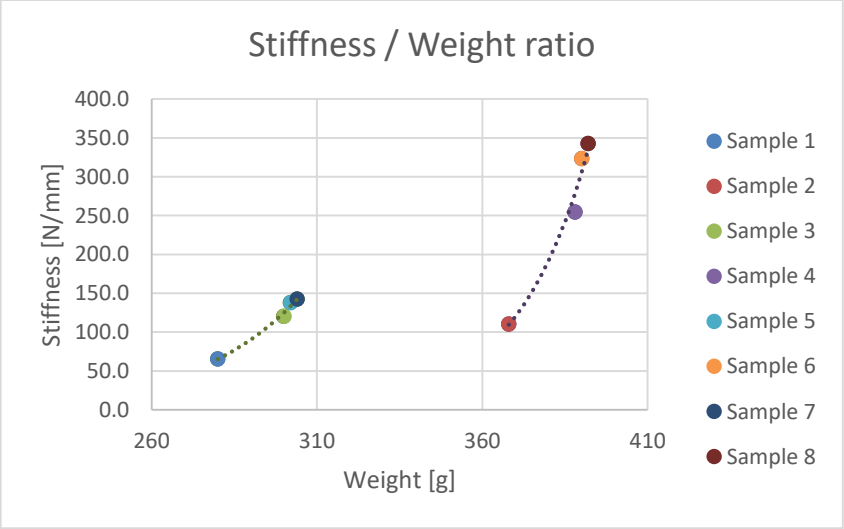

Figure 11: Stiffness to Weight Ratio of Each Sample

In the graph, it can be seen that samples having Structure A are characterized by lower weight, but also lower stiffness reaching an average value of 117 N/mm (points on the left side of the graph). Samples having Structure B are characterized by a higher weight, but also significantly higher stiffness reaching an average value of 258 N/mm (points on the right side of the graph). The average stiffness of samples with Structure B is as much as 120% higher than those with Structure A.

3.3 Material's Model Definition: Based on the reproduction of the results and readings from the strain gauges de-scribed in Section 3.2, the material properties for layers of epoxy resin and resin with carbon fiber powder additives were defined. The value of Young's modulus was adjusted to obtain the strain values previously read from the strain gauges. The Figure 12 shows the results obtained for Sample 8. Result probes were placed around the place where the strain gauge was mounted on the sample. The 4 probes indicated a result of about 1.16•10-3 mm/mm, which was the target value for this sample.

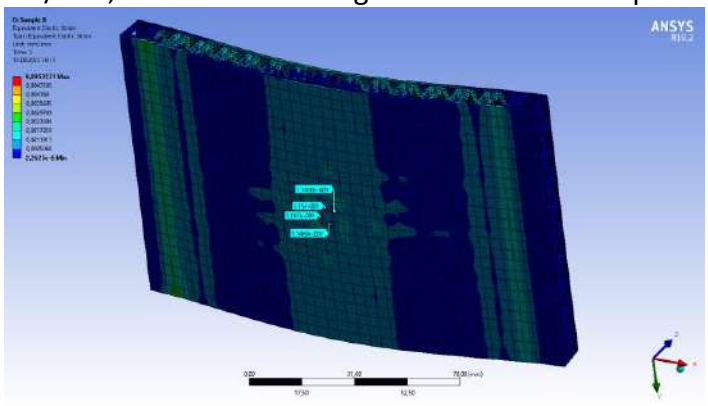

Figure 12: Strain Results for Sample 8

The density of the defined resin was calculated at 0.65 g/gm3, while the Poisson ratio was 0.33. The Young's modulus for each additive layer material is presented in Table 6.

Table 6: Young's Modulus Values Obtained for Each Material

Material	**Young's Modulus [GPa]**
No coating PLA	1.55
Pure epoxy resin LG700	1.20
LG700 + 10% carbon fiber powder	2.00
LG700 + 20% carbon fiber powder	2.25

From the above, it can be seen that the addition of carbon fiber powder to epoxy resin has a significant effect on raising the Young's modulus of the resulting material. The Young's modulus of the resin with 10% addition of carbon fiber powder is 67% higher than that of pure epoxy resin. On the other hand, the Young's modulus of the resin with 20% addition is 12.5% greater than that of the resin with 10% powder addition.

3.4 FEM Analysis of the Driver's Seat: FEA analysis resulted in von Mises-reduced stresses and deformation in the model. The results are shown in Figure 13 below.

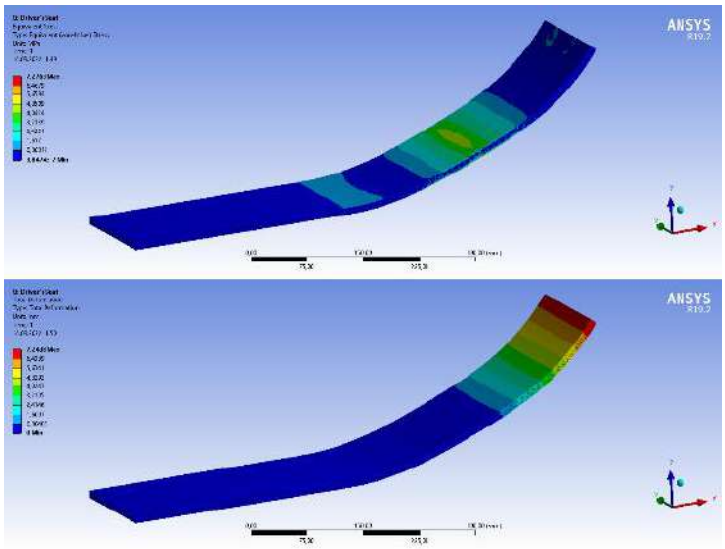

Figure 13: FEM Results For Driver's Seat – Top: Von Mises Stress, Bottom: Deformation

The maximum stress was 7.28 MPa and occurred in the core structure in the back support area. The stresses did not exceed the permissible values. The maximum de-formation was 7.24 mm. The obtained results imply, that they do not exceed safe values for these materials that is tensile strength, and can be adopted as a seat material. It should be noted that the seat designed in this way reduces the weight of the component by 172 g, a reduction of about 25% compared to a seat made entirely of PLA. Covering the driver's seat with a layer of epoxy resin laminate with the addition of carbon fiber powder provides sufficient strength to the component, while the ability to 3D print makes it possible to produce a personalized part for Greenpower's small electric car.

4. Discussion: In the above article, the authors presented novel CFRP sandwich structures using FDM 3D printing. The design of a scalable elementary unit used in an FDM printed core is presented. Two concepts of the elemental unit in a truss concept were present-ed - a simple one and one with an additional diagonal support. During further testing - both FEA and experimental by strain gauging, it was observed that the diagonal sup-port significantly increases the strength of the elementary unit as well as the entire structure in which it is used. During the initial FEA analysis, the properties of the structures were verified, and the possible benefits of successive layers of elementary units in the core were examined. In the following section, a method for manufacturing such structures is presented - 3D printing in FDM technology of a core of thermoplastic material, and then coating its outer layers with resin. Three different coating materials were tested - pure epoxy resin, resin with the addition of 10% and 20% carbon fiber powder. In an experimental study on a resistance strain gauge bench, the behavior of the structures under a force of 200 N was checked, as well as what deformations occur on the bottom surface of the component. From the results collected for a force of 200 N, it can be seen that a layer of pure epoxy resin gives a stiffening of the structure and thus less deformation by 50% compared to PLA alone. It was noted that 10% addition of carbon fiber powder reduces deformation relative to pure epoxy resin by 32%, and relative to PLA alone by as much as 66%. The addition of 20% powder reduced strain relative to the 10% addition by only 5%. The average stiffness of samples with Structure B is as much as 120% higher than those with Structure A. With the results collected, material parameters were reconstructed for individual layers of resin with additives, allowing these material models to be used in computerized strength testing of more complex geometries and components. As an example of the use of both the 3D printed CFRP sandwich structure fabrication technology with carbon fiber powder and the top layer material model, an FEM strength analysis of the Greenpower electric car driver's seat was conducted. In future studies, the authors plan to test other designed core structures produced using the technology described above and to test yet more coating materials.

References: Alshaer, A. W., & Harland, D. J. An investigation of the strength and stiffness of weight-saving sandwich beams with CFRP face sheets and seven 3D printed cores. Composite Structures, 2021, 257, 113391. https://doi.org/10.1016/j.compstruct.2020.113391

Alshaer, A. W., & Harland, D. J. An investigation of the strength and stiffness of weight-saving sandwich beams with CFRP face sheets and seven 3D printed cores. Composite Structures, 2021, 257, 113391. https://doi.org/10.1016/j.compstruct.2020.113391

Audibert, C., Chaves-Jacob, J., Linares, J. M., & Lopez, Q. A. Bio-inspired method based on bone architecture to optimize the structure of mechanical workspieces. Materials & Design, 2018, 160, 708-717. https://doi.org/10.1016/j.matdes.2018.10.013

Baier, A., Zur, P., Kolodziej, A., Konopka, P., & Komander, M. Studies on optimization of 3D-printed elements applied in Silesian Greenpower vehicle. In IOP Conference Series: Materials Science and Engineering, 2018, 400(2), 022010. https://doi.org/10.1088/1757-899X/400/2/022010

Bodaghi, M., Serjouei, A., Zolfagharian, A., Fotouhi, M., Rahman, H., & Durand, D. Reversible energy absorbing meta-sandwiches by FDM 4D printing. International Journal of Mechanical Sciences, 2020, 173, 105451. https://doi.org/10.1016/j.ijmecsci.2020.105451

Dey, A., & Yodo, N. A systematic survey of FDM process parameter optimization and their influence on part characteris-tics. Journal of Manufacturing and Materials Processing, 2019, 3(3), 64. https://doi.org/10.3390/jmmp3030064

Dey, A., & Yodo, N. A systematic survey of FDM process parameter optimization and their influence on part characteris-tics. Journal of Manufacturing and Materials Processing, 2019, 3(3), 64. https://doi.org/10.3390/jmmp3030064

Dudek, P. F. D. M. FDM 3D printing technology in manufacturing composite elements. Archives of metallurgy and materials, 2013, 58(4), 1415-1418. https://doi.org/10.2478/amm-2013-0186

Dudescu, C., & Racz, L. Effects of raster orientation, infill rate and infill pattern on the mechanical properties of 3D printed materials. ACTA Univ. Cibiniensis, 2017, 69(1), 23-30. https://doi.org/10.1515/aucts-2017-0004

Fernandez-Vicente, M., Calle, W., Ferrandiz, S., & Conejero, A. Effect of infill parameters on tensile mechanical behavior in desktop 3D printing. 3D printing and additive manufacturing, 2016, 3(3), 183-192. https://doi.org/10.1089/3dp.2015.0036

Fiał, C., & Pieknik, M. Druk 3D jako technologia przyszłości–część 1. Technologia i Jakość Wyrobów, 2020, 65.

Garzon-Hernandez, S., Garcia-Gonzalez, D., Jérusalem, A., & Arias, A. Design of FDM 3D printed polymers: An experi-mental-modelling methodology for the prediction of mechanical properties. Materials & Design, 2020, 188, 108414. https://doi.org/10.1016/j.matdes.2019.108414

Hao W., Liu Y., Zhou, Chen H. H., Fang D.: Preparation and characterization of 3D printed continuous carbon fiber rein-forced thermosetting composite, Polymer Testing 65, 2018, p. 29-34. https://doi.org/10.1016/j.polymertesting.2017.11.004

http://www.grm-systems.cz/pl/epoxy [accessed 7.09.2022]

https://www.easycomposites.eu/milled-carbon-fibre-powder [accessed 7.09.2022]

Hu, T., Wang, J., Wang, J., & Chen, R. Electromagnetic interference shielding properties of carbonyl iron powder-carbon fiber felt/epoxy resin composites with different layer angle. Materials Letters, 2015, 142, 242-245. https://doi.org/10.1016/j.matlet.2014.12.026

Khosravani, M. R., Zolfagharian, A., Jennings, M., & Reinicke, T. Structural performance of 3D-printed composites under various loads and environmental conditions. Polymer testing, 2020, 91, 106770. https://doi.org/10.1016/j.polymertesting.2020.106770

Kołodziej, A.; Żur, P.; Borek, W. Influence of 3D-printing Parameters on Mechanical Properties of PLA defined in the Static Bending Test. Eur. J. Eng. Sci. Technol. 2019, 2, 65–70.

Kowalewski Z., Szymczak T., Podstawy tensometrii elektrooporowej oraz praktyczne jej zastosowania, Dziewiętnaste Se-minarium Nieniszczące Badania Materiałów Zakopane, Poland, 12-13 March 2013

Kwon, D. J., Kim, J. H., DeVries, K. L., & Park, J. M. Optimized epoxy foam interface of CFRP/Epoxy Foam/CFRP sandwich composites for improving compressive and impact properties. Journal of Materials Research and Technology, 2021, 11, 62-71. https://doi.org/10.1016/j.jmrt.2021.01.015

Lalegani Dezaki, M., & Mohd Ariffin, M. K. A. The effects of combined infill patterns on mechanical properties in FDM process. Polymers, 2020, 12(12), 2792. https://doi.org/10.3390/polym12122792

Lionetto, F., Moscatello, A., & Maffezzoli, A. Effect of binder powders added to carbon fiber reinforcements on the chemoreology of an epoxy resin for composites. Composites Part B: Engineering, 2017, 112, 243-250. https://doi.org/10.1016/j.compositesb.2016.12.031

Liu, Z., Lei, Q., & Xing, S. Mechanical characteristics of wood, ceramic, metal and carbon fiber-based PLA composites fabri-cated by FDM. Journal of Materials Research and Technology, 2019, 8(5), 3741-3751. https://doi.org/10.1016/j.jmrt.2019.06.034

Lubombo, C., & Huneault, M. A. Effect of infill patterns on the mechanical performance of lightweight 3D-printed cellular PLA parts. Materials Today Communications, 2018, 17, 214-228. https://doi.org/10.1016/j.mtcomm.2018.09.017

Mazzanti, V., Malagutti, L., & Mollica, F. FDM 3D printing of polymers containing natural fillers: A review of their mechan-ical properties. Polymers, 2019, 11(7), 1094. https://doi.org/10.3390/polym11071094

Mei, J., Liu, J., & Huang, W. Three-point bending behaviors of the foam-filled CFRP X-core sandwich panel: Experimental investigation and analytical modelling. Composite Structures, 2022, 284, 115206. https://doi.org/10.1016/j.compstruct.2022.115206

Mei, J., Tan, P. J., Bosi, F., Zhang, T., Liu, J. Y., Wang, B., & Huang, W. Fabrication and mechanical characterization of CFRP X-core sandwich panels. Thin-Walled Structures, 2021, 158, 107144. https://doi.org/10.1016/j.tws.2020.107144

Melnikova, R., Ehrmann, A., & Finsterbusch, K. 3D printing of textile-based structures by Fused Deposition Modelling (FDM) with different polymer materials. IOP conference series: materials science and engineering, 2014, 62(1), 012018. https://doi.org/10.1088/1757-899X/62/1/012018

Miłek, M. Metrologia elektryczna wielkości nieelektrycznych. Uniwersytet Zielonogórski, Zielona Góra, Poland, 2006

Nowak, A., Baier, A., Kołodziej, A., & Żur, P. (2021, October). Race car mirror cover production focused on reducing air drag. IOP Conference Series: Materials Science and Engineering, 2021, 1182(1), 012055. https://doi.org/10.1088/1757-899X/1182/1/012055

Podroužek, J., Marcon, M., Ninčević, K., & Wan-Wendner, R. Bio-inspired 3D infill patterns for additive manufacturing and structural applications. Materials, 2019, 12(3), 499. https://doi.org/10.3390/ma12030499

Popescu, D., Zapciu, A., Amza, C., Baciu, F., & Marinescu, R. FDM process parameters influence over the mechanical properties of polymer specimens: A review. Polymer Testing, 2018, 69, 157-166. https://doi.org/10.1016/j.polymertesting.2018.05.020

Sajadi, S. M., Owuor, P. S., Schara, S., Woellner, C. F., Rodrigues, V., Vajtai, R., ... & Ajayan, P. M. Multiscale geometric design principles applied to 3D printed schwarzites. Advanced Materials, 2018, 30(1), 1704820. https://doi.org/10.1002/adma.201704820

Saufi, S. A. S. A., Zuhri, M. Y. M., Dezaki, M. L., Sapuan, S. M., Ilyas, R. A., As' arry, A., ... & Bodaghi, M. Compression Behaviour of Bio-Inspired Honeycomb Reinforced Starfish Shape Structures Using 3D Printing Technology. Polymers, 2021, 13(24), 4388. https://doi.org/10.3390/polym13244388

Schmitt, M., Mehta, R. M., & Kim, I. Y. Additive manufacturing infill optimization for automotive 3D-printed ABS compo-nents. Rapid Prototyping Journal, 2019. https://doi.org/10.1108/RPJ-01-2019-0007

Sebaey, T. A., & Mahdi, E. Crushing behavior of a unit cell of CFRP lattice core for sandwich structures' application. Thin-Walled Structures, 2017, 116, 91-95. https://doi.org/10.1016/j.tws.2017.03.016
Solomon, I. J., Sevvel, P., & Gunasekaran, J. A review on the various processing parameters in FDM. Materials Today: Pro-ceedings, 2021, 37, 509-514. https://doi.org/10.1016/j.matpr.2020.05.484
Tao, Y., Li, P., Zhang, H., Shi, S. Q., Zhang, J., & Yin, Q. Compression and flexural properties of rigid polyurethane foam composites reinforced with 3D-printed polylactic acid lattice structures. Composite Structures, 2022, 279, 114866. https://doi.org/10.1016/j.compstruct.2021.114866
Tian, X., Liu, T., Yang, C., Wang, Q., & Li, D. Interface and performance of 3D printed continuous carbon fiber reinforced PLA composites. Composites Part A: Applied Science and Manufacturing, 2016, 88, 198-205. https://doi.org/10.1016/j.compositesa.2016.05.032
Vedrtnam, A. Novel method for improving fatigue behavior of carbon fiber reinforced epoxy composite. Composites Part B: Engineering, 2019, 157, 305-321. https://doi.org/10.1016/j.compositesb.2018.08.062
Zhang, G., Ma, L., Wang, B., & Wu, L. Mechanical behaviour of CFRP sandwich structures with tetrahedral lattice truss cores. Composites Part B: Engineering, 2012, 43(2), 471-476. https://doi.org/10.1016/j.compositesb.2011.11.017
Zhang, J., & Yanagimoto, J. Design of bendable sandwich sheets with 3D printed CFRP cores via multi-stage topology optimization. Composite Structures, 2022, 287, 115372. https://doi.org/10.1016/j.compstruct.2022.115372
Żur, A., Żur, P., Michalski, P., & Baier, A. Preliminary Study on Mechanical Aspects of 3D-Printed PLA-TPU Composites. Materials, 2022, 15(7), 2364. https://doi.org/10.3390/ma15072364
Żur, P., Kołodziej, A., & Baier, A. Finite elements analysis of PLA 3D-printed elements and shape optimization. European Journal of Engineering Science and Technology, 2019, 2(1), 59-64. https://doi.org/10.33422/EJEST.2019.01.51
Żur, P., Kołodziej, A., Nowak, A., & Baier, A. Manufacturing A Personalised Composite Material Driver's Seat. International Journal of Modern Manufacturing Technologies, 2021, 13(3), 191-196. https://doi.org/10.54684/ijmmt.2021.13.3.191

Automated Dimension Measurement and Surface Defect Detection of Cast Metal Parts Using Computer Vision and Deep Learning

George Kyriakidis
Department of Data Science, Quintessential SFT, Athens, Greece

Alexandros Daskalakis
Quintessential SFT, Athens, Greece

Abstract: This paper presents a comprehensive method for detecting the centers of mounting holes in cast metal parts using computer vision and surface defects using deep learning. The proposed approach involves camera calibration, hole detection algorithm, and deep learning model for defect detection. The camera calibration is performed using a checkerboard image to correct projection effects and radial distortion. The hole detection algorithm accurately detects the centers of mounting holes in sub-pixel level accuracy by comparing the generated graph with a reference graph. The deep learning model, based on fine-tuned DETR architecture, successfully detects surface defects in metal parts. Experimental results demonstrate the effectiveness of the proposed method in accurately detecting mounting holes and surface defects.
Keywords: Quality Control, Deep Learning, Computer Vision, Defect Detection

1. Introduction: In this paper, we propose a method consisting of a computer vision algorithm for detecting the centers of mounting holes in metal parts and measuring their distances, as well as a deep learning model for detecting surface defects. The proposed method combines camera calibration, hole detection algorithms, and deep learning techniques to achieve accurate and efficient detection and measurement.

1.1 Background: In the field of manufacturing, automated quality control has gained significant attention due to its potential for cost reduction, high accuracy in defect detection, and system stability over time. Traditional methods for defect detection, such as computer vision, have limitations when it comes to detecting surface defects on metallic parts due to the surface texture and curvature (Çerezci et al., 2020). Deep learning techniques have emerged as a promising approach for defect detection, as they can learn complex patterns and features from large datasets (Martin et al., 2022). However, the accurate detection of mounting holes in metal parts using computer vision algorithms remains a challenge.

1.2 Motivation: The accurate detection of mounting holes in metal parts is crucial for various industrial applications, such as automotive manufacturing and electronics assembly. Traditional methods for hole detection rely on manual inspection, which is time-consuming and prone to errors. Therefore, there is a need for an automated and efficient method that can accurately detect the centers of mounting holes in metal parts.

1.3 Objectives: The main objective of this research is to develop a method that utilizes computer vision algorithms to detect the centers of mounting holes in metal parts and measure their distances accurately. Additionally, the research aims to develop a deep learning model for detecting surface defects on the metal surfaces. The proposed method will provide a comprehensive solution for quality control in manufacturing processes, enabling faster and more accurate detection of mounting holes and surface defects. To achieve these objectives, the proposed method incorporates camera calibration techniques to ensure accurate image acquisition (Jiang et al., 2011). The hole detection algorithm utilizes sub-pixel level accuracy to detect the centers of mounting holes (Lv et al., 2020). The deep learning model is trained using annotated datasets of surface defects to accurately identify and classify defects on metal surfaces (Çerezci et al., 2020; Martin et al., 2022). The combination of computer vision algorithms and deep learning techniques will provide a robust and efficient solution for detecting mounting holes and surface defects in metal parts. In the following sections, we will discuss the methodology, experimental results, and implications of the proposed method, highlight limitations, and suggest future research directions.

2. Related Work:

2.1 Computer Vision for Hole Detection: Computer vision techniques have been widely explored for hole detection in various applications. Traditional methods often rely on handcrafted features and image processing algorithms to identify and locate holes. However, these methods may struggle with accuracy and robustness when dealing with complex surfaces and varying lighting conditions (Feng et al., 2020). Recent advancements in computer vision have shown promising results in hole detection tasks. For instance, (Feng et al., 2020) proposed a subpixel computer vision detection method based on wavelet transform, which improved the accuracy of hole detection.

2.2 Deep Learning for Surface Defect Detection: Deep learning has emerged as a powerful approach for surface defect detection, surpassing traditional machine vision methods in terms of accuracy and performance (Tabernik et al., 2019). Deep learning models, such as convolutional neural networks (CNNs), have been successfully applied to detect and classify surface defects in various industries, including steel manufacturing and semiconductor inspection (Dey et al., 2022; Ye et al., 2018). These models can automatically learn discriminative features from large datasets, enabling them to detect subtle defects and generalize well to different defect types (Tabernik et al., 2019). For example, (Dey et al., 2022) demonstrated the application of Mask-RCNN, a deep-learning algorithm, to semiconductor defect inspection, achieving improved defect detection and classification.

3. Methodology:

3.1 Camera Calibration: Camera calibration is a critical step in ensuring accurate image acquisition for subsequent analysis. In this study, we employed a checkerboard image acquisition technique to calibrate the camera. The checkerboard pattern provides a known reference that allows for the calibration of the camera. By capturing images of the checkerboard pattern displayed on a retina monitor, we obtained a set of images that were used for subsequent calibration steps.

3.1.1 Checkerboard Image Acquisition: To acquire the checkerboard images, we carefully positioned the camera to capture the entire checkerboard pattern (Figure 1). Multiple images were captured from different angles and positions to ensure comprehensive coverage of the pattern. The acquired images were then used for camera calibration.

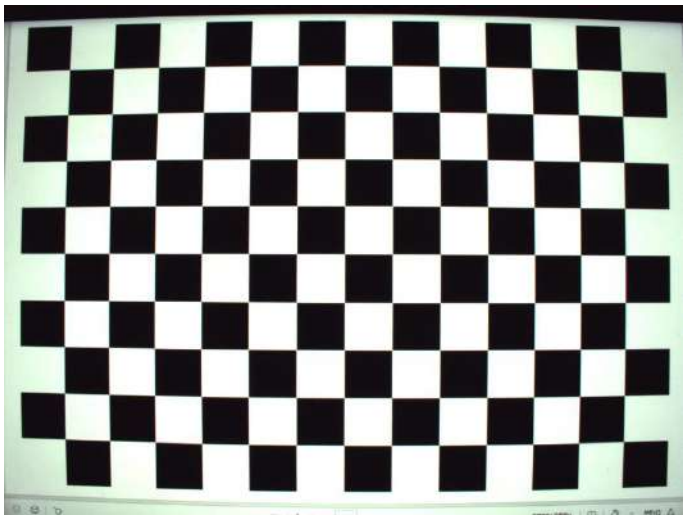

Figure 1: Checkerboard image captured using the camera

3.1.2 Projection Effect Correction: Projection effects can introduce distortions in the acquired images, affecting the accuracy of subsequent measurements. To correct for projection effects, we applied correction techniques to the acquired images. This correction step involved compensating for the perspective distortion caused by the camera's position and angle relative to the object being imaged. By applying appropriate correction algorithms, we were able to rectify the acquired images and minimize the impact of projection effects on subsequent analyses.

3.1.3 Radial Distortion Correction: Radial distortion is another common type of distortion that can affect the accuracy of measurements. It occurs due to the non-linear mapping of light rays passing through the camera lens. To correct for radial distortion, we employed algorithms that estimate the distortion parameters and apply the necessary corrections. By compensating for radial distortion, we were able to improve the accuracy of subsequent measurements and ensure more precise detection of mounting holes and surface defects.

3.1.4 Camera Calibration using discorpy: To achieve accurate camera calibration, we utilized the discorpy Python library. Discorpy provides a comprehensive set of tools and functions for camera calibration, including intrinsic and extrinsic parameter estimation. By utilizing discorpy, we were able to calibrate the camera using the acquired checkerboard images (Figure 2). The calibration process involved estimating the intrinsic parameters (e.g., focal length, principal point) and extrinsic parameters (e.g., camera position and orientation) of the camera. This calibration step ensured that subsequent measurements and analyses were performed with a properly calibrated camera, enhancing the accuracy and reliability of the results.

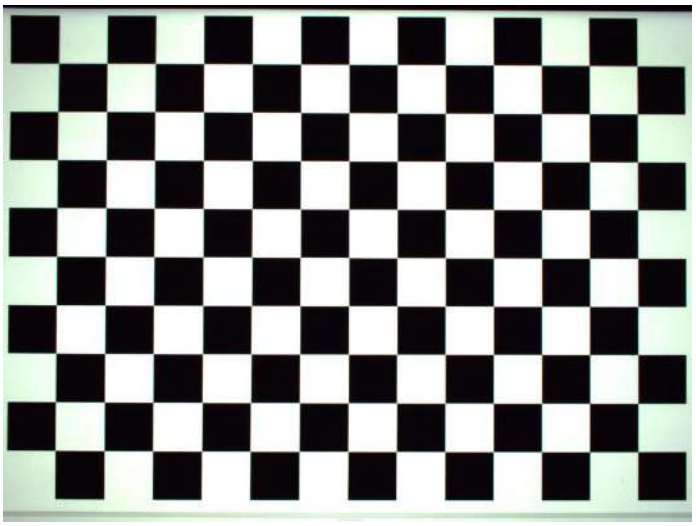

Figure 2: Calibrated checkerboard image

3.2 Mounting Hole Detection Algorithm: The mounting hole detection algorithm aims to accurately detect the centers of mounting holes in the cast metal parts. The algorithm consists of several steps, as described below.

3.2.1 Image Acquisition of Cast Metal Parts: Images of the cast metal parts, specifically passive coolers for automotive hifi systems, were acquired using the calibrated camera. These images served as input for the mounting hole detection algorithm. After the images are corrected for distortion and projection errors, their contrast is increased to make the detection of mounting holes easier (Figure 3).

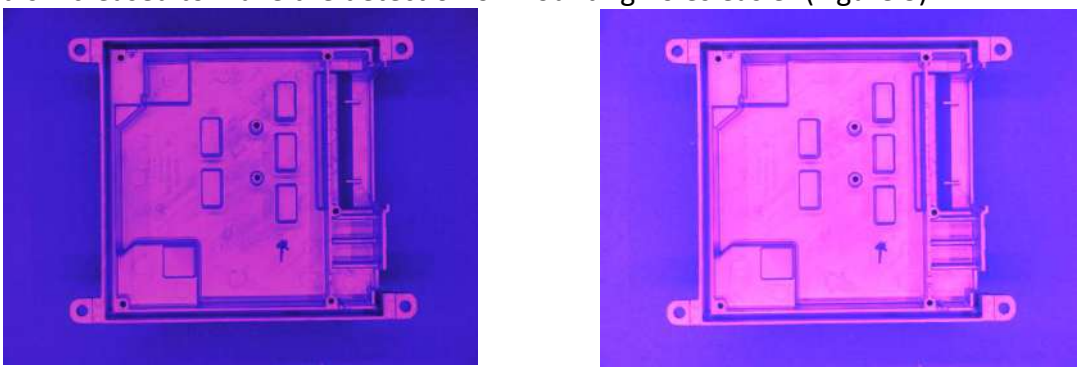

Figure 3: Original (left) and high contrast (right) image

3.2.2 Outer Hole Detection and Reprojection: The algorithm first focuses on detecting the outer mounting holes, which are located at the outermost corners of the square part. By analyzing the acquired images, the algorithm identifies the outer holes and reprojects the square defined by their centers (Figure 4). This reprojection step allows for more accurate measurement of the distances between the inner holes.

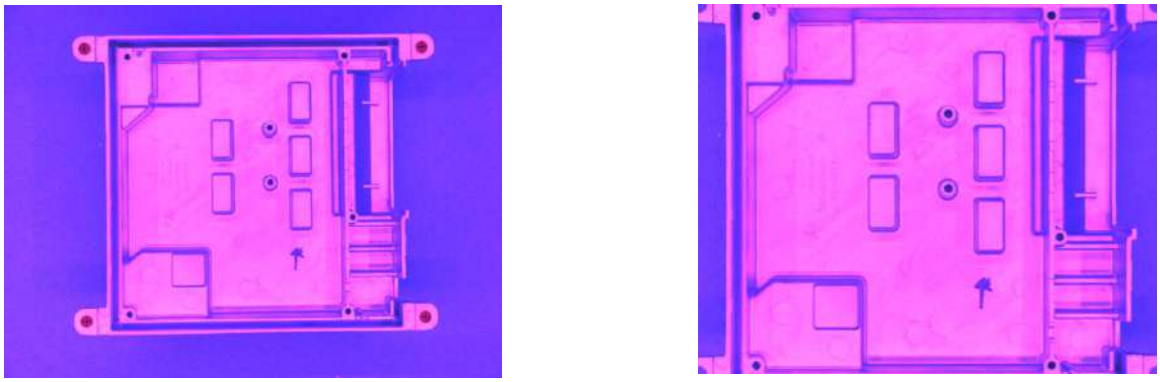

Figure 4: Outer hole detection (left) and re-projeciton (right)

3.2.3 Inner Hole Distance Measurement: Once the outer holes are detected and reprojected, the algorithm measures the distances between the inner holes. This is achieved by analyzing the reprojected square and calculating the distances between the centers of the inner holes. The algorithm considers the known dimensions of the mounting holes and uses geometric calculations to determine the distances accurately. To achieve high accuracy in hole center detection, the algorithm utilizes sub-pixel level accuracy techniques. Traditional image processing techniques often provide pixel-level accuracy, which may not be sufficient for precise hole detection. By employing advanced image processing and feature extraction methods, such as edge detection and sub-pixel interpolation, the algorithm can precisely locate the centers of the mounting holes in the acquired images. This sub-pixel level accuracy ensures more accurate measurements and enhances the overall performance of the mounting hole detection algorithm. To determine whether a part is defective or not, the algorithm compares the generated graph, where each node represents a detected hole center, with a reference graph. The reference graph contains ideal x and y coordinates for each hole center. By comparing the detected hole centers with the reference graph, the algorithm can assess the accuracy of the hole detection and flag any deviations as potential defects. Assuming that the dimensions of the detected holes are within a certain tolerance of the nominal values, the part is flagged as non-defective. This graph comparison approach provides a reliable and objective criterion for defect flagging, ensuring the accuracy and consistency of the defect detection process (Figure 5).

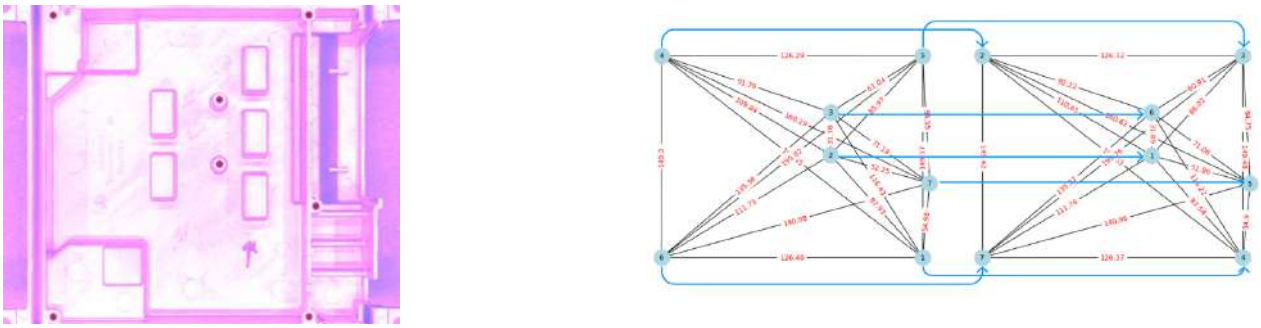

Figure 1: Inner hole detection (top) and graph comparison (bottom)

3.3 Deep Learning Model for Surface Defect Detection: In addition to mounting hole detection, a deep learning model was developed for surface defect detection on the metal parts. The methodology for developing the deep learning model is as follows:

3.3.1 Dataset Preparation and Annotation: A dataset of images of the metal parts with surface defects was prepared. The dataset included various types of defects, such as wrinkles and stains, to ensure the model's ability to detect a wide range of surface anomalies. The images were carefully selected to cover different defect severities and orientations. Each image in the dataset was annotated to indicate the presence and location of surface defects using VGG Image Annotator. The annotations provided ground truth information for training and evaluating the deep learning model.

3.3.2 Fine-tuning DETR Model: To detect surface defects, the DETR (Detection Transformer, Figure 6) model was chosen as the base architecture (Carion et al., 2020). The DETR model has shown promising performance in object detection tasks and is well-suited for our surface defect detection task. The pre-trained DETR model was fine-tuned using the annotated dataset of metal part images with surface defects. Fine-tuning allows the model to adapt to the specific defect detection task and learn to detect and classify surface defects accurately. By leveraging the pre-trained weights and fine-tuning on our dataset, we were able to expedite the training process and improve the model's performance.

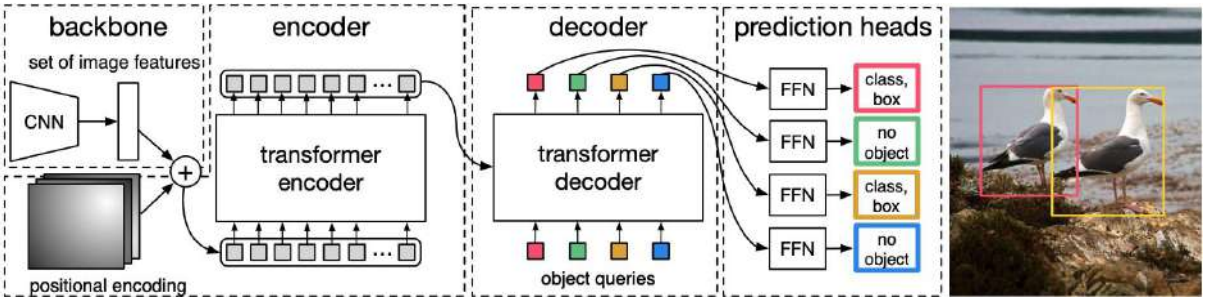

Figure 6: DETR architecture (Carion et al., 2020)

3.3.3 Training Set Augmentation: To improve the generalization and robustness of the deep learning model, data augmentation techniques were applied to the training set. Augmentation involves applying various transformations to the training images, such as horizontal and vertical flipping, rotation, and scaling. These transformations help the model learn to detect defects from different perspectives and orientations, making it more robust to variations in the appearance of surface defects. By augmenting the training set, we were able to increase the diversity of the data and improve the model's ability to generalize to unseen samples.
3.3.4 Model Training and Optimization: The fine-tuned DETR model was trained using the augmented dataset. The training process involved optimizing the model's parameters to minimize the detection loss and maximize the accuracy of defect detection. The AdamW optimizer was employed (Loshchilov & Hutter, 2017), which combines the benefits of adaptive learning rates and weight decay regularization to improve the convergence and generalization of the model. The model was trained for a total of 4000 epochs, with a batch size of 4, to ensure sufficient exposure to the training data and convergence to an optimal solution.
3.3.5 Model Evaluation: To evaluate the performance of the deep learning model, mean average precision with 50% overlap (mAP-50) was used as the evaluation metric. mAP-50 measures the precision and recall of the model's predictions, considering the overlap between the predicted bounding boxes and the ground truth annotations. A higher mAP-50 score indicates better performance in detecting surface defects with high precision and recall. By evaluating the model using mAP-50, we were able to assess its ability to accurately detect and classify surface defects and compare its performance against other state-of-the-art models.

4. Experimental Results:

4.1 Camera Calibration Results: The camera calibration process was conducted using the checkerboard image acquisition technique and the discorpy library (Vo et al., 2015). The acquired checkerboard images were used to estimate the intrinsic and extrinsic camera parameters. The calibration results demonstrated the effectiveness of the calibration process in correcting projection effects and radial distortion. The calibrated camera exhibited improved accuracy and reduced distortions, ensuring more precise measurements in subsequent analyses.

4.2 Mounting Hole Detection Results: The mounting hole detection algorithm was applied to the acquired images of cast metal parts. The algorithm successfully detected the centers of the mounting holes with sub-pixel level accuracy. The distances between the inner holes were accurately measured, and the algorithm compared the generated graph with a reference graph to flag any potential defects. The experimental results showed that the algorithm achieved high accuracy in detecting the mounting holes and effectively flagged defective parts.

4.3 Surface Defect Detection Results: The deep learning model for surface defect detection was trained and evaluated using the annotated dataset of metal part images with surface defects. The model achieved promising results in detecting the various types of surface defects, such as wrinkles and stains. The evaluation metric, mAP-50, indicated the model's ability to accurately detect and classify surface defects with high precision (95.5%) and recall (96%) with an mAP-50 score of 20. The experimental results demonstrated the effectiveness of the deep learning model in detecting surface defects and its potential for industrial

applications.

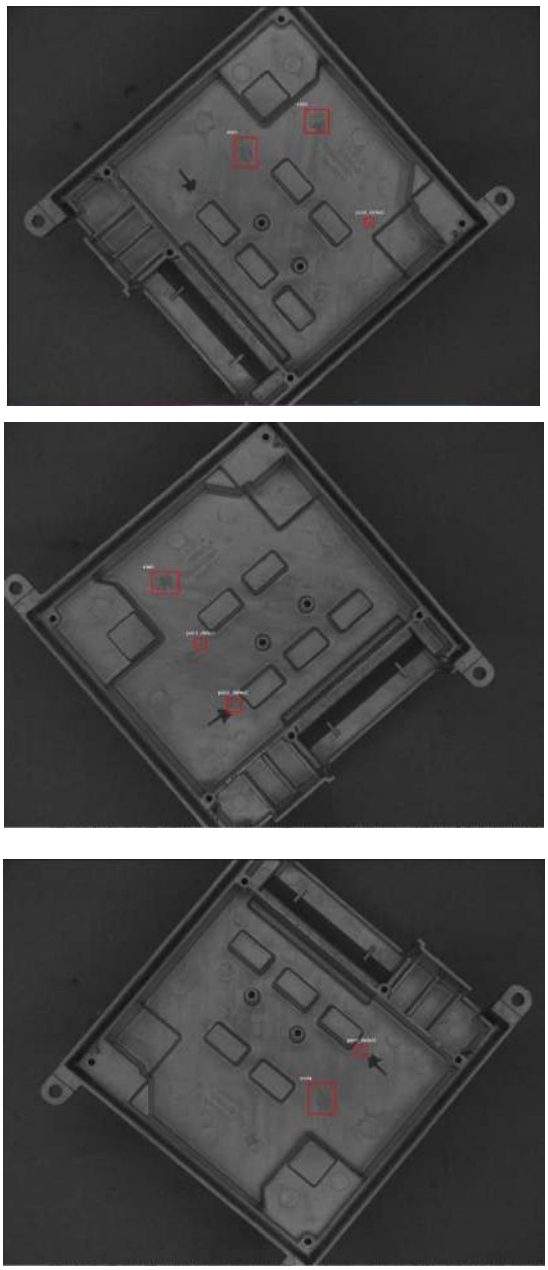

Figure 7: Three instances of defect detection. Note that under certain angles the model is not able to consistently detect all defects

5. Limitations and Future Work: While the proposed method showed promising results, there are some limitations that should be addressed in future work. One limitation is the reliance on annotated datasets for training the deep learning model. Acquiring and annotating large-scale datasets can be time-consuming and resource intensive. Additionally, the proposed method may have limitations in detecting certain types of surface defects under certain angles that exhibit low contrast or complex textures. Further research could focus on improving the robustness of the deep learning model and expanding the dataset to include a wider range of defect types and variations.

6. Conclusion:

6.1 Summary of Contributions: In this study, we presented a comprehensive method for detecting mounting holes in metal parts using computer vision algorithms and surface defects using a deep learning model. The camera calibration process ensured accurate image acquisition, and the mounting hole detection algorithm

achieved sub-pixel level accuracy in detecting the centers of mounting holes. The deep learning model demonstrated high accuracy in detecting various surface defects. The proposed method contributes to the field of automated quality control in manufacturing processes, providing a robust and efficient solution for detecting mounting holes and surface defects.

6.2 Implications and Applications: The proposed method has significant implications for various industries, including automotive manufacturing, electronics assembly, and quality control. Accurate detection of mounting holes and surface defects is crucial for ensuring product quality and reliability. The integration of computer vision algorithms and deep learning techniques in the proposed method offers a reliable and efficient solution for automated quality control processes. The method can be applied in real-time inspection systems, improving productivity, and reducing manual inspection efforts. Furthermore, the methodology can be extended to other domains that require precise detection and measurement of features in complex surfaces.

7. Acknowledgements: This work has been co-financed by the European Union and Greek national funds through the Operational Program Competitiveness, Entrepreneurship and Innovation, under the call "RESEARCH – CREATE – INNOVATE" (project code: T2EDK-04162)

8. References: Carion, N., Massa, F., Synnaeve, G., Usunier, N., Kirillov, A., & Zagoruyko, S. (2020). Retrieved from https://arxiv.org/abs/2005.12872

ÇEREZCİ, F., KAZAN, S., Oz, M. A., Oz, C., Tasci, T., Hızal, S., & Altay, Ç. (2020). Online Metallic Surface Defect Detection Using Deep LearningOnline Metallic Surface Defect Detection Using Deep Learning. https://doi.org/10.21203/rs.3.rs-41274/v1

Dey, B., Dehaerne, E., Halder, S., Leray, P., & Bayoumi, M. A. (2022). Deep learning based defect classification and detection in sem images: A mask R-CNN approach. Metrology, Inspection, and Process Control XXXVI. https://doi.org/10.1117/12.2618178

Dong, H., Song, K., He, Y., Xu, J., Yan, Y., & Meng, Q. (2020). PGA-net: Pyramid feature fusion and global context attention network for automated surface defect detection. IEEE Transactions on Industrial Informatics, 16(12), 7448–7458. https://doi.org/10.1109/TII.2019.2958826

Feng, Y., Yang, T., & Niu, Y. (2020). Subpixel computer vision detection based on wavelet transform. IEEE Access, 8, 88273–88281. https://doi.org/10.1109/ACCESS.2020.2991846

Gou, G., Sui, H., Li, D., Peng, Z., Guo, B., Yang, W., & Huang, D. (2022). Limofilling: Local Information Guide Hole-filling and sharp feature recovery for manifold meshes. Remote Sensing, 14(2), 289. https://doi.org/10.3390/rs14020289

Liu, X., Tian, J., Kuang, H., & Ma, X. (2022). A stereo calibration method of multi-camera based on Circular Calibration Board. Electronics, 11(4), 627. https://doi.org/10.3390/electronics11040627

Loshchilov, I., & Hutter, F. (2019). Retrieved from https://arxiv.org/abs/1711.05101

Lv, X., Duan, F., Jiang, J.-J., Fu, X., & Gan, L. (2020a). Deep active learning for surface defect detection. Sensors, 20(6), 1650. https://doi.org/10.3390/s20061650

Martin, D., Heinzel, S., Kunze Von Bischhoffshausen, J., & Kühl, N. (2022). Deep learning strategies for industrial surface defect detection systems. Proceedings of the Annual Hawaii International Conference on System Sciences. doi:10.24251/hicss.2022.146. https://doi.org/10.24251/HICSS.2022.146

Tabernik, D., Šela, S., Skvarč, J., & Skočaj, D. (2019). Segmentation-based deep-learning approach for surface-defect detection. Journal of Intelligent Manufacturing, 31(3), 759–776. https://doi.org/10.1007/s10845-019-01476-x

Vo, N. T., Atwood, R. C., & Drakopoulos, M. (2015). Radial lens distortion correction with sub-pixel accuracy for X-ray micro-tomography. Optics Express, 23(25), 32859. https://doi.org/10.1364/OE.23.032859

Ye, J., Ito, S., & Toyama, N. (2018). Computerized ultrasonic imaging inspection: From shallow to Deep Learning. Sensors, 18(11), 3820. https://doi.org/10.3390/s18113820

Zetao Jiang, Lianggang Jia, & Shutao Guo. (2011). Research on camera self-calibration of highprecision in Binocular Vision. 2011 5th International Conference on Application of Information and Communication Technologies (AICT). https://doi.org/10.1109/ICAICT.2011.6111011

Casale Monferrato Remediation: Asbestos Pollution and Safety Measures to Protect Workers and Environment

Federica Paglietti
Department of new Technologies for Occupational Safety of Industrial Plants, Products and Human Settlements, INAIL -
Italian Workers' Compensation Authority - Research Division, Rome, Italy

Paolo De Simone
INAIL - Italian Workers' Compensation Authority - Research Division - Department of new Technologies for Occupational Safety of Industrial Plants, Products and Human Settlements, 00143 Roma RM, Via Roberto Ferruzzi, Italy

Sergio Malinconico
INAIL - Italian Workers' Compensation Authority - Research Division - Department of new Technologies for Occupational Safety of Industrial Plants, Products and Human Settlements, 00143 Roma RM, Via Roberto Ferruzzi, Italy

Sergio Bellagamba
INAIL - Italian Workers' Compensation Authority - Research Division - Department of new Technologies for Occupational Safety of Industrial Plants, Products and Human Settlements, 00143 Roma RM, Via Roberto Ferruzzi, 38/40, Italy

Abstract: Asbestos is a natural hazardous substance, which cause an environmental pollution creating a significant impact on human health. Asbestos has long been produced and marketed worldwide for its insulating, fireproof, chemical, and sound-absorbing and tensile strength. Because of its excellent and numerous characteristics it has been widely used, and in some Countries it still is, leaving behind serious health problems as well as complex remediation and management of asbestos containing waste (ACW). Asbestos is considered one of the most harmful occupational carcinogens causing more than 100,000 deaths per year and exposure to airborne asbestos fibers is held responsible for half of the deaths from occupational cancer (caused by mesothelioma, asbestos-related cancer and asbestosis). Because of this, this substance is now banned in 52 Countries, including Italy, which prohibited the extraction, and marketing of asbestos in 1992. Many areas have therefore been identified in this European Country as highly contaminated by asbestos. Among them also the area of Monferrato, which includes the Municipality of Casale Monferrato and 46 neighboring municipalities. The Eternit asbestos cement plant, located in the municipality of Casale, caused the contamination. The aim of this paper is to describe the complex remediation activities conducted in this wide area, located in northern Italy, highlighting the main phases and the most important issues during the remediation execution; moreover the purpose is to recall the appropriate prevention and protection measures to adopt to prevent new asbestos exposures and to emphasize their importance. This study can serve as an important reference for the academic participants involved in this field at European or international level.
Keywords: Asbestos, Remediation, Pollution, Safety measures

1. Introduction: In recent years, the media has brought to the forefront worldwide the issue of asbestos, highlighting various health and environmental concerns. The term "asbestos" refers to a group of minerals (Chrysotile, Crocidolite, Amosite, Tremolite, Anthophyllite, and Actinolite) whose commercial success has been determined by their unique technical characteristics, which are considered "unparalleled." These minerals are capable of withstanding fire, heat, chemical and biological agents, abrasion, and wear. They are also easily woven, possess sound-absorbing and thermal insulating properties, and readily bond with other substances such as lime, plaster, cement, and certain polymers like rubber and PVC. Due to their technical characteristics and low cost, various mixtures incorporating asbestos, primarily with cement, plastics, bitumen, and paints, were developed, leading to the production of over three thousand types of asbestos-containing products (ACPs), with asbestos content ranging from 10% to 99% by weight. These materials were mainly used in sectors such as shipbuilding, railway rolling stock, metallurgy, steelmaking, metalworking, automotive industry, military industry, asbestos-cement industry, construction, sugar refineries, agriculture, oil refineries, textiles, and the glass industry. The Industrial activity had a notable boost in the post-war era, during which asbestos was considered a strategic material. Estimated global consumption of asbestos minerals is currently around 1 million tonnes, mainly for asbestos-cement products. Chrysotile accounted in the past for more than 85% of all asbestos extracted and is at present mined and used predominantly in Asia and Eastern Europe. In recent years, the world leaders in the production of asbestos have been Russia, China, Brazil, Kazakhstan and India, while China is the first world consumer, with 570,000 tons used in 2015. The asbestos extraction by these countries has been declining sharply, although the natural reserves remain enormous. The extraction of the mineral by these mentioned countries has been sharply declining, while the natural reserves of the mineral still remain enormous.

Table 1: *Global Production and Mineral Reserves in Tonnes (U.S. Geological Survey, Mineral Commodity Summaries, January 2022)*

World Mine Production and Reserves:

	Mine production[e]		Reserves[8]
	2020	2021	
United States	—	—	Small
Brazil	[9]71,200	110,000	11,000,000
China	120,000	120,000	95,000,000
Kazakhstan	[10]227,000	250,000	Large
Russia	720,000	700,000	110,000,000
Zimbabwe	8,000	10,000	Large
World total (rounded)	1,100,000	1,200,000	Large

Many epidemiological studies have demonstrated the carcinogenicity of these fibers, and as a result, it has been classified by European legislation (Regulation EC 1272/2008 concerning the "Classification, Labeling, and Packaging of Substances and Mixtures" - Table 1) into:

•Hazard Category 1A - known to be carcinogenic to humans, classification largely supported by human evidence:

•Hazard Category STOT RE 1 - specific target organ toxicity, upon repeated exposure.

The hazard statements are:

•H350: may cause cancer;

•H372: causes damage to organs through prolonged or repeated exposure.

As a consequence, asbestos has left behind numerous problems related not only to health aspects but also concerning the remediation activities and disposal of Asbestos-Containing Waste (ACW).

2. Context: **2.1. International legislation**: Many countries have already banned the extraction and commercialization of asbestos (European Union, Japan, etc.) and are now engaged in remediation actions and management of Asbestos-Containing Waste (ACW). Historically, Europe has heavily utilized this substance, to the extent that between 1920 and 2000, it used over 50% of the asbestos commercially traded worldwide. Currently, it bears the largest global burden of asbestos-related diseases as a consequence of its extensive use and asbestos is the major cause of work-related cancer, with as much as 78 % of occupational cancers recognised in the Member States. Within the European Union, which represents only 13% of the world population, the majority of asbestos-related deaths have been recorded, accounting for approximately 56% of global mesothelioma deaths and 41% of asbestosis deaths. In this context, the European Commission has banned the commercialization and use of products or substances containing asbestos since 2005. Currently, the final discussion is taking place in Brussels regarding the future Directive of the European Parliament and of the Council amending Directive 2009/148/EC on the protection of workers from the risks related to exposure to asbestos at work. At present, it is still being optimized. The current text briefly states that, after a two-year implementation period, the new Occupational Exposure Limit (OEL) of 0.01 asbestos fibers per cm^3 will come into effect. After a transition period of six years, Member States will be required to use only electron microscopy, excluding phase-contrast optical microscopy, which is currently allowed. Later this six years, two options will be possible:

• reducing the asbestos limit value in air to 0.002 f/cm^3, excluding the counting of thin fibers (<0.2 µm),

•setting it at 0.01 f/cm^3 counting thin fibers (<0.2 µm). The regulation always emphasizes the importance of risk assessment, considering removal as the preferred option.

2.2. Italian legislation: In regards to Italy, it is important to note that in the past, approximately 3.7 million tonnes of raw asbestos produced between 1945 and 1992 were used, along with around 1.9 million tonnes of imported raw asbestos during the same period, considering it as a strategic material. However, exports declined due to competition from Canada, and production levels gradually decreased, ultimately ceasing in 1992 with the ban on the substance. Most of Italy's raw asbestos fibers were extracted from the Balangero

site in Turin, which was the largest asbestos mine in Europe, and the Emarese site in the Aosta Valley. Today, many asbestos-contaminated sites still remain, requiring significant remediation and disposal of ACW. Many facilities that produced asbestos were left highly contaminated by companies, and the Italian government had to undertake their remediation to protect the surrounding urban residential areas. Among them, the most emblematic and internationally renowned case is the Casale Monferrato production plant in Piedmont. The safe management of this remediation involved the collaboration of multiple public administrations (Ministry of Environment, Region, Municipalities, Local Health Authorities, Regional Environmental Protection Agencies, etc.) with the technical and scientific support of national scientific institutions. It represents a significant case study that has led to the redevelopment of the territory, including land use recovery, resulting in positive health, environmental, and economic outcomes.

2.3. Casale Monferrato case of study: In 1998, the Casale Monferrato site was declared a Superfund Site (SS) to remediate, encompassing the territory of 48 municipalities with a total area of 739 km². It housed the Eternit and Fibronit plants, which accounted for over 40% of the national production of asbestos-cement products. This led to both occupational and environmental exposure: workers were exposed to pollution within the production facilities or from the dispersion of fibers from the open-air storage of production waste materials. Further dispersion of fibers occurred during the transportation of raw asbestos from the station to the plant or finished products from the plant to general warehouses located on the other side of the city, using uncovered vehicles. Reuse of jute sacks, originally containing crocidolite, for mail or agricultural purposes also contributed to additional airborne exposure. Further improper exposures were generated by the transportation and laundering of work overalls at home, the cultivation of gardens or other recreational activities along the contaminated riverbank, the reuse of non-intact and unsellable waste materials, and the use of "polverino" (a waste powder derived from asbestos processing) received for free from the plant and reused as insulating material for attics or paving courtyards. Moreover, the degradation of asbestos-cement roofs, which were widely spread across the area, also posed an additional risk.

3. Research aim: Casale Monferrato remediation: The remediation of the SS site involved the removal of both friable and compact asbestos-containing materials. The main activities carried out were:

1. The remediation of the Eternit plant and surrounding areas;
2. The remediation of the "Polverino" (asbestos waste powder);
3. The remediation of the asbestos-cement roofing in public and private buildings.

4 Methodology: Inail scientific consultancy activity: INAIL, together with the Local Health Agency and Local Environmental Agency, has conducted several inspections in the Casale National Superfund Site, which have identified the main risk situations and also developed "unusual" remediation procedures specific to the environmental context; in fact the wide area extension and high level contamination required site specific evaluation and remediation actions not defined by law. INAIL has also produced technical-scientific advices following applied for this site and then endorsed by the Ministry of the Environment as general Guidelines for all asbestos Superfund remediations. Inail produced more than 20 specific advices, realized more than 20 on-site surveys and participate more than 50 administrative meeting with regional, local and Ministerial administration to define the best strategy to renovate the entire area. Considering the high amount of indication prescribed, here are reported synthetically only the main precautionary and safety indications provided for the remediation of Ex Piemontese area and to identify and quantify the “polverino” still in place.

4.1. Ex Piemontese Data collection and analysis procedures: The remediation concerned an area of approximately 16,000 square meters with the presence of residential and school urban settlements frequented by young people. The asbestos-containing material was found both in friable matrix and in highly fragmented compact matrix, at depths of up to 1.40 meters, with a quantity of approximately 14,000 cubic meters. Below are the main prescribed measures:

•Operate with static and dynamic enclosures, not exceeding 10,000 cubic meters, in order to allow sufficient air exchange.

•Access to the entire "Ex Piemontese" area must only be through the Personnel Decontamination Unit (PDU) located at the site entrance, following the correct entry/exit procedures.
•Appropriate PDUs and Material Decontamination Units (MDUs) must also be set up at the entrance of each individual confined area (work lot).
•After the remediation of each lot, the concentration of asbestos in the soil must always be verified to be < 1000 mg/kg through sampling and analysis at the bottom and walls of the excavation.
•In confined areas, a certification of reusability of the areas must be carried out if the asbestos concentration in the air does not exceed 0,002 f/cm3. Ambient air sampling should be performed using high-flow pumps at a rate of 8-10 liters per minute, with a minimum of 3000 liters sampled, using polycarbonate or mixed cellulose ester filters and analysis using a scanning electron microscope (SEM).
•The ACW (asbestos-containing waste), properly packaged in big bags, must be deposited, categorized and separated by E.E.R. codes, in a statically and dynamically confined temporary storage area.
•After the removal of contaminated material and certification of reusability of the remediated area, the excavation must be covered with a layer of clean soil of at least 20 cm before any potential reuse of the area.
•Wastewater from the PDU must undergo purification using filtering systems capable of retaining particles equal to or larger than 3 microns. Regarding wastewater discharge into the sewer system, the limit to be adopted is 100 f/cm3.
•Workers must wear personal protective equipment (PPE) during their entire stay within the work area and during all work phases, ensuring that the PPE is kept in full working condition or promptly replaced, even during visual inspections or preliminary activities.
•A specific vehicle washing platform must be provided and installed in the immediate vicinity of the site entrance. For the aforementioned platform, if water reuse is intended, a treatment unit must be included that, at the final stage, retains fibers larger than 3 microns. It is necessary to conduct periodic sampling to monitor the clogging state of these filters, followed by SEM analysis on a bi-weekly or monthly basis.
•Before leaving the "Ex Piemontese" area, all vehicles, especially those used for the handling of excavated soil, must undergo thorough cabin vacuuming using a vacuum cleaner with HEPA absolute filters and complete washing (not just the wheels) at the designated platform at the entrance.
•Proper decontamination procedures must be followed for all PPE, equipment, and vehicles that will be used outside the work area after completion of the work.

4.2. “Polverino”: detection procedure in attics: The peculiarity of the Casale Monferrato Superfund Site lies precisely in the use of asbestos dust as residual of factory production in out-door area paving or as insulation in the attics of private residences. This latter case has led to the contamination of high amount of buildings included in the mentioned 48 municipalities. Most of the “polverino” used in in-door areas has already been removed using static and dynamic confined area or permanently secured (where it was too much complicated to remove). However, numerous situations still remain to be verified if still contaminated or not; so, they pose a potential source of environmental contamination and risks for the local health agency surveyors involved in the controls. To this end, a safety procedure has been agreed upon for inspecting the attics of residential buildings by technicians from the regulatory authorities, aimed at detecting any remaining asbestos dust in place. The procedure includes, among other things:
•Using personal protective equipment (PPE) such as a category III coverall (with a non-woven fabric of class 3 o 4 o 5), gloves, and a full-face mask with a P3 filter.
•Using a portable vacuum cleaner with absolute filters to vacuum the specific coverall.
•Spraying water on the outside of the coverall when exiting the contaminated area.
•Operators wearing a double coverall that should be removed at the end of the sampling process, ensuring that it is rolled down and outwards to contain the contaminated part inside. The used coverall should be immediately packaged in a dedicated sealed bag for disposal on the ground as asbestos-contaminated waste. All exhausted PPE must be classified with the EER code 15.02.02* - Absorbents, filter materials, rags, and protective clothing contaminated with hazardous substances.
•Removing the plastic sheet protecting the platform at the end of the inspection and packaging it in a double

bag and subsequent big bags as soon as it reaches the ground.
•Closing and sealing the access point used for sampling to prevent the dispersion of friable materials in outdoor environments after completion of the operations. All materials used to seal the opening must be brought at the working height before the opening procedure.
•Managing and classifying the waste materials separately from the exhausted PPE. This procedure has been adopted by all local advisors assuring a higher safety level.

5. Findings: The remediation activities that involved both the Eternit and Fibronit plants and the surrounding areas, as well as various municipalities in the district, resulted in the remediation of a large part of the area. Specifically, the following asbestos-related materials were removed from the former industrial plants:
• Approximately 1,500 cubic meters of friable asbestos piles within the plants.
• 54,000 square meters of asbestos-cement roof, including 15,000 cubic meters of sheets that were disposed of in underground production and decantation basins, later buried and secured.
• 160,000 square meters of demolished surfaces.
• 12,000 cubic meters of friable asbestos from the right bank of the Po River, where an actual "asbestos beach" had formed due to the discharge channel of water from the nearby former industrial plants.
• 700,000 square meters of asbestos-cement roof coverings in public and private buildings. Furthermore, the remediation of the SS included approximately 25,000 square meters of insulated courtyards and attics containing "polverino," a material that contained about 10-15% asbestos. This material was present in more than 150 spots spread across all 48 municipalities. For the remediation activities at this site, approximately 47 million euros have been allocated to date, with funding provided by the Ministry of Environment and the Piedmont Region.

Figure 1: *Eternit Factory in Casale Monferrato before and Later Remediation*

6. Conclusion: This Paper describes the complexity of the Environmental Remediation and Restoration

activities carried out at the Superfund site of Casale Monferrato where the former asbestos cement factories Eternit and Fibronit were located. This so complex remediation started in the early ’90, is still in progress, but the major source of fibre’s dispersion are eliminated and the asbestos concentration level in the town is now much lower than the european threshold limit value. This result has been achieved thanks to the cooperation among the Environmental Ministry which funded the remediation, and the regional and local agencies, coordinated by Inail-Dit to guaranty a maximum level of workers safety. This paper also show some technical procedures that could be reused in similar situations often encountered in other Countries, like the removal of “polverino” from buildings or how to prevent exposition of health local agencies workers, uncharged to check if asbestos is still present in the buildings. These procedures, applied in hundreds situations, can be considered strongly accurate and feasibly reproducible in other places. They could be considered useful not only for friable asbestos but also for the safe asbestos cement removal, guarantying the respect of the higher prevention and protection measures established by the new European Directive. This Directive will be soon approved and will require immediately lower asbestos threshold limits and new analytical technics for asbestos sampling and analysis using after the next six years only the electron microscopy.

7. References: Bellagamba, S., Paglietti, F., Malinconico, S., Conestabile della Staffa, B., De Simone, P., & Lonigro, I. (2018). Remediation Activities in an Italian Superfund: Case Study of an Industrial Plant in Broni. 4th World Congress on New Technologies (NewTech'18), Madrid, August 19-21, 2018. Paper No. ICEPR 166. https://doi.org/10.11159/icepr18.166

IARC. (2012). A review of human carcinogens: arsenic, metals, fibres and dusts. Monographs on the evaluation of carcinogenic risks to humans. Volume 100 C. ISSN 1017-1606.

IARC. (2012). Asbestos (Chrysotile, Amosite, Crocidolite, Tremolite, Actinolite, and Anthophyllite), IARC, Lyon.

Opinion of the European Economic and Social Committee on Freeing the EU from asbestos CCMI/130-EESC-2014-05005.

Paglietti, F., Malinconico, S., Di Molfetta, V., Bellagamba, S., Damiani, F., Gennari, F., De Simone, P., Sallusti, F. & Giangrasso, M.. (2010). Asbestos Risk - from raw material to waste management: the Italian experience. Critical Reviews. Environmental Science and Technology, https://doi.org/10.1080/10643389.2011.569875

Resolution EU - P7_TA (2013) 0093 on asbestos related occupational health threats and prospects for abolishing all existing asbestos.

Ro-Ting, L., Ken, T., Antti, K., Tsutomu, H., Donald, W., Takashi, K., Chang-Chuan, C., Chi-Pang, W., Sugio, F., Toshiaki, H., Lung-Chang, C., & Megu, O. (2007). Ecological association between asbestos-related diseases and historical asbestos consumption: an international analysis

The Lancet, Volume 369, no. 9564, p844–849, 10 March 2007. https://doi.org/10.1016/S0140-6736(07)60381-X

WHO. (2019). Asbestos: https://www.who.int/ipcs/assessment/public_health/asbestos/en/.

The Difference in Fitting a Surface with a Standard Topology and a Surface with a Matrix Topology

Milan Ćurković
Faculty of Electrical Engineering, Mechanical Engineering and Naval Architecture, University of Split, Split, Croatia

Andrijana Ćurkovićb
Faculty of Electrical Engineering, Mechanical Engineering and Naval Architecture, University of Split, Split, Croatia

Damir Vučina
Faculty of Science, University of Split, R. Boskovica 33, 21000 Split, Croatia

Abstract. This paper presents the impact of the surface topology of the scanned 3D object on parametric fitting. Whether it is a simple NURBS (Non-uniform rational B-spline) or a more complex hierarchical spline version, it is important to apply the fitting procedure. Here we describe the differences between fitting a surface with a given topology as a result of a 3D scanning system and a matrix topology of the surface, where the original surface is replaced by the result of a preset number of sections of the original geometry.
Keywords. Topology, NURBS, hierarchical spline.

1. Introduction: Surface topology affects the results of many numerical methods. In this paper we describe the implications for fitting a parametric model to a scanned 3D model with different surface topologies. A brief introduction to the creation of a parametric NURBS model is given in this paper, while detailed information can be found in [1–3]. The work shows that the fit of the parametric model in the case of a free-form surface topology (original triangulation) depends on the density of the triangulation mesh and, also on the distribution of vertices in the surface mesh. As a result, the control points of the parametric model are grouped in areas with a higher density of grid points. In the case of a uniform distribution of vertices in the surface mesh, a uniform distribution of control points of the parametric model is to be expected. Using the matrix distribution of the vertices of the model surface in the fitting process leads to a more uniform distribution of the control points of the parametric model, independent of the density of the triangulated mesh.

2. Comparison of fitting with different topologies: In the following, we outline the definition of the standard NURBS parametric model, which is sufficient to demonstrate the effects of different surface topologies when fitting the parametric model to the given model surface. The NURBS surface is defined by its control points, weight factors, degrees of polynomials and the set of knots,

$$\boldsymbol{C}(u,v) = \frac{\sum_{i_0=0}^{n_0}\sum_{i_1=0}^{n_1} N_{i_0,p_u}(u)N_{i_1,p_v}(v)w_{i_0i_1}\boldsymbol{Q}_{i_0i_1}}{\sum_{i_0=0}^{n_0}\sum_{i_1=0}^{n_1} N_{i_0,p_u}(u)N_{i_1,p_v}(v)w_{i_0i_1}} \in \mathbb{R}^3 (1)$$

where n_0,n_1 are the numbers of the control points, and N_(i_0,p_u) (u) and N_(i_1,p_v) (v) are the basic B-spline functions of degrees ⟦p_u,p⟧_v∈N defined by

$$N_{i,0}(u) = \begin{cases} 1, & \bar{u}_i \le u \le \bar{u}_{i+1} \\ 0, & else \end{cases},$$

$$N_{i,p}(u) = \frac{u-\bar{u}_i}{\bar{u}_{i+p}-\bar{u}_i} N_{i,p-1}(u) + \frac{\bar{u}_{i+p+1}-u}{\bar{u}_{i+p+1}-\bar{u}_{i+1}} N_{i+1,p-1}(u). \quad (2)$$

The knots u¯_i∈[0,1], as part of the basic B-spline functions, we set as

$$\bar{\boldsymbol{u}} = \left\{ \underbrace{0, \dots 0}_{p+1}, \bar{u}_{p+1}, \dots, \bar{u}_n, \underbrace{1, \dots 1}_{p+1} \right\}, \left\{ \bar{u}_i = \frac{i}{n} \right\}_{i=p+1}^{n}. \quad (3)$$

Matrix $\boldsymbol{Q}$ presents control points.

$$\boldsymbol{Q} = \begin{bmatrix} \boldsymbol{Q}_{00} & \cdots & \boldsymbol{Q}_{0n_1} \\ \vdots & \ddots & \vdots \\ \boldsymbol{Q}_{n_0 0} & \cdots & \boldsymbol{Q}_{n_0 n_1} \end{bmatrix} \in \mathbb{R}^{3(n_0+1)\times(n_1+1)}. \quad (4)$$

Figure 1 shows an example of a model with the original surface density provided by the scanner system. It is the first example to which we fitted NURBS parametric model using two different surface topologies.

a) Shaded surface.

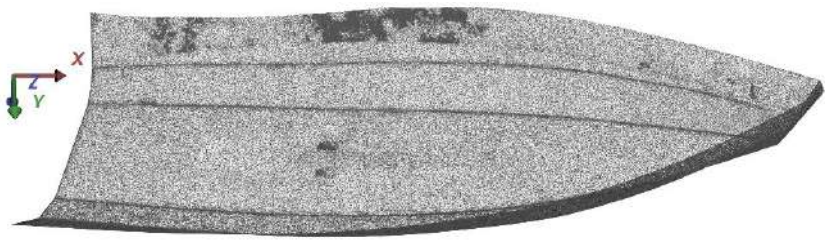

b) Triangulation of a)

Fig. 1: *Example of a Model with the Original Surface Density Provided By the Scanner System*

The following equation shows the error function when fitting the NURBS model to the surface with the original surface topology, where $\boldsymbol{P_j}$ represents the vertices of the triangulated mesh.

$$\boldsymbol{E_{freeform}(Q)} = \frac{1}{2}\sum_{j=0}^{m} \left\| \boldsymbol{C(u_j, v_j)} - \boldsymbol{P_j} \right\|^2 \quad (5)$$

The next equation

$$E_{matrix}(Q) = \frac{1}{2}\sum_{j_0=0}^{m_0}\sum_{j_1=0}^{m_1}\left\|C(u_{j_0j_1}, v_{j_0j_1}) - P_{j_0j_1}\right\|^2 \tag{6}$$

Assumes that the model surface is represented in matrix form,

$$P = \begin{bmatrix} P_{00} & \cdots & P_{0m_1} \\ \vdots & \ddots & \vdots \\ P_{m_0 0} & \cdots & P_{m_0 m_1} \end{bmatrix} \in \mathbb{R}^{3(m_0+1)\times(m_1+1)} \tag{7}$$

Where m_0 is the number of sections and m_1 the number of vertices in each section (see figure Fig2).

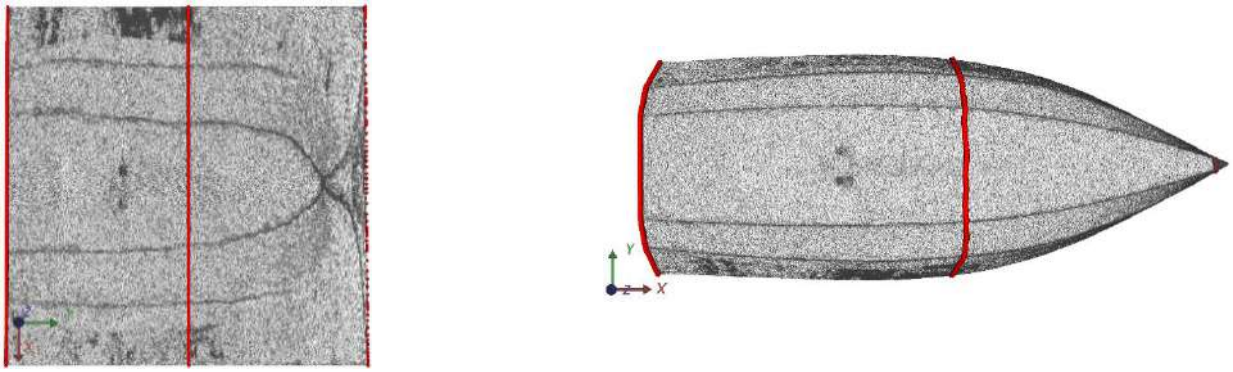

a) Sections of the surface in the parametric domain b) Corresponding points from a) on the original surface

Fig. 2: The Approach to Obtain the Matrix Topology of the Given Surface

The detailed description for the matrix form of the surface can be found in [2, 4].
The next figure below shows the result of fitting NURBS to the model with the original free form surface topology and matrix topology.

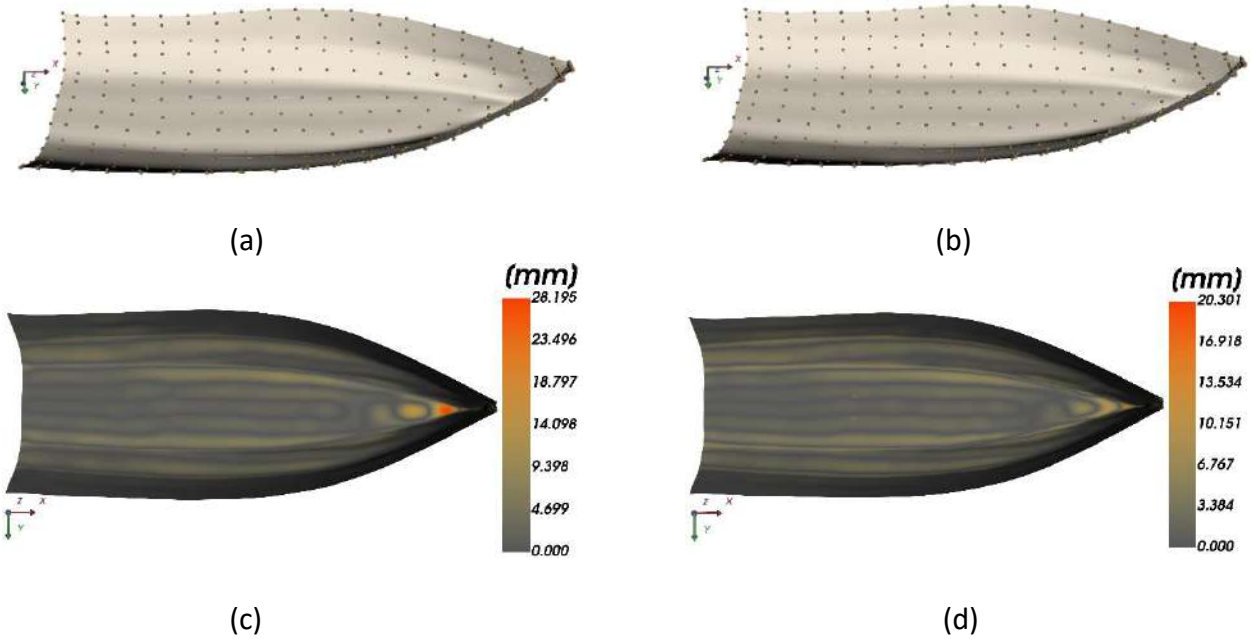

(a) (b)

(c) (d)

Fig. 3: *The Result of NURBS Fitting To the Model with the Original Surface Topology and Matrix Topology*
(a) NURBS with free form surface topology;
(b) NURBS with matrix form surface topology;
(c) Distribution of the distance between (a) and the original surface form Fig1;
(d) Distribution of distance between (b) and the original surface form Fig1.

The above example shows a small difference in the distribution of control points between two NURB models (Fig. 3a and Fig. 3.b), which leads to a small difference in the error distribution (Fig. 3c and Fig. 3.d).
The larger difference in the distribution of control points and the corresponding geometry differences arise in the case of a thinner surface triangulation grid, as shown in figure Fig4. This kind of change affects the connection of multiple NURBS surfaces into a more complex hierarchical spline [5,6], the creation of models of displacement surfaces [7], and so on.

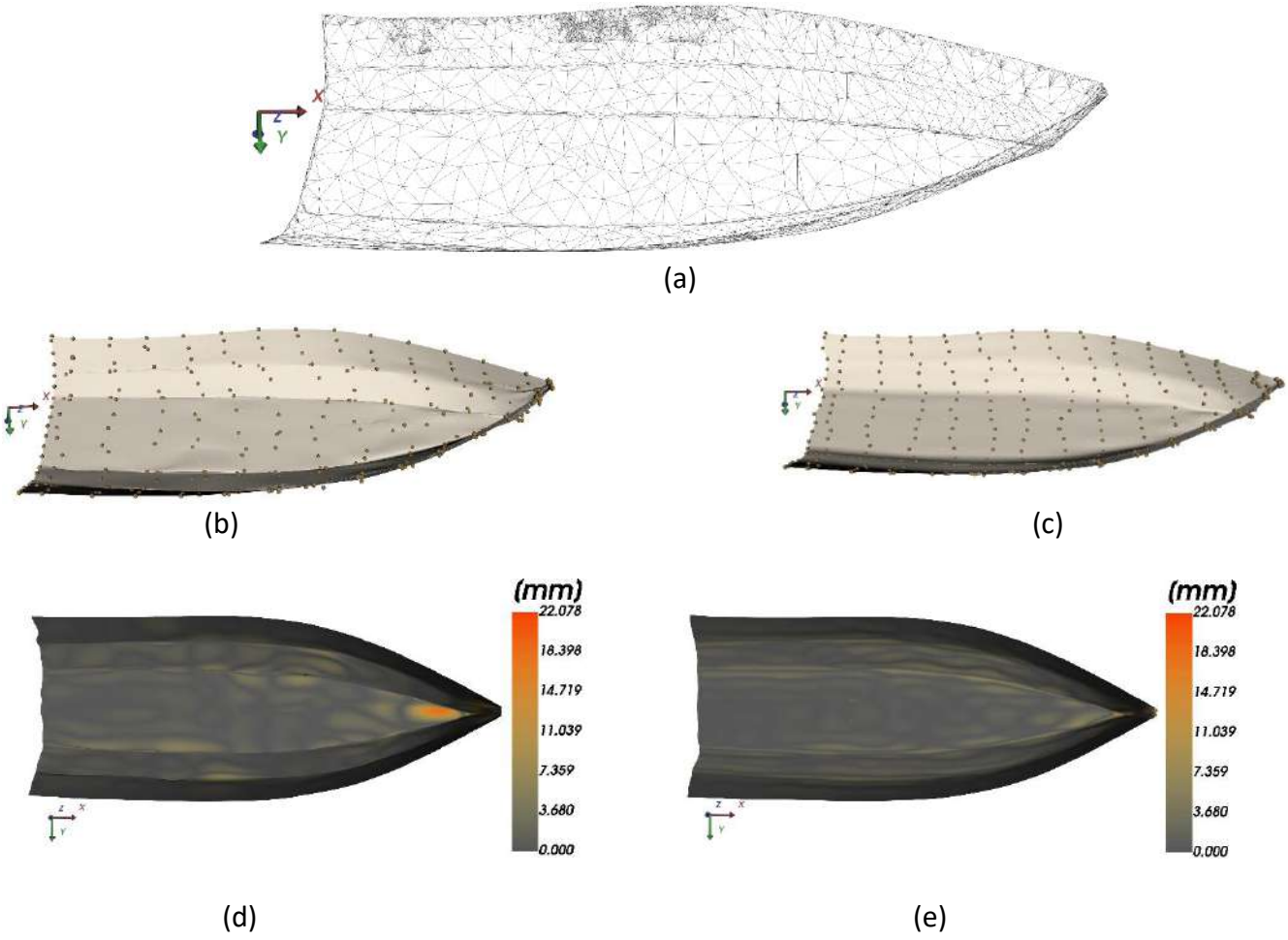

Fig. 4: *The Result of NURBS Fitting to the Thinned Model with the Original Surface Topology and Matrix Topology*
(a) The thinned surface of the surface from Fig.1;
(b) NURBS with free form surface topology;
(c) NURBS with matrix form surface topology;
(d) Distribution of the distance between b) and the original surface form a);
(e) Distribution of distance between c) and the original surface form a).

3. Future work: In the future, we plan to adopt our method of projection into a parametric rectangular domain based on harmonic mapping, so that the redistribution of vertices in 2D depends on whether the vertices belong to geometric features or not. In this way, we can avoid the need for the matrix form of geometry.

4. **References:** Cúrkovic M, Vučina D, Cúrkovic A. Enhanced 3D parameterization for integrated shape synthesis by fitting parameter values to point sets. Integr Comput Aided Eng. 2017; 24(3). https://doi.org/10.3233/ICA-170541

Ćurković M, Ćurković A, Vučina D. Novel re-parameterization for shape optimization and comparison with knot-based gradient fitting method. Comput Methods Appl Mech Eng. 2018 Jul; 336:304–32. https://doi.org/10.1016/j.cma.2018.03.018

Ćurković M, Vučina D. 3D shape acquisition and integral compact representation using optical scanning and enhanced shape parameterization. Adv Eng Informatics. 2014 Apr; 28 (2):111–26. https://doi.org/10.1016/j.aei.2014.01.002

Ćurković M, Vučina D, Ćurković A. Enhanced 3D parameterization for integrated shape synthesis by fitting parameter values to point sets. Integr Comput Aided Eng. 2017 ;(24):241–260. https://doi.org/10.3233/ICA-170541

Giannelli C, Jüttler B, Kleiss SK, Mantzaflaris A, Simeon B, Špeh J. THB-splines: An effective mathematical technology for adaptive refinement in geometric design and isogeometric analysis. Comput Methods Appl Mech Eng. 2016 Feb; 299:337–65. https://doi.org/10.1016/j.cma.2015.11.002

Hong Qin. D-NURBS: Dynamic non-uniform rational B-splines, Ph.D. Dissertation. 1995.

Lee A, Moreton H, Hoppe H. Displaced subdivision surfaces. In: Proceedings of the 27th annual conference on Computer graphics and interactive techniques - SIGGRAPH '00. New York, New York, USA: ACM Press; 2000. p. 85–94. https://doi.org/10.1145/344779.344829

Effect of Cryogenic and Natural Aging Process Applied to Al-Zn-Mg-Cu Alloys on Life Time Calculation

Gozde Altuntas
Metallurgy and Materials Engineering, Gazi Unıversity, Ankara, Turkey

Onur Altuntaş
National Defense University, Alparslan Defense Sciences and National Security Institute, Department of Warfare Weapons and Tools, Ankara, Turkey

Bulent Bostan
Gazi University, Faculty of Technology, Department of Metallurgical and Materials Engineering, Ankara Turkey

Abstract: In this study, life time calculation of aluminum 7075 alloy with cryogenic and natural aging processes was performed by thermal analysis. The aluminum alloy was quenched after solid solution treatment at 480°C and naturally aged for 10-100 days at room temperature (25°C). Other samples were cryogenically treated at -40°C and -80°C for 2 hours after solid solution treatment at 480°C. After the cryogenic treatment, natural aging was done at room temperature for 10-100 days. At the end of each period determined for the samples, the hardness values were measured. It was observed that there was no significant change in hardness values at the end of 10 and 100 days at -80 °C. Thus, it was determined that

the natural aging process does not start after cryogenic treatment at -80 °C. It was observed that the hardness value of naturally aged samples after cryogenic treatment at -40 °C increased more than the natural aged samples only. This showed that -40 °C improved the mechanism by creating a driving force in the material. Life time calculations between 30 °C and 500 °C also showed that -40 °C cryogenic treatment + natural aging increased life time by approximately 20% compared to natural aging alone.
Keywords: Al-Zn-Mg-Cu alloy, Cryogenic treatment, Natural aging, Life time calculation

1. Introduction: Al-Zn-Mg-Cu alloys are also included in the 7xxx series aluminum alloys group. Due to its features such as low density and high strength, it is frequently preferred in structural applications and in the aviation industry. Since this alloy is in the group of aging aluminum alloys, it is often used by applying aging heat treatment (Altuntas et al., 2022). Thanks to this heat treatment, the strength ratio increases and a wide usage area is formed (Chen et al., 2009). The aging heat treatment is divided into two groups as artificial and natural. With natural aging; Depending on the ratio of chemical elements, the solution heat treatment is carried out for 1 or 2 hours at (400-500̊C) in general, and water is given and supersaturated solid solution is formed (Altuntas et al., 2021). The main purpose of the solid solution heat treatment is to increase the solubility of the alloy by heating to high temperature, to dissolve the precipitates in the structure in a single phase and to obtain a supersaturated single-phase solid solution. If the alloy is allowed to cool slowly after solution treatment, coarse precipitates with negative mechanical properties are formed. As a result of rapid quenching, a supersaturated α-phase precipitate is obtained by not allowing the second phase to precipitate in the α solid. The α-phase is unstable due to the effect of flash cooling. The number of atomic cavities in equilibrium in the alloy increases logarithmically with the increase in temperature. The volume fraction of atomic vacancies during the solutioning process is quite high compared to their ratio at low temperatures. In this case, as the equilibrium conditions cannot be achieved as a result of the sudden cooling of the material from high temperatures, the excess of atomic vacancies remains in the structure. Atomic cavities, which are found in large amounts in the structure, are formed as a result of sudden cooling and move away from the structure over time. Atomic cavities that form point defects tend to come together and coalesce, and some of them absorb the atomic cavities and form the basis for the formation of dislocation rings. During quenching, the solid solution becomes unstable and tends to precipitate. It is then left to natural aging by keeping it at room temperature (Mackenzie et al., 2003). It takes about six months to achieve maximum hardness with this process (Mukhopadhyay et al., 2011). Artificial aging heat treatment, on the other hand, is carried out by giving water (80̊C-200 C) after the solution heat treatment (holding for 1 or 2 hours between 400-500̊C) and keeping the material for 12-24 hours. The aging time varies according to the temperature. By keeping the rapidly cooled alloy at a temperature above room temperature, precipitation takes place in a shorter time due to the increased diffusion rate. With both aging, the same phase occurs, which increases the strength of the material. In practice, artificial aging is frequently used to save time. But during natural aging, not only the size and number density, but also the type of clusters and GP zones can change over time, and this can have a profound effect on the metastable η' phase. It has been observed in different studies that the microstructural evolution and the form of the formed phases during natural aging have a deeper effect (Liu et al., 2015). The precipitation sequences formed during aging of Al-Zn-Mg-Cu alloys have been shown in many studies (Sha et al., 2004). It is well known that Guinier-Preston (GP) zones with hardening effect and metastable η' phase precipitates can form from supersaturated solid solution during aging (SSSS) (Couturier et al., 2017). In general, there are two types of GP zones. These are GPI zones and GPII zones. The sequences shown below are most likely to arise during aging..
SSSS → GPI zones → GP II zones → Metastable η' (MgZn2) → Stable η (MgZn2) consists of sequentially (Lendvai, 1996).

It has been reported that the effect on the highest strength increase is associated with the metastable η' phase (Li et al., 1999). The precipitation kinetics of the formation of this phase has been investigated in different studies (Khalfallah, et al., 2019). Thus, the activation energies, growth and nucleation kinetics of the

phases are shown. The precipitate kinetics of the phases after secondary treatments were also investigated in different studies (Leyva-González et al., 2015). However, there are no studies on the precipitate kinetics and life time calculation of the η' phase after natural aging. With this study, information about the degradation time of the material depending on the temperature will be obtained through thermal analysis, especially with life time calculation in all material groups

2. Experimental Studies: The Al 7075 alloy used in this study was purchased commercially. Solution heat treatment of samples cut in 10*10*10 mm3 dimensions was first performed in high temperature furnace at 480 °C for 2 hours. Then it was quenched and some of the samples were left to natural aging for 10 and 100 days at room temperature. These samples were coded as NA10 and NA100, respectively. Other cut samples were cryogenically treated at -40 °C and -80 °C for 2 hours after solution heat treatment and quenching. Then it was left to natural aging for 10 and 100 days. After each aging period, the mechanical change was controlled by measuring their micro hardness. However, there was no change in the mechanical hardness values of the samples that were cryogenically treated at -80 °C during this period. This showed that the aging mechanism could not start after cryogenic treatment at -80 °C. Therefore, these samples were not coded. Due to the effective initiation of natural aging after cryogenic treatment at -40 °C, these samples were coded as CNA10 and CNA100, respectively. Hardness measurements were taken in the Qness hardness device according to the ASTM E384 standard. HITACHI DSC 7020 thermal analyzer was used for differential scanning calorimetry (DSC) experiments. The tests were carried out at a temperature range of 30 °C to 320 °C in an argon atmosphere with a heating rate of 5 °C /min, 10 °C /min, 15 °C /min, 20 °C/min. DSC analysis was carried out with samples of 10 mg mass enclosed in aluminum pans. With the data obtained through this analysis, first of all, the activation energies were found and a life time calculation was made.

Table 1: *Chemical Composition of the Material*

Elements (%)						
Zn	Mg	Cu	Mn	Cr	Fe	Al
5.9	2.7	1.8	0.3	0.25	0.4	Balance

3. Result and Discussion: Figure 1 shows the micro hardness values of the samples. The hardness of the NA10 sample was measured as 105 HV0.5, and the hardness of the NA100 sample was measured as 160 HV0.5. It was observed that the hardness value of the material increased as the natural aging time increased. This is an expected result as observed in the literature (Altuntaş et al., 2022). When we look at the hardness value after cryogenic treatment at -80 °C and 10 days of natural aging, the hardness value was measured as 100 HV0.5. After 100 days, the hardness value was measured as 108 HV0.5. It has been observed that the cryogenic process performed at -80 °C has a bad effect on the progression of natural aging. For this reason, life time calculations of the experiments carried out at -80 °C were not performed. After the cryogenic treatment at -40 °C and 10 days of natural aging, the hardness of the CNA10 sample was measured at 126 HV0.5. The hardness value after 100 days of natural aging was found to be 175 HV0.5. The results showed that cryogenic treatment at -40 °C is an effective force accelerating the aging mechanism. It is thought that the probability of formation of more η' phases by triggering the formation of new nucleation points will increase the hardness.

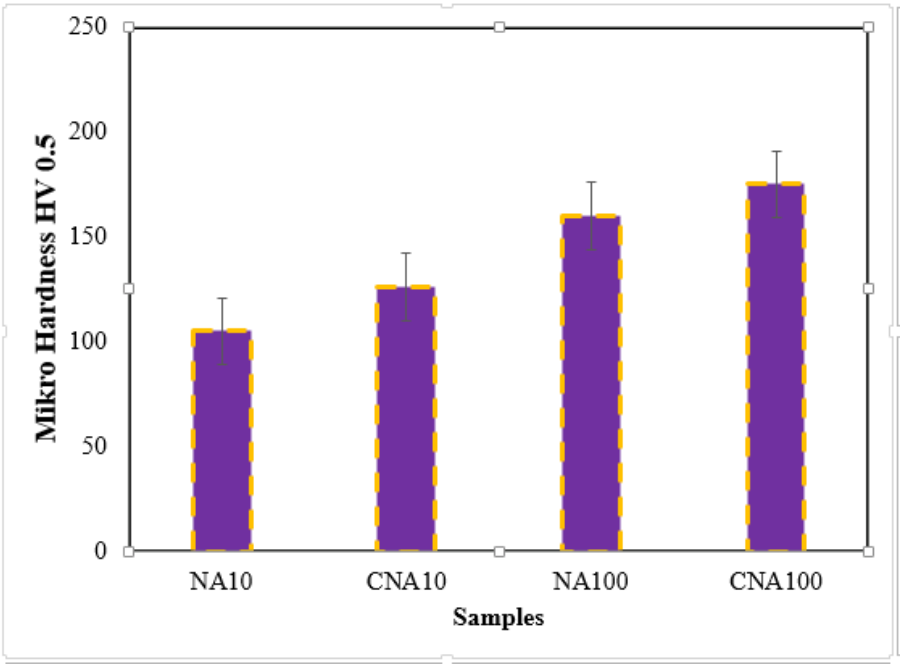

Figure 1: *Micro Hardness Values of Samples According To HV0.5*

As seen in Figure 2, the activation energy graph is shown with the data obtained as a result of the DSC analyzes performed in argon atmosphere with a heating rate of 5 °C / min, 10 °C / min, 15 °C / min, 20 °C / min. Table 2 shows the life time calculation of the NA10 sample between 30 °C and 320 °C. In general, it was observed that the life time value decreased as the temperature increased.

In general, the reaction rate of a sample according to Arrhenius's law is expressed by the following equation:

$$\frac{dx}{\mathrm{dt}} = \mathrm{A}\exp\left(-\frac{\Delta E}{\mathrm{RT}}\right).f(x)$$

Where

x : quantity of reaction, t : time, A : frequency factor, ΔE : activation energy, R : gas constant, T : absolute temperature, f (x) : function of x

In thermal analysis, T (temperature) is a function of t (time) and usually indicates the relationship dT/dt=B (constant). Here B is the heating rate (°C/min). Therefore, if the above expression is reserved for the variables x and t, the following expression can be obtained:

$$\int_{x0}^{x1}\frac{dx}{f(x)} = \int_{t0}^{t1} A\,exp(-\frac{\Delta E}{RT})dt$$

$$= \frac{A}{B}\int_{T0}^{T1} exp(p-\frac{\Delta E}{RT})dT$$

So, if F(x) is defined as:

$$F(x) = \int \frac{dx}{f(x)}$$

and after changing the following variables, integration is performed according to the parts.

$$\frac{\Delta E}{RT} = y$$

$$F(x_1) - F(x_0) = A\frac{\Delta E}{BR}\left[P\left(\frac{\Delta E}{RT1}\right) - P\left(\frac{\Delta E}{RT0}\right)\right]\ldots\ldots$$

$$P(y) = \frac{e^{-y}}{y} - \int_y^{\infty}\frac{e^{-y}}{y}dy$$

Since the relationship T1>T0 is generally true, the 2nd term of the equation on the right is usually negligible, while the 1st term cannot be. Hence, the following relationship is obtained:

$$\frac{A*\Delta E}{BR}P\left(\frac{\Delta E}{RT1}\right) = F(x_1) - F(x_0)\ldots\ldots\ldots\ldots$$

If x1 is calculated assuming x0=0, the value of the right-hand member of the above equation will be a constant as follows:

$\frac{A*\Delta E}{BR}$ P $\left(\frac{\Delta E}{RT1}\right)$=const.

Therefore, when the heating rate B is changed, the temperature T1 with the reaction rate x1 also changes proportionally, and therefore the value on the left side of equation does not change as a whole. Regarding P(y), the following approximate expression is known:

$$LogP(y) = 2.315-0.467y \quad 20<y<60$$

$$Const = log\frac{A*\Delta E}{BR}P\left(\frac{\Delta E}{RT1}\right)$$

$$= log\frac{A*\Delta E}{BR} + log\,P\left(\frac{\Delta E}{RT1}\right)$$

$$= log\frac{A*\Delta E}{BR} - logB - 2.315 - 0.467\left(\frac{\Delta E}{RT1}\right)$$

If we rearrange the above equation for heating rate B and temperature T1, the following equation is obtained:

$$logB = -0.467\frac{\Delta E}{R}*\frac{1}{T1} + constant$$

If at least three measurements are made at different heating rates and the relationship between 1/T1 and log B of each pair of these data is plotted in x-y coordinates, the activation energy of a sample can be obtained from a plotted slope.

Area and partial area calculations are made by determining the temperature point where the phase transformation starts and ends (a-b). A set (Bj, Yi, Xij) is created for all data to be used in the calculation.

Where,

j : Data No.

Bj : Heating rate of j-th data (℃/min)

Yi : j number data obtained in step (4)

Xij : X signal (ºC) for Yij

Convert Xij (temp) to the absolute temperature (°C → K)

Xkij= Xij+273.15

Zij=$\frac{1000}{Xkij}$

Plot the set (Zij, log Bj) on x-y coordinates and approximate it linearly to each of i=1, 2, 3, ... n–1. Then, based on the following linear expression, find a value corresponding to Pi, qi:

$logB=Pi+qi+Zij \quad (i = 1,\ 2,\ 3,\ \cdots n-1)$

Calculate the activation energy (ΔE). Each value of ΔEi for i=1, 2,3, ... n–1 is calculated with the following expression:

ΔEi = -$\frac{R}{0.4567} * qi$ (kj/mol) R=8.31434 (kj/mol)

The constant temperature degradation time (τ) is calculated as

The temperature to be kept is considered as Tc (ºC).

B= $\sqrt{max\ Bj * min\ Bj}$ （use midpoint of logB）

Ti=-$\frac{qi}{logB-Pi}$ (K)

Each respective τi to i=1, 2, 3, ... τi is calculated by the following expression

$$\tau i = \frac{\int_{T0}^{Ti} exp\left(-\frac{\Delta E}{RT}\right)dT}{Bexp\ \left(-\frac{\Delta Ei}{R(Tc+273.15}\right)}$$

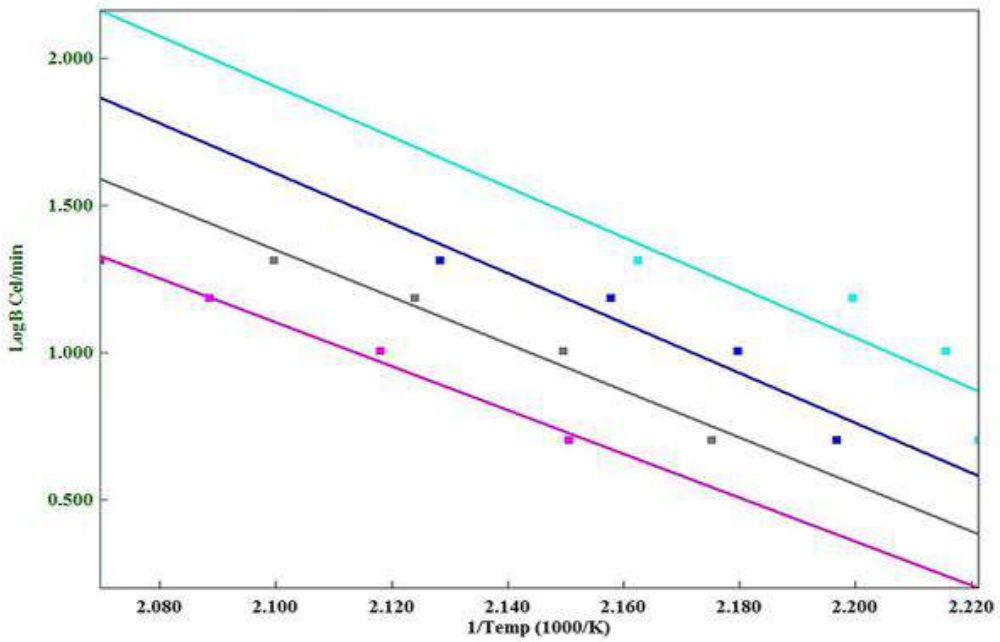

Figure 2: *Activation energy graph of NA10 sample*

Table 2: *Life time calculation and activation energy values of NA10 sample in the range of 30-320*℃

Life Time						
R.F %	ΔE kJ/mol	30℃ day	40℃ day	50℃ day	60℃ day	70℃ day
20	97	3.6E+02	1.1E+02	3.3E+01	1.1E+01	4.1E+00
40	105	1.6+E+03	4.1E+02	1.2E+02	3.7E+01	1.2E+01
60	111	5.5+03	1.3E+03	3.6E+02	1.0E+02	3.2E+01
80	118	2.1+04	4.7E+03	1.2E+03	3.1E+02	8.9E+01
Life Time						
R.F %	ΔE kJ/mol	80℃ day	90℃ day	100℃ day	110℃ day	120℃ day
20	97	1.6E+00	6.2E-01	2.6E-01	1.2E-01	5.4E-02
40	105	4.3E+01	1.6E+00	6.3E-01	2.6E-01	1.1E-01
60	111	1.0E+01	3.6E+00	1.4E+00	5.3E-01	2.2E-01
80	118	2.7E+01	9.0E+00	3.2E+00	1.2E+00	4.5E-01
Life Time						
R.F %	ΔE kJ/mol	130℃ day	140℃ day	150℃ day	160℃ day	170℃ day
20	97	2.6E-02	1.3E-02	6.6E-03	3.5E-03	1.9E-03
40	105	5.0E-02	2.4E-02	1.1E-02	5.7E-03	3.0E-03
60	111	9.3E-02	4.1E-02	1.9E-02	9.2E-03	4.6E-03
80	118	1.9E-01	7.9E-02	3.5E-02	1.6E-02	7.6E-03
Life Time						
R.F %	ΔE kJ/mol	180℃ day	190℃ day	200℃ day	210℃ day	220℃ day
20	97	1.1E-03	6.1E-04	3.6E-04	2.1E-04	1.3E-04
40	105	1.6E-03	8.6E-04	4.8E-04	2.8E-04	1.6E-04
60	111	2.3E-03	1.2E-03	4.7E-04	3.7E-04	2.1E-04
80	118	3.8E-03	1.9E-03	1.0E-03	5.3E-04	2.9E-04
Life Time						
R.F %	ΔE kJ/mol	230℃ day	240℃ day	250℃ day	260℃ day	270℃ day
20	97	8.2E-05	5.2E-05	3.4E-05	2.2E-05	1.5E-05

40	105	9.8E-05	6.0E-05	3.8E-05	2.4E-05	1.5E-05
60	111	1.2E-04	7.3E-05	4.4E-05	2.7E-05	1.7E-05
80	118	1.7E-04	9.6E-05	5.6E-05	3.4E-05	2.1E-05
Life Time						
R.F %	ΔE kJ/mol	280℃ day	290℃ day	300℃ day	310℃ day	320℃ day
20	97	1.0E-05	6.9E-06	4.8E-06	3.4E-06	2.4E-06
40	105	1.0E-05	6.8E-06	4.6E-06	3.1E-06	2.2E-06
60	111	1.1E-05	7.1E-06	4.7E-06	3.2E-06	2.1E-06
80	118	1.3E-05	8.1E-06	5.2E-06	3.4E-06	2.3E-06

In Figure 3 and Table 3, activation energy and life time calculation values of the CNA10 sample, which was cryogenically treated and aged for 10 days, are shown. When we look at the values, it has been calculated that natural aging after cryogenic treatment at -40 °C increases the hardness and has a positive effect on life time. Up to 180 °C, the life time value of the CNA10 sample increased compared to the NA10 sample. In other words, the formation of more nucleation points by cryogenic treatment represents the formation of more η' phase, supporting the increase in life time value. It is thought that the degradation time of the η' phase, that is, the decrease in the life time value in the CNA10 sample after 180 °C, may have entered the extreme aging phase after this temperature (Wang et al., 2022). Formation of more η' phases by cryogenic treatment will require further reduction as degradation occurs or as overaging occurs. For this reason, there may be a greater decrease in the life time value compared to the NA10 sample.

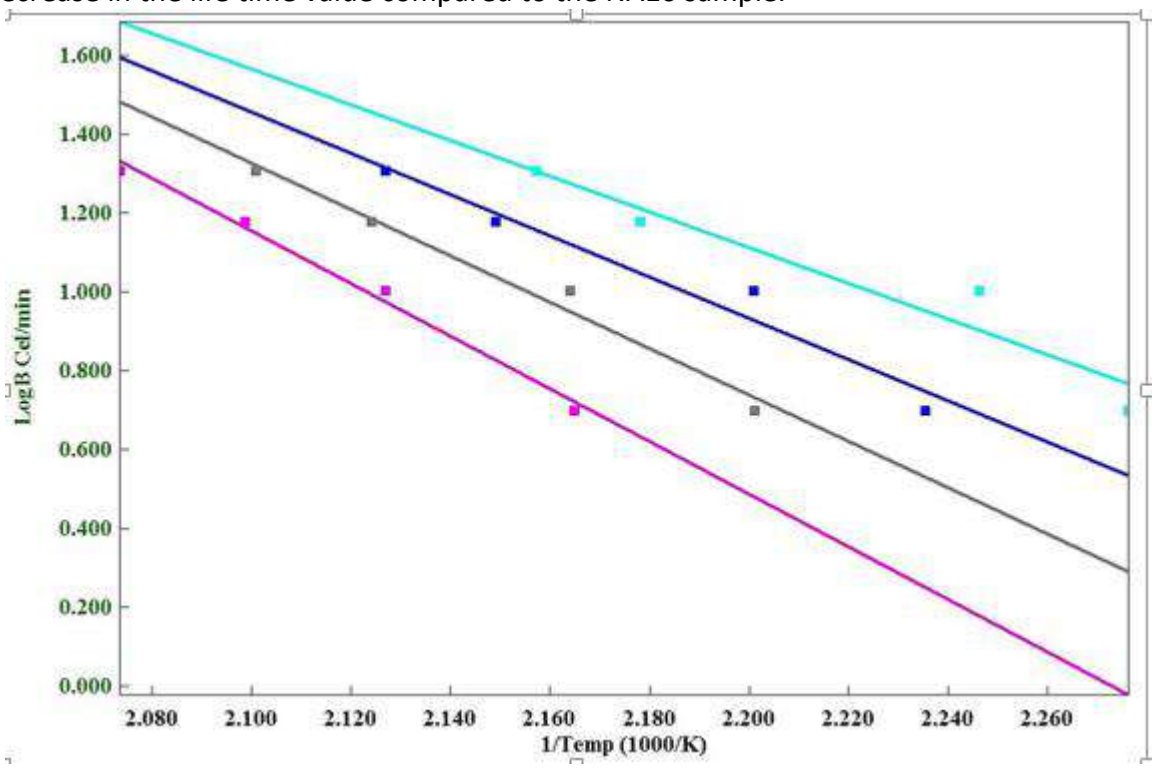

Figure 3: C*NA10 numunesinin aktivasyon enerjisi grafiği*

Table 3: *CNA10 numunesinin 30-320°C aralığında life time calculation ve aktivasyon enerjisi değerleri*

Life Time						
R.F %	ΔE kJ/mol	30℃ day	40℃ day	50℃ day	60℃ day	70℃ day
20	110	1.2E+02	3.2E+02	8.6E+01	2.5E+01	7.7E+00
40	114	3.7E+03	8.6E+02	2.2E+02	6.2E+01	1.8E+01
60	115	7.2+03	1.7E+03	4.2E+02	1.2E+02	3.4E+01
80	116	1.5+04	3.3E+03	8.3E+02	2.2E+02	6.5E+01
Life Time						
R.F %	ΔE kJ/mol	80℃ day	90℃ day	100℃ day	110℃ day	120℃ day
20	110	6.6E+00	9.1E-01	3.4E-01	1.3E-01	5.5E-02
40	114	5.9E+01	2.0E+00	7.4E-01	2.8E-01	1.1E-01
60	115	1.1E+01	3.7E+00	1.8E+00	5.0E-01	2.0E-01
80	116	2.0E+01	6.8E+00	2.4E+00	9.1E-01	3.6E-01
Life Time						
R.F %	ΔE kJ/mol	130℃ day	140℃ day	150℃ day	160℃ day	170℃ day
20	110	2.8E-02	1.3E-02	4.9E-03	3.7E-03	1.2E-03
40	114	5.2E-02	2.5E-02	9.4E-02	5.8E-03	3.1E-03
60	115	9.4E-02	4.2E-02	1.9E-02	7.6E-03	4.8E-03
80	116	2.0E-01	8.1E-02	3.6E-02	1.7E-02	7.7E-03
Life Time						
R.F %	ΔE kJ/mol	180℃ day	190℃ day	200℃ day	210℃ day	220℃ day
20	110	6.1E-04	3.2E-04	1.8E-04	9.8E-05	5.6E-05
40	114	1.7E-03	5.7E-04	3.0E-04	1.7E-04	9.3E-05
60	115	2.6E-03	9.5E-03	5.0E-04	2.7E-04	1.5E-04
80	116	3.8E-03	1.6E-03	8.4E-04	4.6E-04	2.5E-04
Life Time						
R.F %	ΔE kJ/mol	230℃ day	240℃ day	250℃ day	260℃ day	270℃ day
20	110	3.3E-05	1.9E-05	1.2E-05	7.3E-06	4.6E-06

40	114	5.4E-05	3.1E-05	1.9E-05	1.1E-05	7.2E-06
60	115	8.7E-05	5.1E-05	3.0E-05	1.1E-05	1.1E-05
80	116	1.4E-04	8.3E-05	4.9E-05	3.0E-05	1.8E-05
Life Time						
R.F %	ΔE kJ/mol	280℃ day	290℃ day	300℃ day	310℃ day	320℃ day
20	110	3.0E-06	1.9E-06	1.3E-06	8.6E-07	5.8E-07
40	114	4.5E-06	2.9E-06	1.9E-06	1.3E-06	8.5E-07
60	115	7.2E-06	4.6E-06	3.0E-06	2.0E-06	1.3E-06
80	116	1.1E-05	7.3E-06	4.7E-06	3.1E-06	2.1E-06

4. Conclusion:

Acknowledgements

This study has been financially supported by the Gazi University Scientific Research Projects Coordination Unit [under Project Number FDK-2023-7620].

5. Conflict of interest

The authors report no potential conflict of interest.

6. References

Altuntaş, G., Altuntaş, O., & Bostan, B. (2021). Characterization of Al-7075/T651 Alloy by RRA Heat Treatment and Different Pre-deformation Effects. Transactions of the Indian Institute of Metals, 74, 3025-3033. https://doi.org/10.1007/s12666-021-02369-5

Altuntaş, G., Bostan, B. (2022). Metallurgical characterization of natural aging effects on pre-deformed Al 7075/T651 alloy during retrogression and re-aging heat treatment. Kovove Materialy, 60(4) https://doi.org/10.31577/km.2022.4.209

Altuntaş, G., & Bostan, B. (2021). Al–Zn–Mg–Cu Alaşımının Kristalografisine RRA Isıl İşlemi Etkilerinin İncelenmesi. Politeknik Dergisi, 25(2), 871-877. https://doi.org/10.2339/politeknik.919492

Altuntaş, G., & Bostan, B. (2022) 7075 Al Alaşımına Uygulanan Kriyojenik ve Doğal Yaşlandırma İşleminin Avrami Parametresine Etkisi. Gazi University Journal of Science Part C: Design and Technology, 10(4), 691-698. https://doi.org/10.29109/gujsc.1179514

Chen, J., Zhen, L., Yang, S., Shao, W., & Dai, S. (2009). Investigation of precipitation behavior and related hardening in AA 7055 aluminum alloy. Materials Science and Engineering: A, 500(1-2), 34-42. https://doi.org/10.1016/j.msea.2008.09.065

Couturier, L., Deschamps, A., De Geuser, F., Fazeli, F., & Poole, W. J. (2017). An investigation of the strain dependence of dynamic precipitation in an Al-Zn-Mg-Cu alloy. Scripta Materialia, 136, 120-123. https://doi.org/10.1016/j.scriptamat.2017.04.031

Khalfallah, A., Raho, A. A., Amzert, S., & Djemli, A. (2019). Precipitation kinetics of GP zones, metastable η' phase and equilibrium η phase in Al− 5.46 wt.% Zn− 1.67 wt.% Mg alloy. Transactions of Nonferrous Metals Society of China, 29(2), 233-241. https://doi.org/10.1016/S1003-6326(19)64932-0

Lendvai, J. (1996). Precipitation and strengthening in aluminium alloys. In Materials Science Forum (Vol. 217, pp. 43-56). Trans Tech Publications Ltd. https://doi.org/10.4028/www.sciencetific.net/MSF

Leyva-González, K. A., Deaquino-Lara, R., Pourjafari, D., Martínez-Sánchez, R., Hernandez-Rodriguez, M. A. L., & García-Sánchez, E. (2015). Calorimetry study of the precipitation in an Al7075-graphite

composite fabricated by mechanical alloying and hot extrusion. Journal of Thermal Analysis and Calorimetry, 121, 589-595. https://doi.org/10.1007/s10973-015-4581-5

Li, X. Z., Hansen, V., Gjønnes, J., & Wallenberg, L. R. (1999). HREM study and structure modeling of the η′ phase, the hardening precipitates in commercial Al–Zn–Mg alloys. Acta materialia, 47(9), 2651-2659. https://doi.org/10.1016/S1359-6454(99)00138-X

Liu, S., Li, C., Han, S., Deng, Y., & Zhang, X. (2015). Effect of natural aging on quench-induced inhomogeneity of microstructure and hardness in high strength 7055 aluminum alloy. Journal of alloys and compounds, 625, 34-43. https://doi.org/10.1016/j.jallcom.2014.10.195

Mackenzie, D. S., & Totten, G. E. (Eds.). (2003). Handbook of aluminum. New York: Dekker.

Mukhopadhyay, A. K., & Prasad, K. S. (2011). Formation of plate-shaped Guinier–Preston zones during natural aging of an Al–Zn–Mg–Cu–Zr alloy. Philosophical magazine letters, 91(3), 214-222. https://doi.org/10.1080/09500839.2010.547525

Sha, G., & Cerezo, A. (2004). Early-stage precipitation in Al–Zn–Mg–Cu alloy (7050). Acta materialia, 52(15), 4503-4516. https://doi.org/10.1016/j.actamat.2004.06.025

Wang, J., Chen, X., Yang, L., & Zhang, G. (2022). Effect of preheat & post-weld heat treatment on the microstructure and mechanical properties of 6061-T6 aluminum alloy welded sheets. Materials Science and Engineering: A, 841, 143081. https://doi.org/10.1016/j.msea.2022.143081

Comparison of Non-evaporating Spray Characteristics of Gasoline and Methanol for a Swirl Type GDI Injector

Mert Gulum

Faculty of Engineering, Karadeniz Technical University, Trabzon, Turkey

Abstract: During the past decade, gasoline direct injection engines have gained significant traction in the automotive market owing to their advantages over traditional port fuel injection engines. The complex breakup and atomization process in gasoline direct injection engines hold a key role in characterizing the mixture formation (air-fuel mixing) and the ensuing combustion process. Therefore, this study focuses on the nonevaporating spray characteristics of methanol and gasoline for a pressure swirl atomizer. For this, a semi-empirical correlation of Sauter mean diameter suggested by Lefebvre is used under different injection pressures and ambient pressures. Moreover, the main spray tip penetration is calculated using an empirical correlation suggested by Gao et al. for methanol and gasoline. According to the results, with increasing injection pressure, the main spray tip penetration increases at each ambient pressure for gasoline. Sauter mean diameter values of methanol are somewhat higher than gasoline at each injection pressure. The increase in injection pressure decreases Sauter mean diameter for gasoline and methanol. The increase in ambient pressure results in an increase in Sauter mean diameter while a decrease in spray tip penetration for gasoline.

Introduction: Today, people around the world use fossil fuels for generating energy, and consequently, the reserves of fossil fuels are depleting at a swift pace. Increasing worries regarding the future accessibility of fossil fuel reserves along with the imperative to curtail exhaust emissions are driving the escalated adoption of renewable fuels [1]. Alcohols present an attractive alternative fuel for gasoline engines due to their benefits including high octane number over 100, generally less emissions when compared to gasoline, high evaporative cooling effect increasing volumetric efficiency, and low sulfur content. Moreover, alcohols can be obtained from both natural and manufactured sources. However, the low energy content, more aldehydes in the exhaust, and vapor lock in fuel delivery systems are some disadvantages of alcohol fuels [2]. Methanol, ethanol, and 1-propanol are lower alcohols (short-chain alcohols) while 1-butanol and 1-pentanol are higher alcohols (long-chain alcohols). Gasoline engines are mainly used in passenger cars, small trucks, motorcycles, lawnmowers, and small generators [3]. Gasoline engines employ two distinct fuel injection strategies: Gasoline direct injection (GDI) and port fuel injection (PFI). GDI has gained increasing popularity in recent years due to its benefits over PFI as follows: the lower CO2 emissions, the reduced fuel consumption resulting from lower pumping losses, higher compression ratios, decreased octane number requirements, and improved volumetric efficiency. Moreover, the direct injection enables more precise control of the air-fuel mixture [4]. There are three possible injector categories used in direct injection spark ignition engines: multi-hole nozzle, the outwardly opening nozzle, and the inwardly opening pressure swirl injector. The last two produce a hollow-cone spray. Hollow-cone sprays have small droplet diameters, effective fuel-air mixing, reduced penetration, and thus enhanced atomization efficiencies [5, 6]. At present, the pressure swirl injector is commonly used in direct injection spark ignition engines [5]. Pressure swirl injector finds application in generating a hollow-cone spray. Inside the injector, there are internal swirl vanes responsible for inducing rotational movement in the liquid. The swirling motion compels the liquid towards the injector's wall. The liquid forms a film along the inner walls of the injector with an air core in the center. This liquid film undergoes a transition into a free cone-shaped liquid sheet and eventually disintegrates into droplets (breakup), leading to the creation of a hollow cone spray [5, 6]. The initial and critical step in the injection of fuel is the breakup of the spray. Therefore, an in-depth understanding of the breakup mechanisms is of significance and necessity to enhance the mixture formation and improve the combustion process for a GDI engine. Moreover, SMD (Sauter mean diameter) is defined as the diameter of the droplet having the same surface-to-volume ratio as that of the overall spray [7]. The reduction in SMD results in greater surface area per unit volume [5]. Increased surface area leads to enhanced evaporation and improved mixture formation [5]. In other words, SMD shows atomization quality [8]. However, SMD does not offer insights into the distribution of droplet sizes within the spray [5]. In the existing literature, although numerical and experimental studies focusing on the diesel spray mechanism have been performed [9-11], relatively little has been reported for GDI engines. However, this study involves the comparative analysis of the atomization quality of methanol and gasoline under different operating conditions using a semi-empirical relation of SMD suggested by Lefebvre [12] for the pressure swirl injectors. Moreover, main spray tip penetration is calculated using an empirical correlation suggested by Gao et al. [13] for methanol and gasoline. This study can serve as essential preliminary research for further analyses that center on the mixture formation into GDI engines, as well as the performance, combustion, and emission characteristics of GDI engines fuelled with alcohol blends.

Materials and Method: Calculation of SMD and Main Spray Tip Penetration

In order to measure SMD, special and costly advanced equipment like a phase Doppler particle analyzer and CCD camera are required. However, in this study, SMD of a pressure swirl atomizer is computed by using the following semi-empirical relation suggested by Lefebvre [12]:

$$\mathrm{SMD} = 2.25 \cdot \sigma^{0.25} \cdot {\mu_l}^{0.25} \cdot {\dot{m}_l}^{0.25} \cdot \Delta P^{-0.5} \cdot {\rho_a}^{-0.25} \qquad (1)$$

where σ, μ_l, m˙_l, ΔP, and ρ_a are the surface tension (N/m), dynamic viscosity (Pa.s), mass flow rate of liquid (kg/s), difference between injection pressure and ambient pressure (Pa), and density of ambient gas (kg/m3), respectively [12]. For this study, the values of fuel delivery per injection and injection duration are taken as 56.8 mm3 and 3.86 ms, respectively [6].

In order to calculate the main spray tip penetration, an empirical correlation is used suggested by Gao et al. [13] as follows:

$$L = 0.027 \cdot \left(\frac{\Delta P}{\rho_a}\right)^{0.25} \cdot t^{0.5} \quad 0 < t < 3.5 \text{ ms} \qquad (2)$$

where L is the main spray tip penetration (m) and t is the time after the start of injection (s). Gao et al. [13] suggested the correlation (Eq. (2)) under different injection pressures (2, 3.6, 4.6, and 5 MPa) and ambient pressures (0.1, 0.5, 1.0, 1.5, and 2 MPa) for the nonevaporating free spray of a Mitsubishi pressure swirl injector in a GDI engine fuelled with pure gasoline at 300 K (ambient temperature). Therefore, as will be seen later in the Operating Conditions section, Eq. (2) is suitable to the conditions studied in this study. Moreover, it should be noted that only the main spray is taken into account as suggested by Gao et al. [13].

Properties of Test Fuels: In this study, the atomization quality of methanol is investigated and compared to gasoline by computing SMD. The required fuel properties of fuels in determining atomization quality are listed in Table 1 [13, 14].

Table 1: *Fuel Properties of Test Fuels*

Properties	**Gasoline**	**Methanol**
Density at 300 K (kg/m^3)	770	787
Dynamic viscosity at 300 K (mPa.s)	0.50	0.5330
Surface tension at 300 K (mN/m)	23	22.51

Operating Conditions: In this study, the spray characteristics of methanol and gasoline are investigated at different injection pressures and ambient pressures for GDI pressure swirl injectors. The studied operating conditions are given in Table 2. These values given in Table 2 are selected from the following experimental studies [6, 15-20]. It should be noted that the hole diameter (0.5 mm) is for a Mitsubishi swirl-type GDI injector [16].

Table 2: *Operating Conditions*

Injector type	**GDI Pressure Swirl İnjector**
Injection pressure (MPa)	2, 3, 4, 5
Ambient pressure (MPa)	0.5, 1, 1.5
Ambient temperature (K)	300
Hole diameter of the nozzle (mm)	0.5

Results and Discussion: The variation of spray tip penetration depending on injection pressures (2, 3, 4, and 5 MPa) and ambient pressures (0.5, 1, and 1.5 MPa) for gasoline is shown in Figure 1. The spray tip penetration is calculated using Eq. (2). The spray tip penetration progressively rises over time following the injection, irrespective of injection pressure and ambient pressure. The spray tip penetration increases with increasing injection pressure under all investigated ambient pressures since the initial speed of the spray rises with rising injection pressure because of the increase in pressure difference [18]. Moreover, the spray tip penetration decreases under higher ambient pressure conditions compared to lower ambient pressures. This phenomenon occurs because elevated ambient pressure leads to a reduced pressure difference which decreases the fuel injection velocity [13]. Additionally, the increase in ambient pressure leads to greater ambient air density and an increased drag force on droplets which prevents penetration of spray into the combustion chamber [13]. For the injection pressure of 2, 3, 4, and 5 MPa, the maximum spray tip penetration is 33.6203 mm, 38.2000 mm, 41.5523 mm, and 44.2467 mm at 0.5 MPa ambient pressure; 25.5459 mm, 30.3793 mm, 33.6203 mm, 36.1273 mm at 1 MPa ambient pressure; and 19.4107 mm, 25.5459 mm, 29.0257 mm, and 31.5729 mm at 1.5 MPa ambient pressure, respectively.

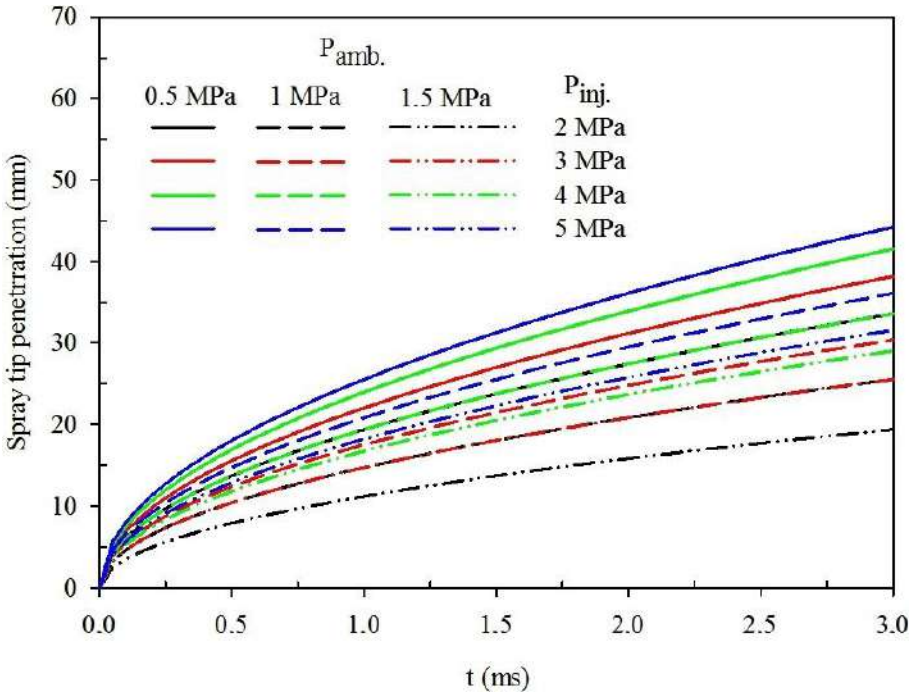

Figure 1: Variation of Spray Tip Penetration Depending On Injection Pressure and Ambient Pressure

Figure 2 shows the comparison of SMD values of gasoline and methanol depending on injection pressures (2, 3, 4, and 5 MPa) at an ambient pressure of 0.5 MPa. SMD values are computed using Eq. (1). Regardless of fuel type, SMD values decrease with increasing injection pressure since the increase in injection pressure (the increase in pressure difference raises the fuel injection velocity) induces more instability factors and adequate energy for break-up process [21]. Moreover, at each injection pressure, SMD values of methanol are somewhat higher than those of gasoline since methanol has higher density and dynamic viscosity preventing break into the spray. The lowest SMD value is determined as 13.0908 µm for gasoline at the injection pressure of 5 MPa. Figure 3 shows SMD values of gasoline at different ambient pressures (0.5, 1, and 1.5 MPa) and a constant injection pressure of 2 MPa. An increase in ambient pressure (i.e. increase in ambient gas resistance) results in an increase in SMD due to a decrease in pressure difference and low spray kinetic energy [21].

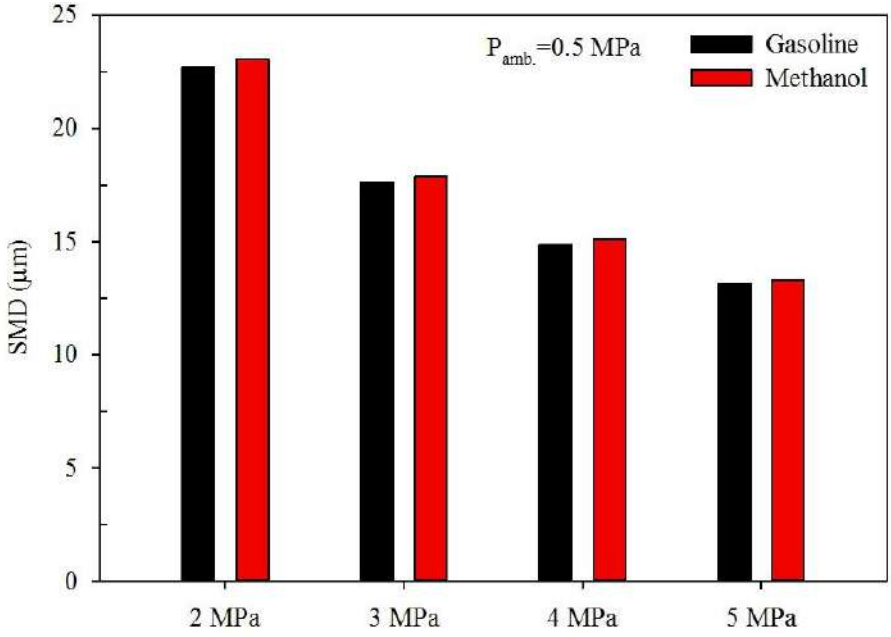

Figure 2: Comparison of SMD Values of Gasoline and Methanol under Different Injection Pressures

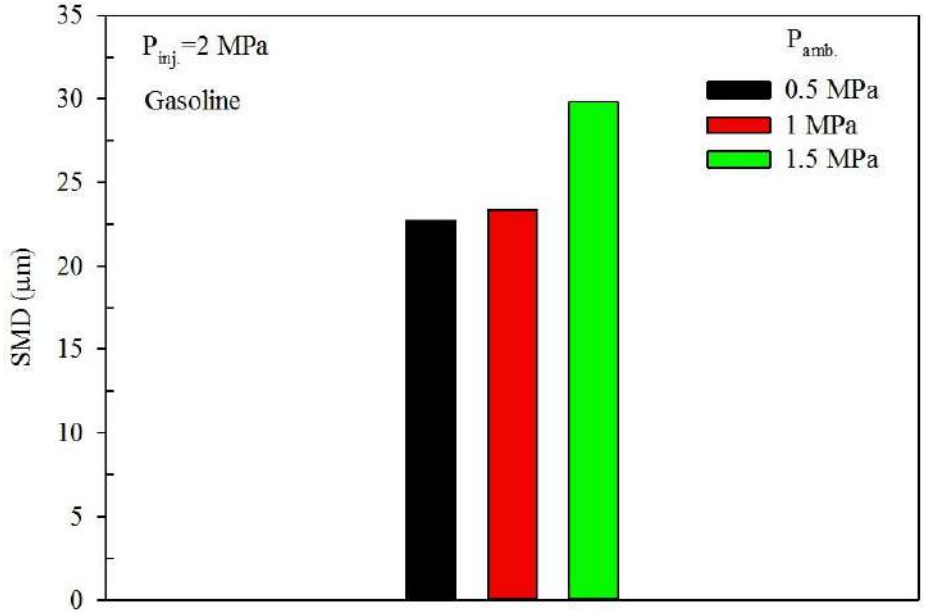

Figure 3: Variation of SMD Values of Gasoline under Different Ambient Pressures

Conclusions: Understanding spray characteristics is essential for optimizing mixture formation, enhancing combustion, and decreasing exhaust emissions in internal combustion engines. Therefore, this study investigates some spray characteristics of methanol and gasoline for a pressure swirl atomizer under different operating conditions. The main findings from this study include as following:

- Injection pressure effects: The spray tip penetration rises with rising injection pressure for gasoline under all ambient pressure conditions. However, for both fuels, SMD values decrease with higher injection pressure due to increased instability and greater energy for the breakup process.
- Ambient pressure effects: Higher ambient pressure leads to decreased spray tip penetration for gasoline due to the higher drop drag force. Moreover, higher ambient pressure increases SMD for gasoline.
- Fuel type: Methanol exhibits slightly higher SMD values compared to gasoline at each injection pressure, primarily due to the higher density and viscosity of methanol.

The numerical investigations of spray characteristics of alternative fuels for GDI engines using computational fluid dynamics can be studied under various operating conditions in future studies.

References: Arun, R. S., Kaushik, S. (December 17-20, 2021). The numerical analysis of spray formation for GDI system using dynamically coupled internal nozzle flow and ELSA spray simulation. Proceedings of the 26th National and 4th International ISHMT-ASTFE Heat and Mass Transfer Conference, IIT Madras, Chennai-600036, Tamil Nadu, India.

Badami, M., Bevilacqua, V., Millo, F., Chiodi, M., & Bargende, M. (2004). GDI swirl injector spray simulation: a combined phenomenological-CFD approach. SAE Transactions, 1620-1632. https://doi.org/10.4271/2004-01-3005

Bae, C., Shin, H., Choi, J., & Lee, S. (2000). Fuel-spray characteristics of high pressure gasoline injection in flowing fields. Proceedings of the 4th JSME-KSME Thermal Engineering Conference, 2, 685-690.

Baumgarten, C. (2006). Mixture formation in internal combustion engines. Springer-Verlag Berlin Heidelberg. DOI: 10.1007/3-540-30836-9. eBook ISBN: 978-3-540-30836-2. https://doi.org/10.1007/3-540-30836-9

Fiengo, G., di Gaeta, A., Palladino, A., & Giglio, V. (2013). Basic concepts on GDI systems. Common Rail System for GDI Engines: Modelling, Identification, and Control, 17-33. https://doi.org/10.1007/978-1-4471-4468-7_2

Gao, J., Jiang, D., & Huang, Z. (2007). Spray properties of alternative fuels: A comparative analysis of

ethanol–gasoline blends and gasoline. Fuel, 86(10-11), 1645-1650. https://doi.org/10.1016/j.fuel.2006.11.013

Gao, J., Jiang, D., Huang, Z., & Wang, X. (2005). Experimental and numerical study of high-pressure-swirl injector sprays in a direct injection gasoline engine. Proceedings of the Institution of Mechanical Engineers, Part A: Journal of Power and Energy, 219(8), 617-629. https://doi.org/10.1243/095765005X31333

Gao, J., Jiang, Huang, & Wei, Q. (2005). Characteristics of nonevaporating free sprays of a high-pressure swirl injector under various ambient and injection pressures. Energy & Fuels, 19(5), 1906-1910. https://doi.org/10.1021/ef0501344

Lefebvre, A. H. (1989). Atomization and sprays. Hemisphere Publishing Corporation, New York. https://doi.org/10.1201/9781482227857

Liu, L., Mei, Q., & Jia, W. (2022). A flexible diesel spray model for advanced injection strategy. Fuel, 314, 122784. https://doi.org/10.1016/j.fuel.2021.122784

McAllister, S., Chen, J. Y., Fernandez-Pello, A. C., McAllister, S., Chen, J. Y., & Fernandez-Pello, A. C. (2011). Premixed piston IC engines. Fundamentals of Combustion Processes, 199-226. https://doi.org/10.1007/978-1-4419-7943-8_10

Park, S. H., Kim, H. J., Suh, H. K., & Lee, C. S. (2009). Atomization and spray characteristics of bioethanol and bioethanol blended gasoline fuel injected through a direct injection gasoline injector. International Journal of Heat and Fluid Flow, 30(6), 1183-1192. https://doi.org/10.1016/j.ijheatfluidflow.2009.07.002

Properties of methanol. http://www.ddbst.de/en/EED/PCP/PCPindex.php#Methanol. Accessed: 03.10.2023.

Pulkrabek, W. W. (1997). Engineering fundamentals of the internal combustion engine. Prentice Hall Upper Saddle River, New Jersey.

Schmidt, D. P., Nouar, I., Senecal, P. K., Rutland, J., Martin, J. K., Reitz, R. D., & Hoffman, J. A. (1999). Pressure-swirl atomization in the near field. SAE Transactions, 471-484. https://doi.org/10.4271/1999-01-0496

Tian, J., Liu, Y., Bi, H., Li, F., Bao, L., Han, K., ... & Lin, Q. (2022). Experimental study on the spray characteristics of octanol diesel and prediction of spray tip penetration by ANN model. Energy, 239, 121920. https://doi.org/10.1016/j.energy.2021.121920

Wang, X., Chen, W., Gao, J., Jiang, D., & Huang, Z. (2007). Spray characteristics of high-pressure swirl injector fueled with alcohol. Frontiers of Energy and Power Engineering in China, 1, 105-112. https://doi.org/10.1007/s11708-007-0012-z

Wang, X., Gao, J., Jiang, D., Huang, Z., & Chen, W. (2005). Spray characteristics of high-pressure swirl injector fueled with methanol and ethanol. Energy & Fuels, 19(6), 2394-2401. https://doi.org/10.1021/ef050135w

Wang, X., Huang, Z., Kuti, O. A., Zhang, W., & Nishida, K. (2010). Experimental and analytical study on biodiesel and diesel spray characteristics under ultra-high injection pressure. International Journal of Heat and Fluid Flow, 31(4), 659-666. https://doi.org/10.1016/j.ijheatfluidflow.2010.03.006

Yamaguchi, A. (2020). Experimental investigation of ultra-high fuel injection pressure spray for GDI engines. Department of Mechanics and Maritime Sciences, Combustion and Propulsion Systems, Chalmers University of Technology (Thesis for the degree of Licentiate of Engineering), Gothenburg, Sweden.

Zhan, C., Feng, Z., Zhang, M., Tang, C., & Huang, Z. (2018). Experimental investigation on effect of ethanol and di-ethyl ether addition on the spray characteristics of diesel/biodiesel blends under high injection pressure. Fuel, 218, 1-11. https://doi.org/10.1016/j.fuel.2017.12.038

XI. LIST OF ABSTRACTS

Accelerating Renewable Energy Generation

Mao Miyazato

Toyohashi University of Technology, Toyohashi University of Technology, Toyohashi, Japan

Abstract: Accelerating renewable energy generation is essential for the development of a sustainable society. Anaerobic digestion (AD) is a potential system for accelerating clean energy production from organic waste; however, the biogas production efficiency of AD is still poor and requires improvement. Recently, the addition of granular activated carbon (GAC) and the use of microbial electrochemical technology（MET） has reported that the efficiency of biogas production can be improved by promoting electron transfer on microbial reactions in the AD system. GAC facilitates direct interspecies electron transfer (DIET) in the AD system and stabilizes biomass decomposition. The strong conductivity, large surface area, and adsorption capability of GAC were supposed to work as an electron conductor for the DIET effect. However, no precise relationship between biogas production rate and GAC characterization has been investigated. The objective of this study is to investigate the effect of carbon-based conductive materials characterizations on biogas production rate, utilizing AC, GAC, and Biochar with different pore sizes and volumes variation. Activated Carbon showed the fastest biogas production rate and the findings revealed that the growth of both micro and macro pores was the main cause for the acceleration of biogas production efficiency. Although it cannot be certain, earlier research suggested that micropores contribute to adsorption and macropores contribute to biofilm formation.

Artificial Neural Network-Based Prediction Model of Properties of Sic Ceramics for the Optimization of Surface Treatment Parameters

Auezhan Amanov

Mechanical Engineering, Sun Moon University, Korea

Abstract: In this study, a novel alternative approach is proposed that is based on the artificial neural network (ANN) concept for predicting the surface properties of SiC ceramic that is subjected to ultrasonic nanocrystal surface modification (UNSM) treatment. In the UNSM treatment, not only the static load but also the dynamic load is exerted. The UNSM treatment is conducted by striking a surface up to 20K times per second with an attached ball to the horn in the range of 1K-100K per square millimeter. Moreover, a post-deposition development of procedures for the successful utilization of UNSM technology in manufacturing will be discussed. The advantage will be taken to provide an understanding of the hardening mechanisms and the microstructural evolution occurring in SiC ceramic by ultrasonic nanocrystal surface modification (UNSM) technology. Experimental measurement data were used in the ANN training process and validation. The

trained model showed the capability of predicting the surface roughness and hardness accurately with a Pearson correlation value (R) of 0.984 and 0.997 for surface hardness and residual stress models when tested using the existing test dataset, respectively. It can be concluded that ANN as the alternative approach is a suitable method for accurately performing prediction for practical use in the absence of a mathematical model. Since the experimental result was used in the ANN model training process, the predicted result by the ANN model appears to agree with the experimental results of the UNSM treatment. Because of these demonstration results, the ANN-based prediction model can be used as a prediction tool to optimize the UNSM treatment parameters.

Optimization Principles of Eddy Current Separator for Mixtures with Different Particle Sizes

Bin Cao
Department of Design and Engineering (BU) & School of Metallurgy (NEU), Bournemouth University & Northeastern
University, United Kingdom & China

Yuan Yia
School of Metallurgy, Northeastern University, Shenyang 110819, China

Wang Qiang
Key Laboratory of Electromagnetic Processing of Materials (Ministry of Education), Northeastern University, Shenyang 110819, China

Amor Abdelkaderc
Department of Design and Engineering, Faculty of Science & Technology, Bournemouth University, Poole, Dorset BH12 5BB, United Kingdom

Ali Reza Kamalia
Energy and Environmental Materials Research Center (E2MC), Northeastern University, Shenyang 110819, China

Diogo Montalvãoc
Department of Design and Engineering, Faculty of Science & Technology, Bournemouth University, Poole, Dorset BH12 5BB, United Kingdom

Abstract: The study of the electrodynamic behavior of non-ferrous particles in time-varying magnetic fields is a promising area of research with wide applications, including recycling of non-ferrous metals, mechanical transmission, and space debris [1]. The key technology for recovering non-ferrous metals is eddy current separation (ECS), which utilizes the eddy current force and torque to separate non-ferrous metals. ECS has several advantages, such as low energy consumption, large processing capacity, and no secondary pollution, making it suitable for processing various mixtures like electronic scrap, auto shredder residue, aluminum scrap, and incineration bottom ash [2]. Improving the separation efficiency of mixtures with different particle sizes in ECS can create significant social and economic benefits. Our previous study [3] investigated the

influence of particle size on separation efficiency by combining numerical simulations and separation experiments. A strong correlation between the eddy current force in simulations and the repulsion distance in experiments was found by Pearson correlation analysis, which confirmed the effectiveness of our simulation model. The interaction effects between particle size and material type, rotational speed, and magnetic pole arrangement were examined, which offered some optimization criteria for eddy current separators. The mechanism behind the effect of particle size on separation efficiency was discovered by analyzing eddy current and field gradient. The results showed that the magnitude and distribution heterogeneity of eddy current and magnetic field gradient increased with particle size in eddy current separation. We have further found that increasing the curvature of magnetic field lines within particles can also increase the eddy current force, providing an optimized method to improve the separation efficiency of fine particles. Based on the results of the above-mentioned studies, a more systematic and comprehensive set of optimization guidelines can be proposed for mixtures with different particle size ranges. The separation efficiency of fine particles could be improved by increasing the rotational speed, curvature of magnetic field lines, and electrical conductivity/density of materials, as well as utilizing the eddy current torque. When designing an ECS, the particle size range of the target mixture should be investigated in advance, and the suitable parameters for separating the mixture can be fixed accordingly. The results can guide the design and optimization of ECS, and also expand the application areas for ECS.

Keywords: Eddy current separation, Metal recovery, Numerical simulation, Particle size.

References: 1. Nature, 2021. 598(7881): p. 439-443. 2. Minerals Engineering, 2019. 133: p. 149–159. 3. Powder Technology, 2022. 410: 117870.

Facile Sol-Gel Preparation of High-Entropy Multielemental Electrocatalysts for Efficient Oxidation of Methanol and Urea

Talifhani Mushiana

Chemistry, University of Science and Technology of China, Hefei, China

Abstract: High-entropy multi-elemental (HEM) electrocatalysts present superior catalytic performance due to the efficient synergism of their components. HEM electrocatalysts are usually prepared through hydrothermal reactions or calcination, which could generate undesired heterogeneous structures that hinder the exploration of the structure–property relationship of these HEM electrocatalysts. Herein, we report a sol-gel method to synthesize homogeneous HEM electrocatalysts for electro-oxidation of methanol and urea (methanol oxidation reaction (MOR) and urea oxidation reaction (UOR)), through an acid-catalyzed gelation at room temperature. With Ni as the primary component for MOR and UOR, Co can reduce the overpotentials, while Fe can increase the catalytic activities and durability. Borate and phosphate can tune the charge distribution in active sites and speed up the reaction kinetics through fast proton transfer. Thus, the optimal Ni2Fe0.5Co0.5-BP HEM catalyst demonstrates superior catalytic activity together with good durability and great resistance to CO poisoning. In addition, a direct methanol fuel cell with Ni2Fe0.5Co0.5-BP electrode can not only provide power, but also produce formic acid with high yield and high Faradaic efficiency. This work presents a simple strategy to prepare high-performance HEM electrocatalysts for fuel cells and production of value- added chemicals.

Keywords: Catalytic Oxidation Reaction, High-Entropy Multi-Elemental Electrocatalysts, Sol-Gel, Formic Acid

Performance Comparison of CNN-Based Image Classification Models to Detect Distracted Drivers

Alagan Anpalagan
Electrical and Computer Engineering, Toronto Metropolitan University, Ontario, Canada

Salman Ghaffar
Electrical and Computer Engineering, Toronto Metropolitan University, Ontario, Canada

Abstract: Vehicle accidents are a major concern in current transportation systems. Many of these accidents are caused by distracted driving such as using a mobile phone, talking to passengers, or smoking while behind the wheel. While efforts have been made to address this issue, there is no perfect solution. One potential approach is to use quantitative measures to assess driver activities and create a classification system that can detect distracting actions. In this paper, a range of deep learning models are implemented that can effectively classify driver distractions and increase driver awareness for improved safety. As a result of this experiment, it has been observed that base CNN model with seven convolutional layers when trained using augmented data performed the best in terms of accuracy; however, ResNet50 outperformed VGG16 based model when comparing transfer learning-based models. The accuracy difference between the best and worst performing models shows a significant difference; therefore, other metrics were also introduced to evaluate the performance like precision, recall and f1 score which also shows an increase in performance for ResNet50 model.
Keywords: CNN, Deep Learning Models, Driver Distraction, Detection, Data Sets

Impact Performance of 3D Printed Kevlar Fiber Reinforced Composites

Emre Oflaz
Department of Mechanical Engineering, TOBB University of Economics and Technology, Ankara, Turkey
Department of Mechatronics Engineering, KTO Karatay University, Konya, Turkey

Recep M. Gorguluarslan
Department of Mechanical Engineering, TOBB University of Economics and Technology, Ankara, Turkey

Emrah Celik
Department of Mechanical and Aerospace Engineering, University of Miami, 1251 Memorial Drive, Coral Gables, FL, USA

Teyfik Demir
Department of Mechanical Engineering, TOBB University of Economics and Technology, Ankara, Turkey

Abstract: As an additive manufacturing method direct ink writing (DIW) technique which based on deposition of rheologically adjusted ink to retain its shape during printing, is an emerging method to fabricate thermoset polymer composites. The aim of this study is to examine the impact strength (IS) and factors affecting IS of 3D printed composites via DIW. Method: Inks to print with DIW technique were prepared with thermoset epoxy, nanoclay, kevlar fibers (KF) and epoxy curing agent. Nanoclay was used to adjust ink viscosity and yield strength, and KF was used for composite reinforcement. Three main groups of inks were prepared. They are pure epoxy (PE) which has no nanoclay or KF, base-ink (BI) group which contains 5% and 8% volume by ratio (vbr) nanoclay but no KF, and KF reinforced (KFR) group which is prepared by adding 3.5% and 6.3% vbr KF into 5% BI. Specimens were printed and tested according to ASTM D4812 standard. Results were compared and statistically analyzed with Mann-Withney U test. Results: 5% BI has the highest average IS but no significant difference with 6.3% KFR. These two groups have significantly higher mean IS than all the other groups. PE group had significantly the lowest mean IS. 3.5% KFR group had lower mean IS that both 5% BI group and 6.3% KF group. 8% BI group had lower mean IS then 5% BI group. Conclusion: Nanoclay and fiber reinforcement have a significant positive effect on IS of 3D printed composite specimens, with some exceptions. Increasing the nanoclay from 5% to 8% vbr reduced IS, which was associated with embrittlement. Although 3.5% KF samples were prepared by reinforcing 5% vbr BI with KF, fiber loading to ink mixture caused unwanted pores which decreased IS. By increasing the KF amount to 6.3% vbr, IS increased, and which means increasing KF amount eliminated the strength loss caused by unwanted pores and had a positive effect on IS.
Keywords: Composite, Additive Manufacturing, Impact Test, Direct Ink Writing, Thermoset Polymer, Kevlar

Recent Advances and Challenges of Cobalt-Based Materials as Air Cathodes in Rechargeable Zn–Air Batteries

Girmaye Ambissa Begaw
Bahir Dar Energy center, Bahir Dar Institute of Technology, Bahir Dar University, Bahir Dar, Ethiopia

Abstract: To mitigate decades of extreme reliance on fossil fuels that have resulted in an increasingly serious energy shortage and environmental problems, extensive research on new clean renewable energy and energy storage technologies with high effectiveness, low cost, and environmental friendliness is required. Zinc-air batteries (ZABs) are effective tools for converting and storing renewable energy. Unfortunately, the low kinetics of the air cathode, as well as the oxygen reduction reaction (ORR) and oxygen evolution reaction (OER) are the principal drawbacks of ZABs. This necessitates the development of high-performance catalysts to accelerate the reaction rates and improve their efficiency. Cobalt-based carbon is an excellent choice for oxygen electrocatalysts due to its low cost, high activity, and stability. Recent advancements in cobalt-based carbon materials used as electrocatalysts in ZABs, as well as the characterization techniques and synthesis procedures, are covered in this paper. It also introduces and analyzes the fundamental mechanisms of ORR and OER electrocatalysis. Finally, we give a description of the present difficulties and potential future developments in the creation of novel high efficiency and bifunctional electrocatalysts.
Keywords: Zinc-Air Batteries, Cobalt-Based Materials, Electrocatalyst, ORR/OER

Web Page Content Block Labeling: A New Approach for Sibling Block Detection

Kiril Griazev
Department of Information Technologies, Vilnius Gediminas Technical University, Vilnius, Lithuania

Abstract: Web sites are developed to present content and lack data tagging to simplify content integration with other systems - integration requires template definition. The potential for integrated data and web data mining content is on the rise, however it requires manual labeling of web site content blocks. This is a time-consuming task and solutions to simplify web page content block labeling would be beneficial in terms of website content block dataset preparation. This paper presents a comprehensive examination of a novel technique for detecting remote sibling blocks in the HTML structure of web pages. It emphasizes its application to automatic web page content labeling. The proposed approach focuses on the identification of two types of content block sibling relationships - 'loose' and 'strict'. Conducted research demonstrated a significant 84% reduction in content blocks selected for labeling due to this method. This improves the labeling process efficiency. These findings offer a promising avenue for improving automatic content labeling and potentially other applications that involve HTML structure analysis.

Molecular Complexes of Five Tricyclic Antidepressants with Chloranilic Acid: Determination of Stoichiometric Ratios, Molar Absorptivities And Stability Constants in Acetonitrile-Chloroform Solvent

Radu Racovita
Department of Inorganic Chemistry, Physical Chemistry and Electrochemistry, University Politehnica of Bucharest, Bucharest, Romania

Maria-Daniela Ciuca
Research Center for Environmental Protection and Eco-Friendly Technologies, University POLITEHNICA of Bucharest, Bucharest, Romania

Daniela Catana
Research Center for Environmental Protection and Eco-Friendly Technologies, University POLITEHNICA of Bucharest, Bucharest, Romania

Maria Mihaly
Department of Inorganic Chemistry, Physical Chemistry and Electrochemistry & Research Center for Environmental Protection and Eco-Friendly Technologies, University POLITEHNICA of Bucharest, Bucharest, Romania

Abstract: Depression is the most common mental condition affecting modern society. An estimated one million people commit suicide every year as a consequence of this serious illness. Therefore, new treatment options are permanently sought, antidepressant medications being often used in combination with psychotherapy. Although tricyclic antidepressants (TCAs) have started to be replaced by newer generation

drugs, they are still used in the treatment of major depressive disorder and some other variants. Methods for monitoring TCA levels in the blood of patients receiving treatment or for TCA residues in environmental samples are thus urgently needed. While TCAs have spectral bands in the UV domain, these are often affected by interference from matrix components, leading to inaccuracies in quantitation. Reactions with selective reagents leading to colored products with absorption bands in the visible region are more convenient for common laboratory settings. If the colorimetric reaction is preceded by a solvent-extraction that isolates TCAs from the aqueous sample, the advantages are obvious. In this work, we present a method of extraction of TCA hydrochlorides from aqueous samples with chloroform, following alkalization, and subsequent colorimetric reaction with chloranilic acid in acetonitrile yielding molecular complexes with absorption bands around 530 nm, which serve for accurate quantitation of five TCAs in amounts ranging from tens to hundreds of ppm. In addition to typical method performance parameters (limit of detection, linear range, sensitivity, etc.), the stoichiometric combination ratio was determined using Job's method and the molar absorptivities and stability constants of resulting complexes were determined from absorbance measurements of several equilibrium mixtures. While the stoichiometry remained 1:1, the other parameters differed, reflecting different donor abilities of TCAs with respect to the chloranilic acid acceptor. Acknowledgment: This work was supported by a grant of the Ministry of Research, Innovation and Digitization, CNCS – UEFISCDI, project number PN-III-P1-1.1-TE-2021-1216, within PNCDI III.
Keywords: Chloranilic Acid, Tricyclic Antidepressant, Job's Method, Molar Absorptivity, Stability Constant

Simulating Molecular Optical Properties of Polyimide for Nonvolatile Resistive Photomemory Devices

Tang-Yi Liu
Department of Electronic Engineering Feng Chia University Taichung, Taiwan

I-Ming Tseng
Department of Electronic Engineering Feng Chia University Taichung, Taiwan

Yi-Huan Pan
Department of Electronic Engineering Feng Chia University Taichung, Taiwan

Pin-En Hsu
Department of Electronic Engineering Feng Chia University Taichung, Taiwan

Wei-Cheng Ou
Department of Electronic Engineering Feng Chia University Taichung, Taiwan

Pei-Ying Jiang
Department of Electronic Engineering Feng Chia University Taichung, Taiwan

Wen-Luh Yang
Department of Electronic Engineering Feng Chia University Taichung, Taiwan

Abstract: In this study, the focus was on utilizing the polyimide (PI) thin film as a resistive conversion layer

for organic polyimide-based resistive random-access memory (ReRAM) applications. We utilized the 3D molecular editor WebMO to manipulate and analyze the structures of Aromatic-PI and Quinoid-PI molecules. The molecular chain length, molecular weight, and HOMO/LUMO molecular orbitals were investigated to gain insights into the fundamental properties of PI molecular structures. The analysis revealed that the Quinoid-PI molecule exhibited a shorter molecular chain compared to Aromatic-PI, attributed to the inability of the cyclic structure in Quinoid-PI to maintain a planar conjugated structure, resulting in an uneven overall structure and reduced molecular chain length (Norcorss, 1988). The research results demonstrate that the optical energy gap of Aromatic-PI remains constant regardless of the number of molecular bonds, with a value of approximately 3.2661 eV. In contrast, for Quinoid-PI, the optical energy gap undergoes a significant decrease as the number of molecular bonds ranges from 1 to 5. As the bond count increases to 20~23, the change in the optical energy gap gradually diminishes, ultimately resulting in an optical energy gap of 0.6932 eV. This observation indicates that longer molecular chains composed of Aromatic-PI act as insulators, while Quinoid-PI transforms into a low-energy gap conductor.

Keywords: Nonvolatile, Photomemory, Polyimide, Simulation, Polymer Organic Material

Comparative Study to Housing Defect Repair Cost through Multiple Regression Analysis

Professor Seo Deok-Seok

School of Architectural Engineering, Halla University, Wonju-Si, Republic of Korea

Abstract: Despite stiff competition in the construction industry, housing quality remains a problem. These quality problems are called defects. Homeowners are experiencing inconvenience and suffering due to home defects, and developers and builders also get severe damage in time, costs, and reputation due to defect repairs. In Korea, lawsuits are increasing due to the rise in housing defects, and the cost of repairing defects determined by lawsuits is of great concern. This study introduced a multiple regression model to predict housing defect repair costs. The repair costs of defects confirmed in a lawsuit against 100 housing complexes in Korea were analyzed. In prior studies, the elapsed period, lawsuit period, value of the subject matter in the litigation, home warranty deposit, total floor area, number of households, main building' quantity, construction cost, location, and highest floor number of main buildings were used as variables. This study judged the total floor area, elapsed period, and lawsuit period as influential independent variables. Moreover, a regression model that predicted defect repair cost using the selected independent variables was proposed. For this model, linearity was assumed, and there was no problem with the independence of residuals and multicollinearity. In addition, the coefficient of determination in this regression model was superior to those models in the preceding studies. Therefore, the regression model suggested in this study might be the most excellent for the studied cases.

Characteristic of the Catalyst for Water Gas Shift Reaction

Cheol-Hwi RYU

Grad. School, Dep. Green Energy Engineering, Hoseo University, Republic of Korea

Min-Ji Kang

Grad. School, Dep. Green Energy Engineering, Hoseo University, Republic of Korea

Jin-Bae Kim

Grad. School, Dep. Green Energy Engineering, Hoseo University, Republic of Korea

Gab-Jin Hwang

Grad. School, Dep. Green Energy Engineering, Hoseo University, Republic of Korea

Abstract: Recently, the waste plastics were occurred the problem in environmental pollution. Many researches are being conducted for the oilification and gasification by the thermal decomposition of waste plastics to solve those problem. In particular, the research is being proceed the production of hydrogen from the carbon monoxide (CO) gas in the syngas (CO+H2) produced by the gasification of waste plastics. The hydrogen production method using CO gas is representative of the water gas shift reaction (WGSR, CO+H2O→H2+CO2). WGSR consists of a process of first generating hydrogen in a high-temperature shift reaction (HTSR, ~500℃) and secondarily generating hydrogen in a low-temperature shift reaction (LTSR, ~300℃). In this research, it was carried out the preparation of Fe/Cr/M catalyst (M=Mg, Cu) for the HTSR and Cu/Zn/Al and Ni/Ce catalyst for the LTSR by the co-precipitation method. And the water gas shift reaction using the prepared catalyst was performed.

Keywords: Hydrogen Production, Water Gas Shift Reaction, Catalyst, High Temperature Shift Reaction, Low Temperature Shift Reaction

Compaction Characteristics Predictive Model from Index Properties of Fine - Grained Soils, Case in Mekelle City, Northern Part of Ethiopia

Freweyni Kassa

Department of Civil Engineering, Ethiopia Institute of Technology, Mekelle, Ethiopia

Abstract: The compaction test Optimum moisture content (OMC) and Maximum dry density (MDD) has been acknowledged as an important parameter to characterize the strength/bearing capacity of earth structures. Technically, the compaction tests are carried out in the laboratory or in the field. However, in large construction sites, the test is a routine time-consuming which requires large amount of soils for laboratory testing and is infrequently performed due to the equipment needed and the fact that the field moisture content keeps changing over time. Over the years, many correlations have been developed for the prediction of OMC and MDD by various researchers. However, in this paper the data are transformed and the empirical predictive models have checked the multicoliniarity and interaction of the predictor parameter was analyzed through the NCSS software and it gives better R2 and RMSE value compared with other models. Therefore, the objective is to develop a compaction predictive model of fine grained soil from their index properties. Accordingly, a total of 24 primary, 91 secondary standard proctor tests data and 114 secondary modified proctor test data were collected from the northern Ethiopia. Specific to this research, statistical software (NCSS-12) was employed. NCSS software has a full array of powerful software tools for regression analysis.

The results show that about five (5) equations with subset selection trials for each modeling one, two and three Parameters OMC and MDD models from various soil index properties were performed. Subset selection with interaction option of the NCSS-12 statistical software is used for the task of finding variables that does a good job of predicting the dependent variable. Moreover, the unique nature of the developed models utilizes only three parameters namely percentage pass of (P200), Liquid limit (LL) and plastic limit (PL) which are simple and to test than compaction tests.
Keywords: Compaction, Index Properties, Predictive Model, NCSS-12, North Ethiopia

Multiple Correlations to Predict Cetane Number of Pure Biodiesels Depending on Other Fuel Properties

Mert Gulum
Faculty of Engineering, Karadeniz Technical University, Trabzon, Turkey

Abstract: The increasing energy demand, swift exhaustion of fossil fuels, and looming environmental threats have sparked novel research endeavors to explore alternative fuels for traditional petroleum fuels. Among alternative renewable fuels, biodiesel has obtained considerable attention over the past decade due to its advantages over diesel fuel (biodegradable, non-toxic, low sulphur, higher flash point, etc). Density, viscosity, heating value, flash point, and cetane number are among the most important fuel properties. Cetane number defines the ignition quality of a fuel. In the existing literature, by using multiple linear regression, machine learning methods, and group contribution methods, the correlations are derived to predict the cetane number of pure biodiesel depending on its properties (the composition of fatty acid esters, the number of carbon atoms, the number of double bonds, the allylic position of the fatty acid esters, the molecular weight of the fatty acid esters, the chain length, the saponification number, the iodine value, etc.). However, a few researchers have made efforts to establish a correlation between the cetane number and other important fuel properties. Therefore, this study aims to employ multiple regression for the prediction of the cetane number of pure biodiesels depending on density, viscosity, heating value, and flash point. For obtaining predictive correlations, the experimental data on the fuel property from the literature covering 100 different biodiesels (methyl and ethyl esters) are collected. Prediction performance factors of R2 (higher than 0.9994) as well as the maximum relative errors (lower than 5%) are calculated for the derived multiple correlations. Such results illustrate high levels of accuracy are achieved in successfully obtaining for estimating cetane number.
Keywords: Biodiesel, Fuel property, Cetane number, multiple regression

Anomaly Detection on Images

Kubra Korkmaz
Mathematics, Marmara University, Istanbul, Turkey

Abstract: Anomaly detection in images has started to be used frequently in many fields such as agriculture, health and security. Along with the developing technology, much progress has been made in this field in a short time, and many methods have been developed as a result of studies on anomaly detection. In this study, a compilation of current anomaly detection techniques adapted for image data is made. While making an evaluation of the existing methods, Producer Contention Networks were also examined in detail. Anomaly detection can be examined in two main branches as traditional methods and modern approaches. While its traditional methods create techniques such as Statistical Methods and Texture Analysis, modern approaches include Machine Learning, Convolutions Neural Networks and Autoencoders. In this study, modern approaches are included. In addition, Producer Contested Networks, which have developed in recent years and are used in anomaly detection, are given in detail along with their varieties. However, the usage areas, efficiency, advantages and disadvantages of these methods are given together. Finally, some ideas for future work are presented.
Keywords: Anomaly Detection, Generative Adversarial Networks, Image Anomaly

References:

Çelikhası, C. (2020). Derin öğrenme algoritmaları ile biyomedikal görüntülerden anomali tespiti (Master's thesis, Kocaeli Üniversitesi, Fen Bilimleri Enstitüsü).

Creswell, A., White, T., Dumoulin, V., Arulkumaran, K., Sengupta, B., & Bharath, A. A. (2018). Generative adversarial networks: An overview. IEEE signal processing magazine, 35(1), 53-65. https://doi.org/10.1109/MSP.2017.2765202

Da Costa, K. A., Papa, J. P., Passos, L. A., Colombo, D., Del Ser, J., Muhammad, K., & de Albuquerque, V. H. C. (2020). A critical literature survey and prospects on tampering and anomaly detection in image data. Applied Soft Computing, 97, 106727. https://doi.org/10.1016/j.asoc.2020.106727

Deecke, L., Vandermeulen, R., Ruff, L., Mandt, S., & Kloft, M. (2019). Image anomaly detection with generative adversarial networks. In Machine Learning and Knowledge Discovery in Databases: European Conference, ECML PKDD 2018, Dublin, Ireland, September 10–14, 2018, Proceedings, Part I 18 (pp. 3-17). Springer International Publishing. https://doi.org/10.1007/978-3-030-10925-7_1

Di Mattia, F., Galeone, P., De Simoni, M., & Ghelfi, E. (2019). A survey on gans for anomaly detection. arXiv preprint https://doi.org/10.48550/arXiv.1906.11632

Gui, J., Sun, Z., Wen, Y., Tao, D., & Ye, J. (2021). A review on generative adversarial networks: Algorithms, theory, and applications. IEEE transactions on knowledge and data engineering, 35(4), 3313-3332. https://doi.org/10.1109/TKDE.2021.3130191

Haselmann, M., Gruber, D. P., & Tabatabai, P. (2018, December). Anomaly detection using deep learning based image completion. In 2018 17th IEEE international conference on machine learning and

applications (ICMLA) (pp. 1237-1242). IEEE. https://doi.org/10.1109/ICMLA.2018.00201
Li, D., Chen, D., Goh, J., & Ng, S. K. (2018). Anomaly detection with generative adversarial networks for multivariate time series. arXiv preprint https://doi.org/10.48550/arXiv.1809.04758
Matteoli, S., Diani, M., & Corsini, G. (2010). A tutorial overview of anomaly detection in hyperspectral images. IEEE Aerospace and Electronic Systems Magazine, 25(7), 5-28. https://doi.org/10.1109/MAES.2010.5546306
Mirza, M., & Osindero, S. (2014). Conditional generative adversarial nets. arXiv preprint arXiv:1411.1784.
Mohammadi, B., Fathy, M., & Sabokrou, M. (2021). Image/video deep anomaly detection: A survey. https://doi.org/10.48550/arXiv.2103.01739
Salimans, T., Goodfellow, I., Zaremba, W., Cheung, V., Radford, A., & Chen, X. (2016). Improved techniques for training gans. Advances in neural information processing systems, 29.
Yang, J., Xu, R., Qi, Z., & Shi, Y. (2021). Visual anomaly detection for images: A survey. https://doi.org/10.1016/j.procs.2022.01.057
Yilmaz, F. N., Arisoy, S., & Kayabol, K. (2021, June). Unsupervised Hyperspectral Anomaly Detection with Convolutional Neural Networks. In 2021 29th Signal Processing and Communications Applications Conference (SIU) (pp. 1-4). IEEE. https://doi.org/10.1109/SIU53274.2021.9477870
Zenati, H., Foo, C. S., Lecouat, B., Manek, G., & Chandrasekhar, V. R. (2018). Efficient gan-based anomaly detection. https://doi.org/10.48550/arXiv.1802.06222 .

Facile Synthesis of an Efficient Antimicrobial Agent as a Promising Therapeutic Drug: Preparation, In Vitro Antimicrobial Evaluation, In Silico Molecular Docking, Drug-Likeness, Pharmacokinetics and Toxicology Prediction

Dr Zakia Hank
Department of Chemistry, University of Sciences and Technology Houari Boumedienne (Usthb), Algiers, Algeria

Noura Kichou
Department of Chemistry, University of Sciences and Technology Houari Boumedienne (Usthb), Algiers, Algeria

Sultana Boutaminea
Department of Chemistry, University of Sciences and Technology Houari Boumedienne (Usthb), Algiers, Algeria

Abstract: Nowadays, antimicrobial resistance in pathogenic bacteria poses a big challenge to discover and design novel antimicrobial agents. The use of transition metals with biologically active ligands is yielding an

unprecedented progress in biological applications. New compounds are developed, with higher biological activity compared to the free ligands. Sorbates are well-known antimicrobial agents, widely used in Food and pharmaceutical landscape. However, metal complexes based on sorbates are far less explored in this regard. This article deals with the coordination behavior of sorbate ligand with copper (II) cation. A variety of techniques were utilized to characterize the Cu(II) sorbate complex. The antimicrobial *properties* of sorbate and its Cu(II) complex were studied in vitro, the complex showed promising antibacterial activity with a quite low MIC value, compared to the free ligand. The structure of the two compounds were subjects to density functional theory (DFT) optimization to prepare them for molecular docking. The optimized structures of both ligand and Cu(II) complex were docked on the active site of DNA gyrase B (PDB ID: 6KZV), to identify the possible interactions causing the inhibition of the tested bacteria. These results were complemented with in silico prediction of drug-likeness pharmacokinetic and toxicity of the newly compound. The findings presented in this study showed that the designed coordination complex might be used not only as potential antibacterial agent but also as a novel therapeutic drug.

Keywords: Drug discovery, Copper-sorbate complex, Crystal structure, Antibacterial resistance, In silico prediction.

Quantitative Analysis of Microvesicles Storage Stability

Sevindzh Kletukhina

Institute of Fundamental Medicine and Biology, Kazan (Volga region) Federal University, Kazan, Russian Federation

Marina Gomzikova

Institute of Fundamental Medicine and Biology, Kazan (Volga region) Federal University, Kazan, Russian Federation

Purpose: Currently, microvesicles of human cells are attracting increased attention of researchers and physicians around the world. Microvesicles (MV) are spherical structures surrounded by a cytoplasmic membrane, released from the cell surface, contain the cytoplasmic content of the parent cell and have a size of 50-2000 nm. The use of MVs from mesenchymal stem cells in medicine as therapeutic agents and drug delivery vectors is of great interest. However, a quantitative assessment of the stability of isolated MVs in solution remain limited investigated. Therefore, the aim of our work is to evaluate the storage stability of MVs-MSCs under various storage conditions within 112 days.

Keywords: Microvesicles, Mesenchymal Stem Cells, Drug Delivery Vectors.

Material & Methods: Microvesicles were obtained by treating MSCs with 10 μg/ml cytochalasin B as described previously. Cytochalasin B is an agent for the cell cytoskeleton disorganization and used in the mass production of MVs. Obtained MVs were resuspended in saline and stored under different conditions at: -20°C, 4°C, 25°C, and 37°C, freeze dried and stored at -20°C. Quantity of MVs was analyzed using flow cytometry with enhanced detector (BD FACS Aria III BD Bioscience, USA).

Results: We found that after 7 days of storage at 37°C only 30% of MVs remained intact. Storage at 25°C for 28 days allowed only 47% of the original amount of MVs to be retained, whilst storage at 4°C kept 59% of the MVs and extended the MVs shelf life to 112 days. Freeze-drying resulted in 49% of the intact MVs been retained. Whereas freezing of MVs suspended in saline at -20°C retained 79.5% MVs after 112 days of storage.

Conclusion: Thus, the storage of MVs-MSCs in saline at -20°C for at least 112 days is the most suitable retention condition for MVs.

Funding: This work was funded by Russian Government Program “Recruitment of the Leading Scientists into the Russian Institutions of Higher Education” (grant number 075-15-2021-600). This work was supported by the Kazan Federal University Strategic Academic Leadership Program (PRIORITY-2030).

Exosome-Like Particles Remain in Fetal Bovine Serum after Depletion by Ultracentrifugation

Valeriia Syromiatnikova
Institute of Fundamental Medicine and Biology, Kazan Federal University, Kazan, Russia

Gomzikova M.O
Institute of Fundamental Medicine and Biology, Kazan Federal University, Kazan, Russia

Introduction: Extracellular vesicles (EVs) are widely studied as carriers of cellular signals involved in many physiological and pathological processes. EVs of cultivated cells are isolated from conditioned medium containing fetal bovine serum (FBS), which is known to contain its own xenobiotic EVs. In order to eliminate EVs of FBS from nutrient medium, FBS was ultracentrifugated 18h at 100000g, +4˚C. The aim of this study was to determine whether 18h of ultracentrifugation completely eliminate EVs from nutrient medium. **Materials and methods**: To prepare EVs-depleted FBS, 50 ml of FBS was centrifuged for 18h at 100,000g in an Optimal L-90K ultracentrifuge (Beckman Coulter). Next, the supernatant was taken and full medium DMEM containing 2 mM L-glutamine, 10% FBS, 1x mixture of antibiotics penicillin and streptomycin was prepared. Amount of EVs was assessed using nanoparticle tracking analysis (NTA) using NanoSight LM-10. **Results**: We found exosome-like particles in the medium prepared using EVs-depleted FBS. The amount of exosome-like particles was 3,2x1010 particles/ml with 70±45 nm in size. The obtained data indicate that ultracentrifugation of FBS at 100000g during 18h does not lead to complete elimination of xenobiotic EVs. Thus, the presence of residual exosome-like particles of FBS in the nutrient medium can introduce a significant inaccuracy in the calculation of yield of EVs derived from cultivated cells.
Funding: This work was funded Russian Government Program “Recruitment of the Leading Scientists into the Russian Institutions of Higher Education” (grant number 075-15-2021-600).
Disclosure: The authors confirm that they have no conflict of interest.

Ultrasound-Mediated Generation of Membrane Vesicles from Human Cells

Anna Doinikova
Institute of Fundamental Medicine and Biology, Kazan Federal University, Kazan, Russia

Syromiatnikova V.Y
Laboratory of Molecular immunology, Kazan Federal University, Kazan, Russia

Khannanov A.A.
Laboratory of Modular Systems Based on Metal-Containing Polymers with Bifunctional Activity Therapeutic Agent/Vector for Targeted Drug Delivery, Kazan Federal University, Kazan, Russia

Gomzikova M.O
Laboratory of Molecular immunology, Kazan Federal University, Kazan, Russia

Introduction: Extracellular vesicles (EVs) produced by cells are natural carriers of biological molecules. Due to their ability to encapsulate various substances and penetrate physiological barriers, they are widely studied as drug delivery vehicles. However, the introduction of EVs into clinical practice is difficult due to the lack of an industrially adapted production method, which ensures their obtaining in meaningful amounts, integrity, homogeneity, and preservation of biological activity of vesicles. Therefore, the goal of our work was to increase the yield of vesicles by ultrasound-mediated generation of membrane vesicles from human cells.

Materials and methods: We isolated natural EVs from conditioned medium obtained as a result of 48-hour incubation of murine adipose tissue MSCs in exosome-depleted medium by ultracentrifugation at 100,000g for 16 h. Natural EVs were isolated by sequential centrifugation at 1) 150g - 10 min; 2) 150g - 20 min; 3) 2300g - 10 min; 4) 10,000g - 45 min; 5) 100,000g - 90 min. To generate vesicles, a suspension of adipose mesenchymal stem cells was treated by ultrasound (US) using a Sonopuls HD 2200 ultrasound homogenizer with a working frequency of 20 kHz for 1 min at 4°C in the mode: amplitude 20%, cycle 5 (working step - 0.5 sec, idle step - 0.5 sec). The vesicles were precipitated by centrifugation at 10,000 g for 45 min and resuspended in DPBS followed by filtration (pore size 1 μm). The morphology of the US-induced vesicles was examined using a Merlin analytical scanning auto emission electron microscopy system. The concentration and size of US-induced vesicles were analyzed using NanoSight LM10.

Results: We found that the US-induced vesicles were round-shaped membrane structures. The average particle size was found to be (115±52 nm) and the number of vesicles was 54,000 particles/cell. The exit of natural vesicles was 55,400 particles/cell.

Conclusion: The method of US-induced vesicles processing makes it possible to obtain vesicles, in a short period of time and with less labor, which makes it a promising way of mass production of vesicles, stimulating their introduction as a means of drug delivery into clinical practice.

Funding. This work was part of Kazan Federal University Strategic Academic Leadership Program (PRIORITY-2030) and funded by Russian Government Program “Recruitment of the Leading Scientists into the Russian Institutions of Higher Education” (grant number 075-15-2021-600).

Disclosure: The authors confirm that they have no conflict of interest.

Combination "Resistant Variety X Botanical Treatment": A Simple Integrated Management Method of Fusarium Wilt of Onion

Pawinde Elisabeth Zida

Institute of the Environment and Agricultural Research, National Center for Scientific and Technological Research, Ouagadougou, Burkina Faso

Abstract: Onion is one of the major vegetables grown in Burkina Faso with an average production of 362,480T. In field, fungi cause between 10 and 23% annual crop losses, in addition to 10 to 20% post-harvest losses. The use of synthetic fungicides remains the main means of combating these pathogens, however, with multiple consequences: development of resistance and toxicity for humans, the environment and animals. Face to these problems and to boost onion production, the use of control practices that are consistent, sustainable, adapted to small farmers and ensuring healthy protection of the crop is needed. The present study aimed to demonstrate to farmers and agricultural support agents that by combining varietal resistance with an antifungal treatment based on plant extract, it is possible to effectively combat Fusarium wilt and significantly increase production. For this, the reaction of five local cultivars to Fusarium wilt was evaluated with a view to identifying those resistant or tolerant, botanical extracts were evaluated in seed or plant treatment, in order to identify those capable of effectively combating Fusarium wilt, and, finally, different "cultivar-antifungal treatment" combinations were evaluated in order to determine the best combination for integrated management of Fusarium wilt. According to the results obtained, the Zimtanga cultivar was more tolerant to the disease than the Violet de Galmi variety, recognized as a susceptible variety. Treatment with essential oils of *L. multiflora* and *O. americanum* contributed to reduce damping offs to 10-15% compared to 50% for the untreated control, with an increase in bulb production of 199.11-204.32 g and 85.31-145.15 g, respectively, compared to the untreated control, with only 30.31-62.73 g of bulbs. Among the combinations, "Zimtanga- *L. multiflora* essential oil", significantly reduced damping off and increased bulb production. Thus, the study showed that there is an integrated method to effectively combat Fusarium wilt of onions in Burkina Faso.

Keywords: Onion, Antifungal Treatment, Essential Oils, Fusarium Wilt, Integrated Control

Delay of Final Account Closing in Malaysia Construction Projects: Implication on Project Implementation

Zakaria Zarabizan

Implementation Coordination Unit, Prime Minister's Department, Putrajaya, Malaysia

Abstract: Delays in preparing and issuing the final account in the final phase of the contract for a construction project are often taken easy by construction industry players. In fact, there are also cases brought to court judgment due to failure in finalising the final account. This shows why it is necessary for the final account to

be prepared within the time period stipulated in the contract. To delve into this issue, this paper is to examine the causes of delay in the preparation of the final account closing and its implications to a project in terms of its implementation if the final account is not resolved within the stipulated period stated in the contract. This aim can be achieved via its objectives and a questionnaire survey was designed based on literature review, case studies and interviews. Therefore, this paper focuses on construction projects of contractor category G7, where 30 respondents who have experience in issues or problems related to the final account closing are involved in the data collection process. The results of the study found that all respondents have stated that the main cause of delay in the final account closing is due to incomplete documentation. While the implications faced by the contractor contributed to the company's cash flow disruption. This paper not only provides an overview of the urgent need for an appropriate action plan in overcoming the problem of delay in the final account closing, but is also in line with the Public Works Department's policy, guidelines, and the standard contract form.

Keywords: Final Account Closing, Delay, Construction Project, Implementation, Malaysia

Strategic Challenges of Poultry Farming in Northern Malaysia: A Case Study on Rural Community in Kedah

Risyawati Mohamed Ismail
Food Security, Innovation and Development Research Centre (FInDER), School of Technology Management & Logistics, Universiti Utara Malaysia, Sintok Kedah, Malaysia

Siti Zakiah Abu Bakar
Food Security, Innovation and Development Research Centre (FInDER), School of Technology Management & Logistics, Universiti Utara Malaysia, Sintok Kedah, Malaysia

Mastora Mustafar
Food Security, Innovation and Development Research Centre (FInDER), School of Technology Management & Logistics, Universiti Utara Malaysia, Sintok Kedah, Malaysia

Abstract: The agricultural sector in Malaysia's rural areas plays a substantial part in the nation's economy, serving as a crucial source of employment and income for numerous communities. Based on the findings of the Department of Statistics Malaysia (2019), it has been determined that the agricultural industry in Malaysia sustains an estimated workforce of around 3.5 million individuals, while simultaneously making a notable contribution of approximately 9.1% to the nation's Gross Domestic Product (GDP). The poultry farming sector holds significant importance within the Malaysian context, as it serves as a crucial industry that generates employment opportunities and money for numerous rural areas. To achieve success, poultry producers must possess a comprehensive comprehension of the market dynamics and formulate strategic initiatives to effectively cater to the requirements of the animal breeding sector. The main objective of this paper was to present a comprehensive analysis of the strategic principles governing chicken farming in rural regions of Malaysia, specifically highlighting a case study involving an economically disadvantaged group

residing in a rural setting. The case study showed the practical use of these rules within a real-life context and the consequential effects they can exert on comparable communities. The data for this study was gathered using a qualitative approach, specifically through face-to-face interviews with the participants. The primary emphasis of the interview revolved around the various obstacles and issues encountered by farmers in the process of chicken rearing. The data that was gathered was subsequently examined in a manner consistent with established methodologies. The findings of the study revealed that the primary obstacles encountered by poultry breeding farmers include the absence of extension agents, limited technical knowledge among farmers, insufficient finance, and inadequate communication infrastructure. The aforementioned issues frequently led to the abandonment of their poultry farm, prompting a transition to alternative economic endeavors, such as rubber tapping. Although the latter option provides individuals with a reduced level of financial reward, it is comparatively less challenging to sustain. The present study provides significant contributions to the understanding of the impact of community empowerment on fostering sustainable rural development. Through a comprehensive comprehension of the dynamics inherent in community-led projects, policymakers and development practitioners possess the ability to construct precise policies aimed at uplifting rural communities, thereby cultivating resilience and facilitating sustainable long-term growth. Future research should look in-depth the governing agencies involvement in the sustainability of such rural economic activity and how it could help strengthened the supply chain involved.

Keywords: Rural development, community empowerment, sustainability, agriculture, farmers, Malaysia

Sustainable Intelligent Operation and Maintenance Theoretical Methods and Application Research in Large Infrastructure Buildings

Zedong Jiao
Faculty of Architecture, Civil and Transportation Engineering, Beijing University of Technology, Beijing, China

Xiuli Du
Faculty of Architecture, Civil and Transportation Engineering, Beijing University of Technology, Beijing, China

Zhansheng Liu
Faculty of Architecture, Civil and Transportation Engineering, Beijing University of Technology, Beijing, China

Abstract: Sustainable development is the overarching goal in the current construction industry, where accurate prediction and control of energy consumption during building operation and maintenance are key research areas. Large infrastructures, characterized by their vast spaces and numerous interrelated factors, present challenges for real-time dynamic control through manual inspection and adjustment, leading to

significant energy wastage. In this study, a smart operation and maintenance model was established based on digital twin technology. Further, methods for data acquisition were developed using deep learning algorithms like natural language processing and image recognition. Subsequently, the LSTM algorithm was optimized for energy consumption prediction, and automatic control strategies were proposed based on the results. Finally, using the energy required for temperature control as an example, the model was validated with Olympic venue data and numerical simulation tools. The study achieved three major optimizations: (1) a multidimensional dynamic interaction operation and maintenance method for large infrastructure; (2) large-space energy consumption prediction incorporating event factors; (3) energy-saving automatic control strategies.
Keywords: Intelligent Operation and Maintenance, Digital Twin, Large Infrastructure Buildings, Sustainable, Energy Consumption Prediction

XII. LIST OF LISTENERS

Amor Vincent Canono Faculty of Computer Science, Union Christian College, Philippines ERCICSTR2302058
Hiroyuki Daimon Student Support Center, Toyohashi University of Technology, Japan ERCICSTR2303057
Tarik Ismail Hassan Khalel Department of computers and communications/ College of Engineering, Nawroz University, Duhok, Iraq ERCICSTR2303066
Joseph Olatunde Ogunfemi Managing Director, 4JS Power Engineering, Lagos, Nigeria ERCICSTR2303078
Reza Mohammadi Master Degree in Electrical Engineering, Shahid Rajaee Teacher Training University, Tehran, Iran ERCICSTR2305055
Dan Napelee Stem-B, Seattle Central College, Seattle, Washington, USA ERCICSTR2307054
Aprian Wara Torang Tandon School of Engineering, New York University, New York City, USA ERCICSTR2309066
Ihsan Abed Project Management, Lebanese French University, Erbil, Iraq ERCICSTR2309070
Julie Washek Student, UMass Chan Medical School, Worcester, United States ERCICSTR2315052

XIII. UPCOMING CONFERENCES:

https://straevents.org/stra

https://straevents.org/symposium

https://straweb.org/stra

https://straweb.org/symposium

EURASIA RESEARCH